

UNIVERSITY OF STRATHCLYDE

Microwave Propagation and Interaction in Fusion Plasma

DAVID J.L. WOODWARD

February 28, 2022



Abstract

The interactions between electromagnetic waves and magnetic fusion plasmas are fundamental to a broad range of technologies considered vital in achieving an efficient, energy producing tokamak. Sophisticated diagnostic instruments utilise the wave-plasma scattering mechanism to make non-invasive plasma measurements while powerful microwaves can be coupled to the plasma to drive heat or currents in the plasma. This research uses endeavours to deepen our understanding of these plasma-wave interactions by utilising a variety of numerical tools and performing novel modelling. The full-wave three-dimensional (3D), finite difference time domain (FDTD) code EMIT-3D is developed and utilised in conjunction with the Hermes fluid code using BOUT++ as a framework to study cross-polarisation Doppler-backscattering, in which a low-amplitude extraordinary (X) mode wave launched into the plasma is back-scattered into an ordinary (O) mode wave on magnetic field fluctuations, and the O mode is recorded and analysed. Benchmarking of the code was achieved by evaluating the simulated scaling relationships between the back-scattered signal strength against perturbation strength, and comparing this to theory. Excellent agreement was found. Further modelling investigated non-Wentzel-Kramers-Brillouin (WKB) effects and their pertinence towards back-scattering measurements and found some significant influences at experimentally relevant density length-scales. Furthermore, the forward scattered original-polar signals are identified to have major contributions towards the perceived back-scattered intensity under certain conditions, and an asymmetry in the back-scattered profile was also identified. In addition, for high-power microwaves having X mode polarisation, electron cyclotron current drive

(ECCD) was modelled using the Torbeam ray-tracing code. However, ECCD was shown to be an ineffective method of driving plasma current in high beta and high density plasmas where the fundamental cyclotron harmonics are cutoff. A promising alternative to ECCD at high plasma densities are electron Bernstein wave (EBW) heating and current drive, in which an O mode is converted into a slow X mode wave that in turn is converted into an EBW that can propagate into the dense plasma. The O-X mode conversion efficiency was studied with EMIT-3D, and excellent agreement was found between this 3D code and several other 2D codes in simple plasma geometries. However, for a few test cases the 3D code predicted lacklustre mode conversion efficiencies when a more complicated high beta MAST-U equilibrium was used in the modelling.

Contents

1	Energy and Magnetic Confinement Fusion	12
1.1	Energy	12
1.2	Magnetic Fusion	23
1.3	Fusion On Earth	27
2	Tokamak Physics	33
2.1	The Spherical Tokamak	33
2.1.1	The Plasma Edge	41
2.2	Micro-turbulence	43
2.3	Perturbation Diagnostics	51
2.3.1	Doppler Back-scattering (DBS)	51
2.3.2	Cross-polarisation Doppler Back-scattering (CP-DBS)	56
3	Cold Plasma Model	59
3.1	Cold Plasma Equations	60
3.1.1	Linearising	61
3.1.2	Slowly changing background limit	62
3.1.3	Plane Wave Solution	63
3.2	Cold Plasma Dispersion Relation	64
3.3	Cold Plasma Waves	69
3.3.1	Perpendicular Propagation	69
3.3.2	Parallel Propagation	74
3.3.3	Mode Conversion	76
3.4	WKB Approximation	78

4	Numerical modelling	83
4.1	Ray-tracing	83
4.2	Full-wave	87
5	EMIT-3D	91
5.1	Plasma Response	92
5.2	Normalisation	95
5.3	Computational Performance	97
5.4	Gaussian Beam	102
5.5	Boundaries	103
5.6	Pedestal	104
5.7	Importing Density and Magnetic Field Maps	104
5.7.1	Importing Background Profiles	105
5.7.2	Importing Perturbation Profiles	106
6	Numerical Turbulence	109
6.1	Kinetic Model	111
6.2	Fluid Model	113
6.2.1	The Hermes code	116
6.2.2	Analytic turbulence	126
7	DBS and CP-DBS Modelling Results	129
7.1	Preliminary Modelling	131
7.2	Simulation Setup	141
7.3	Detecting Backscattering Over Noise	145
7.4	Non-WKB Effects	149
7.5	Experimental Detection	156
7.6	Summary of the DBS and CP-DBS modelling	159

8	Microwave Plasma Heating and Current Drive	162
8.1	Electron Cyclotron Current Drive	162
8.1.1	ECCD in a high beta MAST-U equilibrium	166
8.1.2	ECCD in a low beta plasma with low number density	169
8.1.3	ECCD in a low beta plasmas with strong magnetic fields	172
8.1.4	Summery of the ECCD modelling	174
8.2	Electron Bernstein Wave Heating	177
8.2.1	Elliptical Polarisation	181
8.2.2	Benchmarking of full-wave simulation codes	184
8.2.3	MAST-U equilibria	195
8.2.4	Summery of the EBW heating modelling	204
9	Conclusion	205
9.1	Cross-polarisation Doppler back-scattering	205
9.2	Electron cyclotron current drive	207
9.3	Electron Bernstein wave heating	207
10	Appendix	209
10.1	Plane-wave solution to the homogeneous wave equation	209
10.2	Non-zero background flow dispersion relation	213

List of Figures

1	Analysis of the Human Development Index (HDI)	13
2	UK energy consumption	15
3	UK energy costs	16
4	UK energy sources year 2019	17
5	Remaining global fossil fuel supply	20
6	Quantum tunneling	25
7	Proton-proton chain	26
8	Binding energy per nucleon	27
9	Lawson criterion	28
10	Tokamak diagram	34
11	Edge transport barrier	42
12	Eigenmode structure of ETG and MTM	47
13	Poloidal monochromatic perturbation	51
14	Perturbed surface scattering	53
15	Cold plasma dispersion relation	77
16	Yee Cell	88
17	EMIT-3D performance	99
18	EMIT-3D efficiency scaling	101
19	H-mode plasma edge function	104
20	Hermes electron profiles	117
21	Hermes simulation profiles	120
22	Divergence of magnetic field profile	121
23	Average profile fluctuation strengths	123
24	Fourier analysis of perturbations	124
25	Analytical magnetic perturbations	127

26	Fourier analysis of monochromatic turbulence	128
27	Waveforms of density and magnetic turbulence	130
28	Spherical coordinate system	133
29	Density length-scale calculation	135
30	DBS and CP-DBS scaling	137
31	Re-construction of density profiles	140
32	Co-polar electric fields	142
33	Co-polar electric fields (amplified)	143
34	Time averaged RMS back-scattered signal	145
35	Scaling of DBS and CP-DBS	147
36	Back-scattered signal ratio	148
37	Hermes parameter scan	150
38	Analytical parameter scan	151
39	Cross-polar scattered signals	152
40	Flat-top density profile	153
41	Length-scale parameter scan	154
42	Cross-polar electric field with standard profile	157
43	Cross-polar electric field with flat-top profile	159
44	MAST-U schematic	165
45	High beta MAST-U equilibrium profiles	167
46	Simulated ECCD beam path and frequencies	168
47	Toroidal and poloidal launch sweep	169
48	Synthetic low beta plasma equilibrium	170
49	Low beta ECCD beam path and frequencies	171
50	Low beta toroidal and poloidal sweep	172
51	High magnetic field equilibrium - factor 2	174
52	High magnetic field - beam path and frequencies	175

53	Toroidal and poloidal sweep	176
54	High magnetic field equilibrium - factor 4	177
55	High magnetic field - beam path and frequencies	178
56	Toroidal and poloidal sweep	179
57	Linear polarisation mode conversion	182
58	Elliptical polarisation mode conversion	184
59	Time averaged measurement of divergence	185
60	Analysis of the beam divergence	186
61	Mode conversion window	188
62	Linear and elliptical comparison	191
63	Linear and elliptical comparison - perpendicular	192
64	Time-trace of the conversion efficiency	196
65	MAST-U high beta, high elongation equilibrium	198
66	O-SX mode conversion efficiency	199
67	O-SX mode elliptical conversion	201
68	Artificially flattened equilibrium	203

List of Tables

1	Fourier analysis of perturbations	125
2	Background number density parameters 1/2	139
3	Background number density parameters 2/2	140
4	Analysis of linear conversion	193
5	Analysis of elliptical conversion	194
6	O-SX mode conversion results	202

Acknowledgements

While this work is my own, it was only achieved because of the incredible support structure freely given to me. My supervisors, Drs. Kevin Ronald and Bengt Eliasson are not only world class scientists but caring and empathetic people. The help that they continuously gave me was not only professional in nature, but personal, and was unparalleled in quality. The academics Prof. Roddy Vann and Dr. Alf Köhn hold my greatest respects and thanks for similar reasons, having repeatedly shown great care and interest in my professional development and well-being. Finally, my friend Dr. Liam Walker, who is one of the most intelligent, kind, and honest people I have ever met, was the eternal source of unconditional support and encouragement. Thank you all!

Declaration

I declare that the work presented in this thesis, except where it is otherwise stated, is based on my own research. It is being submitted for the degree of PhD in physics at the University of Strathclyde and has not been submitted previously for a degree in this or any other university.

1 Energy and Magnetic Confinement Fusion

1.1 Energy

The world has an energy problem. A high and consistent consumption of energy has become a cornerstone of life in the developed world. The developing world uses comparatively almost no energy at all. However, this is set to change. Consumption of energy has been seen to be related to economic development. Considering that the international political environment is almost uniquely described by capitalism, economic power is the primary driving force for the development of the quality of human life on earth. It is then both unreasonable and selfish to expect the developing world to curb its industrial revolution in favour of lowering carbon emissions because this would drastically diminish their ability to lift themselves out of poverty and improve the quality of life of their citizens.

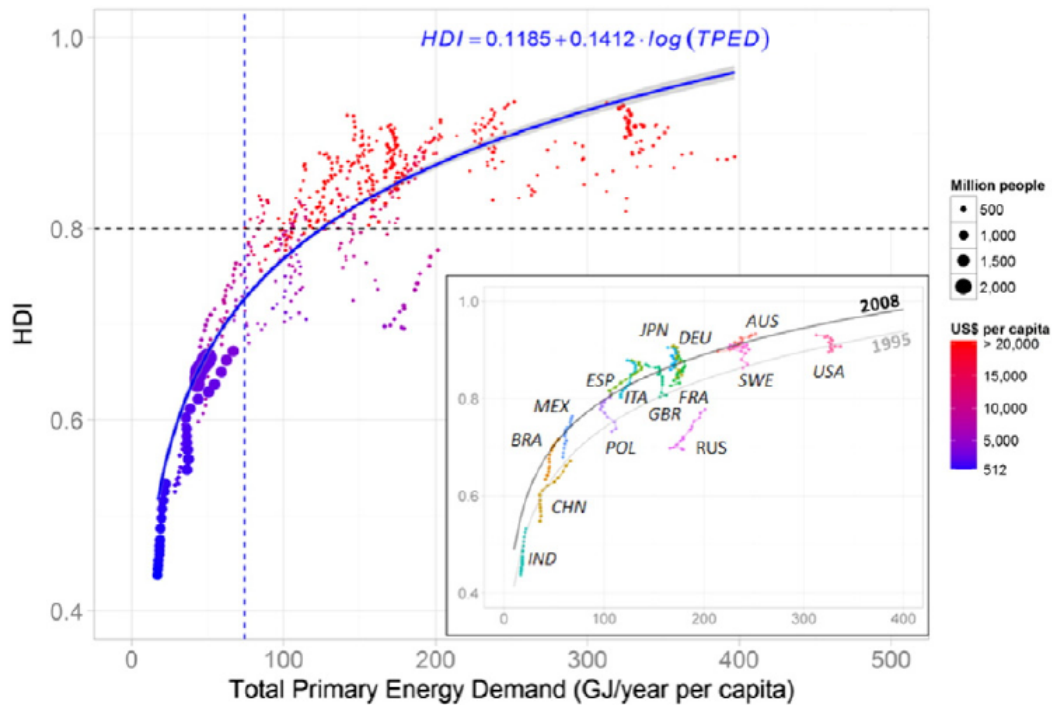


Figure 1: Analysis of the Human Development Index (HDI) against Total Primary Energy Demand (TPED) for a range of countries. Each dot corresponds to a country, with the colour and size indicating US\$ per capita, and population size, respectively. The vertical blue line represents the minimum TPED associated with an $HDI > 0.8$. The inset describes a selection of 15 countries between the years 1995 and 2008. Each data point refers to a year within this range, and its color is solely indented for ease of interpretation. Figure taken from [1].

Figure 1 illustrates this idea by representing the Human Development Index (HDI) [2] against Total Primary Energy Demand (TPED). There are certain outlying data points, however the correlation between TPED and HDI is clear. Countries with an HDI less than 0.8 are considered to be developing nations, and we make the assumption that these nations will aggressively seek to increase their HDI. The increase of HDI is attained through an increase in economic power (one metric

being the US\$ per capita) and this relationship is discussed in [1]. This increase in economic power results in the upward shift in TPED. It remains to be seen whether or not this large, global upward shift in TPED can be done in a sustainable manner. Only 25% of the worlds population [3] live in countries with an HDI greater than 0.8 and as such the increase in TPED from the remaining 75% will be challenging to manage. As the demand on the Earth's resources used for energy production increases, the cost will increase and the availability will decrease. This raises national security concerns and warrants far reaching considerations of future energy policies. Clearly, for the benefit of climate change it would be desirable to source this increase in the demand of energy from renewable sources. However, for the aforementioned reasons it is likely that the choice of energy sources will be largely decided from an economic viewpoint. It is difficult to make an assessment into energy security on a global scale, since the availability of natural resources varies so significantly. This analysis is then limited to an assessment of the energy security to the UK.

The UK's reliance on fossil fuels is often mis-represented. This is because most analyses considers only the methods by which the UK generates electricity. This is misleading because the UK energy consumption is not limited to the consumption of electricity. There are other significant demands, such as the energy required for cars, lorries, gas heating, or aerospace transport. In 2019 the UK consumed a total of $2203.9TWh$. Of this total amount only $328.74TWh$ was electrical energy [4]. This majority reliance on non-electric energy is illustrated in figure 2.

This is intensely pertinent to the discussion of energy security because the reliance on non-electric energy is provided almost exclusively by fossil fuels. Due to the growth of developing countries putting progressive strain on access to natural resources, the overwhelming reliance of the UK on fossil fuels can be considered a serious security concern. The electrification of Britain will put immense pressure on the electrical generation industry, and capacity will inevitably need to be drasti-

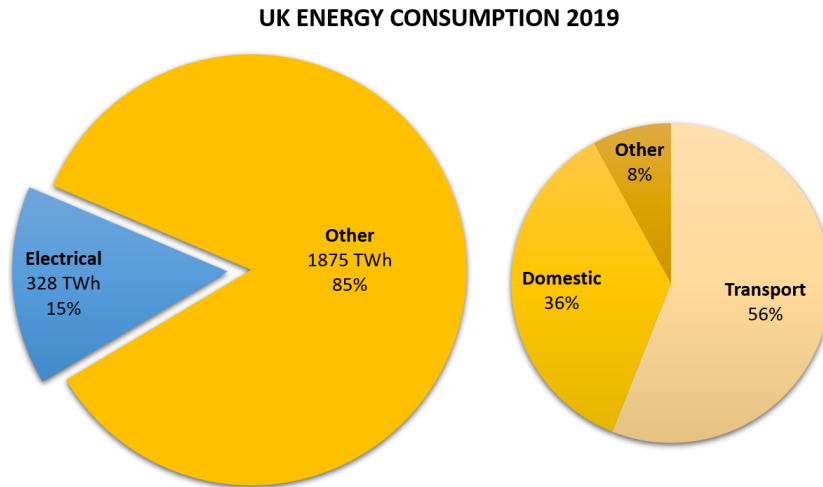


Figure 2: The consumption of electricity in the UK represented as a fraction of the total consumption of energy. Data taken from [4, 5].

cally increased. Figure 2 is reflected in the rest of this document by differentiating between the consumption of *energy* and *electrical energy*. An average European consumes $125kWh$ of energy per day [6]. The UK is relatively conservative, as the annual consumption of $2203.9TWh$ amounts to $90.6kWh$ per person, per day. This is an important number because it is ultimately the amount of energy which will, at some point, need to be provided by renewable electrical energy production.

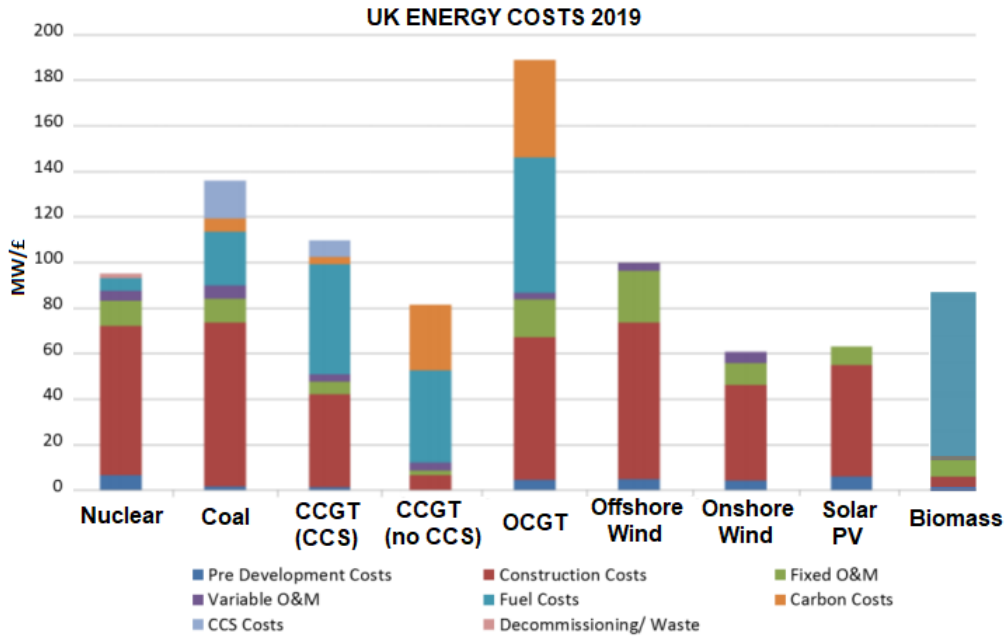


Figure 3: Levelised energy cost estimates for the UK. A levelised analysis indicates that all expenses, from birth until decommissioning, are accounted for. Abbreviated for clarity are Operation and Maintenance (O&M), Closed Circuit Gas Turbine (CCGT), Open Circuit Gas Turbine (OCGT), and Carbon Capture Storage (CSS). Figure taken from [7].

How this electrical energy is produced, and how quickly the UK needs to shift from fossil fuel reliance depends on the cost of renewable energy sources, and the projected access to pertinent fossil fuels. Figure 3 shows an analysis of the cost to the UK for a range of frequently used energy sources. The analysis is 'levelised' meaning that the overall costs are broken down into components. The five most cost effective options, from most expensive to cheapest are nuclear fission, biomass, gas, solar and wind. Considering the earlier political statement regarding the fundamental incentive to pursue a higher HDI via an increase in US\$ per capita (and therefore TPED), we would expect the sources providing energy to the UK to be reflective

of the most cost effective. Figure 4 shows where the UK sourced its *electricity* for 2019. The five aforementioned cost effective energy sources make up 90.4% of the UK's electricity supply.

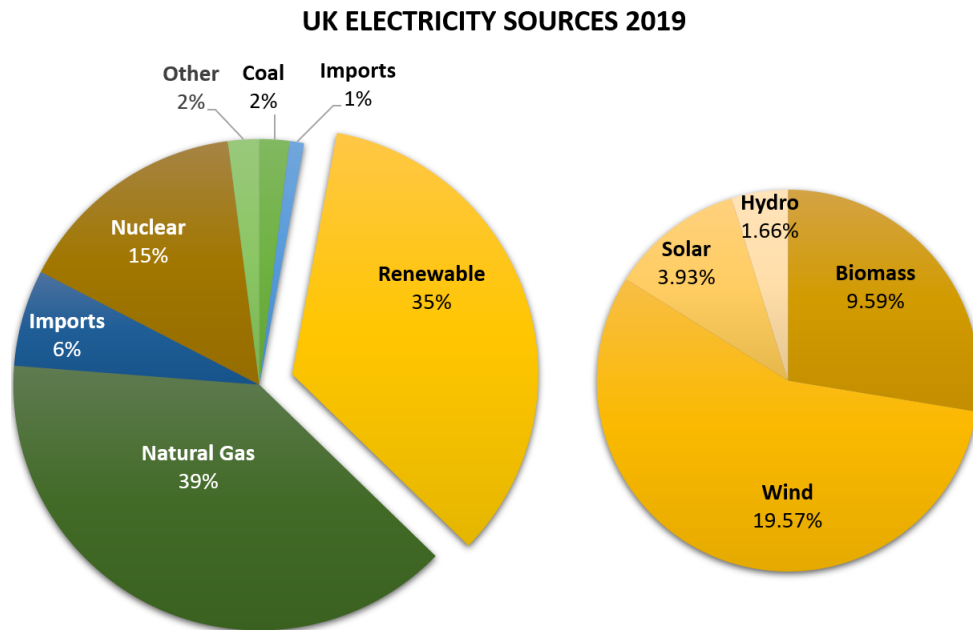


Figure 4: Where the UK sources its electricity for the year 2019 [5] .

It may be surprising that the UK gets only 35.0% of its electricity from renewable sources, considering that wind and solar energy are the two cheapest forms of energy available to the UK. This is doubly interesting when we consider the natural wind resources the UK has. Compared to France and Germany, the UK has a 33% and 71% greater potential for wind energy, respectively. The reason for this is likely to be energy density. Wind energy is cheap, however it suffers from poor energy density. The energy density of onshore and offshore wind energy is approximately $2W/m^2$ and $3W/m^2$, respectively. Onshore space is expensive and restricted, and deep-offshore space is considered economically unviable. If 33% of the UK's shallow offshore space is used for wind turbines the farms would produce $16kWh$ per day, per

person. This amounts to only 17.6% of the UK's annual *energy* consumption. A wind farm capable of delivering enough power to completely satisfy the needs of the UK would need to be 3.67 times the size of Great Britain. A feat of engineering on this scale is unreasonable. The other renewable sources are incapable of making a major contribution towards fulfilling the large overall energy demand. Hydro suffers from very weak energy densities. Lowlands and highlands have densities of $0.02W/m^2$ and $0.24W/m^2$, respectively. The UK is estimated to be capable of producing a maximum of $1.5kWh$ per day, per person with hydro. This amounts to only 1.7% of the UK's energy consumption and would represent increasing the size of the UK hydroelectric industry by a factor of 7.0 [6]. Biomass is already operating near its maximum capabilities. The UK current sources approximately $6.37kWh$ per day, per person from domestic and imported biomass. The government estimates that if biomass policies are aggressively pursued, by 2050 the UK would be capable of delivering $8.02kWh$ of energy per day per person [8]. This amounts to only 8.9% of the current UK energy demands. In regards to solar, there are two technologies; solar thermal and solar voltaic. Solar thermal has a much higher efficiency of converting sunlight to useful energy at about 50%, although only provides low grade (high entropy) thermal energy. Solar voltaic provides electrical energy but at a much lower efficiency of 20%. While solar thermal may be useful for moving away from fossil fuel driven heating, only solar voltaic is considered here for ease of comparison. At the equator the energy density of sunlight is about $1000W/m^2$. However, Britain lies at an approximate latitude of 52° . This, combined with average annual cloud cover, and seasonal effects causes the average energy density of sunlight on south-facing rooftops in the UK to be about $110W/m^2$. Covering every single south facing roof-top in the UK with 20% efficiency solar voltaic panels would yield approximately $5kWh$ per day, per person. This amounts to 5.5% of the UK's energy consumption. Using strongly generous assumptions, wind(17.6%), solar(5.5%),

hydroelectric(1.7%), and bioenergy(8.9%) have the potential of providing a total of 33.7% of the UK's current energy consumption.

In consideration of the inability of renewable sources to meet our energy demands we are forced to conclude that we will be highly dependent on non-renewable energy sources for the foreseeable future. Figure 5 represents an estimate into the number of years of supply of non-renewable energy source remaining globally, assuming that current rates of consumption are maintained, which is optimistic. It is of particular concern to the security of the UK's energy supply to compare figures 4 and 5. Britain is a country which critically depends on natural gas. This problem becomes more concerning when we consider the distribution of natural gas sources. Figure 5 shows that there are globally only about 50 years of supply of global natural gas resources remaining. However, Europe has some of the lowest relative natural gas supplies in the world, and has only 18 years of supply. The implications of this are serious; relying on imports of a diminishing gas supply from countries outside of the single market puts the reliability of British electricity supply into question. While the UK imports negligible amounts of gas from Russia, in 2019 it imported approximately 62% of its gas from Norway [9]. Norway is a politically stable country with strong cultural and historic ties to the UK. In other words this source of gas is unlikely to suddenly stop flowing, and the British government considers the Norwegian supply to be beneficial to the energy diversity of the UK. The British government ranked the UK third highest out of all European countries on the gas supply index, which is a measure of energy security. However, in 2019 the EU imported 27% of its gas supply from Russia, and a further approximate 20% of its gas from Norway. The implications of this must be considered.

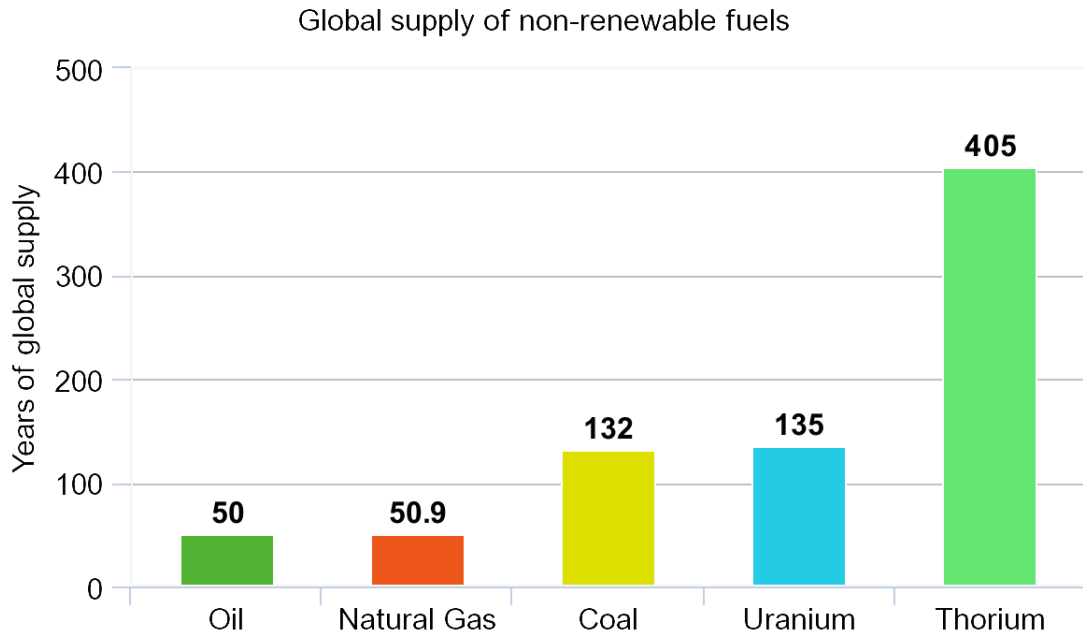


Figure 5: Remaining global non-renewable fuels remaining assuming current rate of consumption is maintained. Data gathered from [10, 11].

Russia is not considered to be as politically stable as Norway. Should the Russian gas supply cease then the EU would find itself heavily short on gas. Considering the close relationship between Norway and the EU, it is conceivable that the Norwegian gas supply would be more heavily relied upon to make up the loss of the Russian supply. Should this occur, the UK may no longer be able to fulfil its gas import demands from a reduced Norwegian source. Due to its inability to meet the demand for gas by indigenous production, the reliance of the UK on gas as a major source of its energy has strong implications for national security. The UK must consider radically shifting its energy production away from natural gas and fossil fuels generally. Considering that we have already ruled out self-sufficiency on renewable sources there are four ways to fill the energy deficit left by fossil fuels.

Firstly, the UK could follow the French in depending on nuclear fission. In 1999

the French government noted that French energy security was a significant concern. At the time France imported more than 50% of its energy. What followed was a massive investment in nuclear fission power. As of 2017 France sources about 75% of its energy from nuclear fission, has become one of the worlds largest energy exporters, a world leading country in the development of nuclear fission technology, and has extremely low carbon emission per capita at 11% lower than the UK [12, 13]. While successful, the French energy program is overshadowed by the ethical considerations of fission energy. The probability of a major nuclear disaster can never be reduced to zero, and nuclear fission power stations may present vulnerable targets for terrorism or foreign powers. This ironically presents a problem for French energy security. Additionally, French fission reactions are dependent on uranium which, similarly to fossil fuels, has a limited global supply. There is an estimated 135 years of supply of uranium remaining. It may also be possible to use thorium as a substitute; it is thought that the abundance of thorium in the Earth's crust is 3-5 times greater than that of uranium, and the supply of thorium would be expected to last 405 years.

Secondly, it would be possible to heavily invest in coal energy. The combustion of coal releases tremendous amounts of carbon dioxide and as a result of this, the use of coal energy in developed nations comes with some political backlash. Additionally, the use of coal in the UK is very expensive at more than double the cost of wind power. Using Carbon Capture Storage (CSS) technologies [14] the carbon emissions of coal can be drastically reduced to become far less than natural gas, and comparable to solar. The use of CSS would incur additional cost, increasing the cost of coal energy by about 25%. The UK itself has almost no coal reserves. However, the EU as a whole does have a significant amount [10]. Most of this coal is concentrated in Germany, Poland, and the Ukraine. While the use of coal imports from these countries is certainly a possibility, a sharp decline in the gas supply to the EU may drastically increase the demand for coal all over the EU. Therefore, this

does not represent a reliable path to energy security.

Thirdly, it would be possible to invest in massive solar energy projects in Northern Africa or the Arabian peninsula. These areas specifically because there is significant amounts of desert which is mostly unusable for other projects, and the intensity of sunlight is high. A solar farm the size of Wales (21025km^2) would be able to provide 100% of the *energy* demands of the UK. A solar farm the size of Germany would completely fulfil the energy demands of Europe. Figuratively it is easier to illustrate the size of a singular solar farm, however realistically projects supporting building these solar farms would likely build many smaller farms, as opposed to a single massive farm. This would increase the security of the energy supply by reducing the importance of any single farm. The three countries near to Europe with the highest economic potential for solar energy are Algeria ($169\text{PWh}/y$), Libya ($140\text{PWh}/y$), and Saudi Arabia ($125\text{PWh}/y$). The whole of Europe consumes approximately $23\text{PWh}/y$ [6]. While Algeria and Libya are acutely unstable countries due to civil unrest, economic instability, and civil war, Saudi Arabia is politically stable and maintains strong, positive relations with the UK and its allies. Solar farms on the Arabian peninsula are a potentially potent source of renewable energy for the UK and Europe. Unfortunately the energy security of the UK would still be a concern as the UK would be permanently, and heavily reliant on a single third party.

The fourth and final option would be to invest in nuclear fusion technologies. As a concept fusion energy is very much still in the research and development phase. However, the UK is a world leader in the development of spherical tokamak technologies, and magnetic confinement fusion poses a real possibility of enabling the UK to become totally energy independent from the rest of the world. The experimental machine ITER is currently being built in Cadarache in France. This machine will be capable of producing 500MW of power, however as a purely experimental machine

it will not deliver any of this to a national grid. The ITER machine is scheduled to achieve its first plasma at the end of 2025. One of the main goals of the ITER project is to demonstrate the capability for fusion energy. The subsequent fusion machines are DEMO and (PROTO). These are estimated to be capable of producing 2.0(4.5)GW of power. This amounts to an incredible 43.21(97.22)kWh per day, per person. This is 47.7%(107.3%) of the UK's energy demand. Fusion energy has the unique potential to give the UK total energy independence, and the possibility of powering the entire UK with a single power plant cannot be overstated. While this is an exciting possibility, it is unlikely to happen due to the energy security implications. Large-scale fusion power plants would share some of the security and environmental concerns of fission plants, due to the handling and storing of nuclear material. In fusion, this can be somewhat mitigated by minimising the stored fuel on site [15], which is possible due to tritium breeding techniques (sec. 1.3). However, one of the most severe concerns would be the total reliance on a single piece of infrastructure for energy. This would be a high values target in human conflict situations, be it terrorism or other, and implies that it is unlikely that fusion reactors will be ran nationally. An international collaboration, building and sharing a number of fusion plants would reducing the reliance on any particular site. As a contributor to the *ITER* project, and provider of strong investment in the cutting edge spherical tokamak machine MAST-U, the UK is uniquely well positioned with trained scientists and fusion technologies to take advantage of fusion energy.

1.2 Magnetic Fusion

We say that we will put the sun into a box. The idea is pretty. The problem is, we don't know how to make the box. - Sebastien Balibar, Director of Research, CNRS.

Most methods for generating energy rely indirectly on the Sun. The Sun radiates energy to Earth via photons. This energy heats pockets of air, causing the wind

which we can harvest via turbines. The wind drives the waves on the oceans which we utilise with wave-energy. These photons also drive the evaporation of water, which condenses into rainfall. Hydro-power generates energy by utilising the gravitational potential energy of water falling in high-altitude regions. Non-renewable fossil fuel energy sources have similar origins. Plant life directly harvests the energy radiating from the sun via photosynthesis. This energy is then transferred down a chain of animal life, first by herbivore then carnivore animals. The deaths of these living organisms over millions of years formed the coal, oil, and gas that we burn today.

The sun itself produces energy through nuclear fusion. Classically this process occurs via a plasma having sufficient pressure for the nuclei to overcome the long-range coulomb repulsive force in order to bind together through the short-range strong nuclear force and form new, heavier nuclei. However, the core of the Sun is quite cold at approximately 15 million degrees Celsius, doesn't meet these conditions and should be unable to fuse hydrogen together. Obviously the Sun does undergo fusion and the mechanism by which this occurred remained a mystery until the discovery of quantum mechanics in the 1920s. Observing figure 6, as two nuclei approach one another the separation between them obviously decreases. As a result the magnitude of the repulsive coulomb force (which is inversely proportional to the square of separation) grows. The Sun is not hot enough for hydrogen nuclei to overcome this *coulomb barrier* ($U(R_0)$). However, with quantum mechanics the hydrogen nuclei are not considered as particles but as waves. The waveform by which the hydrogen nuclei are described has a non-vanishing probability of passing some portion of its energy through the coulomb repulsive barrier, reaching a point of separation whereby the attractive strong nuclear forces are dominant. Even at room temperature the probability for this reaction is non-zero, although negligible. Also in the Sun, the probability of this reaction to occurring is very low, and is partly why all of the Sun's hydrogen does not simply ignite in a single instant, but

burns slowly over billions of years.

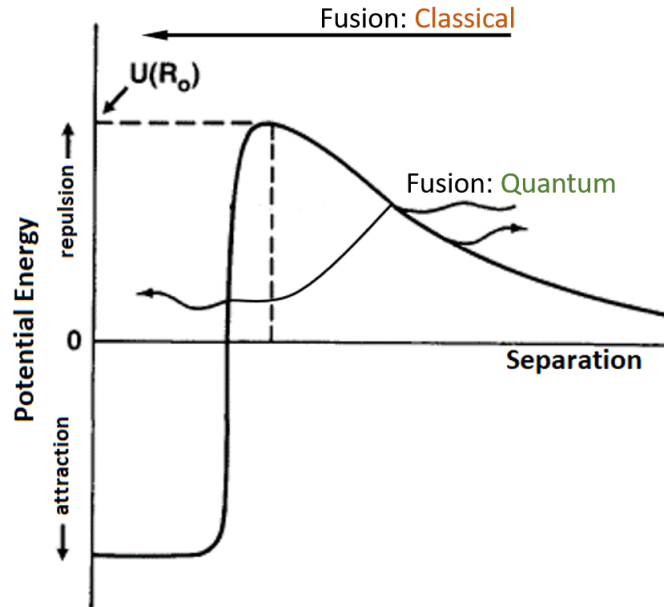


Figure 6: Graphical representation of how quantum tunneling can allow two ions with energy less than the coulomb barrier (U_{R_0}) to fuse. For two ions of equal charge the position of the coulomb barrier is dictated by the point of "contact" $R_0 = R_a + R_b$ for the species a , and b . Underlying image taken from [16].

In the Sun (and in most stars) the chain of reactions by which hydrogen is formed into helium is called the proton-proton (pp) chain. This reaction chain consists of 3 stages which can be seen in figure 7. Due to the requirement of quantum tunneling, this reaction has a low probability of occurring. Additionally, the pp chain is very slow, taking billions of years to complete the overall combination of hydrogen into helium. Fortunately the Sun is massive, with a mass of roughly 333000 times that of the Earth. This sheer size allows for these unlikely, and slow fusion reactions to be sufficient to keep the sun burning and providing the conditions for life on Earth.

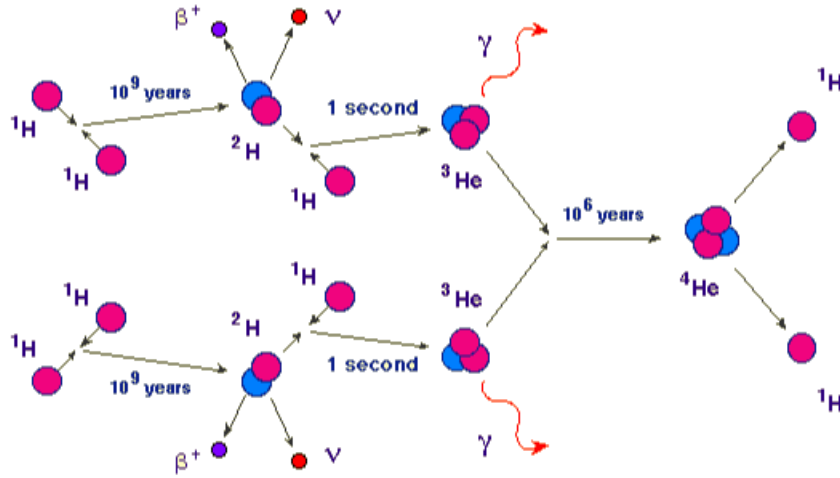


Figure 7: The proton-proton chain by which the Sun generates energy. Image taken with consent from [17]

Fusing hydrogen into helium releases significant amounts of energy. This is because the binding energy of helium is greater than that of hydrogen. The binding energy of an element (figure 8) can be thought of as the amount of energy which is *released* when an element is formed. A nucleus which is said to be held strongly by the nuclear force (high binding energy) exists in a low energy state. It has released the energy (mass, $E = mc^2$) its nucleons once held to become more stable. As such, the binding energy is a measure of the minimum amount of energy that would need to be returned to the nucleus in order to break it apart. The shape of the binding energy curve in figure 8 is a result of the strengths and ranges of the attractive strong nuclear and repulsive coulomb forces. A detailed description of this is given in [18]. Light, and heavy nuclei are not as strongly bound as the intermediate elements which is why it is easier to facilitate nuclear reactions with the very light hydrogen (fusion, joining) and very heavy uranium (fission, breaking).

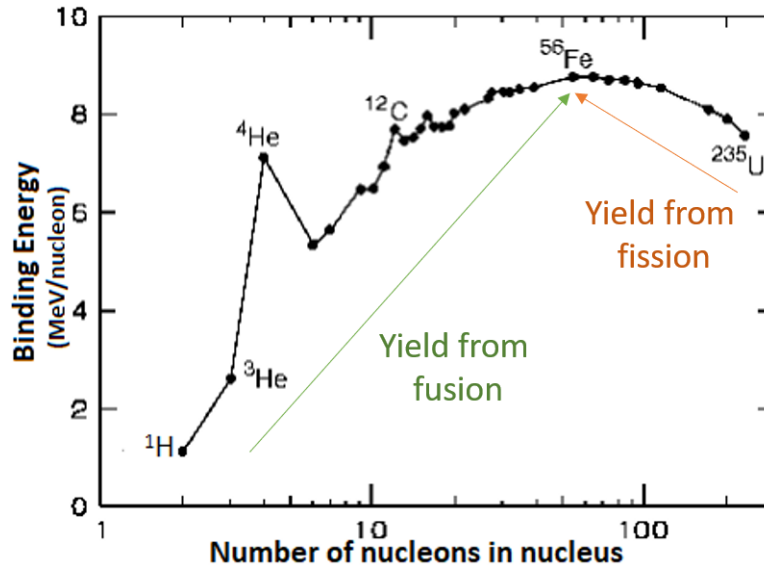


Figure 8: Binding energy per nucleon [19]

1.3 Fusion On Earth

Fusion via the proton-proton chain is unsuitable for our purposes on Earth because the reaction takes billions of years. There are a number of different fuels suitable for fusion on Earth and the most realistic make use of isotopes of hydrogen, ^2H (deuterium) and ^3H (tritium). Observing figure 8 the difference in binding energies between hydrogen and helium indicates that there would be significant yield if one could fuse hydrogen into helium. Fusing nuclei together is difficult. This is especially true on Earth because we do not have the strong gravitational fields of a star to help generate massive pressures. Figure 9 shows the Lawson criterion, which is a commonly used metric to illustrate under what conditions we might expect ignition to occur in a controlled magnetically confined plasma, and included in the diagram are three of the most suitable fuels, deuterium-tritium (D-T), deuterium-deuterium (D-D) and deuterium-helium-3 (D- ^3He). Ignition refers to the critical point when the heat being generated by the fusion reaction has become equal to the heat losses.

Achieving a burning plasma (a plasma that has ignited) is an essential part of magnetic fusion energy, whereby the expensive external heating systems can be turned off.

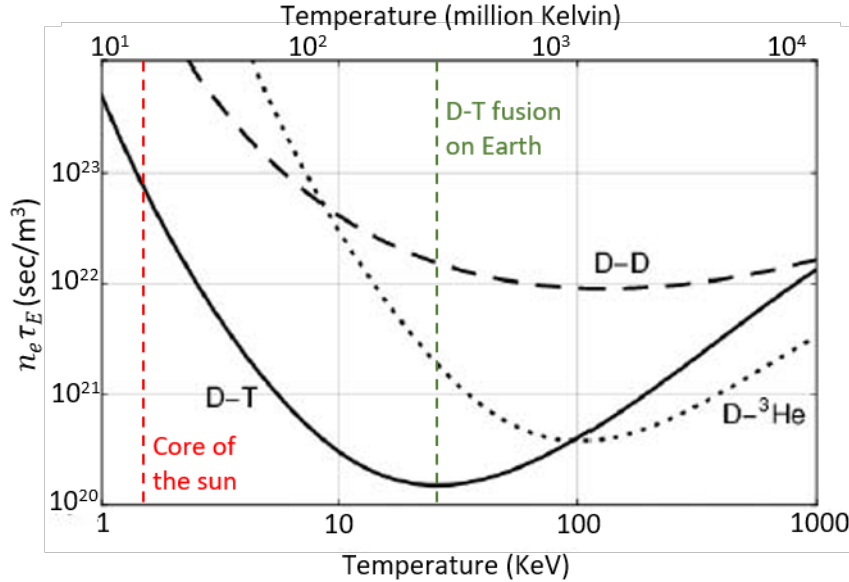
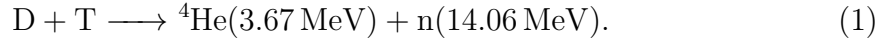


Figure 9: Lawson criterion for ignition. The vertical red and green lines indicate the temperature of the core of the Sun, and the optimal temperature for D-T fusion on Earth. n_e is the electron number density and τ_E is the plasma confinement time. Image from [20].

Of the three fuels indicated in figure 9 the D-T nuclear reaction (solid line) is the easiest to achieve. This is because a D-T plasma has the lowest ignition requirements of temperature, with a minimum at the trough of the D-T line. On the horizontal axis this trough lies at approximately 150 million degrees Kelvin which is about 10 times hotter than the core of the Sun. This extreme temperature is required partly because we lack the Sun's massive gravitational energy, and we compensate for this with increased temperature. The D-T reaction goes as

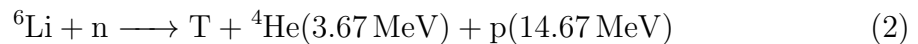


The ${}^4\text{He}$ product is considered ‘ash’ and is a harmless, waste product that must be removed from the plasma. The mechanism for removal is an area of active research [21]. Removing helium ash is important due to bremsstrahlung power losses (photon-radiative losses due to charged particle interaction and de-acceleration) scaling as the square of the species charge. While removing the ${}^4\text{He}$ mass from the plasma is necessary, the energy of the ${}^4\text{He}$ species is utilised in order to maintain a burning plasma. With good confinement it is possible for a fusion plasma to become self-sustaining if the kinetic energy from the ${}^4\text{He}$ is kept within the plasma. It takes a tremendous amount of electrical energy to bring a fusion plasma up to reaction conditions. Starting at 50% tritium the DEMO plasma is estimated [22] to require 20GWh which would cost about 2 million dollars. Utilising the kinetic energy of the ${}^4\text{He}$ ash to keep the reaction running without the need for external heating is essential for economic reasons. Despite this huge initial electrical requirement fusion energy is modelled [23] to cost between $\$0.13/kWh$ and $\$0.24/kWh$ (inflation accounted for). The current price of electricity is about $\$0.13/kWh$. While only the optimistic predictions for the rate of fusion energy fall within acceptable economic limits, the costs will fall significantly with subsequent reactor iterations.

Other than D-T there are other possible fuels for fusion. From figure 9 we can see the Lawson criterion for D-D (dashed line) and D- ${}^3\text{He}$ (dotted line). These other fuels are considerably harder to fuse. Note that figure 9 has a logarithmic scale. To reach ignition with D-D fuel, a temperature of 10 times higher than that of D-T fusion would need to be achieved, in combination of a near 100 fold increase of $n_e\tau_E$. D- ${}^3\text{He}$ fusion again requires a 10 times hotter plasma, but only requires about 3 times higher $n_e\tau_E$. For these alternative fuels, the temperature required to access the troughs of the Lawson criterion are immense, approaching 1000 million

degrees kelvin, or 67 times hotter than the core of the Sun. In addition to this, the fusion reactor must be more sophisticated to be capable of holding a plasma under fusible conditions at the higher $n_e\tau_E$. There are strong benefits to using these alternative fuels, but due to the tough requirements for ignition they would most likely only be seriously considered in the distant future after the use of tritium raises more difficulties than can be justified.

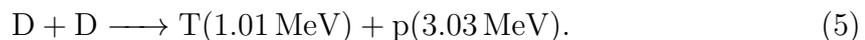
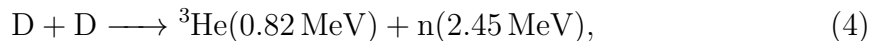
Deuterium is a naturally occurring heavy isotope of hydrogen. In every ton of seawater there is approximately 33g of deuterium. Assuming that Earth has a population of 6 billion people, there would be sufficient deuterium to supply each person with 10000kWh every day for 1,000,000 years [6]. Considering that the average European uses only 125kWh per day, deuterium on Earth is essentially limitless. Tritium is another heavy isotope of hydrogen but it only occurs naturally in trace amounts due to it being radioactive and having a half-life of 12.5 years. It is extremely expensive. The US government is manufacturing tritium for use in nuclear weapons at an estimated cost of \$102,000,000 per kg [24] (adjusted for inflation). Estimates into the global supply capabilities and consumption of tritium for fusion energy have been made, and the most pessimistic scenario predicts that the fusion community will exhaust its supply of tritium as early as 2045 [22]. This poses an immense risk and challenge to fusion energy. The solution to this problem is generally seen as the on-site production of tritium from lithium by



or



The fusion reactors will be surrounded by lithium, which will absorb the high-energy 14.06MeV neutrons given off by the D-T reactions as shown in equation (1), generating further tritium which can be stored and used in future reactions. While this idea is comforting, lithium *breeding blankets* are relatively experimentally un-researched. This is concerning and represents a strong challenge to the fusion community, since the theoretically predicted Tritium Breeding Ratios (TBRs) are uncomfortably close to break-even (1.0) and generally range from 1.0 to 1.20 [25–27]. Due to its atomic number, lithium is one of the most abundant elements on Earth. However, the demand of lithium is high and is increasing. Its use in batteries had lead to immense worldwide demand. Compared to this, the requirements of lithium for fusion energy tritium breeding are likely to be negligible. Regardless, the global supply of lithium is estimated to stretch to a maximum of 435 years [28]. With the exclusion of far-future technologies such as space mining, this limited supply indicates that D-T fusion will need to be phased out in favour of other, more challenging fusible materials. D-D reactions are exciting due to the sheer abundance of deuterium and the safe, non-radioactive nature of the fuel. Two possible D-D reactions are



Both of these reactions release far less energy than the D-T reaction, but may be able to be used in a similar manner to D-T fusion. The ${}^3\text{He}$ would contribute towards the self-sufficiency of the burning plasma but would be considered ash and would ultimately need to be removed from the plasma similarly to the ${}^4\text{He}$ ash in the D-T reaction. The tritium produced through equation 5 would quickly be consumed according to equation (1). The proton product would not exit the plasma; it is a

charged particle which would not be able to escape the magnetic fields which provide confinement. Its kinetic energy would contribute to heating the plasma. $D-{}^3\text{He}$ is another feasible reaction, but not addressed in detail here due to the far-future nature of sourcing ${}^3\text{He}$. Over billions of years solar winds have deposited significant amounts of ${}^3\text{He}$ on the moon's surface. The most likely candidate for ${}^3\text{He}$ sourcing would be moon mining operations.

2 Tokamak Physics

2.1 The Spherical Tokamak

Magnetic Confinement Fusion (MCF) aims to maintain a sustained reaction which will generate energy consistently over time. The conventional tokamak is the most advanced reactor design and a diagram can be seen in figure 10 (left). For Deuterium-Tritium (D-T) ignition the core of the plasma must be heated to 150 million degrees. The significant amount of energy required to do this must be *confined*. This means that the fuel (plasma) must be prevented from touching the vacuum vessel (see fig 10), but also that the hotter fuel towards the core of the plasma must not mix or transfer heat to the cooler parts of the plasma towards the edge. At these temperatures the plasma (D-T fuel) is a ‘soup’ of charged (ionised) particles, and confinement is achieved by application of a series of magnetic fields which hold the plasma in place. In figure 10 the toroidal (blue) and poloidal (red) electromagnets help generate the magnetic fields that confine the plasma. The magnetic fields are named according to the toroidal-poloidal coordinate system; the toroidal dimension is parallel to the toroidal magnets, and similar for the poloidal. The resulting magnetic fields form magnetic flux surfaces; nested torus shaped surfaces which restrict the outward (radial) movement of ions due to the Lorentz force $\mathbf{F} = q(\mathbf{E} + \mathbf{V} \times \mathbf{B})$ which includes a restoring force ($\mathbf{F} = q(\mathbf{V} \times \mathbf{B})$) that acts to resist the movement of charged particles perpendicular to magnetic field lines. The charged particles which make up the plasma have high mobility parallel to these flux surfaces but low mobility perpendicular to them.

Heating the core of the plasma to 150 million degrees is not easy. In order to produce the confining poloidal magnetic fields, it is necessary to drive a strong toroidal plasma current. This current heats the plasma through ohmic friction to

about 20 million degrees. This upper limit is due to a general property of plasma to become more conductive (less resistive) at higher temperatures.

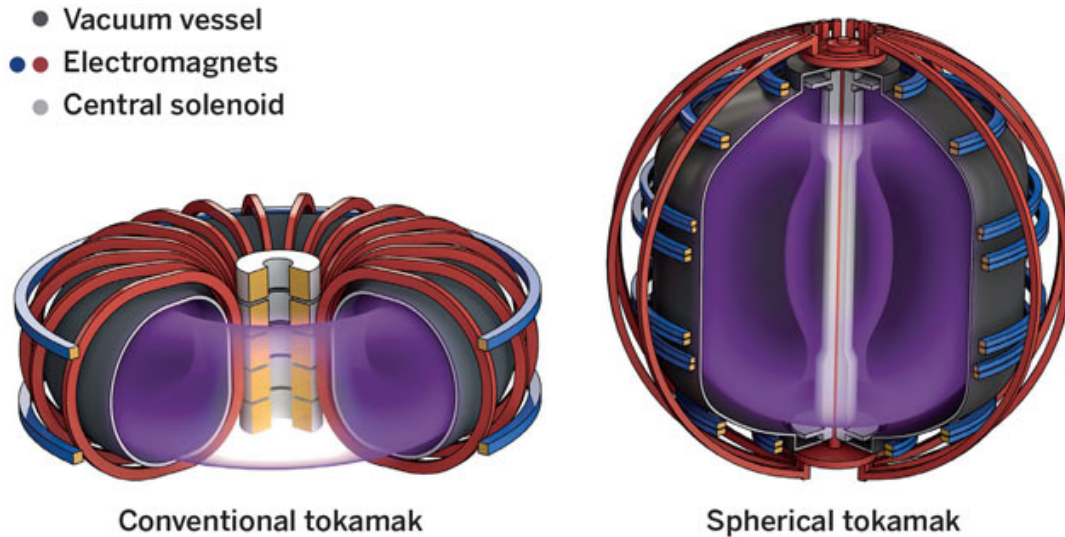


Figure 10: Diagram of a conventional and spherical tokamak. Image from [29].

Heating the plasma further can be done with microwaves (Electron Cyclotron Resonance Heating (ECRH) or Electron Bernstein Wave (EBW) heating), or with particle accelerators (Neutral Beam Injection (NBI)). ECRH [30] uses powerful microwaves which couple to the harmonics of the electron cyclotron frequency (similar to a microwave oven, except with plasma instead of water). EBW heating [31] also couples powerful microwaves to resonant frequencies but it is a much more challenging technique. It is better suited to heating over-dense plasmas (see sec. 3.3) where the microwaves are ‘cutoff’ and do not have direct access to the low resonant harmonics near the plasma core.

A toroidal plasma device capable of reliably delivering fusion energy to an electrical network would need to have high plasma beta (defined below), good confinement, and steady state operation while maintaining a compact form and using as low as

possible magnetic field strengths. The Spherical Tokamak (ST) concept shown in figure 10 (right) is an advancement of the conventional tokamak concept, and is under development to address these points. The advantages that the ST promises derive from its aspect ratio. That is $A = R/a$ where R is the radius of the machine ('major radius'), and a is the horizontal radius of the plasma itself ('minor radius'). These advantages will now be explained. The plasma beta

$$\beta = \frac{P_{Thermal}}{P_{Magnetic}}, \quad (6)$$

refers to the ratio between the thermal pressure of the sustained plasma

$$P_{Thermal} = n_e k_B T_e, \quad (7)$$

to the magnetic pressure that the background magnetic field is generating to confine it

$$P_{Magnetic} = \frac{B^2}{2\mu_0}, \quad (8)$$

where n_e , k_B , T_e , B , and μ_0 are electron number density, Boltzmann's constant, electron temperature, magnetic field strength, and permeability of free space, respectively.

The thermal pressure (Eq. (7)) of the plasma is driven by the high temperature and high number density requirements for fusion. The magnetic pressure (Eq. (8)) is driven by the high electrical powers used to power the toroidal/poloidal electromagnets, and drive a toroidal current to generate the background magnetic field. The plasma beta is then a measure of machine efficiency. It measures a particular machine's attainable fusion parameters and compares it to the magnetic fields which are required to confine such a plasma. As such, a higher plasma beta is favourable. The confinement of a toroidal fusion device refers to the degree by which heat and

particles are unable to move radially, across magnetic flux surfaces. A machine with exceptional confinement will see very little radial movement. Effective confinement is essential for an efficient fusion plasma device as the properties of the plasma at its core will need to continuously be maintained at the required temperature and density for fusion. Radial movement of any heat or density from the plasma core into a colder region which has a lower reaction rate is undesirable as it reduces the efficiency of the machine. The beta in STs is generally higher because of the shape of the machine [32]; much higher safety factors can arise naturally in STs due to the tight aspect ratio. This allows for a reduction in the poloidal background magnetic field strength, reducing the denominator in the safety factor,

$$q = \frac{rB_\phi}{RB_\theta}, \quad (9)$$

which is a measure of MagnetoHydroDynamic (MHD) stability. A fall below $q = 2$ results in the plasma becoming magnetohydrodynamically unstable. Small MHD kink (current driven) or ballooning (pressure driven) instabilities [33] can grow, leading to macroscopic changes to the plasma topology, causing severe degradation of energy confinement or termination of the plasma. The magnetic pitch angle on the outboard side of a ST is aggressive, and at first glance this would imply a low safety factor. However, on the inboard side the pitch angle is more modest, and crucially the toroidal circumference tiny when compared to the poloidal circumference. This inboard difference in circumference vastly increases the safety factor, as the path-length of a single toroidal rotation is very small. In a conventional tokamak the toroidal circumference on the inboard side remains large. As a result stronger background magnetic fields (B_0) are required to keep the safety factor above 2.0. Since the plasma beta scales as $\beta \propto B_0^{-2}$ modest reductions of the background magnetic field strength yield aggressive improvements in the plasma beta. The reductions in the required B_0 when comparing conventional tokamaks to STs are far from modest.

Typically B_0 is a factor of 10 lower on STs than conventional tokamaks [34]. The magnetic fields in ITER (conventional tokamak) can reach $11.8T$ whereas MAST-U (spherical tokamak) has a maximum of field of $0.8T$. Furthermore, the upper limit of achievable beta (the Troyon limit [35]) on a particular machine is limited by the amount of drivable current. Driving higher currents reduces the safety factor, as it increases the magnetic pitch angle. Since STs exhibit a much higher safety factor, they are capable of driving much higher currents, and as such the beta limit becomes higher. The highest plasma beta (normalised, $\beta_N = \beta I/aB$) achieved in a conventional tokamak was in DIII-D at $\beta = 0.125(4.3)$ [36]. On a ST the record is held by PEGASUS at $\beta \approx 1.0(14.0)$ [37]. Simply put, ST machines are more efficient.

Current conventional and spherical tokamak devices cannot be operated continuously. This is because the plasma current is generated by ramping of a DC current through a solenoid positioned at the centre of the toroidal device. Faraday's law

$$\nabla \times \mathbf{E} = -\frac{\partial \mathbf{B}}{\partial t} \quad (10)$$

dictates that this results in a time varying magnetic field. Should this magnetic field interact with another electrically conductive material (i.e. a plasma), there exists some magnetic flux

$$\Phi_B = \int \int_S \mathbf{B} \cdot d\mathbf{S}. \quad (11)$$

Since the original DC current is being ramped, the magnetic flux is varying with time which drives an electromotive force (EMF)

$$\epsilon = \frac{\partial \Phi_B}{\partial t}. \quad (12)$$

Should the EMF be driven in a looped material with some resistance (i.e. a toroidal plasma) a current will arise as

$$V = \epsilon - Ir, \tag{13}$$

where V is the voltage, I is the current density, and r is the internal resistance of the looped conductor (the toroidal plasma). This induced current is vital to the plasma confinement as it is required to negate the effects of particle drifts. The realisation that one cannot continue to ramp a current indefinitely means that such devices must be "pulsed". In other words these devices cannot maintain the toroidal current indefinitely. A fusion device which is generating energy for an electrical grid will need to be able to run continuously in 'steady state'. Current tokamak devices are experimental and as such running in a pulsed configuration can be satisfactory for the development of fusion research. While there are toroidal steady state machines [38] which do not rely on the central solenoid, these Stellarator devices are fundamentally different to tokamak devices and do not present a solution to the pulsed issue of tokamaks. It is possible to directly drive current using microwaves with Electron Cyclotron Current Drive (ECCD). This technique couples powerful microwaves to the electron cyclotron harmonics within the plasma. Electrons travelling in one toroidal direction are selectively heated by matching to the desired gyro-frequency direction. Since the resistivity of a fully ionised plasma scales inversely with temperature (see eq. (173) below), this translates into a reduced collisional frequency and therefore increase in current density. It is also possible to directly drive current with negative ion Neutral Beam Injection (NBI) [39]. Negative ions are accelerated with strong electric fields before being passed through a neutraliser. The now neutral atoms are fired into the tokamak along one toroidal direction and couple their energy to the plasma through collisions. These ions can be deuterium or tritium [40] for fuelling purposes, and negative ionisation is favoured due to better energy retention post-neutralisation at higher energies. NBI has been seen [41] on the conventional JT-60U tokamak to be capable of delivering 1MA of toroidal

current using 3.5MW of power. This can be put into perspective by observing the requirements of NBI in the ITER [42] tokamak which seeks to drive 15MA with 20MW of NBI power. However, the main focus for non-inductive current drive in spherical tokamak machines is the bootstrap current [43]. This current is intrinsically driven by the interactions between trapped (by magnetic fields) and passing particles. The bootstrap current scales linearly with beta, and monotonically with elongation [44]. The high beta advantages of STs have already been discussed, and STs naturally tend towards elongation [45], which describes the shape of the plasma. Defined as $\kappa = b/a$ where b is the vertical plasma radius, and a is the horizontal plasma radius, elongated plasmas have been associated with increased plasma stability. Spherical Tokamak Power Plant design [44] has estimated that the pressure gradient driven bootstrap current may be capable of driving up to 82% of the required toroidal current. The remainder of the required current could be attained through combinations of the diamagnetic currents which naturally arise in a toroidal fusion device (estimated 8%), and small amounts from auxiliary (ECCD, NBI) current drive systems.

Smaller machines are more favourable from a political perspective. While the plasma volume is an important factor in the achievable fusion power, it must be balanced with the cost of the machine. Increasing the major radius of a device simply requires more infrastructure which drives up costs. Private investment into magnetic confinement fusion energy is small, but some does exist [46]. There are also other serious and reputable companies pursuing variations of magnetic fusion [47, 48]. The reasons for poor private investment into magnetic confinement fusion are likely complex, although cost and investor faith in the technology will be major factors. The future of fusion energy lies with commercialisation of the technology. Currently MCF is very much in a development stage which relies on vast governmental financial support. Similarly to the development of consumer electronics such as

the smart-phone [49], private companies will at some stage need to take over when the MCF concept becomes sufficiently developed. In the interest of fusion energy it is desirable that this becomes feasible as quickly as possible. To facilitate this, current public research spending must be carefully targeted towards machines with reasonable build-times, costs, and risks associated with them. These considerations favour small, compact, and efficient machines with low magnetic field requirements, such as the ST.

ST machines [32] have been, and continue to be, developed around the world with the goal of an affordable and efficient fusion power-plant in mind. The UK has seen particularly strong investment with START (1990-1998) [50], and then MAST (1999-2013) [51] which has recently been upgraded to MAST-U (2019-pres.) [52]. The USA has two machines; PEGASUS (2003-2019) [53] which is currently being upgraded to Urania [54], and NSTX (1999-2015) [55] which was recently upgraded to become NSTX-U (2015-pres.) [56]. Worldwide other ST experiments have been built such as GLOBUS-M and GLOBUS-M2 (2001-pres.) [57, 58] (Russian Federation, 2001-pres.), ETE [59] (Brazil, 2000-pres.), and TS-3/4 [60] (Japan). The conventional tokamak is further ahead than the ST in its development cycle. This is evident from the current world records for various important parameters. Virtually all the records are held by conventional tokamaks, with the exception of the highest achieved plasma beta. With the massive international investments being put into the ITER project [61] it is likely that the conventional tokamak will achieve a burning plasma long before any ST machine. The Q-factor is a measure of machine performance, and measures the ratio between energy supplied to a fusion device and energy yielded by fusion reactions. A machine reaching break-even would correspond to $Q = 1.0$. The current world record is $Q = 0.22$ [62] and was achieved in 1997 by the CCFE team on the JET tokamak. ITER is predicted to be the first fusion machine to achieve a burning plasma, and is predicted to obtain $Q = 10.0$. The ST concept is

at heart designed to address the concerns relating to the commercialisation of fusion energy. Favouring small, compact devices with high plasma betas, and low magnetic fields, future machines delivering energy to consumers will likely be STs as opposed to conventional tokamaks.

2.1.1 The Plasma Edge

During low-confinement (L-Mode) experiments on ASDEX [63] a new operational, high-confinement (H-mode) regime was discovered. This accidental discovery of the transition between the L-mode to H-mode plasma immediately saw an improvement of the confinement time by almost a factor of 2. H-mode transition occurs due to a sharp region of strongly improved confinement arising near the plasma edge. This region is named an edge transport barrier, and a sharp increase in edge number density and pressure gradient follows its formation. The region encapsulating the plasma edge up until the top of the high density gradient is called the *pedestal*. Further towards the core, the number density continues to increase more gently and the core profile is said to ‘sit’ on the formed pedestal. One possible explanation for the transition into H-mode is that there exists a sudden and sharp increase in the radial electric field (E_r) strength which causes enhanced stability by inducing a localised change in the plasma particle flow profile.

Figure 11 details experiments on DIII-D [64] which showed that a sudden peak in E_r (fig. 11a) correlates well to a simultaneous increase in ion temperature (fig. 11b), electron temperature (fig. 11c), and electron density (fig. 11d).

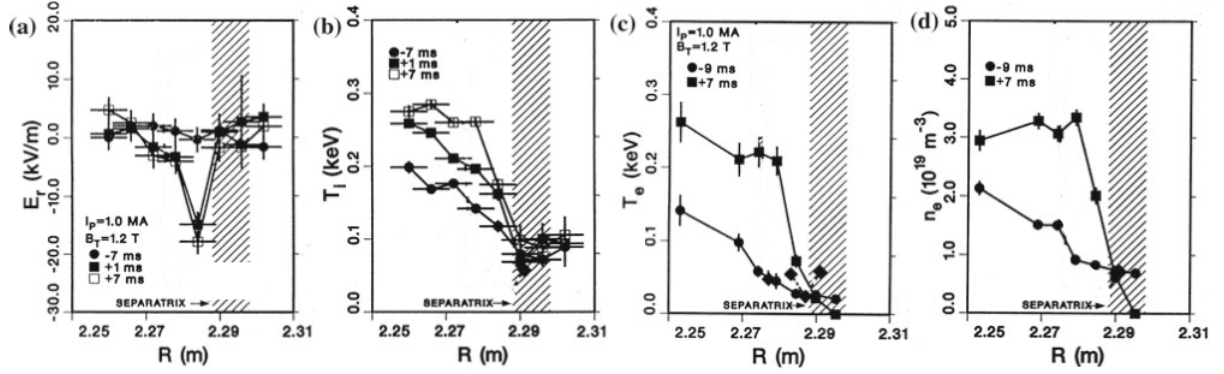


Figure 11: DIII-D tokamak data showing **a)** The radial electric field E_r at various times vs major radius R showing the sharp increase in E_r around the edge transport barrier roughly 0.5cm in from the separatrix edge. **b)** The ion temperature T_i at various times vs R . **c)** Electron temperature T_e vs R and **d)** electron number density n_e vs R [64].

The gradient in the radial electric field $\frac{dE_r}{dr}$ causes sheared flow. Sheared flow has been seen to suppress certain micro instabilities [65], and this sudden change in E_r may cause a localised increase of poloidal ($v_\theta = \frac{-E_r}{B_0}$) and toroidal ($v_\phi = -\frac{E_r B_\theta}{B_0^2}$) flow velocity [64].

The increase in plasma edge density and temperature gradients has a positive effect on the overall performance of a toroidal fusion device. The center of the plasma can more easily reach higher temperatures and densities as the core profiles sits on the top of the pedestal profile. The H-mode has become a standard operating regime for tokamak fusion. Despite this, the L-mode to H-mode transition mechanism remains poorly understood, and empirically derived [66] power threshold formulae are used to estimate the transition point based on fundamental tokamak parameters. While considered baseline for modern tokamak reactors, H-mode and the formation of the pedestal comes with challenges. Small-scale (less than the ion gyro-radius) turbulence or ‘microturbulence’ is driven by the harsh temperature and

density gradients that the pedestal provides. This turbulence is not well understood but is thought to have significant influence over the transport mechanisms in the plasma edge. Refined and controlled confinement, and pedestal control are crucial aspects of running a tokamak plasma for fusion energy. Understanding the underlying mechanisms by which microinstabilities arise and allow for cross-field transport is cutting edge science.

2.2 Micro-turbulence

Fundamentally, Spherical Tokamaks (ST)s have a tight aspect ratio of $a/R \approx 1$, where a is the minor radius and R is the major radius. This is much higher than in conventional tokamaks and enables operation at higher plasma betas. Because of this tight aspect ratio ST plasmas exhibit strong toroidal geometry, meaning that the plasma curvature, and magnetic field pitch angles can be high. This has been seen to influence particle dynamics and the stability of the plasma, in part due to the growth of microinstabilities. Microinstabilities are any non-catastrophic plasma perturbations that have a wavelength smaller than the ion Larmor radius

$$r_i = \frac{m_i v_{\perp}}{q B_0}, \quad (14)$$

which is a measure of how tightly ions are gyrating around the magnetic field lines, where m_i is the ion mass, v_{\perp} is the ion velocity perpendicular to the background magnetic field, q is the ion charge, and B_0 is the background magnetic field strength. These instabilities are driven by strong density $\partial n / \partial r$ and temperature $\partial T / \partial r$ gradients, where r is the radial spatial dimension.

The transition from L-mode into H-mode causes the formation of the ‘pedestal’ region at the plasma edge. Roughly a few centimeters in width, the pedestal is a narrow region with very strong density and temperature gradients. This formation is fantastic for fusion energy, and is able to arise due to the development of the edge

transport barrier. However, due to the strong plasma gradients microinstabilities can become particularly unstable in this region. There are different types of microinstabilities and they are grouped into ‘modes’ based on their physical characteristics. The Electron Temperature Gradient (ETG) modes and Microtearing Modes (MTMs) are two examples of these non-catastrophic turbulent modes. They are of particular interest because they are thought to cause significant ‘anomalous’ cross field transport; transport of particles, momentum, and heat via mechanisms outside of the scope of coulomb collisions in quiescent plasmas (neoclassical transport). These instabilities may constrain the height and shape of the pedestal profiles, and their influence is often described by their contribution towards electron diffusivity, χ_e . This diffusivity is the rate at which heat or particles are transported radially, and can be determined experimentally [67] by observing how the heat or density distribution profiles vary with space and time. Physically, electrostatic turbulence such as the ETG mode can directly perturb the particle flux surfaces. Turbulence with strong magnetic field components such as the MTM can interact with the helical background magnetic field and produce densely packed magnetic islands between rational surfaces [68]. If the islands are large enough then field line "braiding" between overlapping magnetic island chains can cause the breakdown of rational surfaces (where the safety factor (eq. (9)) is a rational number) and coupling of fast parallel particle transport to radial transport.

The pedestal of H-mode plasmas generally grow over time; the peak temperature and number density becomes higher, and the gradients become steeper. This cannot continue indefinitely, and left unchecked the pedestal will become unstable and Edge Localised Modes (ELMs) will arise. ELMs are not microinstabilities, they are large, potentially catastrophic modes which can cause a violent eruption of heat and particles from the plasma. This eruption can damage the tokamak. Even if the plasma is not destroyed, the loss of heat and density causes a large and sud-

den drop in the plasma profiles; the peak density and temperature in the pedestal fall sharply, and the gradients weaken. The pedestal is shunted into a stable state, meaning that the ELMs are no longer present. The pedestal must recover from this, and the density and temperature profiles grow over time. Unchecked, this growth eventually causes the pedestal to become unstable again, which results in another ELM. ELMs are therefore cyclic instabilities. Since microinstabilities may have a substantial role in driving anomalous transport, it is thought that they could be decisive in the recovery and growth of the pedestal. Control over the microinstabilities arising in the plasma edge may not only provide superior confinement but also yield control over the growth of the pedestal. With advanced pedestal control it may be possible to avoid growing the pedestal into an unstable state, avoiding the onset of ELMs altogether. Furthermore, it has been seen [69] that strong plasma shaping combined with exquisite plasma control allows for even more advanced performance confinement regimes.

The ETG mode is generally considered electrostatic, however electromagnetic ETG modes do exist [70] and may also have significant implications for electron heat transport. The electrostatic component of the ETG mode is on the electron scale, with a spatial length-scale on the order of $\sqrt{\rho_e L_{T_e}}$ [71] where ρ_e is the electron Larmor radius. The mode's contribution towards electron diffusivity is approximately given [72] by

$$\chi_e \approx \frac{q v_{T_e}}{L_{n_e}} (\eta_e - \eta_{cr}) \left(\frac{c}{\omega_{pe}} \right)^2 \sqrt{\beta_e}, \quad (15)$$

where $q = \frac{RB_\theta}{rB_\phi}$ is the safety factor, $v_{T_e} = \sqrt{\frac{k_B T_e}{m_e}}$ is the thermal velocity, L_{n_e} is the electron density gradient length-scale, $\eta_e = \frac{L_{n_e}}{L_{T_e}}$ where L_{T_e} is the electron temperature gradient length-scale, ω_{pe} is the electron plasma frequency, and β_e is the electron plasma beta defined in equation (6). η_{cr} is the critical value of η_e , above which turbulence and transport increase locally. Values of $\chi_e \leq 0$ indicate that the ETG mode

is stable. Whereas $\chi_e > 0$ implies that the plasma conditions support some growth of the turbulence which will reduce the quality of the confinement. The density or temperature ‘length-scale’ refers to how strong the respective gradients are. A sharp gradient would have a small length-scale. The electron plasma frequency (ω_{pe}) is the characteristic frequency of the natural oscillations of the plasma. This frequency will be further addressed shortly, briefly in section 2.3.1, and more thoroughly in section 3. While expression (15) is only an approximation of the influence of the ETG towards diffusivity, an analysis yields insight into the drivers of the instability. Electron temperature is indeed important as an increase in T_e would drive up the plasma beta (which is generally desirable), as well as the thermal velocity. However, the diffusivity scales only weakly with these parameters. The driving term is primarily $(\eta_e - \eta_{cr})$ where η_e is the driver while η_{cr} is a restoring term determined by the experiment. Since η_e is the ratio between the density and the temperature length-scales, the prevalence of ETG induced electron transport requires a consideration of both L_{n_e} , and L_{T_e} . The ETG mode is characterised by ‘twisting parity’. Turbulence oscillates, and parity is a measure of the phase difference between the magnetic and density oscillations. These two components are together considered an ‘eigenmode’. This means that while a phase difference can exist, the density and magnetic components oscillate at the same frequency and their amplitudes increase/decrease in proportion to one another. Linear gyrokinetic simulations [73] modelling an H-mode plasma at the mid-plane, near the plasma edge, predict the eigenmode structures in figure 12 for the ETG mode (left) and the MTM (right). The horizontal axis in figure 12 is in degrees, and refers to the poloidal position, where 0° is the outboard mid-plane. The vertical axis is normalised amplitude. The ETG mode shows twisting parity, and the MTM shows tearing parity.

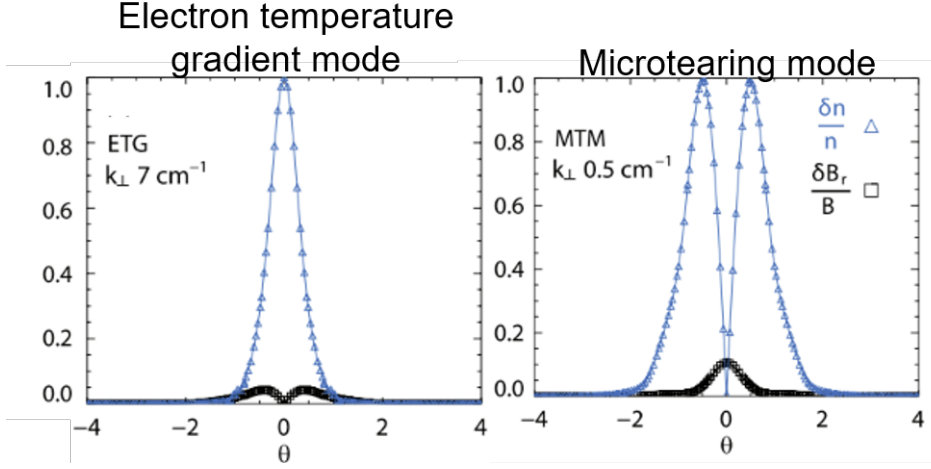


Figure 12: The linear gyrokinetic code GS2 [74] calculated eigenmode structures of the ETG mode (left) and the MTM (right) at the outboard midplane [73].

Micro Tearing Modes (MTMs) are electromagnetic modes and have been under research since the early 1960s. They are characterised by their tearing parity, and large toroidal and poloidal wavelengths. Typically comparable to the *ion* Larmor radius, MTM wavelengths are on a much larger scale than that of the ETG mode. One of the earliest analytical models of MTMs was developed in the late 1970s [75], and the main drive mechanism is shown to come from the electron temperature gradient. This analytical description recognises that the electron-ion collisional frequency is an important variable when considering the growth rate of MTMs, and three separate formulae were developed to describe the collisionless, semi-collisional, and collisional limits. The analytical expressions for these limits becomes increasingly complicated when moving from the collisionless to the collisional limit. However, a driver for all of these limits is the rate of change of the magnetic vector potential, $\partial A_z(r)/\partial r$, where $A_z(r)$ is the potential parallel to the toroidal dimension, which results in a poloidal magnetic field. An electron temperature gradient could induce a magnetic vector potential gradient due to currents induced according to Ampère’s law, by a

gradient in the thermal velocity, since $v_{T_e} = \sqrt{k_B T_e / m_e}$. MTMs are also sensitive to the magnetic shear length-scale [76], which refers to the degree by which the total magnetic field vector varies with the radial dimension. Research into the nature of MTMs is cutting edge science and is not fully understood. High beta devices (like the ST) have been seen to be particularly susceptible to electromagnetic turbulence, and a strong relationship between high beta and MTM growth rates has been seen [77]. This is understandable because higher beta plasmas would require relatively less energy for the magnetic field lines to become perturbed. Although [77] does admittedly also show that very high values of β cause suppression of MTMs, and the reason for this is described as unknown. Numerical simulations [78] have been seen to agree with an early analytical model [75] of the MTM, predicting that electron-ion collisions are a crucial factor in driving an unstable MTM. Whereas, more recent linear gyrokinetic simulations [77, 79] have observed MTM growth rates that are either insensitive, or even, inversely proportional to electron-ion collisionality. Indeed, MTMs have been seen [80, 81] to be unstable towards the plasma edge at low collisionalities. Such discrepancies may be caused by physical differences between MTMs in the core and MTMs in the edge of tokamak plasmas. There may also be a drive mechanism present at low collisionality caused by the interaction between trapped and passing particles [82, 83], an effect which the author's state should vanish without an energy dependent collisional operator. Contradicting this, MTM modes have been found to be unstable even in the presence of an energy *independent* collisional operator [84], and it is acknowledged that there are no known drivers that would make this possible. There are a number of different drivers for the MTM and there may be even more, unknown mechanisms for driving the instability. Nevertheless, it is at least accepted that the growth rate of MTMs has a strong dependence on both the electron temperature gradient $\partial T_e / \partial r$, and the magnetic shear scale length. These properties imply that MTMs could be particularly prevalent in the

edge of spherical tokamak plasmas. The magnetic shear at the plasma edge of such machines can be high. Additionally, the transition of the plasma into H-mode leads to the formation of a pedestal which can lead to large $\partial T_e/\partial r$. It has been theorised [68, 85] that the radial, anomalous, transport of heat and particles in a tokamak is caused by the degradation or destruction of the magnetic flux surfaces. This can cause the magnetic field to become stochastic in nature. It has been demonstrated [86] that in toroidal geometry a single turbulent mode can lead to the destruction of these surfaces. When this happens adjacent, destroyed surfaces can feature magnetic field lines with new stochastic properties that can ‘wander’, and overlap and connect to one another. This effect, sometimes referred to as magnetic field line braiding, can cause coupling between the radial transport and the far more rapid parallel transport, reducing the quality of the confinement of the machine. MTMs are thought to be an important contributor towards anomalous electron transport [81, 87, 88]; their influence towards the electron diffusivity can be described [89, 90] by

$$\chi_e = Rv_{Te} \left(\frac{\rho_e}{L_{Te}} \right)^2. \quad (16)$$

Similarly to the ETG mode, analysis of equation (16) shows that the MTM electron diffusivity is sensitive to the electron temperature gradient. Importantly, equation (15) suggests that the ETG electron diffusivity scales linearly with increasing electron temperature gradients, while equation (16) shows that the MTM scales quadratically with the gradient.

The MTM is not well understood. Both ETG and MTMs are suspected to be significant drivers of the anomalous transport in tokamaks, which can be two-order of magnitude greater than neoclassical transport [91]. H-mode plasmas are prone to sharp temperature gradients in the plasma edge, which has been shown to drive both ETG and MTMs. However, STs seem particularly susceptible to MTM turbulence

because of the higher beta, as well as a relationship between increased magnetic shear [92] (or similarly increased shear flow [93]) and the growth rate of the MTM. In order to improve the quality of confinement and develop the ST concept it is important to study and understand the transport mechanisms occurring in the plasma. Better understanding the MTM will be an important part of this study. Almost all of MTM research is theoretical. This is partly because they are challenging to measure experimentally. Developing a diagnostic technique that can discriminate between heavily electromagnetic (MTM) and electrostatic (ETG) modes would be tremendously helpful in the quest to understand microturbulence. The parity differences between various microturbulent modes may assist in this endeavour. Due to their opposing parity, discrimination between the ETG mode and the MTM may be possible with simultaneous measurements of their produced density ($\delta n/n$) and magnetic ($\delta B/B$) perturbation strengths. The ratio of $(\delta B/B)/(\delta n/n)$ would give an indication as to whether a detected mode was electrostatic, or electromagnetic. Analysis [73] indicates that this ratio is predicted to be 0.38 for the MTM and 0.019 for the ETG mode. The density perturbation strength ($\delta n/n$) could be measured with Doppler Back-Scattering (DBS); a conventional technique. Measuring the magnetic perturbation strength ($\delta B/B$) is far more challenging. This is partly because $\delta B/B$ is generally much weaker than $\delta n/n$, and harder to detect as a result. Cross-Polarisation Doppler Back-Scattering (CP-DBS) is a novel diagnostic technique which aims to measure $\delta B/B$, and is the main focus of this thesis. Successful development could enable access to previously unattainable experimental turbulence information which could advance our understanding of microturbulence, plasma transport, pedestal control, and plasma control.

2.3 Perturbation Diagnostics

2.3.1 Doppler Back-scattering (DBS)

Microturbulence can cause perturbations in a tokamak density gradient or magnetic field. The strengths of these perturbations are generally normalised to the relevant background quantity. For instance, density perturbation strengths are measured as $\delta n/n$ where δn is the perturbed density, and n is the background density. Similarly, the magnetic field perturbations are measured as $\delta B/B$. These perturbations are 3D structures. They are poloidally orientated modes which are extended along the background magnetic field lines due to the excellent parallel transport. This concept is illustrated in figure 13.

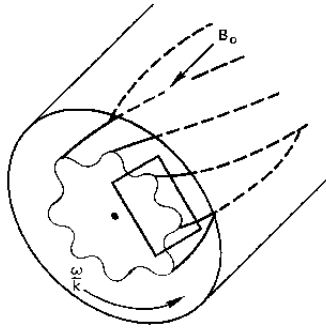


Figure 13: Simplified graphic showing how a poloidally orientated, single frequency perturbation can be extended along the background magnetic field lines [94].

Microturbulent modes therefore have wave-numbers both perpendicular (k_{\perp}), and parallel (k_{\parallel}) to the background magnetic field. These wave-numbers are physical properties which can be measured, and are one piece of information which can be used to help distinguish between different microturbulent modes. For example figure 12 indicates that the MTM has a much smaller wave-number than the ETG mode, at $k_{\perp} = 0.5cm^{-1}$ and $k_{\perp} = 7.0cm^{-1}$, respectively. Plasma theory is cov-

ered in section 3, however there is a single concept which needs to be mentioned before microwave diagnostics can be discussed. Consider a narrow beam of light (of microwave frequency for our purposes) propagating into the plasma, towards the core. If we say that this beam has a linear polarisation, orientated parallel to the background magnetic field, then it is said to be in ‘Ordinary-mode’ (O-mode) polarisation. This O-mode microwave beam will be propagating through increasingly dense plasma. This is important because the plasma itself is also oscillating; the electron plasma frequency

$$\omega_{pe} = \sqrt{\frac{n_e q_e^2}{m_e \epsilon_0}} \quad (17)$$

is a typical frequency of this plasma oscillation, where n_e is the electron number density, q_e is the electron charge, m_e is the electron mass, and ϵ_0 is the electric permittivity of free space. With increasing number density, the plasma frequency also increases. If the plasma frequency (i.e. number density) becomes high enough, the microwave can be ‘blocked’ from propagating further. The region of plasma that the microwave cannot enter is named ‘over-dense’, whereas the region which will allow propagation is named ‘under-dense’. When the microwave hits the boundary between the under-dense and over-dense plasma, it reflects. This boundary is named the ‘cut-off’ and this reflection is utilised in diagnostic techniques. If the cut-off is a homogeneous surface then specular reflection will occur. In reality, plasma turbulence causes the cut-off to be perturbed. The wave-front of the microwave reflects inhomogeneously from this surface resulting in ‘scattering’. That is, there are ordered reflections (fig. 14) propagating in various directions, depending on the wave-number spectrum of the perturbation at the cutoff.

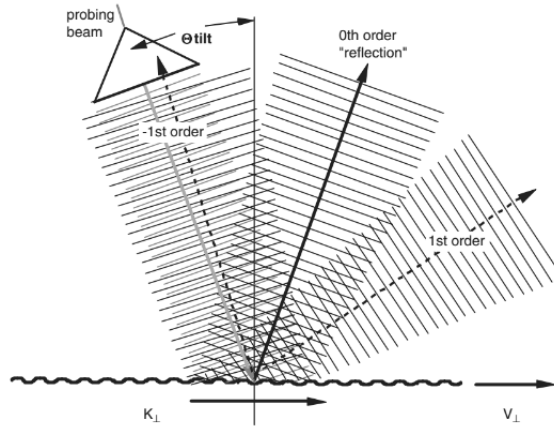


Figure 14: Scattering of a probing beam from a perturbed cut-off. The perturbation has a single wave-number k_{\perp} , and is moving poloidally with a velocity v_{\perp} [94].

The direction that the scattered microwave propagates in is predictable because it is a function of the perturbation wave-number (k_{\perp}). Figure 14 is a simplification, because the cut-off is oscillating with only a single frequency. This produces scattering in predictable ‘ordered’ directions. In reality, a plasma cut-off will be oscillating with many frequencies and the wave-number spectrum is said to be a continuum. This causes the ordered scattering to propagate in many directions. By *only* detecting the scattering which propagates directly back along the original beam path (back-scattering) we can use the Bragg condition to calculate the perturbation wave-number responsible;

$$k_{\perp} = 2k_i \sin(\theta_{tilt}), \quad (18)$$

where k_{\perp} is the perturbation wave-number that caused the back-scattering. The other quantities are defined by the experimental setup; k_i is the wave-number of the probing microwave, and θ_{tilt} is the angle which the microwave is launched at with respect to the normal to the density gradient (defined figuratively in fig.14). The Bragg condition allows back-scattering diagnostics to act as a sort of filter; a single

wave-number can be probed out of the wave-number continuum. Varying θ_{tilt} allows the wave-number continuum to be ‘scanned’, and by observing the relative intensity of the back-scattered signal, we can acquire the perturbation strength ($\delta n/n$ or $\delta B/B$) at a particular wave-number. Furthermore, any frequency change of the return signal is a result of Doppler shift. The turbulence causing the perturbed surface at the cut-off is rotating, and this non-zero poloidal velocity causes the frequency to shift. These three pieces of information are incredibly useful; observing only the back-scattered signal allows for measurement of a single wave-number (k_{\perp}), the back-scattered signal intensity gives the strength of the perturbation ($\delta n/n$ or $\delta B/B$) at this wave-number, and the frequency shift of the return signal gives the rotational velocity (v_{\perp}) of the perturbation wave-number that we are scattering from. These concepts underpin the mechanics of the diagnostic techniques Doppler Back-Scattering (DBS) and Cross-Polarisation Doppler Back-Scattering (CP-DBS).

DBS and CP-DBS are very similar techniques. A launched microwave interacts with a plasma cut-off, scatters, then yields information regarding the perpendicular (to the background magnetic field) orientated turbulence which is perturbing the cut-off surface. The interaction between the parallel orientated turbulence component k_{\parallel} and the probing beam k_i is generally negligible [95] as k_{\parallel} is too small to be detected by a reasonably sized probing beam. This is due to the fast parallel heat/particle transport causing parallel perturbation wave-lengths to be large. Back-scattering diagnostics are highly localised techniques. By this we mean that despite some back-scattered signals being emitted at every point along the beam path, the vast majority of the back-scattered power results from a narrow region of space at the cut-off. There are two main reasons for this. Firstly, as the probing beam approaches the cutoff the amplitude of the electric field \mathbf{E}_i increases. Generally, the back-scattering is strongest when \mathbf{E}_i is largest, and \mathbf{E}_i peaks at the cutoff. Secondly, the amplitude of the turbulence is proportional to $1/k_{\perp}^3$ [96], and the scattering efficiency between

the incident beam and this perturbation is proportional to $1/k_{\perp}^2$ [97]. One would then expect generally stronger scattering for lower wave numbers. As a probing beam propagates into higher densities, its wave number (k_i) decreases. Due to the aggressive scaling of perturbation strength, and scattering efficiency, the back-scattering is highly localised to minimal values of k_i which occur at the cutoff, as the wavelength increases. In essence, the decreasing of k_i , and the increasing of \mathbf{E}_i as the beam approaches the cut-off causes back-scattering diagnostics to be highly localised.

Fundamentally, the scattering mechanism is driven by the interaction between the incident radiation's electric field (\mathbf{E}_i) and the plasma electrons which are driven to oscillation to produce a scattered wave. This interaction can be described by the Lorentz force

$$\mathbf{F} = q(\mathbf{E}_i + \mathbf{v}_e \times \mathbf{B}), \quad (19)$$

where \mathbf{v}_e is the velocity of the electron, \mathbf{B} is some magnetic field that the electron is interacting with, and \mathbf{F} is the force on the electron which drives the oscillations and the resulting scattered beam. DBS is used to measure the density perturbations ($\delta n/n$) and the mechanism is understandable by ignoring the interaction between the electron velocity and the magnetic field. Equation 19 becomes

$$\mathbf{F} = q\mathbf{E}_i, \quad (20)$$

which is simply stating that a force exists when a charged particle is subjected to an electric field. The oscillating force on the electrons drives a current density which is given [98] by

$$\delta \mathbf{J}_{(\delta n_e)} = \frac{\delta n}{n} \bar{\sigma} \mathbf{E}_i, \quad (21)$$

where $\frac{\delta n}{n}$ is the normalised perturbed electron number density. Zou *et al.* have used the unmagnetised conductivity tensor such that $\bar{\sigma} = \frac{i\epsilon_0\omega_{pe}^2}{\omega}$ where ω_{pe} is the plasma frequency.

The DBS technique is powerful; highly localised, non-intrusive, and capable of providing information regarding the wave-number, amplitude, and poloidal rotational velocity of density turbulence. It can give a direct measurement of δn by observing the amplitude of the back-scattered wave generated by the oscillating current density $\delta\mathbf{J}_{(\delta n)}$. Additionally, the diagnostic equipment can be situated far from the plasma with the use of wave-guides. This would cause only a small amount of space in the reaction wall to be required, and would allow for easier shielding of the diagnostic instruments from the powerful neutron radiation that a fusion plasma will emit.

2.3.2 Cross-polarisation Doppler Back-scattering (CP-DBS)

Cross-polarisation Doppler back-scattering (CP-DBS) uses the same fundamental principles as the Doppler back-scattering (DBS) diagnostic technique, and as such it features similar benefits. The diagnostic is highly localised, non-intrusive, the equipment is relatively easy to fit onto a fusion device, and can provide information into perturbation wave-number, amplitude, and poloidal rotational velocity. Whereas DBS measures the density perturbation strength ($\delta n/n$) of turbulence at the cut-off, CP-DBS measures the magnetic perturbation strength ($\delta B/B$). Similarly to DBS the scattering of the probing beam is caused by coupling between the charged electrons and the incident beam's electric field. This can be described by the Lorentz force shown in equation (19). Where the DBS mechanism focused on the first term on the right hand side of this expression, the mechanism behind the CP-DBS diagnostic utilises the second term; the interaction between the velocity of the electron and some magnetic field. A probing beam drives electron oscillations

according to equation (20). Should this new velocity vector \mathbf{v}_e have a component which is perpendicular to a magnetic field, a secondary force will be applied;

$$\mathbf{F} = q_e \mathbf{v}_e \times \delta \mathbf{B}. \quad (22)$$

Similarly to the DBS interaction, a small oscillating current is generated. However, due to the cross-product relationship in equation (22) this new current $\delta \mathbf{J}_{(\delta \mathbf{B})}$ is orthogonal to \mathbf{E}_i . The current $\delta \mathbf{J}_{(\delta \mathbf{B})}$ generates a second scattered wave with polarization perpendicular to that of \mathbf{E}_i . By definition, this second scattered wave features a different polarisation to the launched beam. It is believed that by detecting back-scattering in the polarisation orthogonal to that of the incident wave, the magnetic perturbations can be measured.

Equation (22) illustrates the core principle behind the mechanism responsible for the microwave scattering into the cross-polarisation. However, a more thorough, qualitative representation of the perturbed current density is given [98] by

$$\delta \mathbf{J}_{(\delta \mathbf{B})} = \frac{\omega_{ce}}{\epsilon_0 \omega_{pe}^2} \bar{\boldsymbol{\sigma}} (\bar{\boldsymbol{\sigma}} \mathbf{E}_i \times \frac{\delta \mathbf{B}}{B}), \quad (23)$$

where $\bar{\boldsymbol{\sigma}}$ is the unperturbed plasma conductivity tensor, the form of which is dependent on the particular plasma model as is discussed in section 3. Notably, Zou *et al* features a typo where equation (23) has the ω_{ce} variable displayed incorrectly as ω .

CP-DBS has a number of potential issues [73] which stem from the weak amplitudes of the magnetic perturbations ($\delta B/B \ll \delta n/n$). The back-scattered signal is so weak that it may be difficult to detect over spurious noise emitted from other sources. Secondly, inaccuracies in matching the polarisation of the microwave to the magnetic field pitch angle at the scattering location can lead to spurious and misleading CP-DBS signals. Although, experimentally [73] the influence of the mismatch angle can be minimized by passing the probing beam, and back-scattered signal through the same polariser. Non-WKB effects are also concerning; there exists

no satisfactory analytical descriptions of electromagnetic waves interacting with a strongly inhomogenous medium. The Wentzel–Kramers–Brillouin (WKB) approximation can yield an analytical description of an electromagnetic wave interacting with a near-homogenous medium, as it relies on the assumption that the medium does not vary substantially. H-mode back-scattering diagnostics operate in aggressively inhomogenous plasmas, and there may be important physical effects that the WKB approximation cannot predict. The invalidity of the WKB solution in regards to back-scattering diagnostics, the lack of any better analytical descriptions, and the delicate nature of the CP-DBS signals are the primary drivers for the requirement of numerically expensive, full-wave numerical modelling. The WKB solution is discussed in section 3.4. This research aims to extend current scattering theory to better understand behaviour in the complex, anisotropic, inhomogenous pedestal region and to what extent these potential issues affect CP-DBS measurements.

3 Cold Plasma Model

In numerical modelling, it is often impractical to model all of the physical effects in a particular system. The broad range of physics occurs at an equally broad range of spatial and temporal scales, and depending on the aims of ones investigation some ranges of these scales may be unimportant. The research in this thesis consists of modelling very high frequency electromagnetic waves. The velocity and wave oscillation period is overwhelmingly faster than the plasma thermal motion and oscillations, which is to say that these plasma effects may be negligible; ignoring and excluding them will not significantly reduce the accuracy of the results. Physical approximations are very common in theoretical science because it can enable a reduction in the complexity required to model a system. This is advantageous because the system becomes easier to understand, and often lowers the computational demands required to solve a problem. The ‘cold plasma dispersion relation’ is frequently used for modelling electromagnetic wave propagation in fusion plasmas. This model assumes that the plasma is cold; the electrons and ions have zero background velocity, and thermal effects (such as thermal pressure) are ignored. Furthermore, due to the mass difference between electrons and the ions, the ions are much slower to respond to the stimuli of the electromagnetic wave. Due to the fast time-scales that the plasma-wave interactions take place over, we completely ignore the motion of ions in this model. Section 3.1 sets up the mathematical structure which section 3.2 uses to derive the cold plasma dispersion relation, which describes the propagation of electromagnetic waves in cold, magnetised plasma. In section 3.3 analysis is performed, identifying the possible modes of propagation, and finding some wave-plasma interactions of interest. Finally, in section 3.4 the WKB solution is derived, which allows for the modelling of electromagnetic waves in near-homogeneous mediums. The shortcomings of the WKB solution are identified,

and an argument against the use of it in of modelling Cross-Polarisation Doppler Back-Scattering (CP-DBS) is presented. This ultimately provides justification for the use of full-wave numerical modelling techniques.

3.1 Cold Plasma Equations

In order to numerically model the interactions between electromagnetic waves and plasma, we need to be able to describe the system mathematically. One of the most simple ways of doing this is by using the cold plasma dispersion relation. In order to derive this, we firstly need a closed system of equations which can describe the system; electromagnetic waves interacting with a cold plasma. Electromagnetic waves are coupled oscillations of electric and magnetic fields, and as such can be completely described with Faraday's and Ampère's laws;

$$\nabla \times \mathbf{E} = -\frac{\partial \mathbf{B}}{\partial t}, \quad (24)$$

$$\nabla \times \mathbf{B} = \mu_0 \mathbf{J} + \frac{1}{c^2} \frac{\partial \mathbf{E}}{\partial t}. \quad (25)$$

We need to be able to represent the interaction between the electromagnetic waves and the plasma. We could think of this as the forces that the electromagnetic waves exert on specific particles. The motion of an object as the result of some force can be described by the equation of motion,

$$\mathbf{F} = m\mathbf{a}. \quad (26)$$

Plasma particles are charged, and they are confined by strong magnetic fields. The force exerted on a charged particle due to electric and magnetic fields is described by the Lorentz force which is shown in equation (19). In order to describe the

acceleration of the particle we model the plasma as a fluid, and make use of the ‘convective derivative’

$$\frac{D}{Dt} = \frac{\partial}{\partial t} + (\mathbf{v} \cdot \nabla). \quad (27)$$

We will be using it to measure how the electromagnetic wave driven acceleration of an electron changes with time, while accounting for the background velocity of the plasma. The Lorentz force (eq. 19) combined with the equation of motion (eq. 26) and the convective derivative of acceleration gives a momentum force balance equation

$$q_e(\mathbf{E}_i + \mathbf{v} \times \mathbf{B}) = m \left[\frac{\partial \mathbf{v}}{\partial t} + (\mathbf{v} \cdot \nabla) \mathbf{v} \right]. \quad (28)$$

3.1.1 Linearising

‘Linearising’ is to take a variable and split it into two parts, an equilibrium quantity u_0 and a perturbed quantity u_1 . By doing this the variable can be expressed in the form of $u = u_0 + u_1$, where u_1 is assumed to be much smaller than u_0 . The assumption is then made that any two perturbed quantities multiplied together have a product so small we can consider it to be effectively 0. This simplifies the equations outlined in section 3.1 and makes them easier to work with. Using the cross product identity $\mathbf{A} \times (\mathbf{B} + \mathbf{C}) = (\mathbf{A} \times \mathbf{B}) + (\mathbf{A} \times \mathbf{C})$ our system of equations (eq.s (24), (25), and (28)) becomes

$$(\nabla \times \mathbf{E}_0) + (\nabla \times \mathbf{E}_1) = - \left(\frac{\partial \mathbf{B}_0}{\partial t} + \frac{\partial \mathbf{B}_1}{\partial t} \right), \quad (29)$$

$$(\nabla \times \mathbf{B}_0) + (\nabla \times \mathbf{B}_1) = \mu_0(\mathbf{J}_0 + \mathbf{J}_1) + \frac{1}{c^2} \frac{\partial \mathbf{E}_0}{\partial t} + \frac{\partial \mathbf{E}_1}{\partial t}, \quad (30)$$

$$q \left\{ (\mathbf{E}_0 + \mathbf{E}_1) + [(\mathbf{v}_0 \times \mathbf{B}_0) + (\mathbf{v}_0 \times \mathbf{B}_1) + (\mathbf{v}_1 \times \mathbf{B}_0)] \right\} = m \left\{ \frac{\partial \mathbf{v}_0}{\partial t} + \frac{\partial \mathbf{v}_1}{\partial t} + [(\mathbf{v}_0 \cdot \nabla) \mathbf{v}_0 + (\mathbf{v}_0 \cdot \nabla) \mathbf{v}_1 + (\mathbf{v}_1 \cdot \nabla) \mathbf{v}_0] \right\}. \quad (31)$$

3.1.2 Slowly changing background limit

We can apply a simplification of the system of equations detailed in section 3.1.1 by considering the time-scales over which the background $(\mathbf{E}_0, \mathbf{B}_0, \mathbf{J}_0, \mathbf{v}_0)$, and perturbed $(\mathbf{E}_1, \mathbf{B}_1, \mathbf{J}_1, \mathbf{v}_1)$ quantities, vary significantly. The background plasma profiles are not constant. However, their variation in time is often slow in comparison with the perturbed profiles. This is an important point to make as it allows us to approximate that the differential of these background quantities with respect to time is negligible. Since the microwaves used in back-scattering diagnostics are of high frequency they oscillate very quickly; over a single wave-length, the wave will ‘see’ only a tiny variation in the background quantities, meaning that this approximation is likely safe. Additionally, for back-scattering diagnostics used in the plasma edge the probing beam only propagates through a small amount of plasma, on the order of 1cm . This means that the magnitude of the background quantities $(\mathbf{E}_0, \mathbf{B}_0, \mathbf{J}_0, \mathbf{v}_0)$ is likely to change only very slightly, which also allows us to assume that the differentials with respect to space are approximately zero. Finally, since we have eliminated time and space varying background electric fields (\mathbf{E}_0) , the electric field term on the left side of equation (31) becomes constant, and can be ignored since it will have no contribution towards the scattering mechanism (an oscillatory mechanism by physical requirement). Applying these approximations our system of equations (eq.s (29), (30), and (31)) becomes

$$\nabla \times \mathbf{E}_1 = -\frac{\partial \mathbf{B}_1}{\partial t}, \quad (32)$$

$$\nabla \times \mathbf{B}_1 = \mu_0 \mathbf{J}_1 + \frac{1}{c^2} \frac{\partial \mathbf{E}_1}{\partial t}, \quad (33)$$

$$q[\mathbf{E}_1 + (\mathbf{v}_1 \times \mathbf{B}_0)] = m \frac{\partial \mathbf{v}_1}{\partial t}. \quad (34)$$

3.1.3 Plane Wave Solution

Mathematically, electromagnetic waves are any oscillations in electric and magnetic fields which solve equations (32) and (33). There are potentially an infinite number of solutions to these equations, but by assuming one of the most basic we can simplify our system of equations and more easily derive the cold plasma dispersion relation. Appendix section 10.1 justifies and derives the 3D plane-wave solutions which are

$$\mathbf{E}_1(\mathbf{r}, t) = \mathbf{E}_1 \exp^{i(\mathbf{k} \cdot \mathbf{r} - \omega t)}, \quad (35)$$

$$\mathbf{B}_1(\mathbf{r}, t) = \mathbf{B}_1 \exp^{i(\mathbf{k} \cdot \mathbf{r} - \omega t + \phi)}, \quad (36)$$

where \mathbf{k} is the wave-vector, ω is the angular frequency, \mathbf{r} is a spacial coordinate, and ϕ is some phase difference. This allows us to further evaluate the spatial and temporal differentials which operate on the electromagnetic wave's electric or magnetic components. Furthermore, the velocity induced onto a particle subjected to these plane-waves must oscillate at the same frequency, meaning that

$$\mathbf{v}_1(\mathbf{r}, t) = \mathbf{v}_1 \exp^{i(\mathbf{k} \cdot \mathbf{r} - \omega t + \phi)}. \quad (37)$$

Our system of equations (eq.s (32), (33), and (34)) then becomes

$$i\mathbf{k} \times \mathbf{E}_1 = i\omega \mathbf{B}_1, \quad (38)$$

$$i\mathbf{k} \times \mathbf{B}_1 = \mu_0 \mathbf{J}_1 - \frac{i\omega}{c^2} \mathbf{E}_1, \quad (39)$$

$$q[\mathbf{E}_1 + (\mathbf{v}_1 \times \mathbf{B}_0)] = -i\omega m \mathbf{v}_1, \quad (40)$$

3.2 Cold Plasma Dispersion Relation

The behaviour of electromagnetic waves are described mathematically through ‘dispersion relations’. A dispersion relation is an equation that describes the relationship between a wave’s frequency and wave-vector. The mathematical structure of these relations can become complex in magnetised plasma, because they are dependent on anisotropic medium that the electromagnetic waves are propagating through. Magnetised plasma are complicated environments, but with the simplifications used in section 3.1 we can derive one of the most simple dispersion relations in magnetic fusion; the cold plasma dispersion relation, which we will analyse. Firstly, we identify the different types of electromagnetic waves that can exist in cold, magnetised plasmas. Secondly, we experiment and find interesting scenarios where the electromagnetic wave’s wave-length approaches zero or infinity.

In order to derive the cold plasma dispersion relation we first employ Faraday’s and Ampère-Maxwell’s laws (38)) and (39). To combine them we take the curl of Faraday’s law and make use of the plane-wave solution approximation outlined in section 3.1.3 to give

$$i\mathbf{k} \times (i\mathbf{k} \times \mathbf{E}_1) = i\omega(i\mathbf{k} \times \mathbf{B}_1). \quad (41)$$

At which point Ampère’s law can be substituted into the right hand side, giving

$$\frac{i}{\omega}(\mathbf{k} \times (\mathbf{k} \times \mathbf{E})) = \mu_0 \mathbf{J} - \frac{i\omega}{c^2} \mathbf{E}. \quad (42)$$

We can explore the current term of equation (42) by using Ohm's law,

$$\mathbf{J} = \bar{\boldsymbol{\sigma}} \cdot \mathbf{E}_1, \quad (43)$$

where $\bar{\boldsymbol{\sigma}}$ represents the plasma conductivity tensor; a term which has structure depending on the properties of the plasma that the electromagnetic wave is interacting with. Since we are modelling an anisotropic, magnetised plasma, the conductivity needs to be a tensor,

$$\frac{i}{\omega}(\mathbf{k} \times (\mathbf{k} \times \mathbf{E})) = \mu_0 \bar{\boldsymbol{\sigma}} \cdot \mathbf{E}_1 - \frac{i\omega}{c^2} \mathbf{E}. \quad (44)$$

which can be arranged as

$$\mathbf{k} \times (\mathbf{k} \times \mathbf{E}_1) + \frac{\omega^2}{c^2} \left(\bar{\mathbf{I}} + \frac{i\bar{\boldsymbol{\sigma}}}{\epsilon_0\omega} \right) \cdot \mathbf{E}_1 = 0, \quad (45)$$

where $\bar{\mathbf{I}}$ is an identity matrix. Additionally, we can use the definition of the dielectric tensor $\bar{\boldsymbol{\epsilon}} = \bar{\mathbf{I}} + \frac{i\bar{\boldsymbol{\sigma}}}{\epsilon_0\omega}$ to re-write the second term,

$$\mathbf{k} \times (\mathbf{k} \times \mathbf{E}_1) + \frac{\omega^2}{c^2} \bar{\boldsymbol{\epsilon}} \cdot \mathbf{E}_1 = 0. \quad (46)$$

Because we utilised Ohm's law (eq. 43), \mathbf{E}_1 is a common variable in both of the terms of equation (46), and these terms can be combined. If we assume that the electromagnetic wave described by equation (46) is propagating in the xz plane only ($k_y = 0$), then we can re-write this equation as

$$\begin{bmatrix} -k_z^2 & 0 & k_x k_z \\ 0 & -(k_x^2 + k_z^2) & 0 \\ k_x k_z & 0 & -k_x^2 \end{bmatrix} \cdot \begin{bmatrix} E_x \\ E_y \\ E_z \end{bmatrix} + \begin{bmatrix} \frac{\omega^2}{c^2} \boldsymbol{\epsilon}_x \\ \frac{\omega^2}{c^2} \boldsymbol{\epsilon}_y \\ \frac{\omega^2}{c^2} \boldsymbol{\epsilon}_z \end{bmatrix} \cdot \begin{bmatrix} E_x \\ E_y \\ E_z \end{bmatrix} = 0, \quad (47)$$

or alternatively,

$$\begin{bmatrix} -k_z^2 + \frac{\omega^2}{c^2}\epsilon_{xx} & \frac{\omega^2}{c^2}\epsilon_{xy} & k_x k_z + \frac{\omega^2}{c^2}\epsilon_{xz} \\ \frac{\omega^2}{c^2}\epsilon_{yx} & -(k_x^2 + k_z^2) + \frac{\omega^2}{c^2}\epsilon_{yy} & \frac{\omega^2}{c^2}\epsilon_{yz} \\ k_x k_z + \frac{\omega^2}{c^2}\epsilon_{zx} & \frac{\omega^2}{c^2}\epsilon_{zy} & -k_x^2 + \frac{\omega^2}{c^2}\epsilon_{zz} \end{bmatrix} \cdot \begin{bmatrix} E_x \\ E_y \\ E_z \end{bmatrix} = 0. \quad (48)$$

The form of this expression is sometimes referred to as $\bar{\mathbf{M}} \cdot \mathbf{E} = 0$.

We have combined Ampère's and Faraday's laws into a wave-equation sensitive to some plasma described by the matrix $\bar{\mathbf{M}}$. In order to progress further we need to evaluate $\bar{\mathbf{M}}$ by detailing our plasma; finding expressions for the components of the plasma conductivity tensor. This involves describing how the plasma couples to the electromagnetic wave, or in other words how the plasma particles respond to the stimuli of the waves electric and magnetic fields (\mathbf{E}_1 , \mathbf{B}_1). We can do this by analysing the momentum force balance expression shown in equation (40). We assume that the background magnetic field is parallel to the z axis ($\mathbf{B}_0 = B_0 \hat{e}_z$), and re-write this vector equation (40) as three scalar equations,

$$q(E_x + v_y B_0) = -i\omega m v_x, \quad (49)$$

$$q(E_y - v_x B_0) = -i\omega m v_y, \quad (50)$$

$$q(E_z) = -i\omega m v_z. \quad (51)$$

These three equations can be re-written and simplified using the definition for 'gyrofrequency', $\omega_{ce} = (qB_0)/m$. This is the rate at which particles rotate around background magnetic field lines. Equations (49, 50, 51) become

$$v_x = \frac{q}{m} \left(\frac{q\omega E_x - \omega_{ce} E_y}{\omega^2 - \omega_{ce}^2} \right), \quad (52)$$

$$v_y = \frac{q}{m} \left(\frac{q\omega E_x + \omega_{ce} E_y}{\omega^2 - \omega_{ce}^2} \right), \quad (53)$$

$$v_z = \frac{q}{m} \frac{i}{\omega} E_z. \quad (54)$$

This allows us to form the structure of the conductivity tensor. We use the definition of current density combined with Ohms law (eq. 43) to relate the particle velocities to the conductivity tensor as

$$\mathbf{J} = q\mathbf{v}_1 n = \bar{\boldsymbol{\sigma}} \cdot \mathbf{E}_1, \quad (55)$$

which results in the expression for the conductivity tensor

$$\bar{\boldsymbol{\sigma}} = \begin{bmatrix} \frac{q^2 n}{m} \frac{i\omega}{\omega^2 - \omega_{ce}^2} & -\frac{q^2 n}{m} \frac{\omega_{ce}}{\omega^2 - \omega_{ce}^2} & 0 \\ \frac{q^2 n}{m} \frac{\omega_{ce}}{\omega^2 - \omega_{ce}^2} & \frac{q^2 n}{m} \frac{i\omega}{\omega^2 - \omega_{ce}^2} & 0 \\ 0 & 0 & \frac{iq^2 n}{m \omega} \end{bmatrix}. \quad (56)$$

The known structure of $\bar{\boldsymbol{\sigma}}$ can be used in the definition of the dielectric tensor $\bar{\boldsymbol{\epsilon}} = \bar{\mathbf{I}} + \frac{i\bar{\boldsymbol{\sigma}}}{\epsilon_0 \omega}$ to yield

$$\bar{\boldsymbol{\epsilon}} = \begin{bmatrix} 1 - \frac{\omega_{pe}^2}{\omega^2 - \omega_{ce}^2} & -\frac{\omega_{ce}}{\omega} \frac{i\omega_{pe}^2}{\omega^2 - \omega_{ce}^2} & 0 \\ \frac{\omega_{ce}}{\omega} \frac{i\omega_{pe}^2}{\omega^2 - \omega_{ce}^2} & 1 - \frac{\omega_{pe}^2}{\omega^2 - \omega_{ce}^2} & 0 \\ 0 & 0 & 1 - \frac{\omega_{pe}^2}{\omega^2} \end{bmatrix}. \quad (57)$$

Equation (57) shows the derived structure of the dielectric tensor. From here we know the components (ϵ_{xx} , ϵ_{xz} , ϵ_{yy} , ϵ_{zx} , ϵ_{zz}) that we were seeking to evaluate, and we could use these directly in equation (48). Although, there are quite a few variables in equation (57) and it can be visually simplified by stating some relations,

$$R = 1 - \frac{\omega_{pe}^2}{\omega(\omega + \omega_{ce})} = 1 - \frac{X}{1 - Y}, \quad (58)$$

$$L = 1 - \frac{\omega_{pe}^2}{\omega(\omega - \omega_{ce})} = 1 - \frac{X}{1 + Y}, \quad (59)$$

$$S = 1 - \frac{\omega_{pe}^2}{\omega^2 - \omega_{ce}^2} = 1 - \frac{X}{1 - Y^2} = \frac{R + L}{2}, \quad (60)$$

$$D = \frac{\omega_{pe}^2}{\omega} \frac{\omega_{ce}}{\omega^2 - \omega_{ce}^2} = \frac{-XY}{1 - Y^2} = \frac{R - L}{2}, \quad (61)$$

$$P = 1 - X. \quad (62)$$

Using these relations, equation (57) becomes

$$\bar{\epsilon} = \begin{bmatrix} S & -iD & 0 \\ iD & S & 0 \\ 0 & 0 & P \end{bmatrix}, \quad (63)$$

which can be more easily combined with equation (48) to give

$$\begin{bmatrix} \frac{\omega^2}{c^2}S - k_z^2 & -\frac{\omega^2}{c^2}iD & \frac{\omega^2}{c^2}k_xk_z \\ \frac{\omega^2}{c^2}iD & \frac{\omega^2}{c^2}S - (k_x^2 + k_z^2) & 0 \\ \frac{\omega^2}{c^2}k_xk_z & 0 & \frac{\omega^2}{c^2}P - k_x^2 \end{bmatrix} \cdot \begin{bmatrix} E_x \\ E_y \\ E_z \end{bmatrix} = 0. \quad (64)$$

We can simplify expression (64) by multiplying through by a factor of c^2/ω^2 , and then using the definition of refractive index, $\mathbf{N} = \mathbf{k}c/\omega$. We can also allow θ to describe the angle between the background magnetic field ($\mathbf{B}_0 = B_0\hat{e}_z$) and \mathbf{N} . This allows for $N_x \rightarrow N \sin \theta$ and $N_z \rightarrow N \cos \theta$, and equation (64) becomes

$$\bar{\mathbf{M}} \cdot \mathbf{E} = \begin{bmatrix} S - N^2 \cos^2 \theta & -iD & N^2 \sin \theta \cos \theta \\ iD & -N^2 + S & 0 \\ N^2 \sin \theta \cos \theta & 0 & -N^2 \sin^2 \theta + P \end{bmatrix} \cdot \begin{bmatrix} E_x \\ E_y \\ E_z \end{bmatrix} = 0. \quad (65)$$

The determinant of $\bar{\mathbf{M}}$ in expression (65) can be solved for both $\sin^2 \theta$ and $\cos^2 \theta$

$$\cos^2 \theta = \frac{SN^4 - N^2(PS + RL) + P(S^2 - D^2)}{N^4(S - P) + N^2(PS - (S^2 - D^2))}, \quad (66)$$

$$\sin^2 \theta = \frac{-P(N^4 - 2SN^2 + RL)}{N^4(S - P) + N^2(PS - RL)}. \quad (67)$$

Finally, equations (66) and (67) can be combined divisively to give the cold plasma dispersion relation

$$\tan^2 \theta = \frac{-P(N^2 - R)(N^2 - L)}{(SN^2 - RL)(N^2 - P)} \quad (68)$$

3.3 Cold Plasma Waves

An analysis of the cold plasma dispersion relation (68) gives insight into the types (polarisations) of electromagnetic waves that can exist in our cold, magnetised plasma, and also gives information regarding interesting conditions under which the wave's wave-length tends to zero or infinity. There are two stages to this analysis, which centre around θ ; the angle between the background magnetic field and the wave-vector (direction of propagation). The first is propagation perpendicular to the background magnetic field where $\theta = \pi/2$, and the second is parallel propagation where $\theta = 0$. The regions of interest are described by changes in the wave refractive index (reciprocal wave-length) of $N^2 \rightarrow 0$, and $N^2 \rightarrow \infty$. When the refractive index of a wave becomes zero, the wave is 'blocked' from propagating further. The region of plasma that the microwave cannot enter is named 'over-dense', whereas the region which will allow propagation is named 'under-dense'. When the microwave hits the boundary between the under-dense and over-dense plasma, it reflects. The wave is said to be 'cut-off'. When $N^2 \rightarrow \infty$ an electromagnetic wave is said to be at 'resonance'. This is a region of space where the wave couples strongly to the plasma particles, and can drive heat and/or current.

3.3.1 Perpendicular Propagation

Propagation perpendicular to the background magnetic field gives $\theta = \pi/2$. Observing equation (68) this yields

$$\infty = \frac{-P(N_{\perp}^2 - R)(N_{\perp}^2 - L)}{(SN_{\perp}^2 - RL)(N_{\perp}^2 - P)}, \quad (69)$$

which implies that the denominator has gone to zero,

$$(SN_{\perp}^2 - RL)(N_{\perp}^2 - P) = 0. \quad (70)$$

For equation (70) to be satisfied, either

$$SN_{\perp}^2 - RL = 0, \quad (71)$$

and/or

$$N_{\perp}^2 - P = 0. \quad (72)$$

Since the definition of refractive index is $N = kc/\omega$, equations (71) and (72) describe how the wave's wave-length and frequency vary according to certain plasma parameters, S, R, L , and P (definitions in section 3.2). This means that, by definition, equations (71) and (72) are dispersion relations; they describe electromagnetic waves. Specifically, equation (71) is called the 'Extraordinary' mode (X-mode), and equation (72) is the 'Ordinary' mode (O-mode).

3.3.1.1 The Ordinary Mode

An electromagnetic wave that has a pure O-mode polarisation is defined by the dispersion relation

$$N_{\perp}^2 = P = 1 - X = 1 - \frac{\omega_{pe}^2}{\omega_0^2}. \quad (73)$$

The refractive index of equation (73) has dependency only on the plasma frequency ω_{pe} , and the angular frequency ω_0 . In order for the refractive index to tend to infinity, either the plasma frequency would need to tend to negative infinity ($\omega_{pe} \rightarrow -\infty$),

or the angular frequency would need to tend to zero ($\omega_0 \rightarrow 0$). Since neither of these frequencies can be negative the O-mode polarisation does not feature any resonances.

Now observing conditions where N^2 can tend to zero, the single condition for this requires $\omega_{pe}^2/\omega_0^2 = 1$. Since ω_0 is fixed and is defined by an experimental choice of the frequency of the launched beam, ω_{pe} is the variable of interest. The plasma frequency is a function of the number density. At the plasma-vacuum boundary the plasma frequency will be close to zero, but this increases and will peak in the core of the plasma. If the plasma frequency (i.e. number density) becomes high enough such that $\omega_{pe} = \omega_0$ the O-mode polarisation features a cut-off.

In conclusion, an electromagnetic wave behaving according to equation (73) is in the O-mode polarisation. O-mode waves do not have any resonances, as the refractive index cannot tend towards infinity. However, the dispersion relation does allow for a single cutoff when the angular frequency equals the plasma frequency.

3.3.1.2 The Extraordinary Mode

An electromagnetic wave that has a pure X-mode polarisation is defined by the dispersion relation

$$N_{\perp}^2 = \frac{RL}{S}. \quad (74)$$

As with all electromagnetic waves described by the cold plasma dispersion relation, the interactions of major interest occur when the refractive index tends to either zero or infinity. Equation (74) is substantially more complex than the O-mode dispersion relation (73), and the definitions for R , L , and S are given in equations (58), (59), and (60).

In order for the refractive index of equation (74) to tend towards infinity, either $R \rightarrow \infty$, $L \rightarrow \infty$, or $S \rightarrow 0$. The R variable is defined as

$$R = 1 - \frac{X}{1 - Y}, \quad (75)$$

which cannot tend to infinity because the X and Y variables are always positive. The second condition $L \rightarrow \infty$ is easier to assess. From the definition

$$L = 1 - \frac{X}{1 + Y}, \quad (76)$$

it can be seen that L cannot tend to infinity due to the variables X and Y being positive. Finally, a resonance condition of $S \rightarrow 0$ is possible. S can be written as

$$S = \frac{R + L}{2}, \quad (77)$$

and $S = 0$ would require

$$X = 1 - Y^2. \quad (78)$$

Since equation (78) is a multidimensional function of $f(X, Y)$ there are a range of conditions whereby this expression could be satisfied and would cause the X-mode polarisation (74) to feature a refractive index of $N^2 \rightarrow \infty$. This is called the upper hybrid resonance. It is described by

$$\omega_{UH} = \sqrt{\omega_{pe}^2 + \omega_{ce}^2}, \quad (79)$$

and represents the X-mode coupling to both the plasma frequency, and the cyclotron frequency. For perpendicular polarisations this is unique to the X-mode, as the O-mode dispersion relation shown in equation (73) does not feature any condition where $N^2 \rightarrow \infty$.

Observing now, conditions whereby the X-mode dispersion relation (74) can feature a refractive index which is tending to zero, $N^2 \rightarrow 0$. For this to occur we could need either $S \rightarrow \infty$, $R \rightarrow 0$, or $L \rightarrow 0$. Firstly, the variable S cannot tend to

infinity as this would require $X \rightarrow \infty$, and the impossibility of this has already been addressed. However, the variables R and L can indeed go to zero. Respectively, this would require

$$1 - \frac{X}{1 - Y} = 0, \quad (80)$$

or

$$1 - \frac{X}{1 + Y} = 0. \quad (81)$$

Similarly to equation (78), equations (80,81) are multidimensional functions of $f(X, Y)$, so there are a range of combinations of X and Y where they could be satisfied. These two expressions represent the two X-mode cut-offs denoted ω_R and ω_L , respectively. They can be evaluated in terms of frequencies as the fast X-mode cutoff

$$\omega_R = \frac{\omega_{ce} + \sqrt{\omega_{ce}^2 + 4\omega_{pe}^2}}{2}, \quad (82)$$

and the slow X-mode cutoff

$$\omega_L = \frac{-\omega_{ce} + \sqrt{\omega_{ce}^2 + 4\omega_{pe}^2}}{2}. \quad (83)$$

In conclusion, an electromagnetic wave behaving according to equation (74) is in the X-mode polarisation. X-mode waves have a single resonance where the refractive index tends towards infinity. This is called the upper hybrid resonance (ω_{UH}) and is described by equation (79). The dispersion relation also allows for two cutoff frequencies ω_R and ω_L according to equations (82) and (83), respectively.

3.3.2 Parallel Propagation

Propagation parallel to the background magnetic field gives $\theta = 0.0^\circ$. Observing equation (68) this yields

$$0 = \frac{-P(N_{\parallel}^2 - R)(N_{\parallel}^2 - L)}{(SN_{\parallel}^2 - RL)(N_{\parallel}^2 - P)}, \quad (84)$$

which implies that the numerator has gone to zero,

$$-P(N_{\parallel}^2 - R)(N_{\parallel}^2 - L) = 0. \quad (85)$$

Equation (85) implies that at least one of the three terms must be zero;

$$P = 1 - X = 0, \quad (86)$$

or

$$N_{\parallel}^2 - R = 0, \quad (87)$$

or

$$N_{\parallel}^2 - L = 0. \quad (88)$$

A dispersion relation describe how a wave's wave-length and frequency vary according to certain plasma parameters. While equation (85) does not strictly satisfy this definition, it is still a dispersion relation because it can be understood that the wave frequency is independent of the wave-number. From this, one can deduce that the group velocity is equal to zero ($v_g = \partial\omega/\partial k$) and under the cold plasma approximation, this wave does not propagate. With a fixed, non-zero frequency of $\omega_0 = \omega_{pe}$ this is an electrostatic wave representing the 'plasma oscillations' whereby particles simply oscillate around their equilibrium position. Equations (87) and (88)

are more obviously dispersion relations. They describe electromagnetic waves called the ‘right-hand’ and ‘left-hand’ waves, respectively.

3.3.2.1 The Right-Hand Mode

The right-hand wave (R-wave) is a circularly polarised wave that rotates clockwise, and is described by the dispersion relation

$$N_{\parallel}^2 = R = 1 - \frac{X}{1 + Y}. \quad (89)$$

As discussed in section 3.3.1.2 the variable $Y = \omega_{ce}/\omega_0$ describes the electron cyclotron frequency and is negative. Given this, the refractive index in equation (89) can tend to infinity when $\omega_0 = \omega_{ce}$. This represents the circularly polarised R-wave oscillating in synchrony with the electron gyro-oscillations, coupling to the plasma by driving the electron motion.

A cut-off also exists for the R-wave where $N^2 \rightarrow 0$, and requires

$$\frac{X}{1 + Y} = 1, \quad (90)$$

which can occur for a range of combinations of X and Y . This cut-off is also featured in the X-mode polarisation and is shown in terms of frequencies in equation (82).

3.3.2.2 The Left-Hand Mode

The left-hand wave (L-wave) is very similar to the right-hand wave. It’s also circularly polarised except where the right-hand wave rotated clockwise, the left-hand wave rotates counter-clockwise. Its described by the dispersion relation

$$N_{\parallel}^2 = L = 1 - \frac{X}{1 - Y}. \quad (91)$$

The L-mode does have a resonance at the ion-cyclotron frequency (ω_{ci}), however since ions have been neglected in our model, a resonance does not arise from an analysis of the cold plasma dispersion relation. The only region of interest for the L-wave is a cutoff ($N^2 \rightarrow 0$) which occurs when

$$1 - \frac{X}{1 - Y} = 0, \quad (92)$$

which may be satisfied for a range of combinations of X and Y . Similarly to the R-wave, this cut-off also features in the X-mode polarisation and is shown in terms of frequencies in equation (83)

3.3.3 Mode Conversion

By taking perpendicular ($\theta = \pi/2$) and parallel ($\theta = 0$) limits of the cold plasma dispersion relation (68) we have identified the different polarisations of electromagnetic waves that can exist in a cold magnetised plasma. One drawback of this method is that the θ assumptions have restricted the possible modes to 'pure' O,X,R, and L waves. In other words by taking $\theta = \pi/2$ and $\theta = 0$ we have caused the refractive index to become $N \rightarrow N_{\perp}$ and $N \rightarrow N_{\parallel}$, respectively. It is possible to achieve a more general solution by re-arranging equation (68) in terms of N^2 . This is called the Appleton-Hartree dispersion relation

$$N_{\perp}^2 + N_{\parallel}^2 = 1 - \frac{2X(1 - X)}{2(1 - X) - Y^2 \sin^2 \theta \pm \Gamma}, \quad (93)$$

where

$$\Gamma = [Y^4 \sin^4 \theta + 4(1 - X)^2 Y^2 \cos^2 \theta]^{1/2}, \quad (94)$$

and it allows for calculation of the refractive index for arbitrary propagation angles $0 \leq \theta \leq \pi/2$. At non-absolute angles $0 < \theta < \pi/2$ the O-mode becomes left-

hand circularly polarised, and forms a hybrid polarisation of the O-mode and the L-mode. Similarly, the X-mode and R-mode are coupled. The choice of the positive or negative sign before the Γ term causes the dispersion relation to describe either the O-mode/L-mode or the X-mode/R-mode hybrid, respectively.

The nature of the dispersion relation can be explored by modelling N_{\perp}^2 as a function of X . Figure 15 shows how the fast X-mode (FX), O-mode (O), and slow X-mode (SX) dispersion curves vary as a function of plasma density.

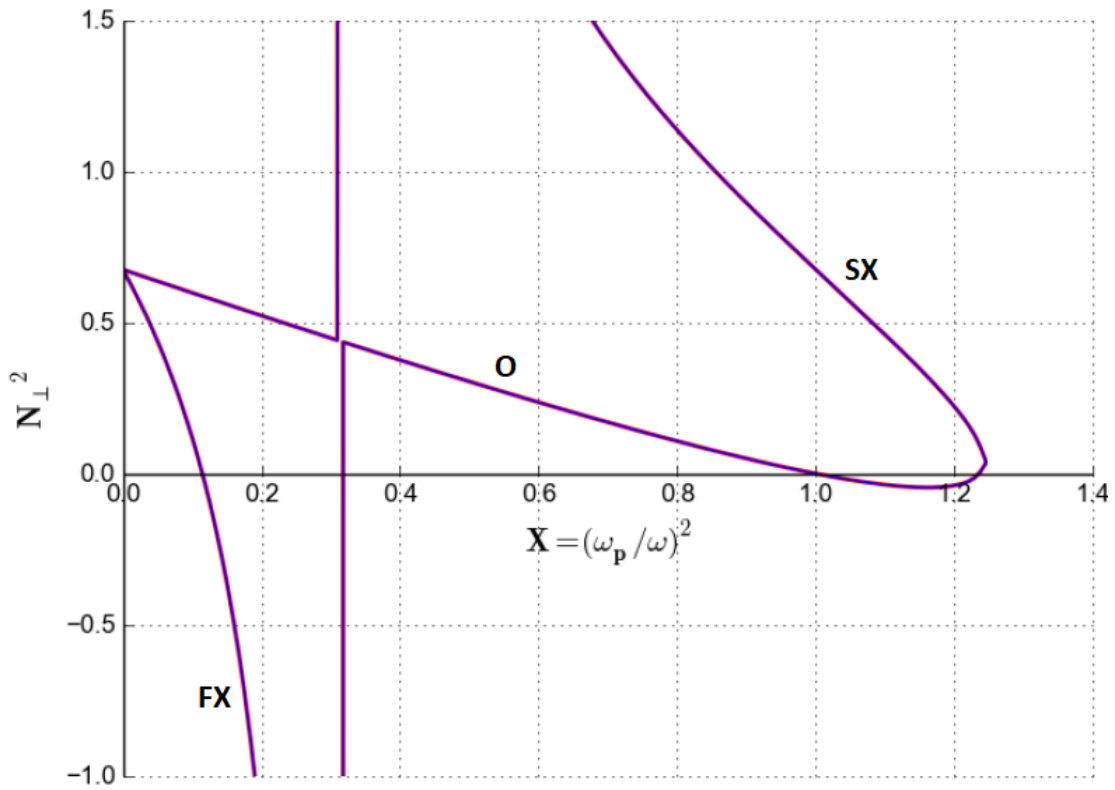


Figure 15: Perpendicular refractive index as a function of X , with $\theta = 6^\circ$. The curves FX, O, and SX, are the fast X-mode, O-mode, and slow X-mode, respectively.

The fast X-mode is quickly rejected from the plasma due to the background magnetic field choice of $Y = 0.20$. This corresponds to the ω_R cutoff detailed in sections 3.3.1.2 and 3.3.2.1. The O-mode curve passes through its cutoff at $X = 1.0$ and enters an

evanescent region whereby it becomes damped, when $N_{\perp}^2 < 0$. Just above $X = 1.2$ the O-mode and slow X-mode curves can be seen to join onto one another. When this occurs the two polarisations are said to become degenerate, and energy can pass from one state to another. This is the principle of OX mode conversion. Its possible to enable this conversion without the O-mode propagating into the evanescent region. Such a condition leads to the maximum attainable conversion efficiency, as wave-damping is avoided. This is achieved by launching the O-mode wave at an optimal angle [99]

$$N_{\parallel,critical} = \sin(\theta) = \sqrt{\frac{Y}{1+Y}}, \quad (95)$$

where the parameter Y is the normalised cyclotron frequency $Y = \omega_{ce}/\omega_0$, and θ is the launch angle with respect to the density gradient. The converted SX mode cannot propagate further into the plasma because of the ω_L cut-off which is detailed in sections 3.3.1.2 and 3.3.2.2. It propagates towards lower density plasma until it approaches the upper hybrid resonance, ω_{UH} , detailed in section 3.3.1.2. If our plasma model allowed for warm plasma effects, it would be possibly for the X-mode to couple to the plasma at ω_{UH} and mode convert into the electrostatic Electron Bernstein Wave (EBW). EBWs do not feature any cut-offs, and can propagate freely into high density plasma. They can be used to drive heat and current near the plasma core. The chain of mode conversion from the O-mode, to the SX-mode, and then the EBW waves is called OXB mode conversion and is a plasma heating and current drive technique under research for use on highly over-dense spherical tokamak plasmas.

3.4 WKB Approximation

The Wentzel–Kramers–Brillouin (WKB) approximation is a method for finding approximate analytical solutions to time independent linear differential equations. It is

useful when exact solutions are difficult or impossible to find. Consider an O-mode polarised wave interacting with a homogeneous, magnetised plasma. Ignoring ions, the electron particle motion as a consequence of the wave electric field must vary sinusoidal. Assuming this oscillating has the form $\exp -i\omega t$, a simple equation of motion ($\mathbf{F} = m\mathbf{a}$) would then be

$$\mathbf{v}_e = -\frac{q_e}{i\omega m_e} \mathbf{E}. \quad (96)$$

The current density induced by this motion has the form

$$\mathbf{J} = qn\mathbf{v}_e = -\frac{q_e^2 n_e}{i\omega m_e} \mathbf{E} = -\epsilon_0 \frac{\omega_{pe}^2}{i\omega} \mathbf{E}. \quad (97)$$

Ampère's law can then be written as

$$\nabla \times \mathbf{B} = \frac{i\omega_{pe}^2}{\omega c^2} \mathbf{E} - \frac{i\omega}{c^2} \mathbf{E}, \quad (98)$$

or alternatively,

$$\nabla \times \mathbf{B} = \frac{-i\omega}{c^2} \left(1 - \frac{\omega_{pe}^2}{\omega^2} \right) \mathbf{E}, \quad (99)$$

where for an O-mode wave it can be said that the refractive index has the relation

$$N^2 = 1 - \frac{\omega_{pe}^2}{\omega^2}. \quad (100)$$

Using the relation $\omega = ck_i$ Faraday's law can be simply written

$$\nabla \times \mathbf{E} = ik_i c \mathbf{B}, \quad (101)$$

Let the O-mode wave be linearly polarized and propagating along the z axis. Let there also exist a background magnetic field $\mathbf{B} = B\hat{e}_y$. Due to the O-mode polarisation, the wave's oscillating electric field must be parallel to \mathbf{B} . We can combine Ampère's (eq. (99)) and Faraday's (eq. (101)) laws to give

$$\frac{d^2 E_y(z)}{dz^2} + k_i^2 N^2 E_y(z) = 0. \quad (102)$$

If we assume a plane-wave solution, which is derived and justified in the abstract in section 10.1, solutions to equation (102) are of the form

$$E_y(z) = A e^{i\phi(z)}. \quad (103)$$

Combining equations (102) and (103) we get

$$\left(\frac{d\phi}{dz}\right)^2 = k_i^2 N^2 + i \frac{d^2 \phi}{dz^2}. \quad (104)$$

In order to evaluate this we need to know the phase ϕ relationship. For homogeneous plasma

$$\phi = k_i z N. \quad (105)$$

However, this is not necessarily the case for an inhomogenous plasma where the refractive index is dependent on position; $N(z)$. The phase relationship may vary greatly from equation (105) however if $N(z)$ varies only weakly the structure of ϕ will be similar to that in equation (105). Leaving exactly how small $\frac{dN(z)}{dz}$ needs to be to satisfy this condition ambiguous for now, using equation (105) we can say that

$$\frac{d\phi(z)}{dz} \simeq \pm k_i N(z), \quad (106)$$

and

$$\frac{d^2 \phi(z)}{dz^2} \simeq \pm k_i \frac{dn(z)}{dz} \simeq 0. \quad (107)$$

Using equations (106) and (107) in equation (104) we get

$$\frac{d\phi(z)}{dz} \simeq \pm k_i n(z) + \frac{i}{2n(z)} \frac{dn(z)}{dz}. \quad (108)$$

Equation (108) can be integrated to give $\phi(z)$ as

$$\phi(z) \simeq k_i \int^z n(z) dz + i \ln \sqrt{n(z)}. \quad (109)$$

This phase relationship can be used with the plane wave solution in equation (103) to give an analytical expression for the electric and magnetic fields

$$E_y(z) \simeq A n^{-\frac{1}{2}}(z) \exp\left(\pm i k_i \int^z n(z) dz\right), \quad (110)$$

where also equation (101) gives the magnetic field

$$cB_x(z) \simeq A n^{\frac{1}{2}}(z) \exp\left(\pm i k_i \int^z n(z) dz\right). \quad (111)$$

Electromagnetic wave propagating into a medium with a slowly changing refractive index will undergo a small amount of reflection. However, equations (110) and (111) don't predict this. It may be that this is an acceptable approximation as in practicality the amount of reflection may be negligible. However, when applied to scattering theory such as a wave scattering from a plasma cutoff, the refractive index can change considerably over a short distance. Equations (110) and (111) again have no explanation of this and are incapable of describing this physical effect. An approximate condition [100] for validity of the WKB approximation is

$$\left| \frac{1}{n(z)} \frac{dn(z)}{dz} \right| \ll k_i \quad (112)$$

The WKB approximation is satisfied and valuable in DBS ray-tracing for obtaining the radial position and the beam perpendicular wave number at the scattering location *near* the cutoff. However the validity limit (eq. (112)) is invalidated in a tokamak *at* cutoffs ($N(z) \rightarrow 0$) and resonances ($n(z) \rightarrow \infty$) (since $\frac{dn(z)}{dz} \rightarrow \infty$ faster than $n(z)$, when magnetic shear is great or when the density gradient length scales are comparable to the wavelength). In these strongly varying regions of refractive

index the WKB approximation breaks down and may fail to predict the complex physics associated with electromagnetic wave scattering. Of great importance is the failure to predict any coupling [101] between the O-mode and X-mode waves. Their dispersion relations become increasingly indistinguishable (degenerate) when their wave numbers become similar. An approximate condition for this effect at a given location in space is given by

$$|k_O - k_X| \ll \frac{2\pi}{L_n}, \quad (113)$$

where k_O and k_X are the O-mode and X-mode wave-numbers, and L_n is the density gradient length scale. With the absence of more sophisticated analytical models, such complex regions require full-wave numerical modelling in order to fully understand the physics.

4 Numerical modelling

A magnetised fusion plasma is a complex inhomogeneous and anisotropic environment. Often modelled as a fluid, tokamak plasmas are said to be a 'soup' of charged particles. The number density of fusible plasma is of the order $10^{20}m^{-3}$. The modelling of an electromagnetic wave under a full kinetic description would require calculating the influence of the electromagnetic wave on each particle, while tracking the electromagnetic interactions between each particle on every other particle. This full encapsulation of the complete range of physical effects is both complex and tremendously computationally expensive. It is also likely unnecessary; for instance, the temperature at the core of an energy producing fusion plasma will likely be of the order 30keV [102]. Ionised deuterium species will have an approximate thermal speed of $v_{th} \approx 0.002c$. When compared to the speed of an electromagnetic wave, it is not an unreasonable approximation to consider the ions as completely stationary. The choice of numerical method for a particular problem is heavily influenced by a consideration of which approximations can be satisfactorily made, i.e., what physics is thought to have little influence and can be excluded. In this chapter we discuss two of the most common models utilised for the simulating of electromagnetic waves in magnetised plasmas. In section 4.1 we briefly cover the ray-tracing method, which is based on similar assumptions to the WKB approximation. In section 4.2 we discuss the full-wave, finite difference time domain modelling technique and justify its usage as the main modelling method for this thesis.

4.1 Ray-tracing

One of the most computationally cheap methods of modelling electromagnetic waves is ray-tracing. As we have seen in section 3 the interaction between an electromagnetic wave and a plasma can be written as a set of coupled, linear, first order

partial-differential equations of the form

$$\bar{\mathbf{M}}(i\partial/\partial t, -i\delta, \mathbf{r}, t)\boldsymbol{\psi} = 0, \quad (114)$$

where the position vector $\mathbf{r} = (r_x, r_y, r_z)$, the vector field $\boldsymbol{\psi}$ contains all of the vectors important for electromagnetic wave propagation through plasma such as wave properties \mathbf{E}_1 and \mathbf{B}_1 , and plasma properties like \mathbf{J} and \mathbf{E}_0 . The matrix $\bar{\mathbf{M}}$ describes the unperturbed plasma by containing all of the important physics for any particular modelling problem. If we assume that the plasma is only varying slightly with respect to one vacuum wavelength of the electromagnetic wave, then the structure of $\boldsymbol{\psi}$ will vary only slightly from the form which resembles an homogeneous plasma. This is to say that we are applying the WKB approximation to assume that the spatial and temporal dependence of $\boldsymbol{\psi}(\mathbf{r}, t)$ can be completely described through the phase $\phi(\mathbf{r}, t)$ of the wave. This is comparable to some of the approximations made in the derivation of the cold plasma dispersion relation in section 3. Firstly, we've assumed the slowly changing background limit detailed in section 3.1.2, where any time or space derivatives of background quantities are zero, e.g.,

$$\frac{\delta \mathbf{E}_0}{\delta t} \approx \nabla \times \mathbf{B}_0 \approx 0. \quad (115)$$

Secondly, we assume that perturbed plasma quantities vary with the same frequency as the electromagnetic wave that induced them. This is identical to the assumption that allowed the formation of equation (37) in section 3.1.3. This allows us to evaluate equation (114) according to the mathematical structure of the electromagnetic waves driving the wave-plasma interactions. In other words, we have forced the structure of $\boldsymbol{\psi}$ to feature a common factor of $\exp(i\phi)$, where ϕ is fully described by the type of electromagnetic wave. For instance, for plane-wave solutions (derived in section 10.1)

$$\phi = \mathbf{k} \cdot \mathbf{r} - \omega t. \quad (116)$$

Given this common factor of $\exp(i\phi)$, equation (114) then becomes

$$\bar{\mathbf{M}}(\omega, \mathbf{k}, \mathbf{r}, t)\psi = 0. \quad (117)$$

In general equation (117) has a seemingly infinite number of solutions. In one of the most simple forms for a magnetised plasma, the matrix $\bar{\mathbf{M}}$ could be formed using the cold plasma approximation as we have in section 3. In that case, the structure of $\bar{\mathbf{M}}$ would be akin to that of equation (65). We can obtain the dispersion relation of this plasma described by $\bar{\mathbf{M}}$ by taking the determinant and setting it to zero, as

$$\xi(\omega, \mathbf{k}, \mathbf{r}, t) = \det(\bar{\mathbf{M}}(\omega, \mathbf{k}, \mathbf{r}, t)) = 0. \quad (118)$$

Each solution of this corresponds to a polarisation of wave that can exist in the plasma, similarly to the identification of polarisations in section 3.3. Equation (118) will typically have many solutions. However, for a given wave-vector \mathbf{k} at a specific position in space and time (\mathbf{r}, t) then the dispersion relation will yield a unique frequency for a wave described by $(\mathbf{k}, \mathbf{r}, t)$. With the only unknown being frequency, we could use equation (118) to say that

$$\omega = \Omega(\mathbf{k}, \mathbf{r}, t), \quad (119)$$

where Ω is the known dispersion relation for our particular wave solution. In order to model the dispersion relation given in equation (119), we use the ray-tracing equations, which are

$$\frac{d\mathbf{r}}{dt} = \frac{\partial \Omega}{\partial \mathbf{k}}, \quad (120)$$

$$\frac{d\mathbf{k}}{dt} = -\nabla\Omega, \quad (121)$$

and

$$\frac{d\omega}{dt} = \frac{\partial\Omega}{\partial t}. \quad (122)$$

Given the arguments to equation (119) at two adjacent time-steps as initial conditions, equations (120)-(122) can be used to evaluate ω , \mathbf{k} , and \mathbf{r} . It would then be possible to update $\Omega(\mathbf{k}, \mathbf{r}, t)$, and this process could then be repeated any number of times desired, allowing modelling of the chosen polarisation as it propagates through the medium described by $\bar{\mathbf{M}}(\omega, \mathbf{k}, \mathbf{r}, t)$.

Ray-tracing calculations are fast and computationally inexpensive. The drawback is that their derivation relies upon the WKB approximation; the background plasma gradient is assumed to be varying slowly with respect to the wavelength of the electromagnetic wave, and the wave-vector is assumed to be changing slowly, and there are several points of interest where this may be inappropriate. As an electromagnetic wave approaches cutoffs and resonances the coupling between the plasma and the wave becomes strong, and the wave-vector must change rapidly in order for the electromagnetic wave to maintain its original polarisation. In addition to these two cases, H-mode plasmas have steep plasma edge pressure gradients where the plasma changes rapidly over a distance on the order of 1cm . This 1cm length-scale is comparable to many microwave diagnostic and heating beams of interest for spherical tokamaks. There exist numerical methods [103] which attempt to combine ray-tracing and full-wave methods. These techniques would be most applicable to cases where an electromagnetic wave is expected to propagate for a long time before interacting with a non-WKB environment. These hybrid solvers are much more computationally efficient than pure full-wave codes, however the coupling of the two techniques may be challenging, and raises reliability concerns which need

to be addressed on an individual basis. Bench-marking some solutions of a hybrid code against a full-wave code would likely be required to justify accuracy.

4.2 Full-wave

Unlike ray-tracing, full-wave simulations give a full representation of the wave, and this is achieved by directly solving Maxwell’s equations coupled with the equations governing the plasma dynamics. A common approach for the modelling of electromagnetic waves under a full-wave model is the Finite Difference Time Domain (FDTD) [104–106] method. This technique allows for numerical solutions to the partial differential forms of Faraday’s (24) and Ampère’s laws (25). Evolving the calculation in the time-domain allows for a broad range of frequencies to be studied with a single simulation. Additionally, important wave-scattering effects such as Doppler shift are intrinsically accounted for. It also allows for visualisation of the evolving electromagnetic waves which can be invaluable in developing a deeper and more intuitive understanding of the physical processes.

The FDTD technique is based on the ‘discretisation’ of Faraday’s and Ampère’s laws over a 3D grid; the values of the electric and magnetic field components in space, plus time are described at discrete points in space. The discretisation used here is called a ‘Yee Cell’ [107] which is illustrated in figure 16. This is achieved using centered finite difference formulae

$$\frac{\partial}{\partial x} u|_{i,j,k}^n = \frac{1}{\Delta x} (u|_{i+\frac{1}{2},j,k}^n - u|_{i-\frac{1}{2},j,k}^n) + O[\Delta x^2], \quad (123)$$

$$\frac{\partial}{\partial t} u|_{i,j,k}^n = \frac{1}{\Delta t} (u|_{i,j,k}^{n+\frac{1}{2}} - u|_{i,j,k}^{n-\frac{1}{2}}) + O[\Delta t^2], \quad (124)$$

where Δx and Δt represent the Yee cell spatial and time steps, respectively. The $u|_{i,j,k}^n$ notation represents some calculated field at spatial integers i, j, k and time-step n . $O[\Delta x^2]$ and $O[\Delta t^2]$ represent higher order approximation errors.

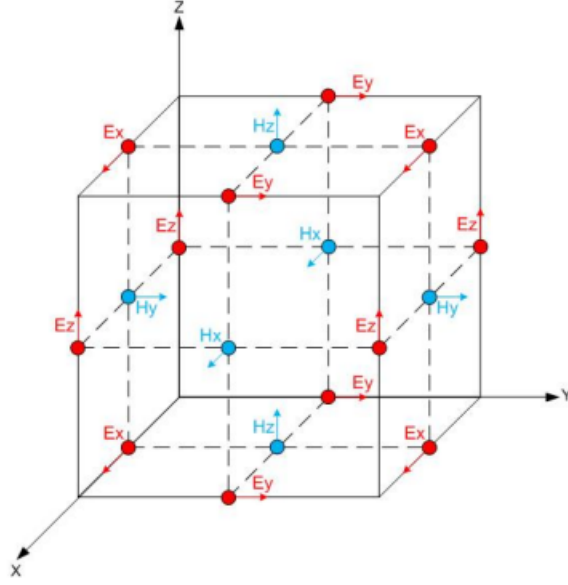


Figure 16: Diagram of a Yee Cell. Each side length is Δx [108].

In figure 16, the electric and magnetic fields can be seen to be staggered; at any single grid point there is only information regarding the electric field *or* the magnetic field, but not both. This is a natural consequence of the centered difference formulae. Applying equations (123) and (124) to Faraday's and Ampère's laws, we derive the following expressions,

$$B_x|_{i,j+\frac{1}{2},k+\frac{1}{2}}^{n+\frac{1}{2}} = B_x|_{i,j+\frac{1}{2},k+\frac{1}{2}}^{n-\frac{1}{2}} + \frac{\Delta t}{\Delta x} \left[E_y|_{i,j+\frac{1}{2},k+1}^n - E_y|_{i,j+\frac{1}{2},k}^n - E_z|_{i,j+1,k+\frac{1}{2}}^n - E_z|_{i,j,k+\frac{1}{2}}^n \right], \quad (125)$$

$$B_y|_{i+\frac{1}{2},j,k+\frac{1}{2}}^{n+\frac{1}{2}} = B_y|_{i+\frac{1}{2},j,k+\frac{1}{2}}^{n-\frac{1}{2}} + \frac{\Delta t}{\Delta x} \left[E_z|_{i+1,j,k+\frac{1}{2}}^n - E_z|_{i,j,k+\frac{1}{2}}^n - E_x|_{i+\frac{1}{2},j,k+1}^n - E_x|_{i+\frac{1}{2},j,k}^n \right], \quad (126)$$

$$B_z|_{i+\frac{1}{2},j+\frac{1}{2},k}^{n+\frac{1}{2}} = B_z|_{i+\frac{1}{2},j+\frac{1}{2},k}^{n-\frac{1}{2}} + \frac{\Delta t}{\Delta x} \left[E_x|_{i+\frac{1}{2},j+1,k}^n - E_x|_{i+\frac{1}{2},j,k}^n - E_y|_{i+1,j+\frac{1}{2},k}^n - E_y|_{i,j+\frac{1}{2},k}^n \right], \quad (127)$$

$$E_x|_{i+\frac{1}{2},j,k}^{n+1} = E_x|_{i+\frac{1}{2},j,k}^n - \frac{c^2 \Delta t}{\Delta x} \left[B_y|_{i+\frac{1}{2},j,k+\frac{1}{2}}^{n+\frac{1}{2}} - B_y|_{i+\frac{1}{2},j,k-\frac{1}{2}}^{n+\frac{1}{2}} - B_z|_{i+\frac{1}{2},j+\frac{1}{2},k}^{n+\frac{1}{2}} + B_z|_{i+\frac{1}{2},j-\frac{1}{2},k}^{n+\frac{1}{2}} - \frac{\Delta t}{\epsilon_0} J_x|_{i+\frac{1}{2},j,k}^{n+1} \right], \quad (128)$$

$$E_y|_{i,j+\frac{1}{2},k}^{n+1} = E_y|_{i,j+\frac{1}{2},k}^n - \frac{c^2 \Delta t}{\Delta x} \left[B_z|_{i+\frac{1}{2},j+\frac{1}{2},k}^{n+\frac{1}{2}} - B_z|_{i-\frac{1}{2},j+\frac{1}{2},k}^{n+\frac{1}{2}} - B_x|_{i,j+\frac{1}{2},k+\frac{1}{2}}^{n+\frac{1}{2}} + B_x|_{i,j+\frac{1}{2},k-\frac{1}{2}}^{n+\frac{1}{2}} - \frac{\Delta t}{\epsilon_0} J_y|_{i,j+\frac{1}{2},k}^{n+1} \right], \quad (129)$$

$$E_z|_{i,j,k+\frac{1}{2}}^{n+1} = E_z|_{i,j,k+\frac{1}{2}}^n - \frac{c^2 \Delta t}{\Delta x} \left[B_x|_{i,j+\frac{1}{2},k+\frac{1}{2}}^{n+\frac{1}{2}} - B_x|_{i,j-\frac{1}{2},k+\frac{1}{2}}^{n+\frac{1}{2}} - B_y|_{i+\frac{1}{2},j,k+\frac{1}{2}}^{n+\frac{1}{2}} + B_y|_{i-\frac{1}{2},j,k+\frac{1}{2}}^{n+\frac{1}{2}} - \frac{\Delta t}{\epsilon_0} J_y|_{i,j,k+\frac{1}{2}}^{n+1} \right], \quad (130)$$

where equations (125)-(127) update the magnetic field components, and equations (128)-(130) update the electric fields. Careful analysis of one of the update equations shows that the magnetic field components never need to evaluate an electric field component at the same position in space, and vice versa, the same is true for the electric field components. This is one of the advantages of the FDTD technique; only requiring a single grid point to hold information regarding the magnetic field, *or* the electric field, significantly reduced the computational memory requirements which can be large in full-wave calculations. Further memory efficiency is yielded by consideration of the advancement of one of the electromagnetic components in time. Calculation of time-step, say $t = n + 1$, only requires information regarding the previous time-step ($t = n$). This results in only the current, and previous time-step information requiring to be stored into memory at any single moment which is of major significance.

In order to model to interaction between the electromagnetic wave and the medium, Ampère's law is coupled to the plasma through the current density term (\mathbf{J}). The structure of the equation representing \mathbf{J} forms the 'plasma response'. Aptly named, the plasma response expression has structure depending on the physics that has been included into the model. It literally dictates what the plasma is capable of doing in response to the stimuli of the electromagnetic wave. The plasma response equation generally does have some simplifications applied. This is done primarily for three reasons. Firstly, incorporating a large range of physical effects into the plasma response equation can lead to the expression becoming overly complicated. This will have an adverse effect on the computational requirements of the simulation. In 3D space, full-wave simulations are quite computationally expensive simply due to the massive number of equations they are required to solve. The real cost of computing

time drives efforts to minimise the number of calculations required to run an expensive code. Furthermore, a complicated expression for the plasma response increases the difficulty of the implementation of the code. Maxwell's equations are wonderfully simple, and keeping the plasma response expression as simple as possible will not only reduce the probability of a mistake arising when writing the code but also makes the physical model easier to understand. A simple physical model will allow users to more easily identify its capabilities and likely lead to a wider digestion of the research. Thirdly, it can be wholly unnecessary to include a complete picture of the wave-plasma interactions. The choice of plasma model ultimately depends on the type of physics one wishes to model. The cold plasma model is frequently used due to its simplicity. However, no kinetic or thermal effects are included. This approach is perfectly reasonable providing that the physics of interest are thought to be negligibly effected by these excluded effects. For the purpose of modelling electromagnetic waves such as back-scattering diagnostics, or O-X mode conversion, the cold plasma model is likely justified.

5 EMIT-3D

EMIT-3D is an MPI parallelised, 3D, full-wave code developed at the University of York by Williams, Thomas. [109] and Thomas, Matthew. [110]. It is a cold plasma code that models an electromagnetic wave interacting with a plasma by coupling Faraday’s and Ampère’s laws (24) and (25) to a plasma response equation. has been Benchmarked [111] against the full-wave code IPF-FDMC [112] developed by Alf Köhn at Stuttgart University, Germany, and used to generate data which amounted to publicised research [96, 113]. Faraday’s and Ampère’s laws are discretised over a 3D Yee Cell (fig. 16) using the Finite Difference Time Domain (FDTD) method outlined in section 4.2. These equations model how an electromagnetic wave interacts with some medium described by the plasma response equation, which is derived under the cold plasma approximation in section 5.1. Being in the time-domain, EMIT-3D allows for visualisation of the evolution of the electric and magnetic fields. The interpretation of numerical simulations can be difficult; the ability to observe the microwave-plasma interaction over time can often assist, sometimes greatly, in understanding the physics behind the interaction. This also helps to develop a deeper understanding and intuition of the wave mechanics. Written in programming language C, EMIT-3D has been developed into a software package; it has a github page with documentation that gives detail into the usage of the code and the input parameters. There are instructions and makefiles designed to expedite the process of building and running the code on a range of commonly used supercomputers. Currently private, access to the github repository can be achieved through Prof. Roddy Vann at the University of York. This chapter describes the fundamental theoretical structure of the code, and includes developments that have been made in advancing the numerical algorithm and widening the scope of physics that EMIT-3D is capable of modelling. In section 5.1 the plasma response equa-

tion is derived, which mathematically describes the physical capabilities of the code. EMIT-3D uses certain normalisations as detailed in section 5.2, which may be of help to future users. Section 5.3 covers the scaling performance of the code on the Archer supercomputer. The Gaussian beam algorithm is discussed in section 5.4 with information on both linear and elliptically polarised waves; the latter being particularly useful for mode conversion studies. Finally, section 5.5 describes how EMIT-3D deals with the boundary of the simulation domain. For further details or support regarding EMIT-3D contact roddy.vann@york.ac.uk.

5.1 Plasma Response

The structure of the plasma response equations contain the mathematical details of the physics model that full-wave simulations are approximating. EMIT-3D uses the cold plasma approximation (see sec. 3.2) in order to couple the electromagnetic waves to the plasma; a stationary, magnetised, inhomogeneous, and anisotropic medium which is capable of sustaining electric fields. In this model these fields arise solely due to the electromagnetic wave. The plasma response expression in EMIT-3D uses equation (34) which was derived in section 3. Firstly, this expression is re-written in terms of the current density, by multiplying through by a factor of qn/m giving

$$\frac{\partial \mathbf{J}_1}{\partial t} = \epsilon_0 \omega_{pe}^2 \mathbf{E}_1 + \omega_{ce} (\mathbf{J}_1 \times \hat{\mathbf{b}}_0), \quad (131)$$

where $\mathbf{J}_1 = qn\mathbf{v}_1$. To form equation (131) a unit-vector describing the direction of the background magnetic field $\hat{\mathbf{b}}_0 = (b_x, b_y, b_z)$ is used, along with the definitions of the plasma frequency

$$\omega_{pe}^2 = \frac{q_e^2 n_e}{\epsilon_0 m_e}, \quad (132)$$

and the cyclotron frequency

$$\omega_{ce} = \frac{q_e B_0}{m_e}, \quad (133)$$

which are the frequencies of the natural plasma oscillations, and the gyration of electrons around background magnetic field lines, respectively. Equation (131) could now be discretised in the same manner as Maxwell's equations in section 4.2, and used in a full-wave code. However, one further modification is made, and this is due to the choice of technique for representing the boundaries of the simulation. Discussed in further detail in section 5.5, a collisional damping term is added to equation (131)

$$\frac{\partial \mathbf{J}_1}{\partial t} = \epsilon_0 \omega_{pe}^2 \mathbf{E}_1 + \omega_{ce} (\mathbf{J}_1 \times \hat{\mathbf{b}}_0) - \mathbf{J}_1 \nu, \quad (134)$$

where ν represents collisionality. This allows us to remove energy from the simulation to prevent un-physical boundary reflection of the electromagnetic waves.

The numerical solution to equation (134) is non-trivial and is derived in detail in the PhD thesis of Williams, T. [96], and the result is presented; a discretised, temporal update equation as

$$\mathbf{J}_1|^{n+\frac{1}{2}} = e^{-\nu \Delta t} \Theta \mathbf{J}_1|^{n-\frac{1}{2}} + \frac{\epsilon_0 \omega_{pe}^2}{(\nu^2 + \omega_{ce}^2) \Delta t} \Xi \mathbf{E}_1|^{n}, \quad (135)$$

where

$$\Theta = b_i b_j [1 - \cos(\omega_{ce} \Delta t)] - \epsilon_{ijk} b_k \sin(\omega_{ce} \Delta t) + \delta_{ij} \cos(\omega_{ce} \Delta t), \quad (136)$$

$$\Xi = b_i b_j \alpha - \epsilon_{ijk} b_k \beta + \delta_{ij} \gamma, \quad (137)$$

$$\alpha = \frac{\omega_{ce}^2 \Delta t}{\nu} + \Delta t e^{-\nu \Delta t} \left\{ \nu [\cos(\omega_{ce} \Delta t) - 1] - [\omega_{ce} \sin(\omega_{ce} \Delta t)] - \frac{\omega_{ce}^2}{\nu} \right\}, \quad (138)$$

$$\beta = \omega_{ce} \Delta t - \Delta t e^{-\nu \Delta t} [\omega_{ce} \cos(\omega_{ce} \Delta t) + \nu \sin(\omega_{ce} \Delta t)], \quad (139)$$

$$\gamma = \nu\Delta t + \Delta t e^{-\nu\Delta t} [\omega_{ce} \sin(\omega_{ce}\Delta t) - \nu \cos(\omega_{ce}\Delta t)]. \quad (140)$$

where δ_{ij} is the Kronecker delta which is defined as

$$\begin{aligned} \delta_{ij} &= 0 \text{ if } i \neq j, \\ \delta_{ij} &= 1 \text{ if } i = j. \end{aligned} \quad (141)$$

and ϵ_{ijk} is the Levi-Civita symbol defined as

$$\begin{aligned} \epsilon_{ijk} &= +1 \text{ if } (i, j, k) \text{ is } (1, 2, 3), (2, 3, 1), \text{ or } (3, 1, 2), \\ \epsilon_{ijk} &= -1 \text{ if } (i, j, k) \text{ is } (3, 2, 1), (1, 3, 2), \text{ or } (2, 1, 3), \\ \epsilon_{ijk} &= 0 \text{ if } i = j, \text{ or } j = k, \text{ or } k = i. \end{aligned} \quad (142)$$

This is a simple model, and as such eliminates a wide range of interesting physics. The simplicity has enabled the undertaking of this research, while maintaining all the key physics which are thought to be of interest to (at least) plasma edge back-scattering, electromagnetic mode-conversion, and beam broadening due to turbulence. Of the made approximations, two are most note-worthy. The first is the assumption that the plasma is cold. The cold plasma approximation is frequently used in full-wave electromagnetic wave modelling, and heavily simplifies the theory required to solve certain problems. For the aforementioned phenomena, this approximation is unlikely to have significant effect on the result. The reasoning for this is the comparative time-scale of the evolution of the electromagnetic wave, and the evolution of the plasma, which was discussed briefly in section 4. In forcing the plasma to be stationary, this causes notably unphysical effects for waves coupling to the upper-hybrid resonance (UHR), and careful analysis is required to avoid misinterpreting the simulation results. This disadvantage can be mitigated by using a collisional damping term in the plasma response equation [114] with a non-zero value near the UHR. Furthermore, the electrostatic Bernstein wave cannot exist under the cold plasma approximation. This causes X-B mode conversion modelling to be impossible as the description of Bernstein waves require warm plasma theory [115]. It

is possible [114] to advance the numerical algorithm of a cold plasma full-wave code to include some warm plasma effects by including an additional term in the dielectric tensor of equation (57). This allows for the modelling of electrostatic Bernstein waves. It also has the advantage of better representing the UHR, and removing the need for the artificial collisional damping term. The second potentially significant made approximation was that there are no background plasma flows ($\mathbf{v}_0 = 0$). Once again, this approximation heavily simplifies the equation that EMIT-3D is required to solve, both improving the ease of comprehension of the model and reducing the computational resources required to solve the equations. The influence of this is though to have a small effect on the X-mode dispersion relation. Original work developing the mathematical treatment which is required for developing a $\mathbf{v} \neq 0$ cold plasma dispersion relation is shown in section 10.2.

5.2 Normalisation

EMIT-3D uses a mixture of normalised and non-normalised variables. All of the frequencies (ω_{pe} , ω_{ce} , ω_0 , ν) where ν is the collisional frequency, are normalised, whereas the vector fields (\mathbf{E} , \mathbf{B} , \mathbf{J}) are not. This represents a change from the code's original implementation and allows for easier comparison between simulations which use different values for fundamental numerical parameters such as the resolution and Courant–Friedrichs–Lewy (CFL) number [116].

EMIT-3D uses Faraday's law (24), Ampere's law (25) and the plasma response equation (134) derived in section 5.1. Normalising time to the time-step Δt and distance to the spatial step Δx where spatial steps in all three spatial dimensions are equal $\Delta x = \Delta y = \Delta z$,

$$t' = \frac{t}{\Delta t}, \tag{143}$$

$$x' = \frac{x}{\Delta x}. \quad (144)$$

Applying these normalisation to the partial derivative with respect to time and the del operator,

$$\frac{\partial}{\partial t} \Rightarrow \frac{\partial}{\partial t'} \frac{1}{\Delta t}, \quad (145)$$

$$\nabla \Rightarrow \frac{\nabla'}{\Delta x}. \quad (146)$$

The frequencies are also normalised as

$$\omega'_0 = \omega_0 \Delta t, \quad (147)$$

$$\omega'_{ce} = \omega_{ce} \Delta t, \quad (148)$$

$$\nu' = \nu \Delta t, \quad (149)$$

$$\omega_{pe}^2{}' = \omega_{pe}^2 \Delta t^2. \quad (150)$$

Applying the normalisation of the time (145) and space (146) derivatives, along with the normalised frequencies (147)-(150) to EMIT-3D's governing equations (24),(25), and (134) we get

$$\frac{\partial \mathbf{B}}{\partial t'} \frac{1}{\Delta t} = -\frac{1}{\Delta x} \nabla' \times \mathbf{E}, \quad (151)$$

$$\frac{\partial \mathbf{E}}{\partial t'} \frac{1}{\Delta t} = \frac{1}{\Delta x} c^2 \nabla' \times \mathbf{B} - \frac{1}{\epsilon_0} \mathbf{J}, \quad (152)$$

$$\frac{\partial \mathbf{J}}{\partial t'} \frac{1}{\Delta t} = \epsilon_0 \frac{\omega_{pe}^2{}'}{\Delta t^2} \mathbf{E} - \frac{\omega'_{ce}}{\Delta t} \mathbf{J} \times \mathbf{b}_0 - \frac{\nu'}{\Delta t} \mathbf{J}. \quad (153)$$

The use of the definition of the CFL number

$$C_r = c \frac{\Delta t}{\Delta x}, \quad (154)$$

and the free space relation

$$\mathbf{B} = \mu_0 \mathbf{H}, \quad (155)$$

and the definition of the impedance of free space

$$Z_0 = c\mu_0, \quad (156)$$

Equations (151)-(153) simplify and become

$$\frac{\partial \mathbf{H}}{\partial t'} = -\frac{C_r}{Z_0} \nabla' \times \mathbf{E}, \quad (157)$$

$$\frac{\partial \mathbf{E}}{\partial t'} = C_r Z_0 \nabla' \times \mathbf{H} - \frac{\Delta t}{\epsilon_0} \mathbf{J}, \quad (158)$$

$$\frac{\partial \mathbf{J}}{\partial t'} = \frac{\epsilon_0}{\Delta t} \omega_{pe}^2 \mathbf{E} - \omega'_{ce} \mathbf{J} \times \mathbf{b}_0 - \nu' \mathbf{J}. \quad (159)$$

Equations 157-159 represent the normalised, theoretical usage of the governing expressions (24), (25) and (134) in EMIT-3D. Practically, these equations still need to be discretised as we have done in sections 4.2 and 5.1.

5.3 Computational Performance

Understanding how well a piece of software performs under varying conditions is important for the effective use of computational resources. It may be possible to constrain simulations to one, or more dimensions, in order to reduce the computational demand, and increase the scientific output for a given amount of computational time. The relationship between varying dimension size and performance

may be non-linear, and the reasonings behind this are numerous. A major potential contributor being the code parallelisation; certain sizes of sub-process can be more efficient than others. The performance is also dependent on each particular system's architecture. Several different High-Performance Computing (HPC) facilities were utilised during the research towards this PhD, including Archer, Marconi, Cirrus, Archie-West and multiple lower-tiered machines. While a thorough analysis would require the computational performance of the code to be tested on each of these machines, this is unnecessary; with entire node allocation (no sharing of nodes with other users) the scaling of the efficiency is unlikely to change dramatically from one machine to another. The following efficiency tests were conducted on the tier-1 machine Archer, based at the University of Edinburgh. Initially, the length ratio between each of the 3 spatial dimensions is investigated for performance variation. A spatially cubic simulation is compared to three of harsh dimensionality, and the time-step duration is measured as the number of cores used for the simulations is varied. In each of the 4 data sets the volume of the simulation is equal. Figure 17 shows the results of this analysis.

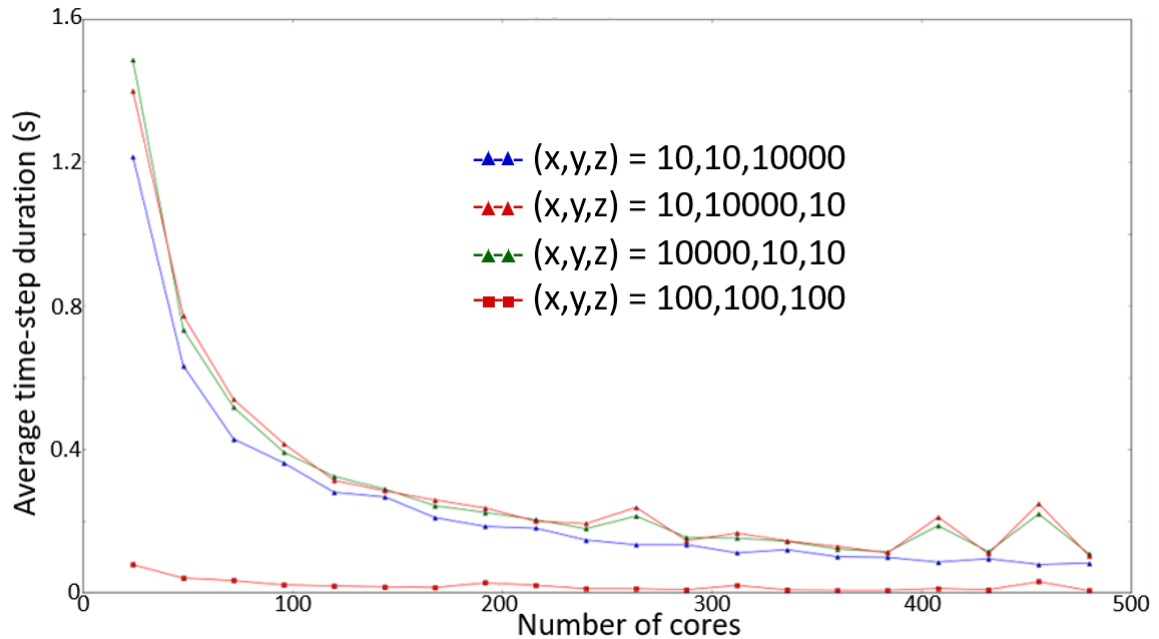


Figure 17: An analysis into the computational performance of EMIT-3D when the ratio between the 3 spatial dimensions are varied. The volume is kept constant in each of the data sets. The red (squares) line shows a spatially cubic simulation, whereas the blue, green and red (triangles) lines show an extreme ratio of the spatial dimensions in the x, y and z dimensions, respectively. The simulation domain is split such that each of the processors have an identical (or as close to as possible) geometry.

While it is interesting to see that certain spatial dimensions fare better than others, it is clear from figure 17 that spatially cubic simulations perform at much higher efficiencies, whereas simulations utilising extended dimensions should be avoided if possible.

Given that spatially cubic simulations perform better than non-cubic counterparts, it is also important to assess how well a particular experiment-relevant geometry scales with an increasing number of allocated cores. If the number of cores

(i.e, the processing power) is increased by a factor of N , it would be desirable to see the time taken to complete the calculation reduce by $1/N$. In practise this is not feasible for 2 main reasons. Firstly, each core is surrounded by ghost cells. These are a layer of cells which surround a process, and store information which can be passed to other processes. They are essential for the parallelisation, as they allow for communication between neighbouring cores. The computational performance will begin to saturate when the number of ghost cells in a simulation becomes significant compared to the overall size of the domain. Secondly, it is commonplace for parallel codes to use multiple nodes. This adds some networking demands as signals must be passed and interpreted between different pieces of hardware. Many HPC facilities now use very high performance interconnect systems between their nodes, such as InfiniBand, which is capable of delivering speeds of up to 15GB/s. For context, an L1 processor cache can deliver speeds of over 1TB/s, and the slower, larger and generally shared L3 cache has a theoretical limit of 175GB/s. While it is interesting to compare the above data-rates it would be an oversimplification to use these speeds in order to attribute InfiniBand as the bottleneck, and conclude that using an interconnect system which could match the L1 cache speed would result in a linear increase in computational performance. The rate of a computation when using a multitude of nodes is a function of many variables, and while a detailed analysis of each electrical component is possible it would be tremendously complicated, and costly in terms of time. It is far more widespread to perform an empirical analysis of a particular piece of software. Figure 18 uses a spatially cubic box size of 1000x1000x1000 grid points, which was deemed an approximately appropriate size for future simulations. The average time-step duration is analysed for fixed simulation parameters, over a range of cores. Conducted on the now retired Archer-1 HPC machine, each node features 48 cores. Every other data-point in figure 18 then not only refers to an increase in cores allocated to the computation but also an increase

in the number of nodes. Speed-up here is in reference to a single node (48 cores) which has a speed-up value of 1.0.

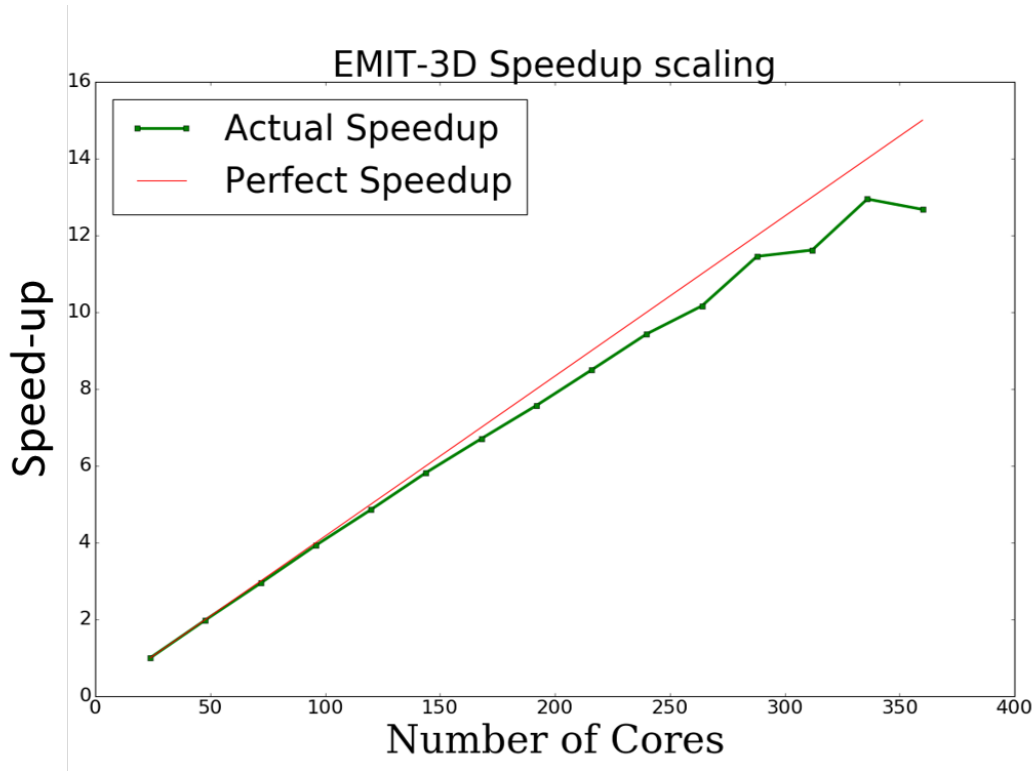


Figure 18: Efficiency scaling of EMIT-3D running a 1000x1000x1000 grid point domain, for a variety of cores. The red line indicates the perfect speed-up while the green line indicates the achieved. The speed-up is in reference to a single node (48 cores).

The line in red refers to the perfect rate of speed-up, where the speed of the calculation has increased by a factor of N , where N is the factor by which the number of cores used to perform the calculation has increased. As discussed previously this theoretical rate is impossible to achieve because of additional computational demands added when using additional cores and nodes. 3D Full-wave codes have intense memory demands, and this forms the hard limit to the minimum number

of nodes that can be used for a calculation. For the size of simulation used here (1000x1000x1000) the code required approximately 250GB of memory. Each node on Archer contains 64GB so the minimum node requirement here was 4. Figure 18 contains data-points which use less than 4 nodes (i.e, the lowest data-point used 24 cores, which is half a node.). This was achieved by purchasing 4-nodes for the computation, and then ordering most cores to stand idle. While this is important for the empirical analysis it is a waste of computational resources and should be avoided. Using 4 nodes (192 cores) EMIT-3D scales extremely well, and has and retains an efficiency of 94.25%. While the efficiency remains very good all the way up to 384 cores (8 nodes) it does start dropping off beyond this point. Due to the Archer-1 system using the high-quality InfiniBand interconnect system (as opposed to Ethernet), this drop off is likely due to the influx of ghost cells into the simulation. Each additional core increases the amount of ghost cells required, and the efficiency starts to worsen when the number of ghost cells becomes a significant fraction of the overall simulation domain, meaning that additional cores would have an increasingly noticeable non-linear effect on the speed-up.

5.4 Gaussian Beam

A linearly polarised Gaussian beam may be launched in EMIT-3D over a 2D antenna-plane by using the fundamental solution to the paraxial wave equation [117]. For a beam propagating along the z-axis, the time-independent electric field distribution is described by

$$E_x(r, z) = E_0 \frac{\omega_0}{\omega(z)} \exp \left[\frac{-r^2}{\omega(z)^2} \right] \exp \left[i \left(kz + k \frac{r^2}{2R(z)} - \psi(z) \right) \right], \quad (160)$$

where the second, third, and fourth factors represent the beam amplitude, Gaussian profile, and phase, respectively.

An elliptically polarised beam may also be launched. This allows for pure O-mode or X-mode beams to be launched at arbitrary angles to the background magnetic field. Using the relations defined in [118] the field distributions are described as

$$E_z = -\cot(\theta)E_x, \quad (161)$$

$$E_y = \frac{2\cot(\theta)E_x}{Y^2\sin^2(\theta) + \sqrt{Y^2\sin^2(\theta) + 4\cos^2(\theta)}}. \quad (162)$$

where θ is the angle between the background magnetic field and the beam wave vector, and $Y = \omega_{ce}/\omega_0$.

5.5 Boundaries

The boundaries of the simulation contain a damping layer designed to reduce the reflected wave amplitude to zero. setting the boundary values to zero, for example, electromagnetic waves interacting with the edges of the simulation domain would simply reflect. By removing all the energy that enters the boundary an infinite box is effectively simulated. Within the boundary layer the wave's electric field is multiplied by a cubic damping function $D(r)$ of the form

$$D(r) = 1 + \frac{13}{T} ((r - d_{\text{bound}})/d_{\text{bound}})^3, \quad (163)$$

where T is the wave period, d_{bound} is the boundary thickness and $r \leq d_{\text{bound}}$. The boundary layer is three vacuum wavelengths thick, and at the edge the condition $E = 0$ is enforced. This causes total reflection of any remaining signals, causing them to propagate back through the damping region. This results in a total propagation distance of six vacuum wavelengths over which the wave is damped.

5.6 Pedestal

In order to model the H-mode plasma edge a modified tanh function [119] was implemented. This function, shown in figure 19 allows for great control over the simulated pedestal. The function and the definitions of the variables can be seen from the figure.

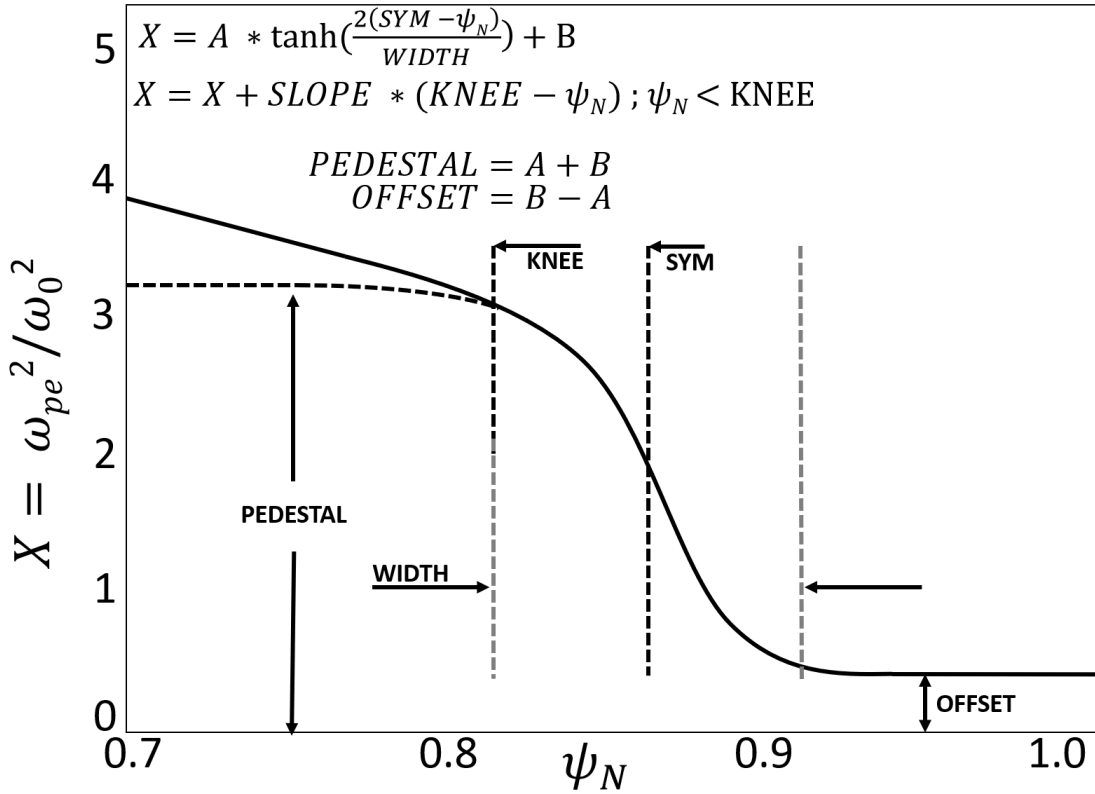


Figure 19: Modified tanh function used for representation of the aggressive H-mode plasma edge number density profile.

5.7 Importing Density and Magnetic Field Maps

The ability to import 2D density, and magnetic field maps was implemented into EMIT-3D. This is essential for realistic modelling when the simulation domain needs

to well represent an experimental environment. These maps can be attained through the use of turbulence modelling software, or collaboration with fusion research centers such as Culham Centre for Fusion Energy (CCFE). Both of these sources were ultimately utilised for the research in this PhD.

5.7.1 Importing Background Profiles

CCFE supplied reconstructed MAST-U [52] density, and magnetic field equilibrium profiles. These were given for the purpose of Ordinary-Slow Extraordinary-Bernstein (O-X-B) mode conversion studies for research into microwave-source O-X-B heating systems. This research can be seen in section 8.2.

In order to import maps into a piece of software, care must be taken to ensure that all of the necessary pre-run-time steps are taken for the map to be valid under the simulation parameters. For instance, the spatial scales given to the software, and defined in the map must match. For importing a background map, these considerations are detailed in section 8.2. Importing a density background map is fairly straightforward. The file must exist before run-time and represent a 2D radial-vertical plane. Due to the scalar nature of number density, the data can be imported and directly taken to be the values of the plasma background density profile. At run-time the density information is imported, and then extended along the toroidal dimension, representing the excellent transport parallel to the background magnetic field lines.

The magnetic background map requires some further considerations. The three Cartesian components corresponding to the radial (B_r), vertical (B_z), and toroidal (B_t), must exist in separate, 2D radial-poloidal files before run-time. These files are individually imported, at which time the spherical co-ordinate system uses them to calculate the magnetic field vector on each grid-point, as

$$\phi = \arctan\left(\frac{B_z}{B_t}\right), \quad (164)$$

$$\theta = \arctan\left(\frac{\sqrt{B_z^2 + B_t^2}}{B_r}\right). \quad (165)$$

The magnetic field magnitude is also required, and calculated on each grid-point as

$$B = \sqrt{B_t^2 + B_r^2 + B_z^2}. \quad (166)$$

These vectors and magnitudes are stored in memory for later usage by the plasma response equation (135).

5.7.2 Importing Perturbation Profiles

Density and magnetic field perturbation maps were acquired by fluid turbulence modelling with the Hermes (with BOUT++ framework) [120] code. The description of the code and its usage is given in section 6.2.1. These perturbation maps were combined with analytically produced background profiles, and used for the modelling of Doppler Back-Scattering (DBS) and Cross-Polarisation Doppler Back-Scattering (CP-DBS) experimental techniques. These scattering simulations are discussed in section 7.

Similarly to section 5.7.1, importing and using the density maps is more straightforward than the magnetic field map. A small complication arises due to the need to combine the perturbation map with the prescribed background profile. The 2D radial-vertical file must exist before run-time. For the purpose of back-scattering simulations, *critically* this profile must be normalised to the radial position whereby one expects an electromagnetic wave to scatter from. This is key because this will be the only radial location in the 2D plane where the perturbation is of the desired strength. At run-time, this 2D profile is imported into EMIT-3D and extended along

the background magnetic field lines. The values of the normalised 2D density profile (n_1) are set to appropriate magnitudes by the user input parameter $\delta n/n_0$, as

$$n_1 \rightarrow \frac{\delta n}{n_0} n_0, \quad (167)$$

where n_0 is the strength of the analytically produced background density profile.. This density perturbation is then combined with the background as

$$n_0 \rightarrow n_0 + n_1. \quad (168)$$

The magnetic field perturbations are dealt with similarly. Differing from section 5.7.1, the code does not deal with perturbations parallel to the background magnetic field as these are assumed to be negligible. The perturbed 2D radial-poloidal components B_r and B_z must be normalised to the expected radial position of scattering. These profiles are imported into EMIT-3D at run-time and set to appropriate magnitudes by the user input parameter $\delta B/B_0$, as

$$B_z \rightarrow B_z * \frac{\delta B}{B_0} B_0 \quad (169)$$

$$B_r \rightarrow B_r * \frac{\delta B}{B_0} B_0 \quad (170)$$

where B_0 is the background magnetic field strength, which is assumed to be homogeneous and set as a single-value user input. The variations in the magnetic field vector are calculated as

$$\phi = \phi_0 + \arctan\left(\frac{B_z}{B_0}\right), \quad (171)$$

$$\theta = \theta_0 + \arctan\left(\frac{B_r}{B_0}\right), \quad (172)$$

where ϕ_0 and θ_0 are the spherical coordinates describing the unperturbed background magnetic field. The resultant magnetic field is then calculated with equation (166).

The magnitude and direction of the magnetic field at each grid-point are now ready to be passed to the plasma response equation (135) which couples these effects to the electromagnetic wave.

6 Numerical Turbulence

Turbulence is the most important unsolved problem of classical physics.

- Richard Feynman.

A plasma that is free from instabilities will feature a very low degree of cross-field heat and particle transport, that is described by 'neoclassical' physics. Building upon classical transport theory, neoclassical transport [121] uses the Fokker-Planck collision operator to analyse transport both parallel and perpendicular to the background magnetic field. It is a kinetic description which predicts transport due to collisional effects. Where neoclassical expands on classical transport, is the inclusion of transport effects as a result of non-uniform magnetic fields. Classical theory assumed that the spatial variation of the magnetic field had no influence towards particle transport. This is not applicable for tokamak devices, because the magnetic field variation can be strong. This variation causes particle trapping, and the perpendicular motion of the gradient-B and curvature drifts of gyrating particles; two naturally arising particle-motion effects, consequential of toroidal, magnetised devices. Neoclassical transport theory then builds upon classical theory by including non-uniform magnetic field effects into a model that already observed collisional effects. Importantly, neoclassical theory assumes that the plasma is in a quiescent state. Turbulent effects are excluded from the model. In reality, fusion plasmas are not quiescent, and exhibit turbulence on a range of length-scales, including many small scale fluctuations. These fluctuations are an effective way of transporting heat and mass across magnetic field lines [122]. Described by anomalous transport theory, the contribution of turbulence towards transport is often expressed through electron or ion diffusivities. Compared to neoclassical transport, anomalous transport can be an order of magnitude higher for the ions, and three orders of magnitude higher for the electrons [123]. Turbulent behaviour is complex and not well understood,

but the nature and drivers of the Electron Temperature Gradient (ETG) mode, and the Micro-tearing Mode (MTM) are detailed in section 2.2.

In magnetic fusion plasmas, the electron temperatures can be so high that the ions cannot trap them. The electrons escape the ion orbits, and the plasma can be thought of as a ‘soup’ of charged particles. The particle interactions are dominated by long range coulomb deflections that occur at distances far greater than the atomic radius. In a fully ionised plasma this is the dominant type of interaction and leads to a majority preference for small angle deflections. In such a case, these plasmas are named collision-less. Collision-less plasmas can arise in the core of a tokamak, where the pressures are high enough for fusion to occur on a reasonable time-scale. It can be shown [124] that the resistivity of a *fully ionised* plasma goes as

$$\eta \propto T_e^{-\frac{3}{2}}, \quad (173)$$

where η and T_e are the resistivity and the electron temperature, respectively. Commonly referred to as the Spitzer resistivity, expression (173) indicates that for very high temperature plasmas, the resistivity will be low. This leads to the core of fusion plasmas having turbulent mechanisms that are dominated by non-collisional effects. In the H-mode plasma edge the dominant damping mechanism is collisional damping [125]. Fluid models are particularly suitable to plasmas where the motion of the plasma is dominated by the $\mathbf{E} \times \mathbf{B}$ drift. This drift is well described by a fluid model, because the motion itself is fluid-like; the velocity is the same for every charged particle.

Understanding and being able to predict plasma turbulence is critical for the development of future fusion reactors. Progress is gained by creating theoretical models, and testing them against rigorous experimental measurements. Validated models can be used to generate numerical turbulence. These turbulence maps can then be used within full-wave codes to give detailed simulations of wave-plasma

interactions. There exist several popular types of numerical methods for the modelling of plasma turbulence. The choice of which depends on the region of plasma one wishes to model and the goals of the experiment. In this chapter gyro-kinetic and fluid plasma models are discussed.

6.1 Kinetic Model

Mechanisms such as Landau damping or neoclassical transport are ‘kinetic effects’ because they involve the finite Larmor radius or particle-wave interactions. There are certain plasma regimes where kinetic mechanisms are thought to be closely related to the plasma turbulence. Under such regimes it is necessary to include kinetic effects in any plasma model aimed at well describing the turbulence. One example of such, are gyrokinetic models. Gyro-kinetic simulations form a kinetic description of the plasma turbulence, while respecting the gyrating nature of particles in a magnetised plasma.

The description of a plasma can be thought of as the closure of Maxwell’s equations using constitutive variables such as density, temperature, or velocity. It is convenient to describe these variables in terms of a phase-space distribution function

$$N(\mathbf{x}, \mathbf{v}, t) = \sum_{k=1} \delta[\mathbf{x} - \mathbf{x}_k(t)] \delta[\mathbf{v} - \mathbf{v}_k(t)] \quad (174)$$

where $\mathbf{x}_k(t)$ and $\mathbf{v}_k(t)$ satisfy the following equations of motions

$$\frac{d\mathbf{x}_k(t)}{dt} = \mathbf{v}_k(t) \quad (175)$$

,

$$\frac{d\mathbf{v}_k(t)}{dt} = \frac{q}{m} \mathbf{E}[\mathbf{x}_k(t), t] + \mathbf{v}_k(t) \times \mathbf{B}[\mathbf{x}_k(t), t] \quad (176)$$

where $\mathbf{E}(\mathbf{x}, t)$ and $\mathbf{B}(\mathbf{x}, t)$ are the microscopic electric and magnetic fields, respectively. An expression for $\partial N/\partial t$ can be derived [126, 127] and is called the Klimontovich equation

$$\frac{\partial N}{\partial t} + \mathbf{v} \cdot \frac{\partial N}{\partial \mathbf{x}} + \frac{q}{m}(\mathbf{E} + \mathbf{v} \times \mathbf{B}) \cdot \frac{\partial N}{\partial \mathbf{v}} = 0. \quad (177)$$

This is an elegant expression which hasn't utilised any statistical averaging and takes into account all scales. Unfortunately since the Klimontovich equation tracks the trajectory and interactions of each particle it is not tractable when modelling any significantly sized plasma. In order to obtain a tractable expression the ensemble average $f = \{N\}$ of equation (177) can be taken

$$\frac{\partial f}{\partial t} + \mathbf{v} \cdot \frac{\partial f}{\partial \mathbf{x}} + \frac{q}{m}(\mathbf{E} + \mathbf{v} \times \mathbf{B}) \cdot \frac{\partial f}{\partial \mathbf{v}} = C_s, \quad (178)$$

where C_s is the collisional operator. C_s varies depending on the situation and it can lead to equation (178) being very challenging to solve. However, there are some cases where it may be acceptable to ignore collisions and thus set the collision operator to zero. This $C_s = 0$ condition yields the Vlasov equation

$$\frac{\partial f}{\partial t} + \mathbf{v} \cdot \frac{\partial f}{\partial \mathbf{x}} + \frac{q}{m}(\mathbf{E} + \mathbf{v} \times \mathbf{B}) \cdot \frac{\partial f}{\partial \mathbf{v}} = 0. \quad (179)$$

This is a tractable, kinetic description of a plasma. It has been obtained through averaging of the Klimontovich equation, and as such retains all of the kinetic physics. The scope of the modelable physics of the Vlasov equation is somewhat reduced from the Klimontovich equation due to the removal of the collisional operator. Certain plasma regimes are indeed collisionless, however there are other situations where a non-zero collisional operator is necessary for the accurate modelling of the plasma. While the Vlasov equation is tractable it remains computationally challenging due

to the phase-space (velocity-position) distribution function requiring 6 dimensions. It is possible to reduce the computational demands further, by excluding kinetic effects and considering the plasma as a fluid. This would certainly reduce the scope of the modelable physics, but it represents an advancement in the theory and will be discussed in the next section.

6.2 Fluid Model

Kinetic descriptions of fusion plasmas can be achieved through the Vlasov equation (179). While this equation is tractable, it is demanding to solve due to the use of 6 phase-space dimensions. The metric of this kinetic equation can also be difficult to work with, as the significance of a distribution function may not be immediately obvious. Additionally, in an experiment distribution functions can be a difficult to accurately measure. These two considerations imply that there is a certain disconnect between the theory and experiment. Due to this, the advancement of kinetic theory into fluid theory is appealing. It is more intuitive to work with fluid quantities (such as density and temperature), and these also tend to be some of the easier to experimentally measure. The computational demand of fluid codes is tremendously reduced from their kinetic counterpart, since only 3 dimensions are required.

In order to obtain the fluid equations the moments of the ensemble-averaged kinetic equation (178) are taken. The zeroth, first, and second moments become the continuity, momentum conservation, and energy conservation equations, respectively [128],

$$\frac{\partial n_s}{\partial t} + \nabla \cdot n_s \mathbf{v}_s = 0, \quad (180)$$

$$m_s n_s \frac{\partial \mathbf{v}_s}{\partial t} + \nabla \cdot \mathbf{P}_s = q_s n_s (\mathbf{E} + \mathbf{v}_s \times \mathbf{B}) + \mathbf{F}_s, \quad (181)$$

$$\frac{\partial}{\partial t} \left(\frac{3}{2} p_s + \frac{1}{2} m_s n_s v_s^2 \right) + \nabla \cdot \mathbf{Q}_s = q_s n_s \mathbf{E} \cdot \mathbf{v}_s + W_s + \mathbf{v}_s \cdot \mathbf{F}_s, \quad (182)$$

where for particle species s , n_s is the number density, \mathbf{v}_s is the velocity, \mathbf{P}_s is the stress tensor, \mathbf{F}_s is the collisional friction with other species, W_s is the energy exchange with other species, and \mathbf{Q}_s is the energy flux density. Equations (180), (181) and (182) are conservation equations and can be intuitively analysed by considering the convective derivative. Let G be some physical quantity, and $g(\mathbf{r}, t)$ be its density. We would expect

$$G = \int g d^3 \mathbf{r} \quad (183)$$

and considering G is conserved, then $g(\mathbf{r}, t)$ must vary according to the convective derivative as

$$\frac{\partial g}{\partial t} + \nabla \cdot \mathbf{g} = \Delta g, \quad (184)$$

where the divergence term $\nabla \cdot \mathbf{g}$ represents the flow of the quantity $g(\mathbf{r}, t)$ into, or out of some local region, and the differential term represents the change of $g(\mathbf{r}, t)$ according to any sources or sinks described by Δg . An understanding of equation (184) can yield some intuition into equations (180)-(182). Equation (180) indicates that, locally, there are no sources or sinks of number density for species s . Equation (181) shows that the momentum varies locally according to the Lorentz force and the collisional friction term. Equation (182) shows that the energy changes locally according to electrical work, energy exchange with some other species and by frictional heating. In order to perform modeling with the fluid equations we need to obtain a closed system. Currently there are too many variables and too few equations. In order to close a fluid system of equations an asymptotic scheme may be used. This can be mathematically challenging and involves the detailed analysis of

some small parameter. The choice of the small parameter depends on the system one is attempting to describe. For instance, for collisional plasmas one choice may be the ratio of the mean-free-path to the macroscopic length-scale of the system. For collisionless and magnetised plasmas another option would be to choose the ratio of the Larmor radius to the macroscopic length-scale. The details of the mathematics describing asymptotic closure of the fluid equation in magnetised plasma are complicated and are considered outside of the appropriate scope of theory for this thesis. However, the process involves finding expressions for the unknown quantities \mathbf{P}_s , \mathbf{F}_s , \mathbf{Q}_s , and \mathbf{W}_s in terms of density, velocity and energy. In plasma physics a common asymptotic technique is based on the work of Braginskii [128] which uses the ratio of the mean-free-path to the macroscopic length scale of the system.

Fluid models are frequently used to predict the behaviour of plasmas in a magnetic field. Fluid codes are best suited to regions of the plasma where perpendicular particle motion is dominated by $\mathbf{E} \times \mathbf{B}$ drifts, because the motion of the plasma is fluid-like. This is figuratively visualised by considering that the $\mathbf{E} \times \mathbf{B}$ drift acts uniformly on all particles, rather than kinetic transport mechanisms.

While fluid turbulence is generally low frequency $\omega < 10^6 \text{rads}^{-1}$ [129], tokamak plasma particles also gyrate around the magnetic field lines. For each species the gyro-frequency is $\omega_c = ZeB/m$ where Z and m are the charge state and mass, respectively. Since generally $\omega \ll \omega_c$ the timescale over which fluid-like turbulence evolves is much greater than that required to resolve the gyration. Due to this, fluid turbulence codes typically treat each particle by its gyro-center, effectively ignoring the effects of particle gyration. However, certain gyro-fluid codes [130–132] do include some kinetic effects by using some moments of the gyrokinetic equation, and including certain mechanisms that are typically ignored by the fluid equations. The most prominent application of these models is to the tokamak plasma core.

Fluid codes are more applicable in regimes where collisional damping is the dom-

inant damping mechanism. Unsurprisingly, collisional damping is significant under regimes where the plasma is considered collisional. Observing the Spitzer resistivity (173), these collisional plasma regimes occur in the colder regions, namely the plasma edge. In such regions fluid models make an approximation that kinetic effects are insignificant in driving turbulence, and thereby reduce both the complexity of the model and the computational cost required to simulate it.

6.2.1 The Hermes code

The 3D plasma-edge fluid modelling code Hermes [120] uses the Braginskii closure [128] mentioned in section 6.2. It employs the drift-reduction technique [133] which allows for the simplification of the conservation of momentum expression (181). This approximation assumes that perpendicular motion is dominated by the $\mathbf{E} \times \mathbf{B}$ drift, which is likely reasonable when applied to the plasma edge since temperatures are low. This approximation reduces the computational demand of Hermes, which can be high, and allows for an expression for the vorticity to be obtained which assists in closing the equations described in section 6.2.

Hermes is open-source software that is used in this research in conjunction with the full-wave code EMIT-3D for the modelling of the Cross-Polarisation Doppler Back-scattering (CP-DBS) technique. The Hermes turbulence calculation uses the electron number density, electron temperature, and background magnetic field profiles as simulation inputs. It evolves these profiles over time to produce self-consistent electromagnetic, fluid turbulence maps. These maps are then used in EMIT-3D for the full-wave modelling of CP-DBS.

The simulation domain was set with the radial, poloidal, and toroidal axes having sizes of 120cm, 60cm, and 1cm, respectively. The toroidal dimension was kept small as the length of this dimension had some relationship to the code stability. The plasma beta is set to $\beta = 5.43\%$ with the background magnetic field being

homogeneous and parallel to the toroidal dimension. The electron number density (blue) and electron temperature (red) profiles can be seen from figure 20. For the initial time-step, this profile is homogeneous in the poloidal and toroidal dimensions. After turbulence has had time to arise, this is no longer true, particularly for the poloidal dimension.

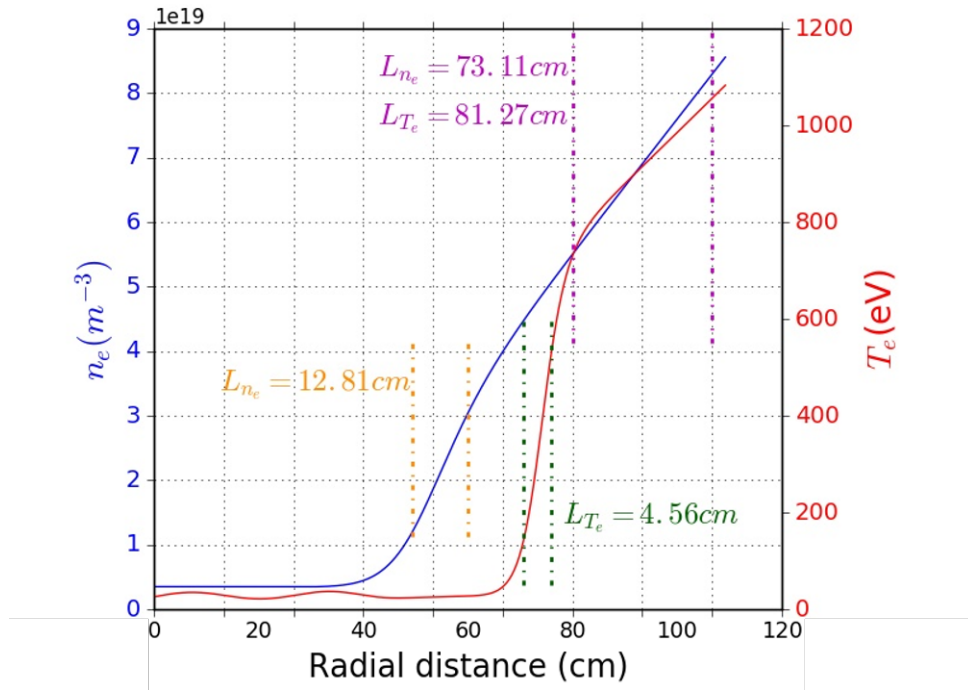


Figure 20: Electron number density and electron temperature profiles used as inputs into the Hermes turbulence calculation. These 1D profiles are initially homogeneous in the poloidal and toroidal dimensions.

Figure 20 shows the electron number density and temperature length-scales of the background profiles provided to Hermes at different spatial locations, which are calculated, respectively, as

$$L_{T_e} = \frac{\partial r}{\partial \ln(T_e)}, \quad (185)$$

$$L_{n_e} = \frac{\partial r}{\partial \ln(n_e)}. \quad (186)$$

The length-scales shown in figure Figure 20 are gentle compared to that of the edge of an H-mode MAST plasma which could have an electron density length-scale on the order of $L_n \approx 1.0\text{cm}$. Attempts were made to provide Hermes with more aggressive profiles which would be more comparable with the MAST experiments. However, the Hermes calculation unfortunately becomes un-stable when the density or temperature length-scales are pushed too low. The profiles shown in figure 20 were attained by trial and error. The length-scales were increased until unacceptable instability was seen, and then reduced until a simulation remained stable for a satisfactory period of time. While this misrepresentation of the length-scales is unfortunate, it is not problematic as the Hermes turbulence simulations do not need to provide an accurate representation of the turbulence on any specific MAST shot. The reason for this is two-fold. Firstly, it would be challenging to prove beyond reasonable doubt that the results of a fluid turbulence calculation accurately represent a particular MAST shot, because making the necessary experimental measurements is a difficult task in itself. Fluid calculations may be satisfactory, however certain physical effects are omitted in these models. Non-linear gyrokinetic simulations are more thorough because they contain the kinetic effects that fluid codes have neglected. However, these calculations are an active area of research and do not presently exist for the plasma-edge region. Secondly, the purpose of the full-wave simulations of the CP-DBS diagnostic is not to find agreement with a particular experiment. This research is not in the position to conduct such simulations because our understanding of the mechanism behind the cross-polarisation scattering interaction is poor. This research seeks to better understand the mechanism behind

the interaction, and identify if there are any underlying non-WKB physical effects which need to be taken into account when interpreting experimental CP-DBS measurements. For these two reasons it is therefore deemed that providing Hermes with electron number density and temperature profiles with length-scales greater than that of experimentally relevant H-mode shots is acceptable.

One major advantage of using a numerical code to produce the turbulence profiles is that both the density and magnetic field perturbations are calculated self-consistently. Using an analytic expression to induce perturbations in a full-wave code would raise difficult questions as to how the perturbation phase difference has influenced the result. By self-consistently producing the electromagnetic turbulent profiles this issue is less of a concern. Although the exclusion of kinetic effects cannot be dismissed and may also influence the result.

It has been pre-determined that the profiles (fig. 20) used as inputs for the Hermes code result in a simulation with a period of stability. The results are observed, and the point at which any instabilities becomes significant is recognised. A single time-step, taking during the stable phase is identified. The density (left) and magnetic (right) turbulence profiles at this step are shown in 2D poloidal-radial plane in figure 21.

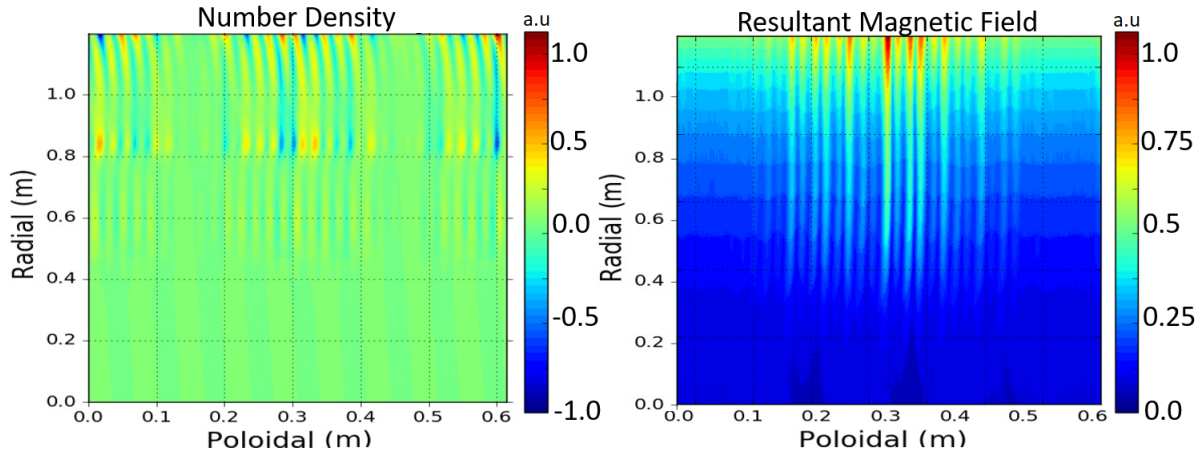


Figure 21: Density (left) and magnetic (right) 2D turbulence profiles taken at some stable time-step from a Hermes turbulence calculation.

The perturbations shown in figure 21 in both the density and magnetic profile appear to be almost exclusively radial. This can be explained by considering the initial conditions supplied to the Hermes calculation. At time-step $t = 0$ the profile shown in figure 20 is homogeneous in both poloidal and toroidal (into the page) dimensions. This means that all of the ‘free energy’ available for the driving of the turbulence is directed in the radial dimension, since this is the only direction that the density and temperature gradients are non-zero. This leads to the perturbations in this linear growth phase to be orientated radially. Free energy is described mathematically as gradients in the plasma profiles and has been discussed in section 2.2. The Hermes simulation became unstable shortly after the time-step shown in figure 21. However, if the simulation remained stable and was ran for more time then free energy would begin to arise in the poloidal dimension as a result of the radial perturbations. This would cause some poloidally orientated turbulence to grow, causing non-linear growth. This effect would be heightened by the reduction of free energy in the radial dimension. While Hermes does also track the temperature profile fluctuations, this

data has been excluded from figure 21 because it is not used for the EMIT-3D simulations as the plasma model is cold.

Previous attempts to produce electromagnetic fluctuations without turbulence modelling software using analytical expressions failed. This is because the analytical expressions were poorly designed and introduced significant amounts of divergence in the magnetic field perturbations. It is useful to compare these previous attempts with the turbulence simulations as it was unknown as to what an acceptable level of divergence would be for use in a full-wave code. The divergence of the 2D radial-poloidal magnetic field perturbation map shown in figure 21 (right) is calculated and plotted in figure 22. The average degree of divergence is approximately 3×10^{-14} which confirms that the magnetic field is divergence-free up to the precision of the computer.

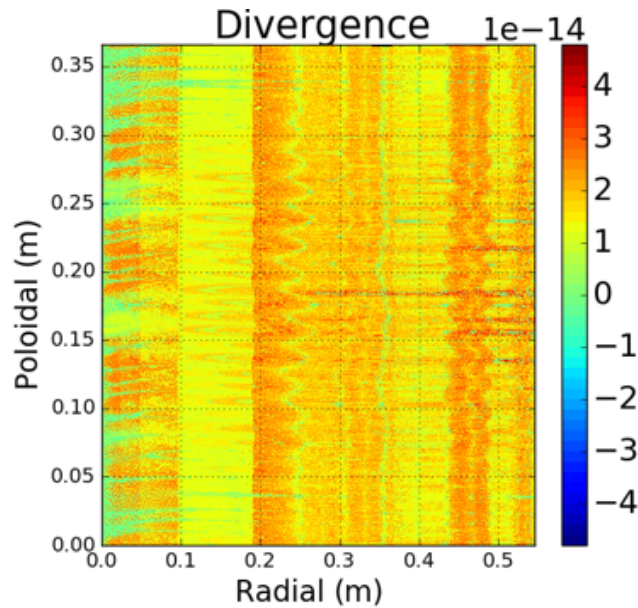


Figure 22: The calculated divergence of the radial-poloidal magnetic field perturbation map shown in figure 21 (right).

Figure 23 shows how the average density and temperature (left) and resultant

magnetic field (right) fluctuation strength varies with the radial axis. These graphs are used to locate a reasonable radial position about which to normalise the 2D profiles shown in figure 21. The density and temperature fluctuation strengths vary strongly with radial position. Whereas the average resultant magnetic fluctuation strength increases monotonically. For the normalisation, the radial position of $R = 100cm$ was chosen. This was done for three reasons. Firstly, if an antenna is situated at the radial position of $R = 0.0cm$, there is a significant amount of vacuum that the beam would be required to propagate through before interacting with the normalised fluctuations at $R = 100cm$. This is important because test simulations in modelling CP-DBS have made it clear that there must be a substantial vacuum propagation path-length in order to detect the weak back-scattered signals over the strong reflected probing beam. Secondly, at the position of $R = 100cm$ we can see from figure 23 that the density, temperature, and magnetic fluctuations are all apparent to a significant degree. This may be unimportant but it indicates that, in this region of space, all three fluctuating parameters have been able to interact with one another in the Hermes calculation, perhaps leading to more realistic turbulence. Thirdly, these exist approximately $15cm$ behind the $R = 100cm$ position. This is important to allow for the wave to evolve correctly around the scattering surface; a cut-off situated too close to the $R = 120cm$ boundary may erroneously damp signals that are important in creating the back-scattered interference pattern.

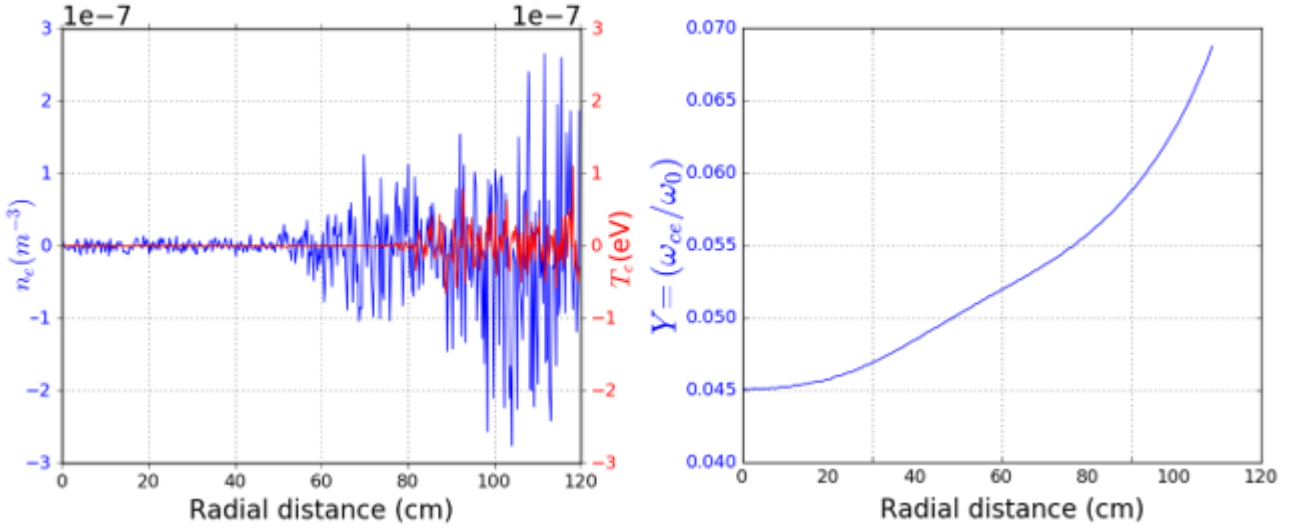


Figure 23: Average fluctuation strengths for the density and temperature (left) , and the magnetic (right) profiles.

The perturbation field maps are normalised at the aforementioned radial position of $R = 100cm$. It is now necessary to perform Fourier analysis to determine the wave-number spectrum of the turbulence. This is critical for the CP-DBS simulations because the wave-vector condition (18) for back-scattering must be satisfied. The results of this analysis are shown in figure 24, where the wave-number spectra of the density and magnetic turbulence profiles are shown in black and blue(radial)/red(vertical), respectively.

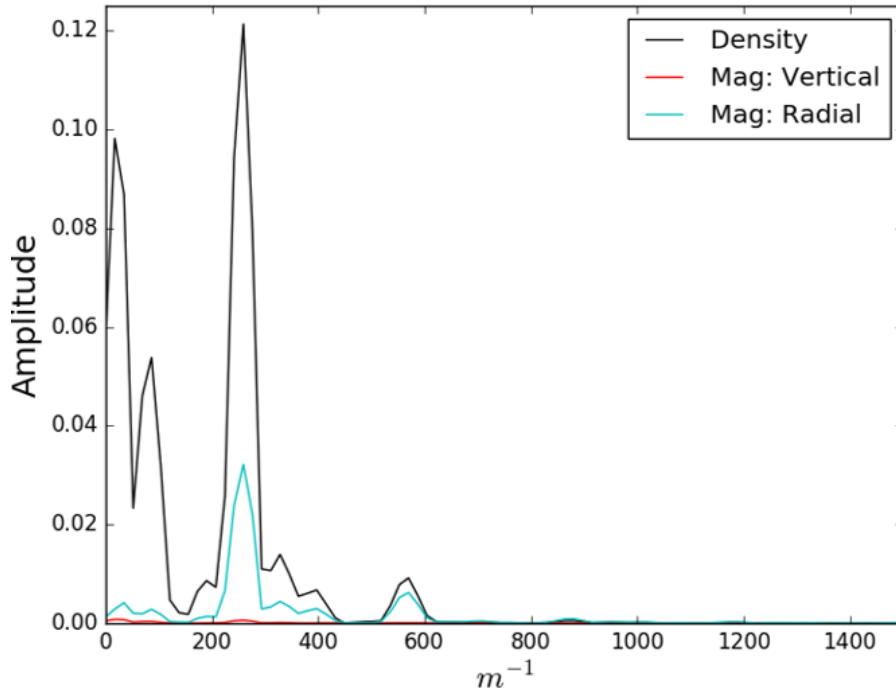


Figure 24: Wave-vector Fourier analysis of the 2D perturbation maps shown in figure 27. The 1D signal was taken from each of the density and magnetic perturbation profiles at a radial position of $R = 100\text{cm}$. The density wave-number spectrum is shown in black, and the magnetic perturbation components in blue(radial) and red(vertical). A major complimentary wave-number is identified at $k_0 = 2.63\text{cm}^{-1}$.

An important distinction must be noted between the wave-number spectra of the simulated turbulence (fig. 24), and the turbulence expected to be present in an H-mode tokamak plasma edge. The spectrum of the turbulence produced by the Hermes code is discrete, whereas the turbulence in a tokamak has been modelled [134] to be a continuum. The reason for this is that in reality there are a wide range of turbulent modes at a broad range of length-scales, which are simultaneously unstable to some degree in the complex and strongly inhomogeneous environment of an H-mode tokamak plasma edge. The Hermes simulation is a fluid approximation. As such it does not include all of the relevant physics; most notably, it excludes

Wave-number (cm^{-1})	$\theta(^{\circ})$
2.63	7.223
3.34	9.164
5.61	15.559

Table 1: Wave-vectors which are apparent in both the density, and the magnetic field turbulence maps shown in figure 21. Wave-vector Fourier analysis of these maps is shown in figure 24. The θ column refers to the angle to the normal of the density profile at which one must launch a $55GHz$ probing beam in order to match the approximate condition for back-scattering shown in equation (18).

kinetic effects. The reasoning for using a simplified turbulence model has already been made. The result of this, is that only certain turbulent modes, at certain length-scales, can be modelled. This has resulted in the produced wave-number spectrum to be discrete. In order to minimise the impact of this notable difference it is important to choose a discrete wave-vector that is present in both the density, and the magnetic wave-vector spectrum. So that when scattering using the Bragg approximation for back-scattering it can be justifiably said that both the density, and the magnetic wave-number spectra were appropriately matched. Three notable wave-numbers are identified from figure 24. Given a launched wave of $f = 55GHz$, these wave-numbers and the resulting required launch angle (calculated with equation (18)) are shown in table 1.

All of the wave-vectors identified in table 1 could be argued to be appropriate in one way or another, and there is no clear choice as to which to focus on. Ultimately the wave-vector $k_0 = 2.63cm^{-1}$ was chosen for use in the CP-DBS simulations. This was because of two reasons. Firstly, both the density, and the magnetic signals have a major peak at this wave-number. Secondly, the angle required to match the

approximate condition for back-scattering is small, but substantial. Smaller angles can be more favourable due to the smaller computational domain required for the simulations. For a given plasma and antenna configuration, larger injection angles potentially require a larger simulation domain because of the increased poloidal beam propagation path. With knowledge of the wave-vector spectra, the normalised density, and magnetic perturbation maps (fig. 21) are ready for use in the full-wave EMIT-3D simulations.

6.2.2 Analytic turbulence

The turbulence generated with the Hermes fluid code in section 6.2.1 constitutes a reasonable attempt to generate a plausible scattering surface. Steps have been taken to ensure this turbulence is as accurate as possible, however, we identify several key expected differences between these numerically generated fluctuations and real plasma turbulence. As a result of this, it is desirable to generate a secondary set of electromagnetic fluctuations. This will allow for a comparison between the observed scattering mechanics and will assist in identifying any physical effects which arise as a result of the nature of the fluid turbulence.

In this section we create a simple, monochromatic piece of turbulence using a trigonometric function of the form

$$\delta B_{vertical}[j, k] = \sin \frac{j}{\lambda} 2\pi. \quad (187)$$

Here, $\delta B_{vertical}[j, k]$ is the perturbed radial magnetic field at the grid position of j, k which are indices. The λ variable is the desired wave-length of the fluctuation. The toroidal component of the turbulence is assumed to be zero, and the radial component is calculated according to the divergence free nature of magnetic fields

$$\delta B_{radial}[j, k - 1] = \delta B_{radial}[j, k] - \delta B_{vertical}[j - 1, k] + \delta B_{vertical}[j, k]. \quad (188)$$

Equations (187) and (188) give rise to the radial (left) and vertical (right) magnetic field maps shown in figure 25.

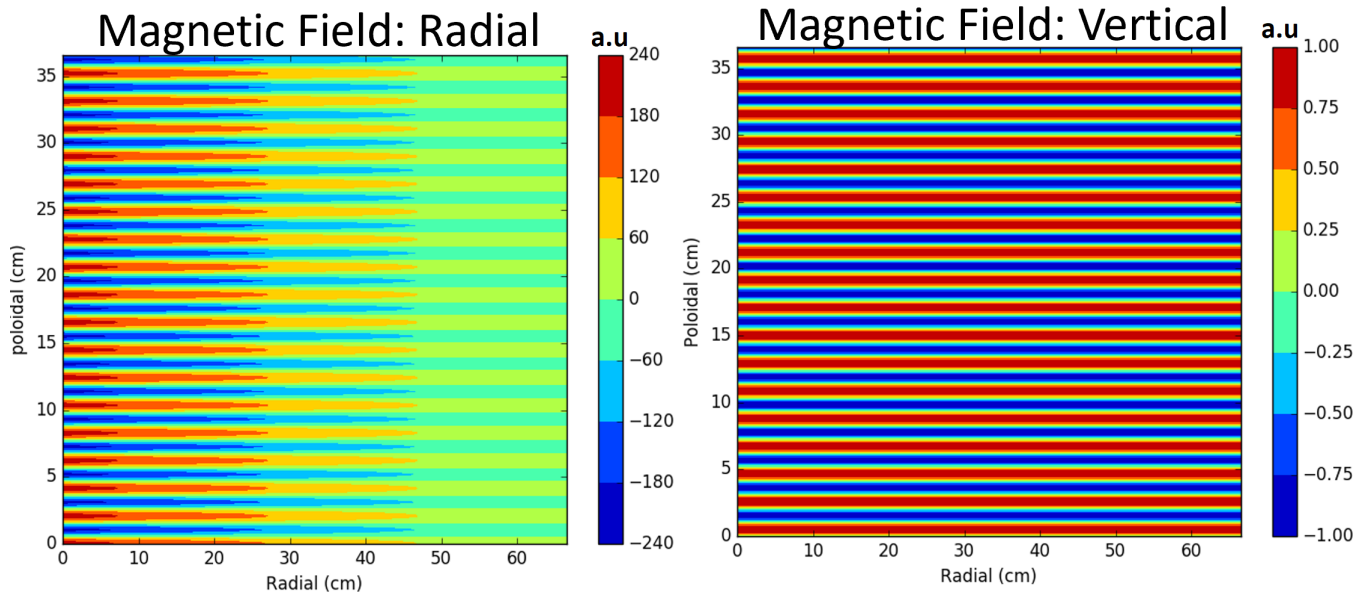


Figure 25: Radial (left) and vertical (right) magnetic field perturbation maps generated analytically.

Fourier analysis of these analytically produced magnetic field perturbations is shown in figure 26.

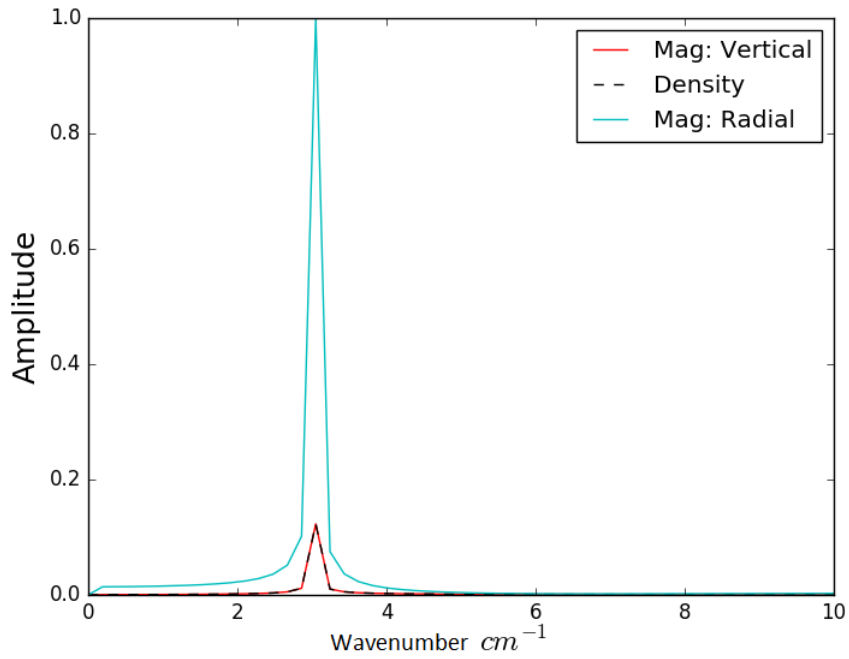


Figure 26: Fourier analysis of the monochromatic turbulence produced with the analytical equations (187) and (188). All three signals have wave-number $k = 3.052\text{cm}^{-1}$

These fluctuations are then used within EMIT-3D in the same way as the Hermes fluctuations described in section 6.2.1. This import process is detailed in section 7.1.

7 DBS and CP-DBS Modelling Results

Cross-polarisation Doppler back-scattering (CP-DBS) is a novel diagnostic technique that seeks to measure the wave-number, amplitude, and poloidal velocity of magnetic perturbations induced by micro-turbulence. Outlined in section 2.3.2, this technique is similar to conventional Doppler back-scattering (DBS) outlined in section 2.3.1, but is much more challenging. The research presented in this chapter seeks to set the fundamental basis for the modelling of CP-DBS simulations, addressing some of the concerns with the diagnostic technique.

As discussed in section 2.3.2, the magnetic fluctuations ($\delta B/B$) measured by CP-DBS can be small. This causes the CP-DBS electromagnetic signals to be weak and one challenging aspect of the diagnostic is detecting the CP-DBS above noise and signal contamination. This issue is discussed in section 7.3. Another major concern for the feasibility of the diagnostic is coupling between the characteristic O and X-mode waves due to non-Wentzel–Kramers–Brillouin (WKB) effects. Current experimental CP-DBS diagnostic measurements rely on the O and X-mode waves being independent modes that have negligible interaction with one another. This may not be a valid assumption; interaction between the O and the X-mode can occur when the polarization of the probing beam changes quickly [101, 135]. This can happen when magnetic shear, or the background plasma density gradient is large. It is thought that this interaction effect could be significant when the inequality

$$\frac{|k_x - k_o|}{2\pi/L_n} \ll 1.0 \quad (189)$$

is approximately satisfied. This problem is discussed in section 7.4.

As described in section 6.2.1, the Hermes turbulence simulation runs in the time domain. A snapshot is taken during the linear growth phase and a 2D poloidal-radial slice is captured. The 2D electromagnetic turbulence snapshot is then normalized

such that the RMS fluctuation amplitude is unity at a radial location that will ultimately correspond to the microwave scattering location. At run-time EMIT-3D can either omit the magnetic component and import solely electrostatic turbulence, or import the fully electromagnetic turbulence snapshot. During the import the 2D turbulence structures are extended in the third dimension along background magnetic field lines. These 3D turbulence structures are then multiplied by user specified values to attain the desired fluctuation amplitudes. Figure 27 shows the density and magnetic field fluctuations of the turbulence.

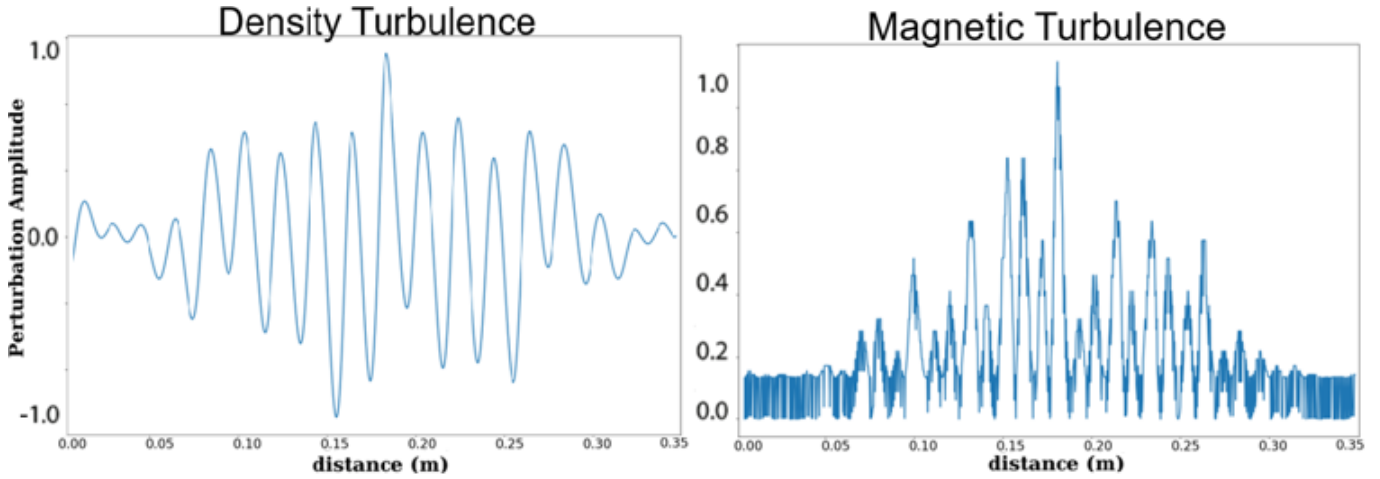


Figure 27: Waveform of the normalised number density (left) and the resultant magnetic field (right). Signals are used for Fourier analysis.

A 50GHz X-mode Gaussian beam of 9cm diameter is launched perpendicular to the background magnetic field, towards the plasma at an angle of $\theta = 7.223^\circ$ to the normal of the scattering surface. This matches the vacuum approximation condition for back-scattering shown in equation (18) since the wave-number analysis of figure 24 gives a strong peak at $k_{\perp} = 2.63cm^{-1}$. The microwave propagates through approximately 13cm of vacuum before encountering the plasma. After a short optical path length of $\Lambda \approx 2.5\lambda_0$ the X-mode wave interacts with the fast

X-mode cutoff where the measurement of the background density length-scale is important and is described in section 7.1. Highly-localised to the cutoff, Bragg back-scattering from turbulence causes some scattered wave energy to propagate back along the beam path. The cross-polarised O-mode signal generated by the microwave interaction with magnetic turbulence has a slightly different beam path to the back-scattered X-mode due to the different dispersion relation. However, the short overall optical path length causes this difference to be negligible. The back-scattered radiation propagates back to the antenna where it is detected. The power ratio between the back-scattered O-mode and back-scattered X-mode is measured, which is representative of the turbulence fluctuation.

7.1 Preliminary Modelling

The density perturbations are normalised such that the magnitude at the location corresponding to the cutoff of the launched microwave is equal to unity. The desired magnitude of the density perturbation can then be set as an input parameter to the simulation, and varied easily without modifying the density perturbation map. The resultant number density at some position in space is then calculated as

$$n \rightarrow n_0 + \frac{\delta n}{n_0} n_0 \delta n \quad (190)$$

where n is the resulting number density, n_0 is the background density, δn is the normalised perturbation density, and $(\delta n/n_0)$ is the desired magnitude of the perturbation, given as user input and constant across the simulation domain. This expression is part of the EMIT-3D algorithm and as such shouldn't be treated as an equation which can be manipulated by algebra. Specifically, the $(\delta n/n)$ term is fundamentally different to the δn term, because as mentioned δn is normalised (has a value of unity at the scattering location).

The magnetic field perturbations are more challenging to deal with due to their vectoral nature. Hermes assumes that there are no magnetic perturbations parallel to the background magnetic field which is parallel to the x – $axis$ in this work. The two perpendicular 2D radial-poloidal perturbed magnetic field maps are attained from the Hermes turbulence calculations. These components are then combined into a 2D map of the resultant magnetic field perturbation as

$$\delta B = \sqrt{\delta B_y^2 + \delta B_z^2}. \quad (191)$$

This field map is normalised in an analogous manner to the density map. The normalisation occurs in such a way that the value of the resultant magnetic field is equal to unity at the radial spatial position which will ultimately correspond to the X-mode cutoff location in the forthcoming full-wave simulation. The spatial location chosen for the normalisation is the same as when normalising the density perturbation map. In other words, the resultant magnetic field and number density perturbations maps are normalised, respectively, to the same position in space. The normalised resultant magnetic field is then used to determine by what factor the non-normalised magnetic field component needs to be multiplied by. This results in two separate 2D magnetic field perturbations; one for each perpendicular (to the background) magnetic field component. This has the advantage of allowing the desired magnetic field perturbation strength ($\delta B/B$) to be prescribed as an input parameter into the simulation, and can be modified without requiring any pre-simulation changes to the 2D perturbed magnetic field maps. The two normalised 2D magnetic field maps are imported into EMIT-3D at run-time which. Each grid-point over the 2D radial-poloidal plane reads the magnitude of the three magnetic field components corresponding to that particular grid-point position in space. These two components are then used to calculate the local direction of the magnetic field vector in spherical coordinates according to the usual coordinate transform expressions

$$B = \sqrt{B_0^2 + \delta B^2} \quad (192)$$

$$\phi = \arctan [B_y/B_0] \quad (193)$$

$$\theta = \arctan [(B_0^2 + B_y^2)/B_z] \quad (194)$$

$$(195)$$

where B_y , and B_z are the magnitude of the magnetic field components parallel to the Cartesian axes y and z , respectively, and δB is the resultant magnetic perturbation aquired from equation 191. The above system of equations are unique to the case where the background magnetic field is parallel to the x-axis. In other words $\mathbf{B}_0 = B_0 \hat{e}_x$. The spherical coordinates θ and ϕ are defines as per the physics standard for spherical coordinate systems shown in figure 28.

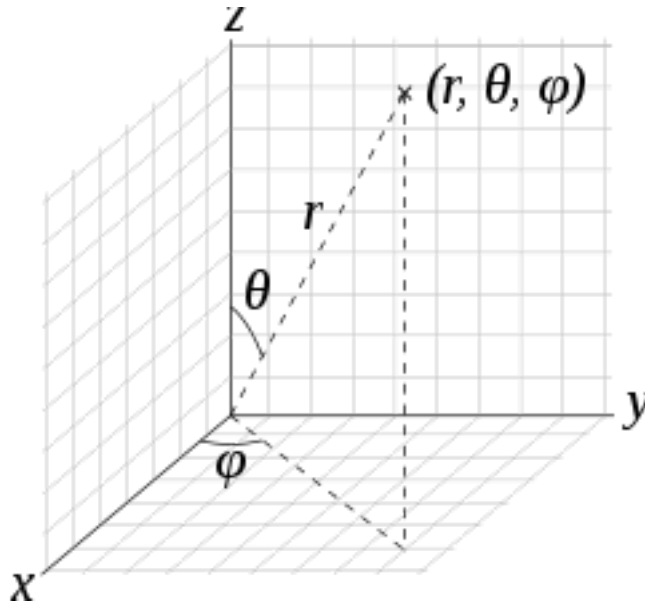


Figure 28: Physics standard for the spherical coordinate system.

The underpinning scattering theory [136, 137] predicts that for perpendicular propagation ($\mathbf{k}_i \cdot \mathbf{B} = 0$), when $\delta B_{\parallel} = 0$ the microwave scattering efficiency scales

linearly with respective perturbation strength, and the density perturbations have negligible contribution towards cross-polarization scattered signals, and vice-versa. Using the cold plasma form of the conductivity tensor (56),

$$E_{XX} \propto J_{\delta n} = \frac{\epsilon_0 \omega_{pe}^2 Y E_x \delta n}{\omega(1 - Y^2) n} \quad (196)$$

$$E_{XO} \propto J_{\delta B} = \frac{i \epsilon_0 \omega_{ce} \omega_{pe}^2 Y E_x \delta B}{\omega^2(1 - Y^2) B} \quad (197)$$

where \mathbf{E}_{XX} and \mathbf{E}_{XO} are the electric fields of waves scattered from the original X-mode, into the X-mode and orthogonal O-mode polarizations, respectively. These relations allow useful checks to see if the scattering is performing as we would expect. Using a magnetic field perturbation strength of

$$\frac{\delta B}{B} = \frac{\delta n}{n} \frac{1}{20}, \quad (198)$$

we scan through a range of values for $\delta n/n$. The perturbation ratio chosen and shown in equation (198) was done so, as this was experimentally measured with pioneering CP-DBS measurements on MAST [73].

Initially the plasma is described by setting the background plasma density and magnetic fields. A modified tanh function [119] is used to model the aggressive density profile of the H-mode pedestal. The expression along with the definition of the variables are described in figure 5.6. A thin, roughly 2λ thick region around the X-mode cutoff was used to measure the background density length-scale [138] according to

$$L_{n_e} = \frac{\delta r}{\delta \ln(n_e)}. \quad (199)$$

Figure 29 shows an example of how the δr region is specified. The radial position of the fast X-mode cutoff is determined (blue) and a thin $\delta r = 1.0\lambda_0$ spatial region

(red, dashed) is centered around the cutoff. Over the same region the change in natural logarithm of the number density $\delta \ln(n_e)$ is measured which allows the use of equation (199) for calculation of the density length-scale.

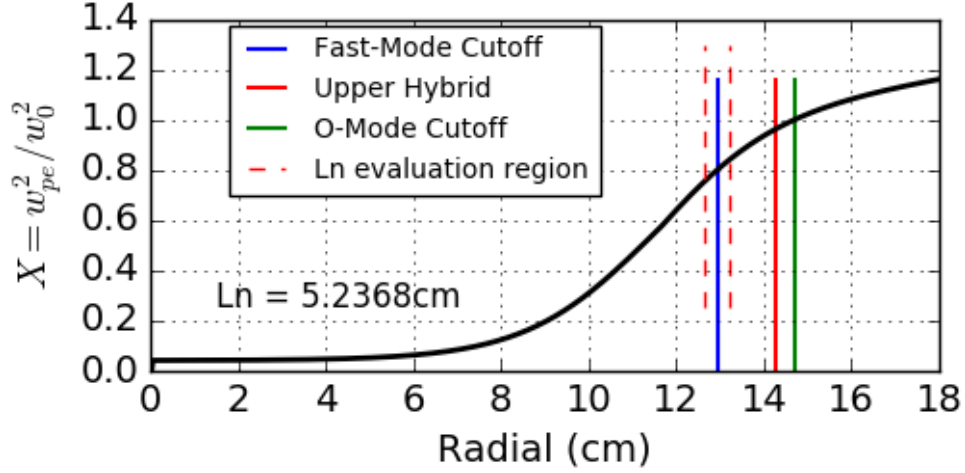


Figure 29: An example of how the density length-scales are calculated around the X-mode cutoff (blue). The O-mode cutoff (green) is also featured. The red dashed lines indicate the spatial region whereby δr and $\delta \ln n_e$ are measured for use in equation (199).

Observing equation (21), it can be seen that an increase in the magnitude of the density perturbation strength, $\delta n/n$ should produce a linear response in the strength of the scattered radiation. Similarly, equation (23) predicts the same linear relationship with regards to the magnetic field perturbation strength and the cross-polarised scattering. These relationships hold true until very high perturbation strengths where an enhanced non-linear scattering response begins to become significant [139]. This allow the formation of a basic parameter scan to confirm that the scattering mechanism is functioning as expected. The expression calculating the scaling is consistent with that used in [139] and is

$$n_i = \frac{\ln(P_{i+1}/P_i)}{\ln(\sigma_{i+1}/\sigma_i)} \quad (200)$$

where P_i and P_{i+1} are the detected powers for the present and subsequent data-points, respectively. The σ variable refers to the perturbation strength, and n_i is the scaling power (i.e. $P \propto \sigma^{n_i}$). The ratio of $(\delta B/B_0)/(\delta n/n_0) = 1/20$ was kept constant. Using the electromagnetic turbulence described in section 6.2.1, a scan through the perturbation strength was conducted over the range $10^{-5} < \delta n/n_0 < 10^0$. The simulation domain was 3D with the radial, poloidal, and toroidal dimensions having sizes of 60cm , 30cm , and 30cm , respectively. The antenna was located deep into the radial dimension at $r = 45\text{cm}$ so that there was plenty of space behind the antenna to discriminate backscattering from reflections. Figure 30 shows the results of these simulations, where the vertical axis represents the variable n_i . The parameter scans were conducted with the launch angle of $\theta = 7.0^\circ$ and multiple values of the normalised cyclotron frequency $Y = \omega_{ce}/\omega_0$ were used. The value of $n_i = 2.0$ is the expected linear scaling between the scattered electric field strength and the perturbation strengths. This is showing that the scattered power is varying as the square of the perturbation strength.

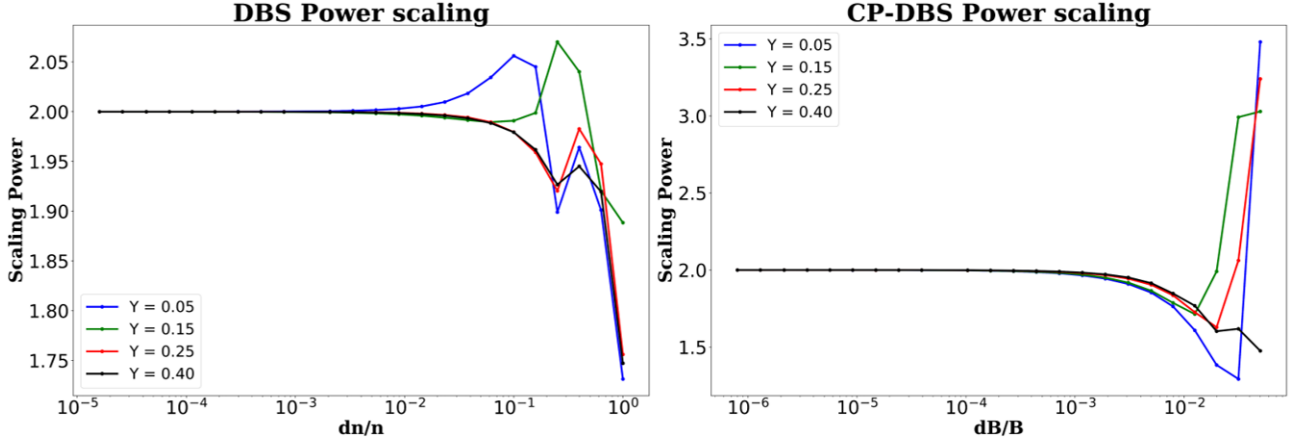


Figure 30: Scaling of the DBS and CP-DBS signal strength with increasing density, and magnetic perturbation strengths. At all data points the ratio $(\delta B/B)/(\delta n/n) = 1/20$ is kept constant. The vertical axis Scaling Power is the variable n_i in equation (200)

At low perturbation strengths the scattering response is linear as expected. The non-linear enhanced scattering regime can be seen to become noticeable in the DBS signal (left) at around $\delta n/n = 10^{-2}$. The enhanced non-linear regime gives way to heavy suppression at extremely highly dn/n . This is roughly anticipated from [139]. It is interesting to note that the background magnetic field strength seems to play a significant role in determining the transition point between the linear and non-linear regimes. Furthermore, certain values of $Y = \omega_{ce}/\omega_0$ seem to not feature enhanced scattering at all. The CP-DBS signal (right) scaling performs similarly well for low values of $\delta B/B$, showing that the power is scaling as the square of the perturbation strength, as expected. The CP-DBS mechanism transitions into a suppressed regime at about $\delta B/B = 10^{-3}$. At the highest values of $\delta B/B$ the scaling power increases sharply. The DBS and CP-DBS scaling power seem to have a rough inverse relationship, and the sharp increase of the CP-DBS scaling power at very high $\delta B/B$ may suggest that there is some degeneracy between the X-mode

and O-mode polarisations whereby energy is transferred between them.

The behaviour of the scattering mechanisms at very high perturbation strengths is interesting, but complicated and unpredictable. These non-linear regimes are actively avoided when conducting further DBS and CP-DBS simulations. This is achieved by keeping the density and magnetic perturbations strengths below the $\delta n/n = 10^{-2}$ and $\delta B/B = 10^{-3}$ thresholds observed in figure 30. The ratio of $(\delta B/B)/(\delta n/n) = 1/20$ is applicable to MAST CP-DBS experiments [73] and was kept constant in the scaling power parameter scan. It is conceivable that the transition point from the predictable linear regime ($n_i = 2$) to the unpredictable regimes ($n_i \neq 2$) may vary if the perturbation ratio $(\delta B/B)/(\delta n/n) \neq 1/20$. As such, this is kept constant in all presented simulations using electromagnetic plasma fluctuations.

Experimental DBS shot 30150 and CP-DBS shot 30422/23 [73] feature H-mode plasmas. These plasmas ‘grow’ over time, meaning that the temperature and number density gradients increase and pedestal knee shifts outward. This causes the plasma to move through stable peeling-ballooning space towards a region of instability. When the unstable region is reached a type III ELM can occur. Ejecting heat and density from the plasma, this dramatic event lowers the temperature and number density magnitudes and gradients in the pedestal, and shunts the plasma back into a stable region of the peeling-ballooning limit. As a result of this, the plasma profiles can significantly vary over the entire ELM cycle. In order to account for this variation, the ELM cycle was split temporally into thirds. Each third of the ELM cycle had density and temperature profiles associated with it, which were obtained by averaging over many cycles. A second hyperbolic tangent-like function was used to re-construct these profiles using a handful of experimentally obtained variables. Developed by Culham Centre for Fusion Energy, this function is

$$\frac{a_2 - a_4}{2} \left[\frac{(1 + a_3 x_2) e^{x_2} - e^{-x_2}}{e^{x_2} + e^{-x_2}} + 1.0 \right] + a_4, \quad (201)$$

ELM third	a_0	a_1	a_2	a_3	a_4
1/3	0.992830	0.00482286	3.99573	0.0142420	0.911161
2/3	0.990538	0.00606494	5.01674	0.0100596	0.845323
3/3	0.987711	0.00576811	5.00048	0.000948642	1.00656

Table 2: Parameters for use in equation (201), for reproducing the background number density profiles for each ELM cycle third, for the shot 30150.

where the variable x_2 is given by

$$x_2 = \frac{(a_0 - x)/2}{a_1}. \quad (202)$$

The variables x and a in expressions (201) and (202) are similar to that of the controlling variables in figure 5.6. The variable x is the value of the normalised minor radius at some spatial position. The five a variables are

- a_0 \longrightarrow The value of ψ at the mid-point of the pedestal.
- a_1 \longrightarrow The pedestal half-width.
- a_2 \longrightarrow Number density at the top of the pedestal, in units of $10^{19}m^3$.
- a_3 \longrightarrow The core plasma linear gradient.
- a_4 \longrightarrow The pedestal offset, in units of $10^{19}m^3$.

The values required to reproduce the number density profiles for each of the ELM cycle thirds, for the shots 30150, and 30422/30423 [73], are in tables 2 and 3, respectively. These tables are used in equation (201) in order to re-construct the density profiles. These are shown in figure 31 for the DBS shot 30150 (left) and the CP-DBS shot 30422/23 (right).

Taken around the fast X-mode cutoff, the number density length-scale changes as the pedestal recovers post-ELM. The length-scales for each third of the ELM cycle

ELM third	a_0	a_1	a_2	a_3	a_4
1/3	0.99356401	0.0055039399	3.0572400	0.0045404201	0.53272003
2/3	0.990640	0.00477613	3.42404	0.00362940	0.776848
3/3	0.989230	0.00523902	3.75963	0.000615675	0.731248

Table 3: Parameters for use in equation (201), for reproducing the background number density profiles for each ELM cycle third, for the shot 30422/30423.

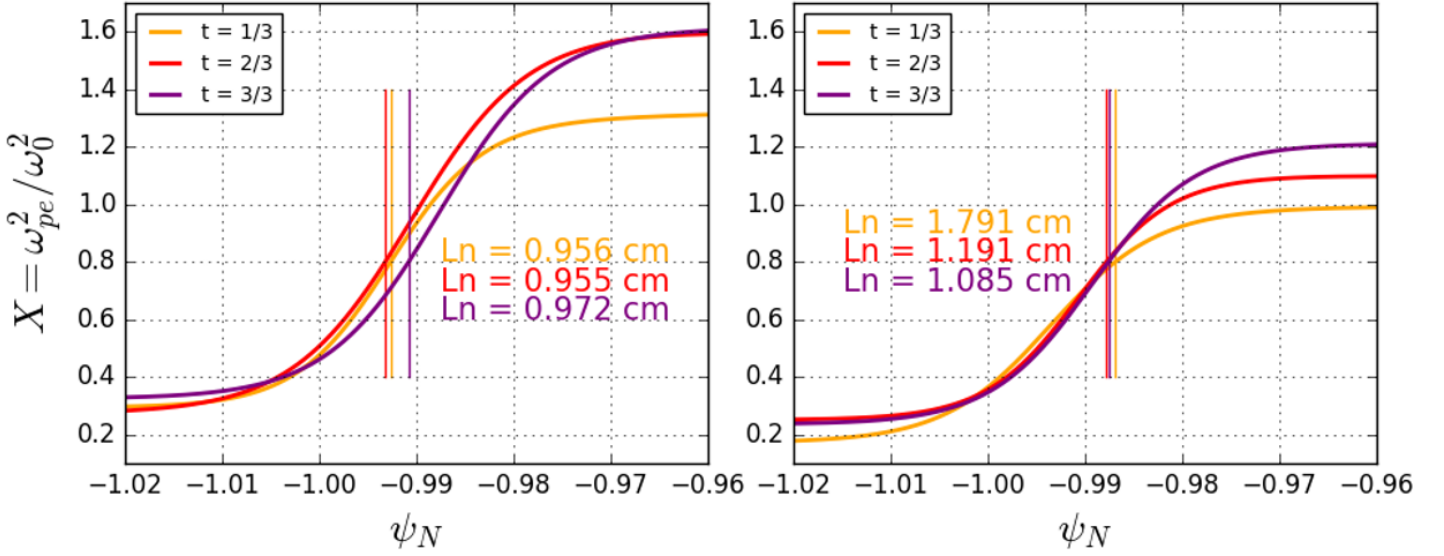


Figure 31: Re-constructed density profiles for the DBS and CP-DBS experiments conducted in shots 30150 (left), and 30422/23 (right), respectively. Vertical lines represent the position of the X-mode cutoff. Profiles have been re-created using equation (201) along with the variables detailed in tables 2 and 3.

can be seen printed in figure 31 for both shots 30150 (left) and 30222/23 (right). Shot 30150 used conventional DBS and maintains a consistent density length-scale of $L_n = 0.961\text{cm}$ on average, with a tight standard deviation of 1.0%. Shot 30222/23 used the CP-DBS diagnostic. Comparatively, the number density length-scale varies much more. The average value is $L_n = 1.36\text{cm}$ and the standard deviation is 28.1%. This discrepancy is the result of experimental parameters that are difficult to control, and has important consequences. It has been suspected that the scattering mechanism underpinning the CP-DBS diagnostic may be sensitive to non-WKB polarisation interaction induced by polarisation degeneracy [73]. The degree to which this may be apparent is indicated by the difference between the O-mode and X-mode wave-numbers at the point of scattering. It is thought that when the wave-number separation is small (eq. (189)) the injected beam may be able to freely exchange energy between the O-mode and X-mode polarisations. Considering that the CP-DBS diagnostic relies critically on the detection of very weak signals, this effect may be detrimental to the reliability of the diagnostic. The variation of the density length-scale over the inter-ELM period of shot 30422/23 may cause non-WKB effects to vary in significance over the same period. This could lead to variation in the CP-DBS signal which may be misinterpreted as variations in turbulent perturbation strength. As such, the significance of non-WKB effects must be better understood for the CP-DBS diagnostic technique to warrant credibility. Simulations addressing this are now discussed.

7.2 Simulation Setup

A 50GHz X-mode wave is launched perpendicular to the background magnetic field with $Y = 0.28$, at a poloidal angle of $\theta = 7.223^\circ$ which corresponds to wave-number matching for back-scattering according to expression (18) of $k_\perp = 2.63\text{cm}^{-1}$. The electromagnetic wave interacts with electrostatic and electromagnetic turbulence

in the plasma and scatters. An example of a typical simulation showing co-polar electric fields only is shown in figure 32 where the antenna is situated at $r = 45\text{cm}$. This is denoted the "main" simulation.

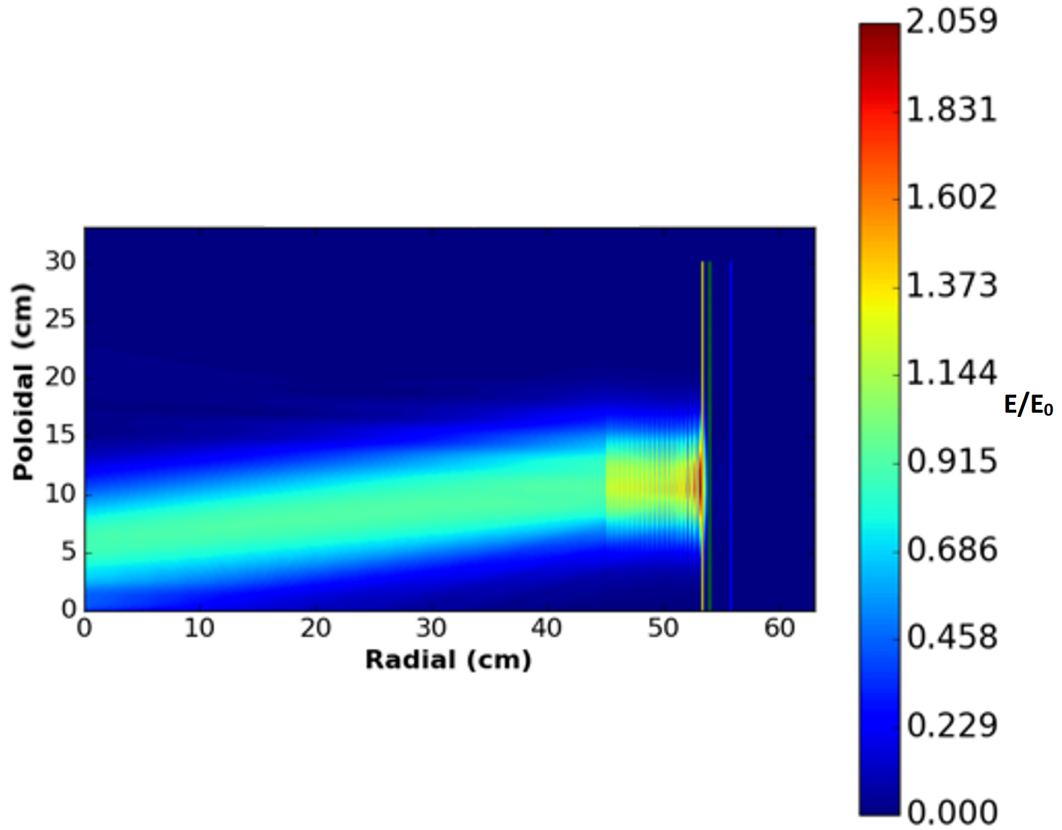


Figure 32: Co-polar electric fields as a result of a 50GHz X-mode beam launched perpendicular to the background magnetic field at an angle of $\theta = 7.223^\circ$ from a position of $r = 45\text{cm}$. The beam propagates into the plasma and interacts with electrostatic and electromagnetic turbulence. The resultant scattering cannot be seen since the incident beam is overpowering the weak scattering signals. For measurement, post-processing must be conducted to remove .

The scattered signals in figure 32 cannot be seen. This is in part due to the powerful beam launched from the left side of the antenna dominating over the weak scattering

beamlets. In order to measure the back-scattering, post-processing must be done in order to highlight the scattered signals. An analogous simulation is conducted to that of figure 32, except without any plasma; the wave simply propagates through vacuum. This is denoted the ‘reference’ simulation. The signals being emitted from the left side of the antenna in both the main and reference simulations never encounter plasma. As such, during post processing it is possible to ‘eliminate’ this signal by subtraction. Only the positions left of the antenna are altered in this way; the signal emitted from the right side of the antenna remains unmodified. This causes the antenna in the main simulation to appear as if there is only a signal being emitted from the right side. This can be seen from figure 33 (left).

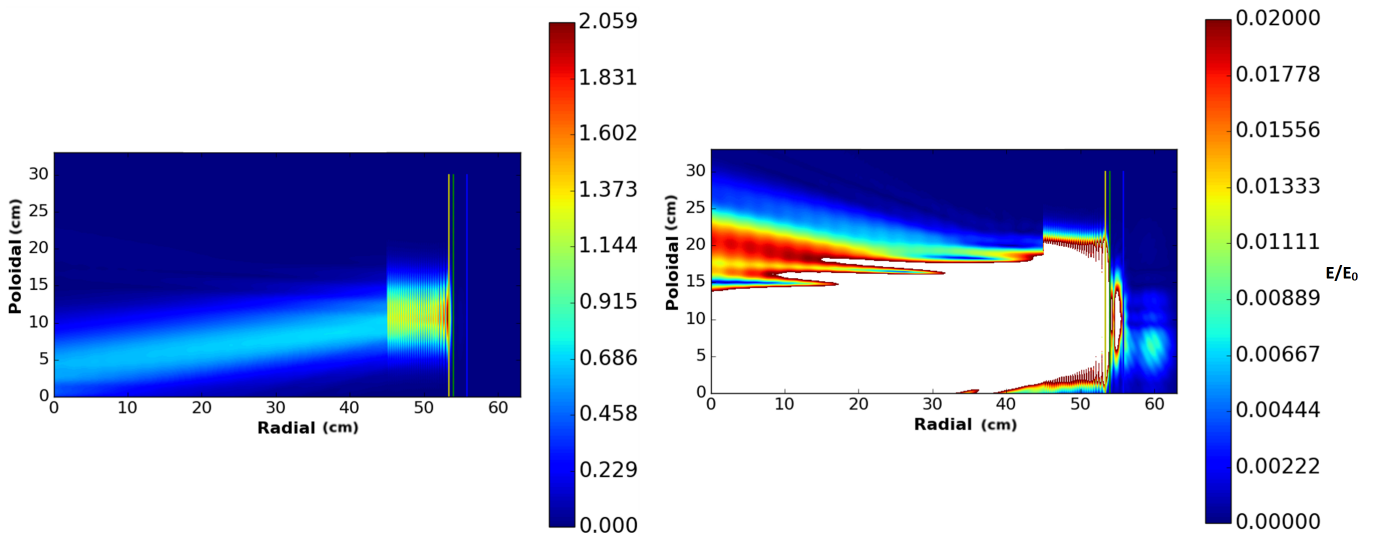


Figure 33: The same simulation as shown in figure 32. The signal being emitted from the left side of the antenna has been removed in post-processing by subtracting the same signal of the reference simulation. The color scale has also been drastically reduced to highlight the back-scattering (right). The white color here signifies that the electric field values are not represented by the vertical color scale.

It can be noted from figure 33 (left), that despite there being a region of apparently

no electric field signal on the left side of the antenna, the back-scattering still cannot be seen. This is because the colour-scale has been chosen to be appropriate for the strongest present signals; it is not fine enough to detect the weak back-scattering. In order to visualise these weak electric fields, the colour-scale range must be drastically reduced, which eliminates the ability to observe the features of the launched beam. This can be seen from figure 33 (right). Now detectable, the back-scattered signals can now be measured and parameter scans can be conducted in order to perform physical investigations into the cross-polarisation scattering mechanism.

EMIT-3D is a 3-dimensional code, and as such a robust measurement of the back-scattered signal can be taken by observing the toroidal-poloidal plane. Figure 34 shows these planes in the co-polar (left) and cross-polar (right) polarisations at a radial position of $r = 0\text{cm}$, where the electric field signals have been time-averaged to eliminate phase effects.

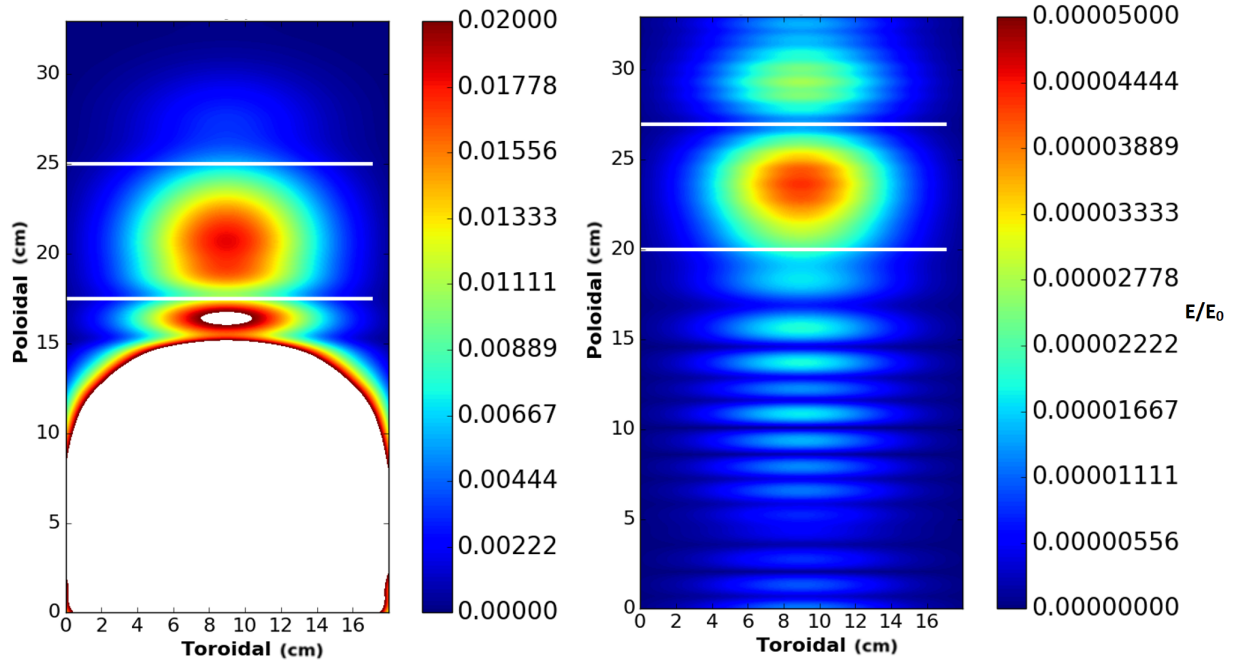


Figure 34: The same simulation as shown in figure 32. Toroidal-poloidal planes showing the time-averaged RMS signal of the co-polar (left) and cross-polar(right) polarisations. This 2D plane is taken at the radial position of $r = 0\text{cm}$.

A 2D integration is performed over the surface bound by the white horizontal lines, therefore fully evaluating the back-scattered signal.

7.3 Detecting Backscattering Over Noise

Of primary interest to the cross-polarisation Doppler back-scattering (CP-DBS) diagnostic, is whether the weak back-scattered signals can be detected over spurious noise. Many sources of noise are not representable in EMIT3D. For instance, there could be other electromagnetic instruments present in the tokamak. Signals emitted from other machines could reflect in some way and be detected and misinterpreted by

the CP-DBS system. Such issues must be considered by experimentalists, however, in this work we evaluate only noise generated by the wave-plasma interaction itself. Full-wave simulation in this section seek to compare back-scattering from simulations using solely electrostatic turbulence, and others containing both electrostatic and electromagnetic turbulence. This is in effect comparing the signals generated by the DBS and CP-DBS systems and will help to identify the significance of the magnetic perturbations towards cross-polar scattering. For the CP-DBS diagnostic system to be useful the cross-polar signals generated by the interaction between the wave and the magnetic fluctuations must be detectable over any similar signals originating from the density perturbations. A parameter scan was conducted twice. The turbulence perturbation strength was varied as $10^{-5} \leq \delta n/n \leq 10^{-1}$ while keeping $(\delta B/B)/(\delta n/n) = 1/20$ constant. The background plasma density was modelled with the tanh function described in section 7.1, with a length-scale of $L_n = 2.0\text{cm}$. In the first set of simulations the turbulence was electrostatic; there were no magnetic perturbations and the back-scattered cross-polar signals arise from the wave interacting with the density fluctuations. In the second set of simulations, the turbulence was both electrostatic and electromagnetic. The back-scattered electric fields were measured as described in section 7.2, and the original-polar signal was compared to the cross-polar signal. The results can be seen from figure 35.

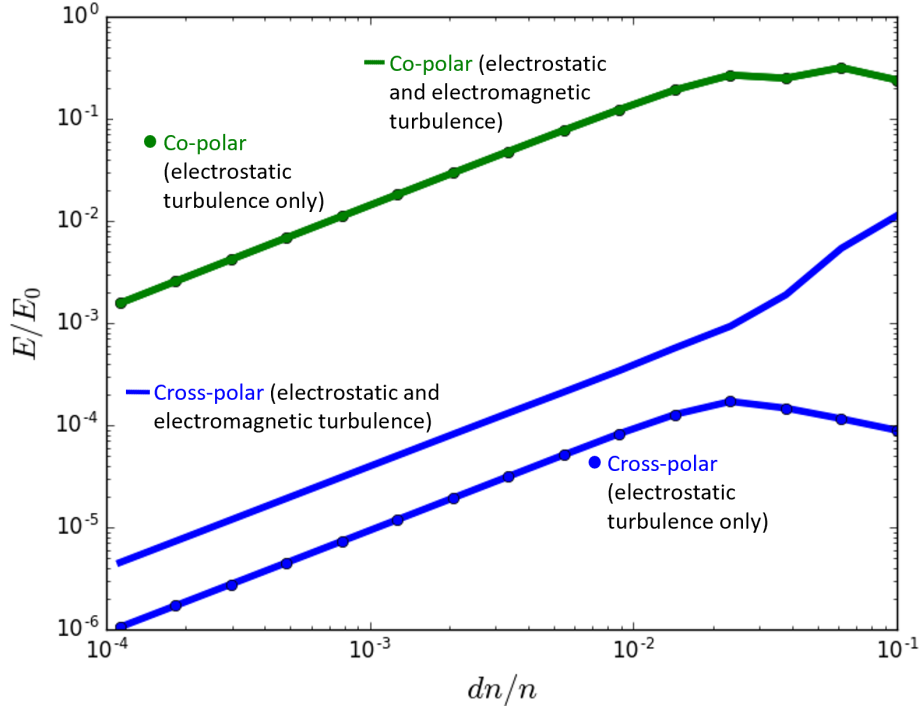


Figure 35: Scaling of the DBS (co-polar) and CP-DBS (cross-polar) signals with increasing density perturbation strength. The magnetic field perturbation strength is varied such that the ratio $(\delta B/B)/(\delta n/n) = 1/20$ is held constant.

The green line shows the measured back-scattering into the original polarisation. This is the signal that the DBS system would measure and represents back-scattering from density perturbations. The strength of this signal remained unchanged when moving from solely electrostatic turbulence to both electrostatic and electromagnetic. This is expected because the magnetic signals should have negligible influence on original-polar scattering. The cross-polarised back-scattered signals are shown in blue and these represent the signals that the CP-DBS system would measure. When purely electrostatic turbulence was used (solid blue line with no dots), no magnetic turbulence is present and cannot therefore cause any scattering. The cross-polar signals detected here are from the divergence of co-polar signals originating from the

density perturbations. With the inclusion of electromagnetic turbulence into the simulation the strength of the cross-polar signal rose by almost an order of magnitude. While this is expected, it is an excellent result; it shows that in this simplistic environment the cross-polar signals can be detected over any contributions from the density perturbations. However, it must be noted that the CP-DBS signals in simulations containing electromagnetic turbulence are weaker than expected. Figure 36 shows the ratio of E_{XO}/E_{XX} where E_{XO} and E_{XX} refer to the cross-polar and co-polar signals, respectively. These two variables are measured according to the 2D toroidal-poloidal integration technique described in section 7.2.

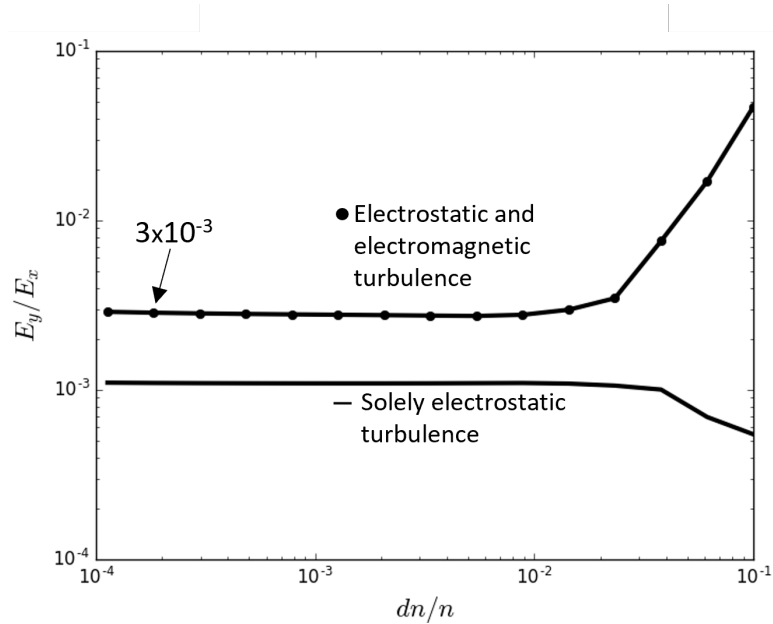


Figure 36: The ratio between the cross-polar and co-polar signals displayed in figure 35. The undotted line represents simulations with exclusively electrostatic turbulence. The simulations constituting the dotted line featured both electrostatic and electromagnetic turbulence. In all of these simulations the ratio of $(\delta B/B)/(\delta n/n) = 1/20$ is held constant.

The dotted line in figure 36 represents data taken from simulations which contained

both electrostatic and electromagnetic fluctuations. The linear regime approximately $10^{-4} < dn/n < 10^{-2}$ gives a ratio of approximately $E_{XO}/E_{XX} = 3 \times 10^{-3}$. Since the fluctuation strength ratio was held constant at $(\delta B/B)/(\delta n/n) = 1/20$, the back-scattered appears unduly weak. However, observing the ratio between equations (196) and (197) one can predict that

$$\frac{E_{XO}}{E_{XX}} = Y^2 \frac{\delta B/B}{\delta n/n}. \quad (203)$$

Since the value of the normalised cyclotron frequency in these simulation is $Y = 0.28$, the expected value of E_{XO}/E_{XX} can be calculated to be $E_{XO}/E_{XX} = 3.92 \times 10^{-3}$ which is reasonably close to the simulated value of $E_{XO}/E_{XX} = 3 \times 10^{-3}$.

7.4 Non-WKB Effects

In order to evaluate the significance of interactions between the characteristic frequencies (non-WKB effects) the inequality (113) is investigated. The numerator is determined by the choice of normalised cyclotron frequency while the denominator may be varied by altering the background density length-scale. The magnetic field is set to $Y = 0.28$ which a scan through density length-scale is conducted. The results are shown in figure 37.

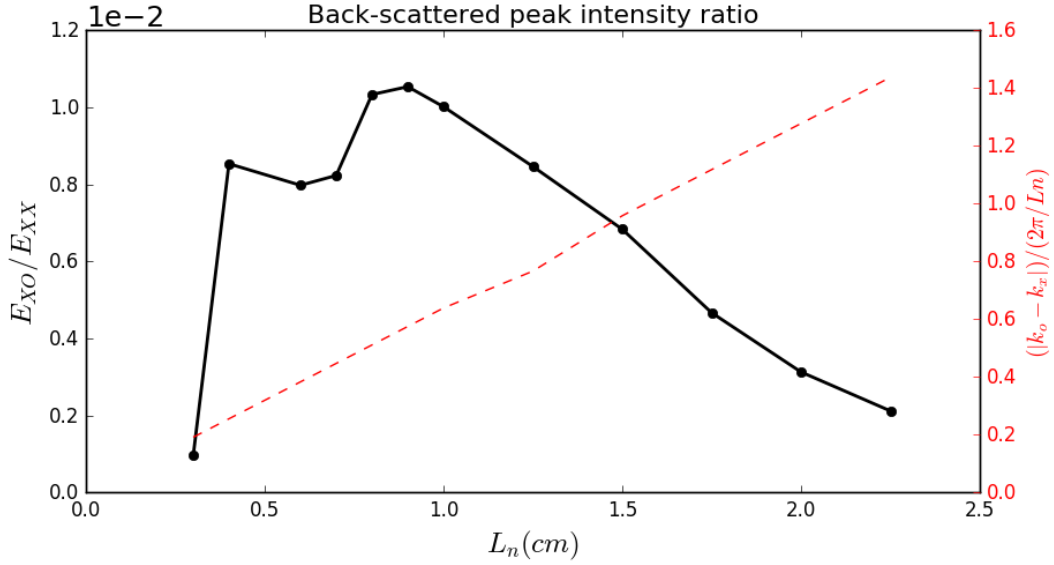


Figure 37: Parameter scan using Hermes fluid turbulence described in section 6.2.1. The background density length-scale was varied while all other simulation parameters are consistent with that of section 7.3. The left-side vertical axis measuring the backscattering signal ratio between the cross-polar (E_{XO}) and co-polar (E_{XX}) electric fields. The right-side vertical axis in red indicates the limit of the inequality (113) which represents the predicted significance of non-WKB effects.

It can be seen that the length-scale has a strong and non-monotonic effect on the length-scale. While it is possible that non-WKB effects are causing the strong variation there is not enough evidence to form this conclusion. There are factors originating from the Hermes produced turbulence which may be causing difficult to diagnose effects. Using monochromatic turbulence produced analytically the parameter scan was repeated and vastly extended. This can be seen from figure 38.

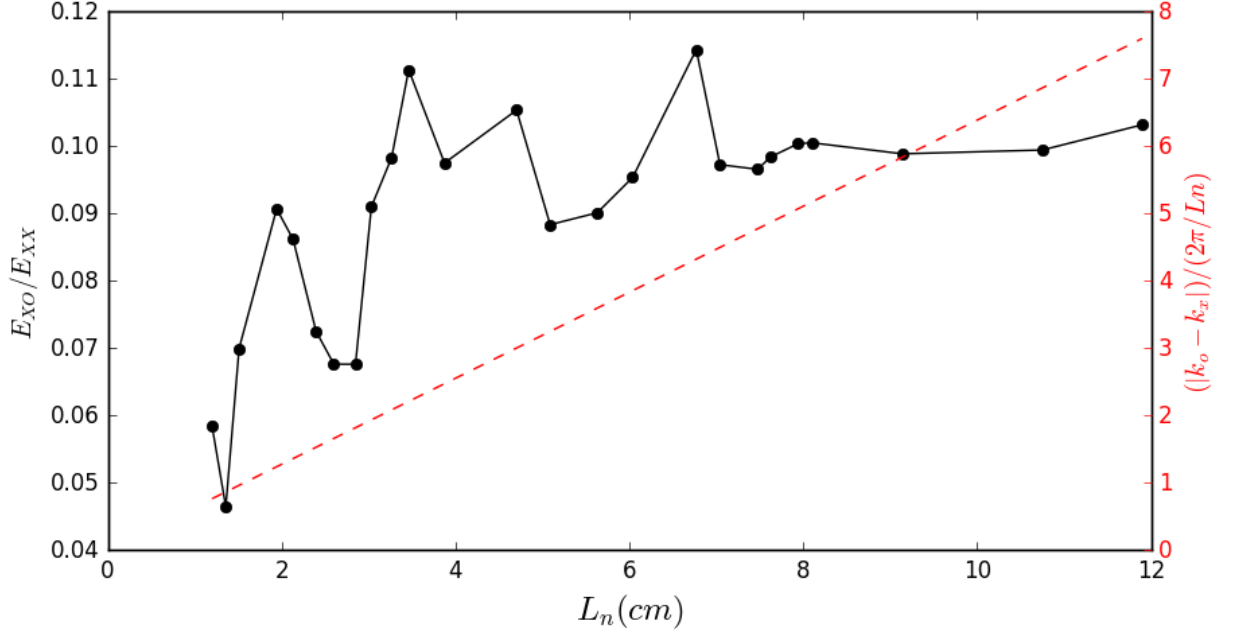


Figure 38: An analogous parameter sweep to that shown in figure 37, however, analytical turbulence described in section 6.2.2 was used instead of the Hermes fluid turbulence described in section 6.2.1. The range of the background density length-scale was also vastly extended. The ratio between the cross-polar and co-polar electric fields is displayed along with the limit of the inequality (113).

Similarly to figure 37, figure 38 shows a parameter scan through background density length-scale. However, the analytical turbulence described in section 6.2.2 was used instead of the Hermes fluid turbulence described in section 6.2.1. This analytically produced turbulence is a vast simplification on reality, however, the interpretation of the scattering mechanism may be easier as a result. The scattering efficiency has generally drastically improved with the transition from the Hermes fluid fluctuations to the monochromatic analytically produced turbulence. While this much higher measurement of E_{XO}/E_{XX} is no longer in agreement with equations (196) and (197), this is to be expected due to the overly simplistic nature of the

turbulence. As with the initial parameter scan of figure 37, figure 38 also shows a non-monotonic tendency, with a strong dependency of the scattering efficiencies with background density length-scale. The data also seems to be cyclical in nature, at least below length-scales of $L_n = 8.0\text{cm}$. Observing the 2D simulation planes in the cross-polarisation an interesting change in scattering mechanism was noted towards higher length-scales which is related to the position of the O-mode cutoff.

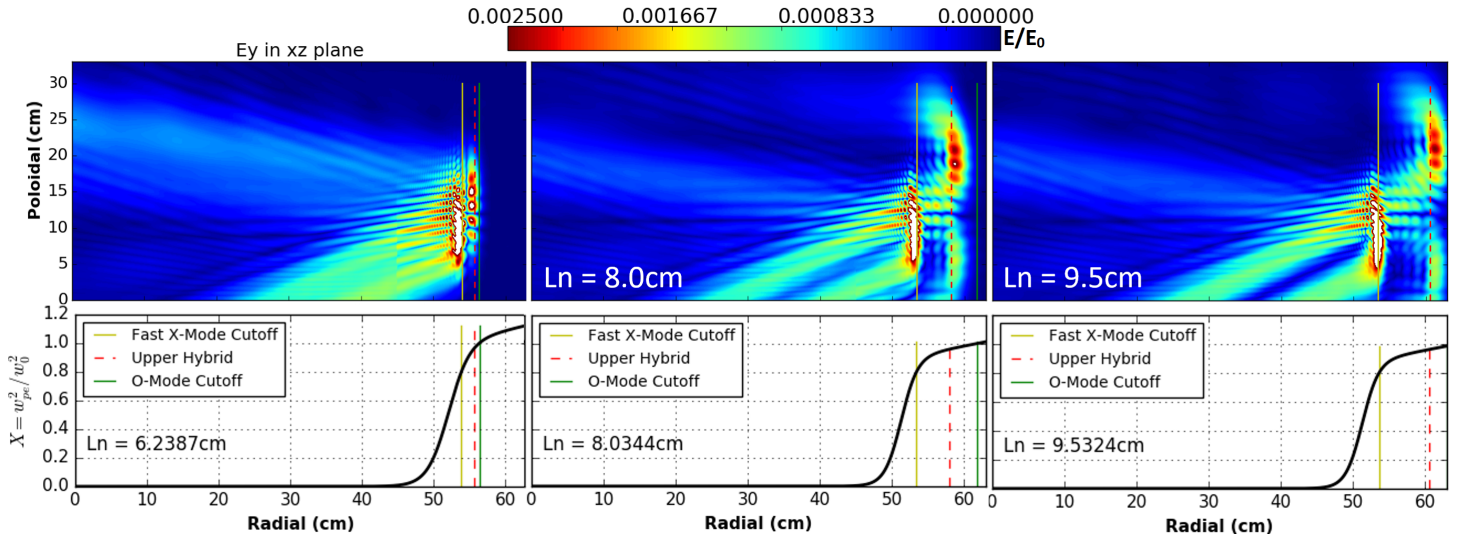


Figure 39: Three simulations showing the cross-polar electric fields. The analytically produced turbulence described in section 6.2.2 was used. The background density length-scale is varied in each case, and correspond to three data points in figure 38 which are $L_n = 6.2\text{cm}$ (left), $L_n = 8.0\text{cm}$ (middle), $L_n = 9.5\text{cm}$ (right). The vertical coloured lines indicate the position of the fast X-mode cutoff (yellow), the upper hybrid resonance (red) and the O-mode cutoff (green).

Figure 39 shows the cross-polar electric fields. The images are 2D radial-poloidal plane of the data points $L_n = 6.2\text{cm}$ (left), $L_n = 8.0\text{cm}$ (middle), $L_n = 9.5\text{cm}$ (right) taken from the parameter scan detailed in figure 38. The coloured lines indicate the fast X-mode cutoff (yellow), upper hybrid resonance (red), and O-mode cutoff

(green) and the visible electric fields are in the cross-polarisation. Observing the X-mode cutoff of the $L_n = 9.5\text{cm}$ (right) simulation it can be seen that not only are cross-polar signals being scattered back out of the plasma towards lower values of the radial axis, but they are also forward scattering. Since this is the cross-polarisation these electric fields are in the O-mode polarisation. The forward scattering can be seen to propagate into higher density plasma until interacting with the O-mode cutoff. At which point, the O-mode reflects from the cutoff surface. Depending on the position of the O-mode cutoff relative to the X-mode cutoff, this reflected signal can propagate back towards the antenna and interact with the back-scattered wave, as can be seen in figure 39(left) the $L_n = 6.2\text{cm}$ simulation. In order to evaluate the significance of this reflected cross-polar signal a series of simulations were setup with a flat core density profile. An example of which is displayed in figure 40.

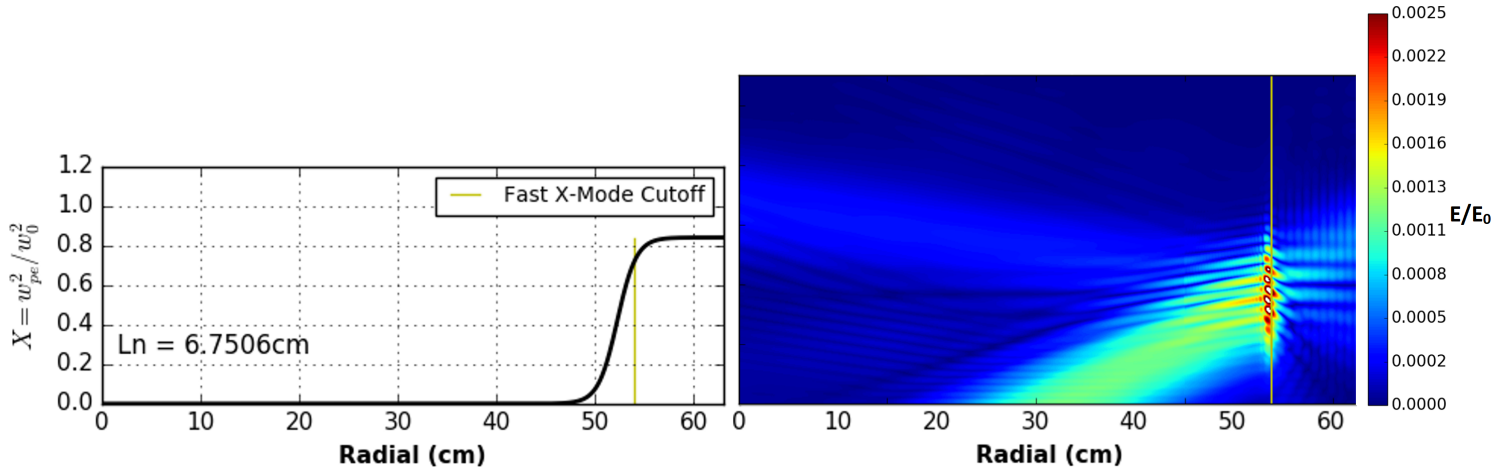


Figure 40: Density profile of an example "flat-top" simulation (left) where the core profile gradient has been reduced to zero. Cross-polar electric field signals (right) are shown as a result of an X-mode beam scattering off of the X-mode cutoff. The X-mode cutoff (yellow) is marked accordingly.

These flat-top simulations remove the O-mode cutoff from the simulation domain

and hence remove the interaction between the back-scattered and reflected O-mode waves. Another parameter sweep through background density length-scale is conducted and overlaid onto the data shown in figure 37 for comparison. This is displayed in figure 41.

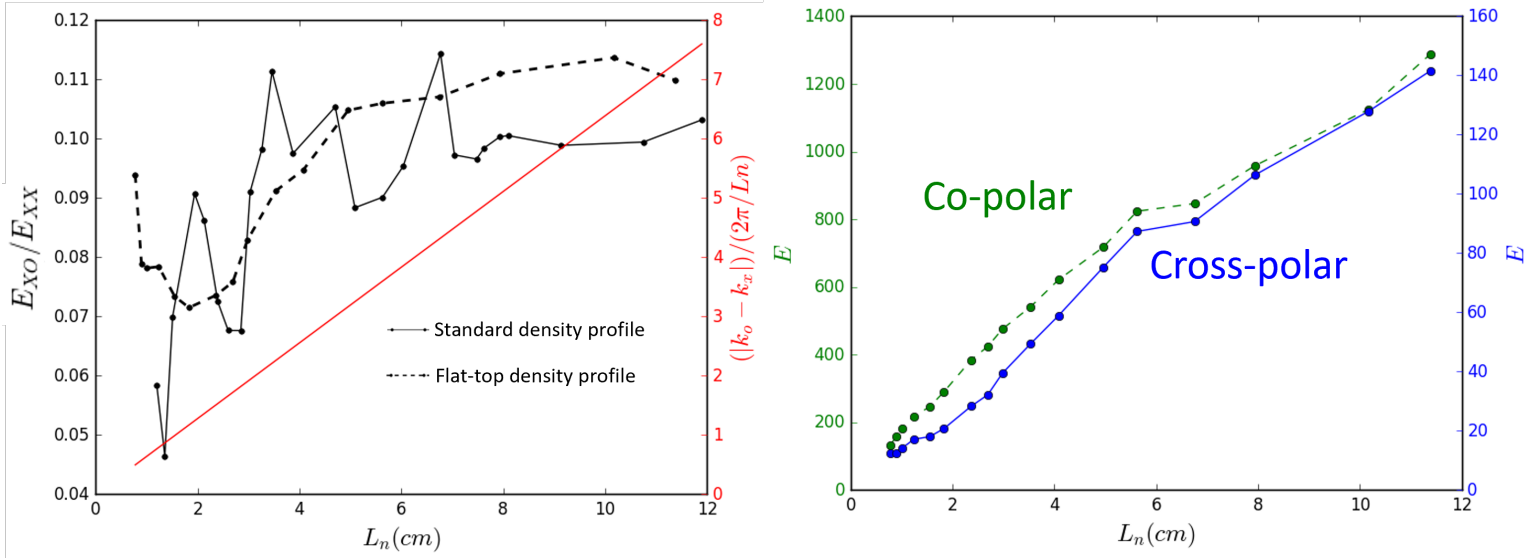


Figure 41: Length-scale parameter scan (left) showing the polarisation interaction equation (189) in red. Simulations that used standard (solid black line) and flat-top (dashed black line) background density profiles are shown comparatively. Co-polar (green) and cross-polar (blue) independent electric field measurements are also shown (right).

The simulations which used the standard background density profile detailed in figure 39 feature the cyclical nature previously described. However, the simulations that used a flat-top background density profile illustrated in figure 40 are near to monotonic. The implication is that the reflection of the forward scattered O-mode signal is causing the complex interaction resulting in cyclical behaviour which is likely due to some relationship between the beam's wavelength and the distance

between the O-mode and X-mode cutoffs. The result of this effects is that the back-scattering signal ratio varies significantly. The non-monotonic length-scale parameter scan conducted with the Hermes turbulence shown in figure 37 could be explained by this interaction, where only a half-cycle is being observed due to the modest range of L_n . Furthermore, Both the standard and flat-top profiled simulations suggest that the back-scattering efficiency has a strong relationship with the background density length-scale towards shorter length-scales which could make absolute experimental measurements challenging. The implications of this variation with length-scale, as well as the structure of the back-scattered signals is investigated in section 7.5.

It was expected that non-WKB effects could become significant when inequality (113) was satisfied. In order words when the red vertical axes of figure 41(left) has a value of much less than one. The trend of the flat-top data represented by the dashed line in the same figure is monotonic at length-scales above $L_n = 2.0cm$. This density gradient of $L_n = 2.0cm$ also correlates roughly to the value of $(|k_o - k_x|)/(2\pi/L_n) = 1.0$. At length-scales shorter than $L_n = 2.0cm$ the values of E_{XX}/E_{XO} change dramatically. This sudden change is likely explained by non-WKB effects becoming significant, where the O-mode and X-mode characteristic waves become degenerate at the scattering location. Considering figure 31, the MAST experimental shots back-scattered from the steepest regions of the pedestal where the density length-scales were around $L_n = 1.0cm$. It may be that these hypothesised non-WKB effects could be influencing the measurement. Additionally, three separate effects may be compounding; the non-WKB effects seen at $L_n < 2.0cm$, then general strong relationship between length-scale and scattering efficiency, and the complex interaction effect seen in the standard density profile simulations where the O-mode cutoff is reflecting the forward scattered cross-polar waves.

Evidently, more work in needed in this area. The simulations presented here

represent a parameter sweep through background density length-scale, but many other parameters remain constant. For instance the value of the normalised cyclotron frequency (i.e. the relative background magnetic field strength) and the turbulence fluctuation ratio $(\delta B/B)/(\delta n/n)$ may also have relationships with the above discussed mechanisms. In order to apply CP-DBS effectively in these short length-scale environments these potential relationships must be better understood and give motivation for further full-wave simulations.

7.5 Experimental Detection

Beyond the significance of the non-WKB effects and spurious cross-polar reflection described in section 7.4 there exist further experimental challenges relating to the structure and position of the back-scattered cross polar signal. Figure 42 shows the cross-polar electric fields in the poloidal-toroidal plane at a radial location of $r = 0\text{cm}$ for three different background density length-scales.

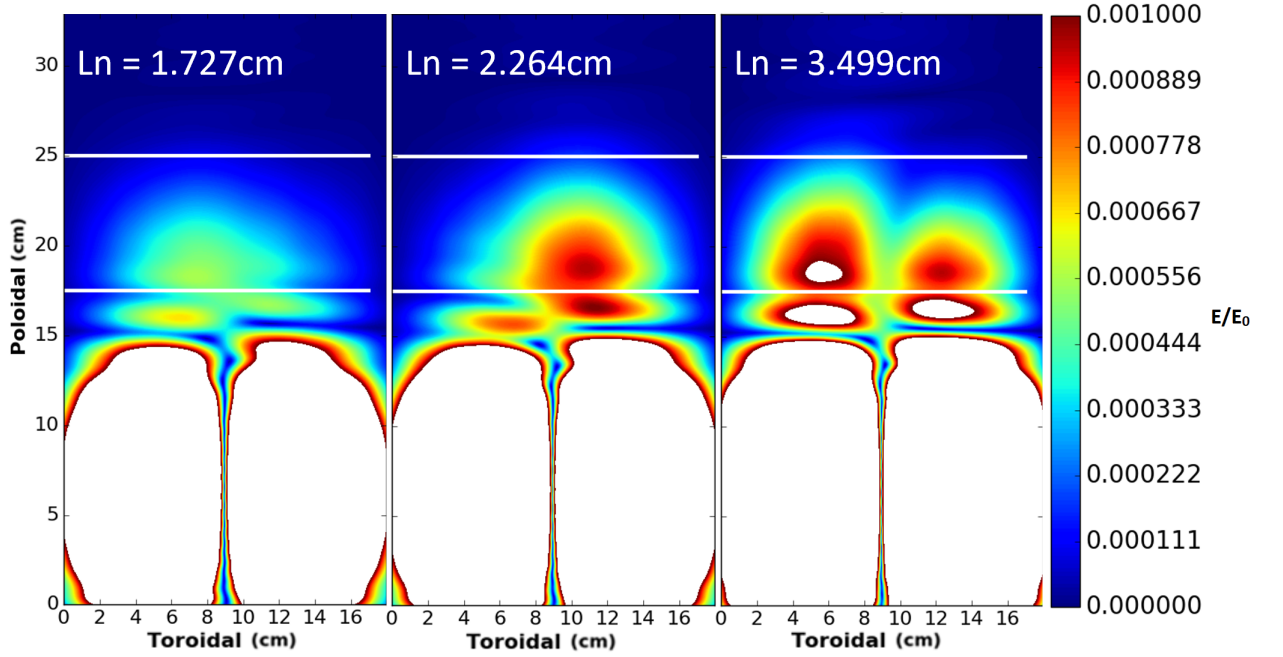


Figure 42: Cross-polar electric fields in the poloidal-toroidal plane at the radial location of $r = 0\text{cm}$. Three different simulations are shown with background density length-scale of $L_n = 1.727\text{cm}$ (left), $L_n = 2.264\text{cm}$ (middle), and $L_n = 3.499\text{cm}$ (right). All three simulations are using the same parameters described in section 7.2, with a standard background density profile featuring both the fast X-mode and O-mode cutoffs.

While the co-polar electric field back-scattering returns reliably along the beam path as is shown in figure 34, the cross-polar signal does not. As can be seen from figure 42 the structures varies apparently according to the value of the background density length-scale. While the detection method used in this theoretical work uses a 2D system by integrating between the white horizontal lines, the typical experiment cannot do that. CP-DBS systems do not use any sort of 2D detection method, and are usually in a monostatic antenna configuration. This leads to the detection of signals which propagate exactly back along the beam path, and would

correspond to a 1D line taken at the centre of the toroidal dimension. Since there is significant variation in the back-scattered structure of the cross-polar signal this may lead to misinterpretation of the back-scattered signal ratio, and therefore inaccurate measurements of the electromagnetic component of scattering fluctuations. It has been seen in simulations that the variation of the back-scattered cross-polar electric field structure is due to the complex interaction between the back-scattered, and reflected forward-scattered cross-polar signals. This occurs when both the fast X-mode and O-mode cutoffs are present in the pedestal and is described in detail in section 7.4. Using the flat-top background density profiles also described in section 7.4 and in figure 40, the structure of the back-scattering stabilises, and no longer varies with the value of the background density length-scale, as is shown in figure 43.

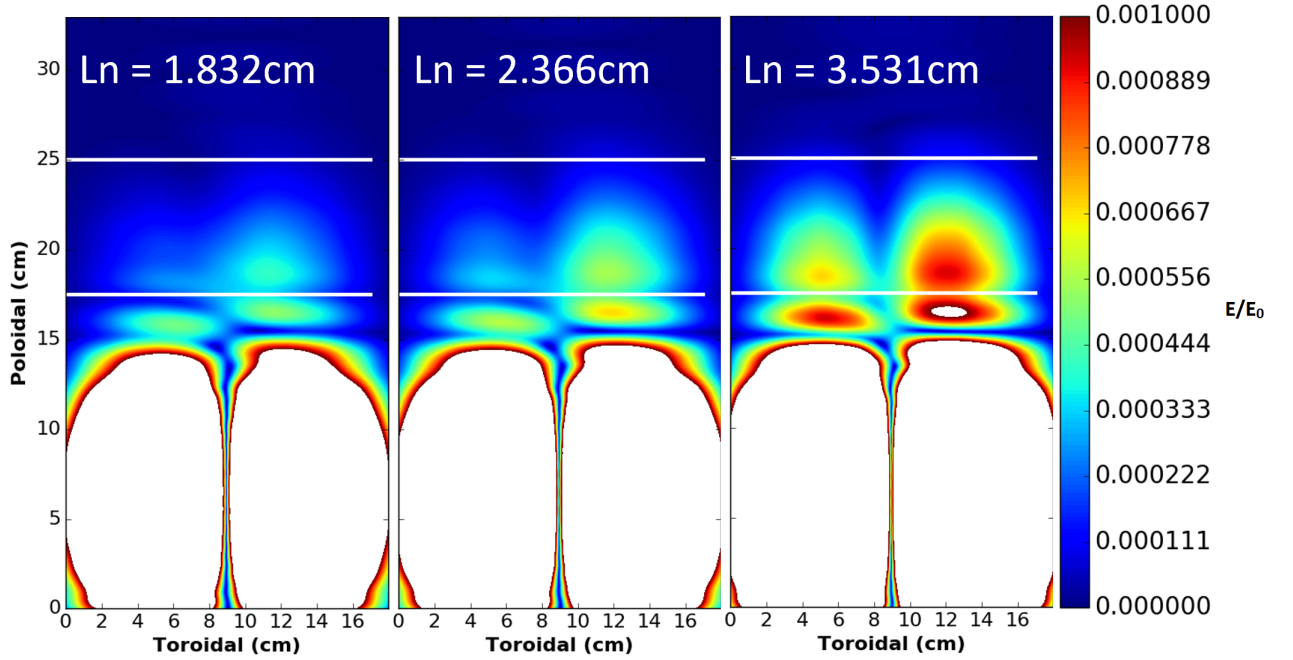


Figure 43: Cross-polar electric fields in the poloidal-toroidal plane at the radial location of $r = 0\text{cm}$. Three different simulations are shown with background density length-scale of $L_n = 1.832\text{cm}$ (left), $L_n = 2.366\text{cm}$ (middle), and $L_n = 3.531\text{cm}$ (right). All three simulations are using the same parameters described in section 7.2 but with a flat-top background density profile featuring exclusively the fast X-mode cutoff described in figure 40

The reasoning behind the strong asymmetry in the back-scattered cross-polar electric fields is unknown, and further study into this area would help in improving the CP-DBS monostatic antenna experimental technique as well helping to better interpret the measurements.

7.6 Summary of the DBS and CP-DBS modelling

The CP-DBS study has a dual focus; non-WKB effects as well as unforeseen possible difficulties in experimentally detecting the cross-polar back-scattering.

Simulations shown in figure 41 using a standard background density profile cannot be relied upon due to their cyclical nature driven by the interactions between cross-polar back-scattering and cross-polar reflections resulting from the fast X-mode and O-mode cutoffs, respectively. The flat-top simulations give a more reliable representation of the nature of the back-scattering mechanisms due to the removing of the cross-polar reflection from the O-mode cutoff. Most striking in the data is the strong dependency on background density length-scale above $L_n = 2.0cm$. According to equation (41) we would not expect non-WKB effects to be significant in the region, and this relationship may lead to absolute measurements of electrostatic and electromagnetic turbulent components to be challenging. However, relative measurements should be feasible due to the predictable nature of the data in figure 41 above length-scales of $L_n = 2.0cm$ and particularly towards the higher length-scales. According to inequality (113) we expect non-WKB effects to become significant below a value of one. Indeed in figure 41 we see a sudden and sharp change in the trend of E_{XX}/E_{XO} when the value of inequality (113) falls to one at approximately $L_n = 2.0cm$ and below. Since the variation is seen to be only in the tens of percent relative or even absolute experimental measurements could be possible so long as the background density length-scale can be measured accurately. However, measurements above $|k_o - k_x|/(2\pi/L_n) = 1.0$ would be far more simple to interpret. The feasibility of using CP-DBS in the complex environment of $|k_o - k_x|/(2\pi/L_n) < 1.0$ would rely on a wide range of further full-wave simulations exploring these relationships at parameters not investigated here. Of particular interest is the role of normalised cyclotron frequency (which was fixed here at $Y = 0.28$ and turbulence fluctuation ratio (fixed here at $(\delta B/B)/(\delta n/n) = 1/20$).

Experimental difficulties arising from unexpected asymmetries in the structure of the back-scattered cross-polar electric fields may be significant, particularly if a monostatic antenna configuration is used. Since the majority of the energy does

not come back along the beam path it may be that experiments underestimate the electromagnetic component driving the cross-polar back-scattering, causing the turbulence to appear more electrostatic than it really is. It is far too premature to adjust diagnostic design to account for this mechanism because the reason for the asymmetry is unknown. More comprehensive work is required using a variety of full-wave codes that use a range of different turbulent profiles to yield a deeper understanding of the physics.

8 Microwave Plasma Heating and Current Drive

The core of the sun is approximately 15 million degrees kelvin. This is sufficient to enable fusion to occur via the p-p chain, over tremendously long timescales. The Sun's large mass makes this possible; the overwhelming pressure enables sufficient fusion reaction rates in the core. On Earth, it isn't possible use comparable pressures to that of the sun. Additionally, depending on the p-p chain to instigate fusion would be unfeasible due to the long timescales. As discussed in section 1.3 fusion for energy must be achieved through classical mechanics. In order to do this the temperature inside a tokamak fusion reactor must be far greater than that of the sun. The core of the conventional tokamak ITER seeks to reach temperatures of 150 million degrees kelvin.

Plasma heating and current drive techniques are critical to the success of fusion, and in this section we explore the use of high-powered microwave beams to achieve this. In section 8.1 we investigate Electron Cyclotron Current Drive (ECCD) which directly couples microwaves to the cyclotron frequencies in order to drive toroidal current. Using a MAST-U equilibrium, ray-tracing calculations are performed. The viability of the ECCD technique is determined for use on spherical tokamaks (STs) where access to the fundamental harmonics can be difficult due to the plasma being strongly overdense. In section 8.2 Electron Bernstein Wave (EBW) heating is investigated. This technique utilises the O-X-B mode conversion process in order to bypass the electromagnetic wave cutoffs. EBW heating is thought promising for use on strongly overdense plasmas.

8.1 Electron Cyclotron Current Drive

The development of non-inductive heating and current drive methods is a critical issue for the viability of future fusion reactors. Pulsed devices rely on ramping a DC

current through a central solenoid in order to induce the majority of the toroidal current. Nonviable for steady-state devices, alternative current drive methods need to be developed. It is possible [140, 141] to drive significant amounts of current in a tokamak using high-power microwaves, and one such technique for doing so is Electron Cyclotron Current Drive (ECCD) where current is driven by directly coupling a launched microwave beam to the cyclotron resonances which naturally occur in a magnetised plasma. However, spherical tokamak (ST) plasmas can be strongly overdense to microwave frequencies which could couple to the lower cyclotron harmonics near the plasma core. This has driven research into using ECCD at higher harmonics such as the 2nd, 3rd, or even the 4th. It is expected that current drive at the higher harmonics would be far below what is required for fusion energy. This section aims to assess this concern by using the ray-tracing (sec. 4.1) code Torbeam [142], with a high beta MAST-U pressure and magnetic field equilibrium as an input in order to simulate the current drive. The density and magnetic field profiles of this equilibrium can be seen from figure 45, while the spatial dimensional information is shown in figure 46. In section 8.1.1 ECCD capabilities in the high beta MAST-U equilibrium will be assessed by launching a 70GHz O-mode beam which couples to the second and higher cyclotron harmonics. In section 8.1.2 a synthetic "low beta" scenario is investigated by reducing the number density of the MAST-U high beta equilibrium used in section 8.1.1 by a factor of 3.85. This enables access to the first cyclotron harmonic with a 35GHz O-mode beam and corresponds to a potential extreme low density MAST-U operating scenario. In section 8.1.3.1 another synthetic "low beta" plasma is analysed by increasing the magnetic field strength of the high beta MAST-U equilibrium by a factor of 2.0 giving an axial magnetic field strength of approximately 1.12T, while the number density is unchanged. In this high magnetic field case the first harmonic is accessed by launching a 70GHz O-mode beam from the outboard side. In section 8.1.3.2 another synthetic "low beta" plasma is

synthesised by increasing the magnetic fields of the MAST-U high beta equilibrium by a factor of 4.0. Here, a 70GHz O-mode beam couples to the fundamental cyclotron resonance. Finally, section 8.1.4 addresses the conclusions. In all ECCD simulations the beam is launched with 1.0 MW of power, has a beam waist radius of $\omega_0 = 2cm$, and a focal point chosen to give convergence at the absorption layer.

This work is intended to be pertinent to MAST-U and ultimately any current drive technique which utilises microwaves will require the physical installation of an antenna on the machine. The position of this antenna with respect to the plasma has an influence on the beam propagation path, and hence, the achievable driven plasma current. Figure 44 shows a schematic of MAST-U and gives an indication towards the availability of free space. The super-x divertor [143, 144] configuration shown in green causes the situation of an antenna with a high vertical position to be challenging. The most obvious positions for the placement would be either close to the equatorial plane, or between the P5 and P6 coils. Preliminary testing of ECCD with Torbeam has shown that it is easier to obtain a longer path length at the absorption surface with a more polar launch location. For this reason the simulations detailed here have all used launch positions which would correspond to situating the antenna between the P5 and P6 coils.

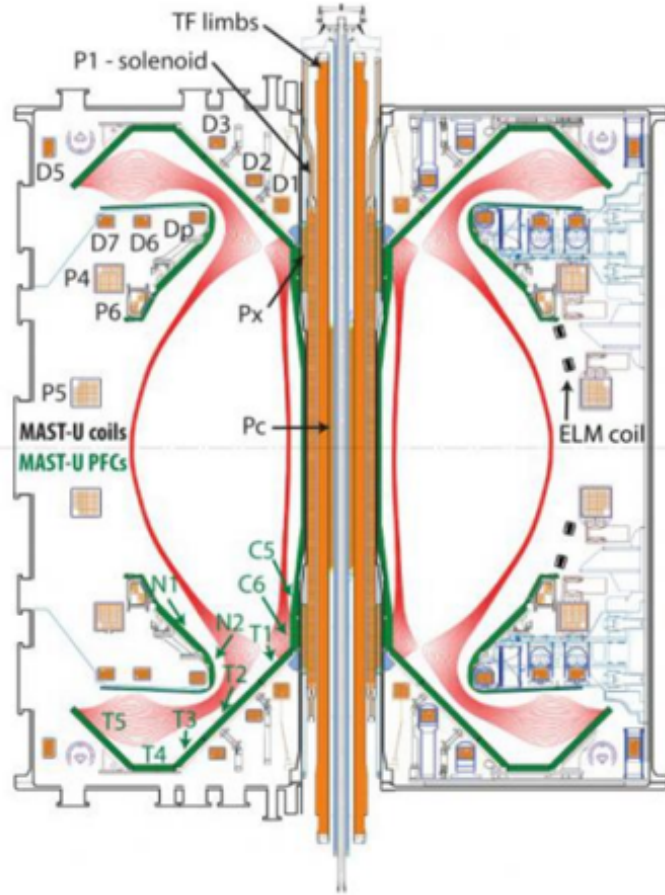


Figure 44: A schematic of the MAST-U tokamak. The simulated ECCD antenna position is situated between the P5 and P6 coils primarily because of the availability of free space. An equatorial launch was not chosen due to longer beam propagation path lengths at the absorption surface being easier to achieve with more polar launch angles. Image from the MAST-U Users Website.

ECCD is a technique that exploits the cyclotron frequency to directly drive current within a plasma. The absorption of these electromagnetic waves is achieved via satisfaction of the resonance condition

$$\omega_i - k_{\parallel} v_{\parallel} - l\omega_{ce}/\gamma = 0 \quad (204)$$

where ω_i is the incident wave frequency, k_{\parallel} is the incident wave parallel wavenumber, v_{\parallel} is the parallel electron velocity, l is an integer denoting harmonic number, ω_{ce} is the cyclotron frequency, and γ is the relativistic factor defined as

$$\frac{1}{\sqrt{1 - v^2/c^2}}. \quad (205)$$

When equation (204) is satisfied, coupling exists between the plasma electrons and the wave, allowing energy to pass from one to the other. An overall parallel current can be driven in the plasma due to three mechanisms. Coupling between the wave and the plasma must exist via the satisfaction of equation (204). However, due to the nature of the cyclotron frequency the electrons driven by this mechanism are accelerated in the perpendicular direction. The collisional frequency has an inverse relationship to particle energy, so when the electrons are accelerated there exists a "hole" in the distribution function. The restoration via collisions of the distribution function occurs faster than the accelerated electrons become isotropic, resulting in a small net current. Finally, due to the mass difference between the electrons and ions, the required ion velocity for momentum conservation is small and causes a negligible amount of cancellation current.

8.1.1 ECCD in a high beta MAST-U equilibrium

Since the plasma is strongly overdense, ECCD coupling near the core of high beta MAST-U plasmas will only be possible at higher cyclotron harmonics. In this section we launch a 70GHz O-mode beam with $P_0 = 1.0MW$ and a beam waist of $\omega_0 = 2.0cm$ which couples to the second and higher cyclotron harmonics. Figure 45 shows how the number density, temperature, and magnetic field components vary as a function of radial distance plasma in the equatorial plane. Figure 46 shows the launch configuration. Images 46A and 46C show the antenna position and the beam propagation path. Image 46B shows the radial positions where the beam interacts

with the cyclotron harmonics as it propagates into the plasma. The red numbers on images 46A and 46B denote the cyclotron harmonics.

High beta case: MAST-U equilibrium

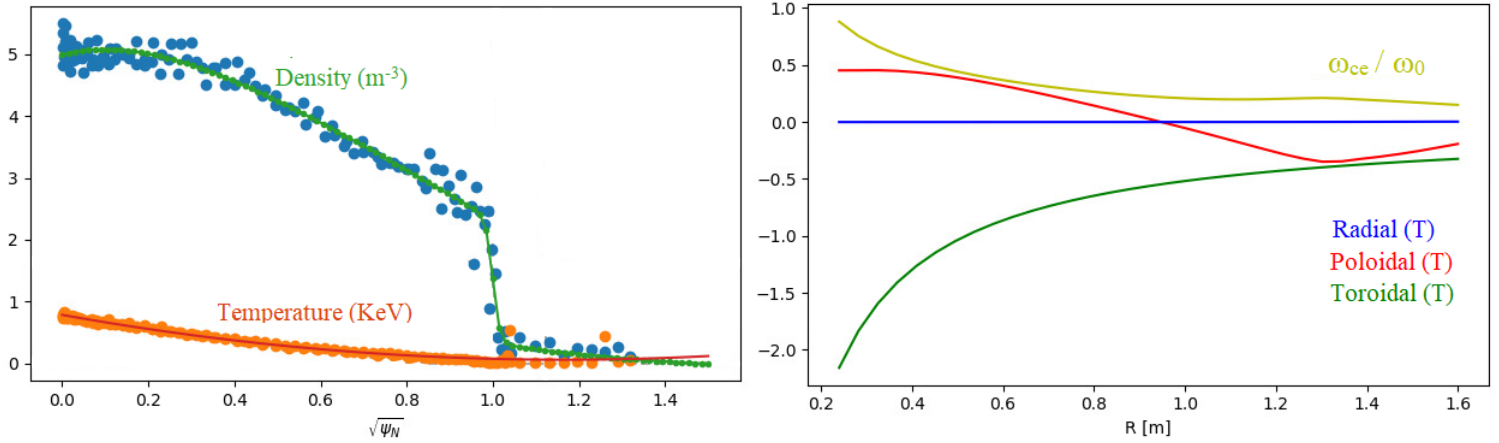


Figure 45: High beta MAST-U equilibrium: Number density and temperature (left panel) and magnetic field profiles (right panel) as a function of normalised minor, and major radius. The dots represent experimental data which the software uses to reconstruct the density and temperature profiles analytically.

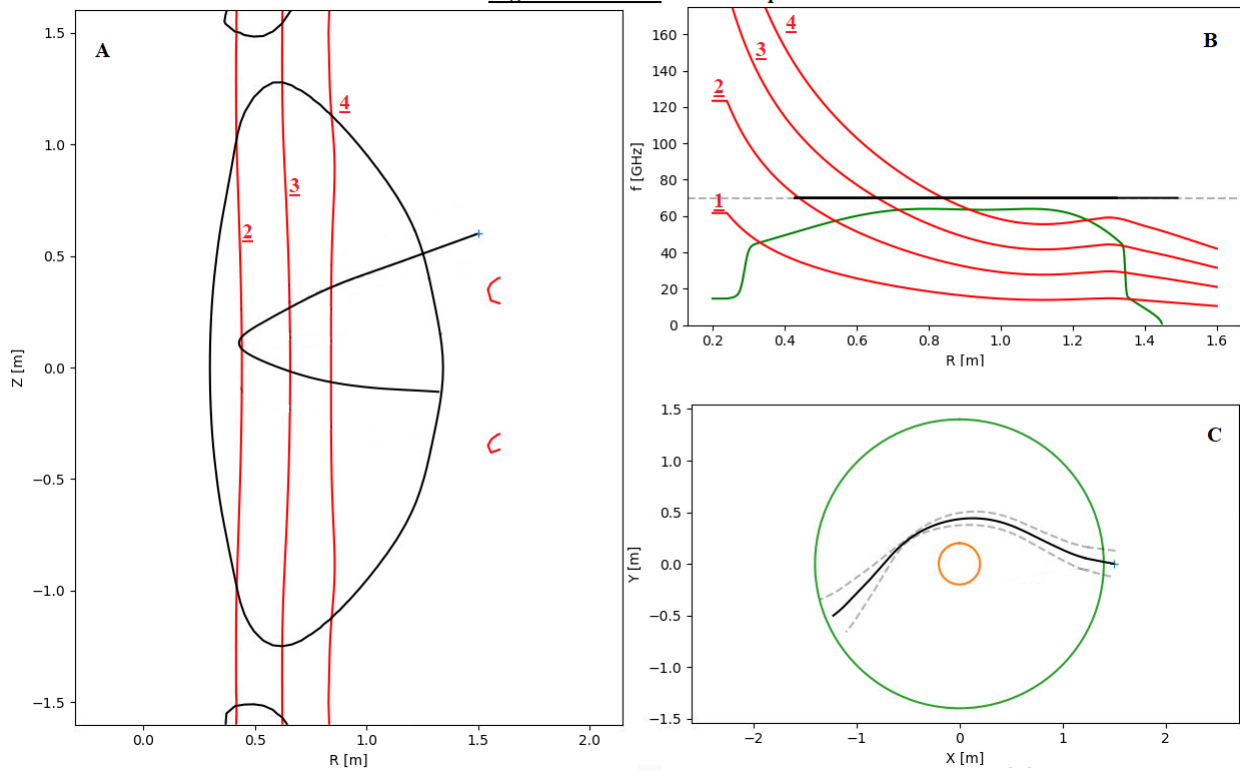


Figure 46: High beta MASTU-U equilibrium: A: Radial and vertical plasma cross section showing the beam propagation path. B: Frequencies of the cyclotron resonances and the critical surfaces as a function of radial ordinate. The black horizontal line indicates where the 70GHz O-mode beam will interact with the cyclotron harmonics. C: top-down cross-section of the tokamak and path of the launched beam. This individual simulation corresponds to toroidal and poloidal launch angles of 7.5° and 10.0° , respectively

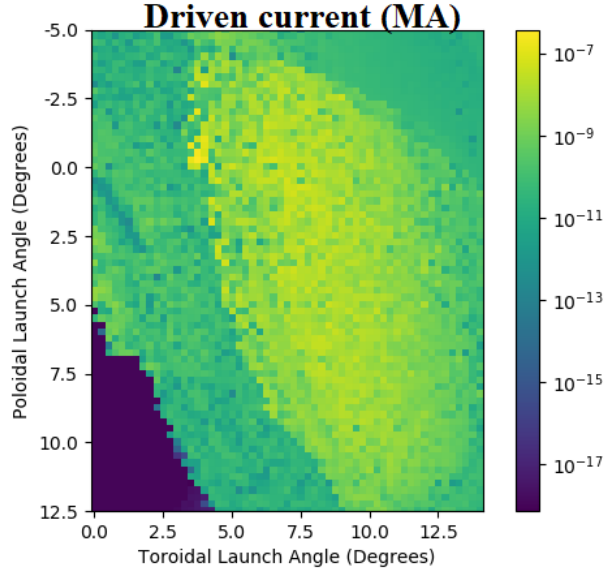


Figure 47: High beta MASTU-U equilibrium: A toroidal and poloidal launch angle parameter sweep detecting the greatest possible driven current efficiency from an 70GHz O-mode launched from between the P5 and P6 coils with $P_0 = 1.0MW$ coupling to the second and higher cyclotron harmonics.

In order to properly assess the capabilities of ECCD in this regime a 2D angular parameter scan was conducted. The antenna position was fixed and variations in the toroidal and poloidal launch angles were induced to find the maximum possible current drive. Figure 47 shows the results of this scan. The peak current drive achieved is poor at $4.0 \times 10^{-7} \text{ A W}^{-1}$.

8.1.2 ECCD in a low beta plasma with low number density

STs can be strongly overdense, and this causes difficulty in accessing the lower harmonics with ECCD. Lowering the plasma density would mitigate this problem; a sufficiently sparse plasma density can result in low frequency waves having direct access to the fundamental cyclotron harmonic. In this section the high beta MAST-U equilibrium is modified by artificially reducing the number density by a factor

of 3.85 to a maximum of $1.25 \times 10^{19} \text{ m}^3$. This is understood to correspond to an extremely low density, but possible, MAST-U operating scenario. A 35GHz O-mode beam is launched with $P_0 = 1.0 \text{ MW}$ and a beam waist of $\omega_0 = 2.0 \text{ cm}$ into the low density plasma and couples to the first and higher cyclotron harmonics. Figure 48 shows the same equilibrium as in figure 45, but with the number density reduced by a factor of 3.85.

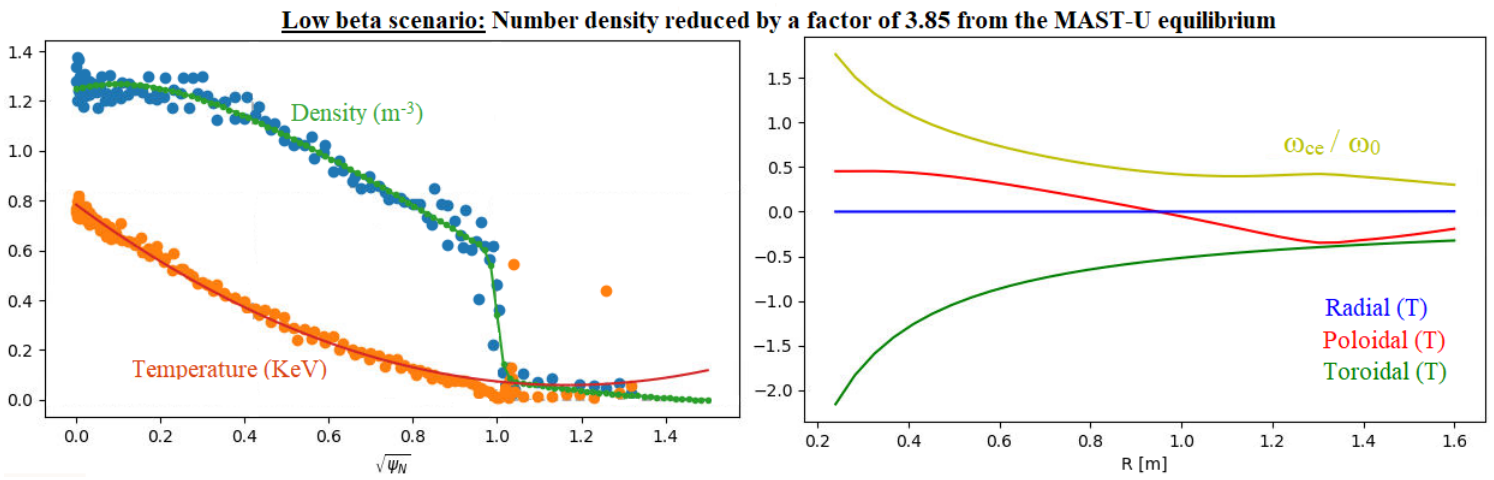


Figure 48: "low beta" scenario due to low n_e : The same MAST-U high beta equilibrium used in section 2 but with the number density profile (left panel) lowered by a factor of approximately 3.85. Compared to the original high beta case shown in figure 45 the temperature (left panel) and magnetic field profiles (right panel) are unchanged.

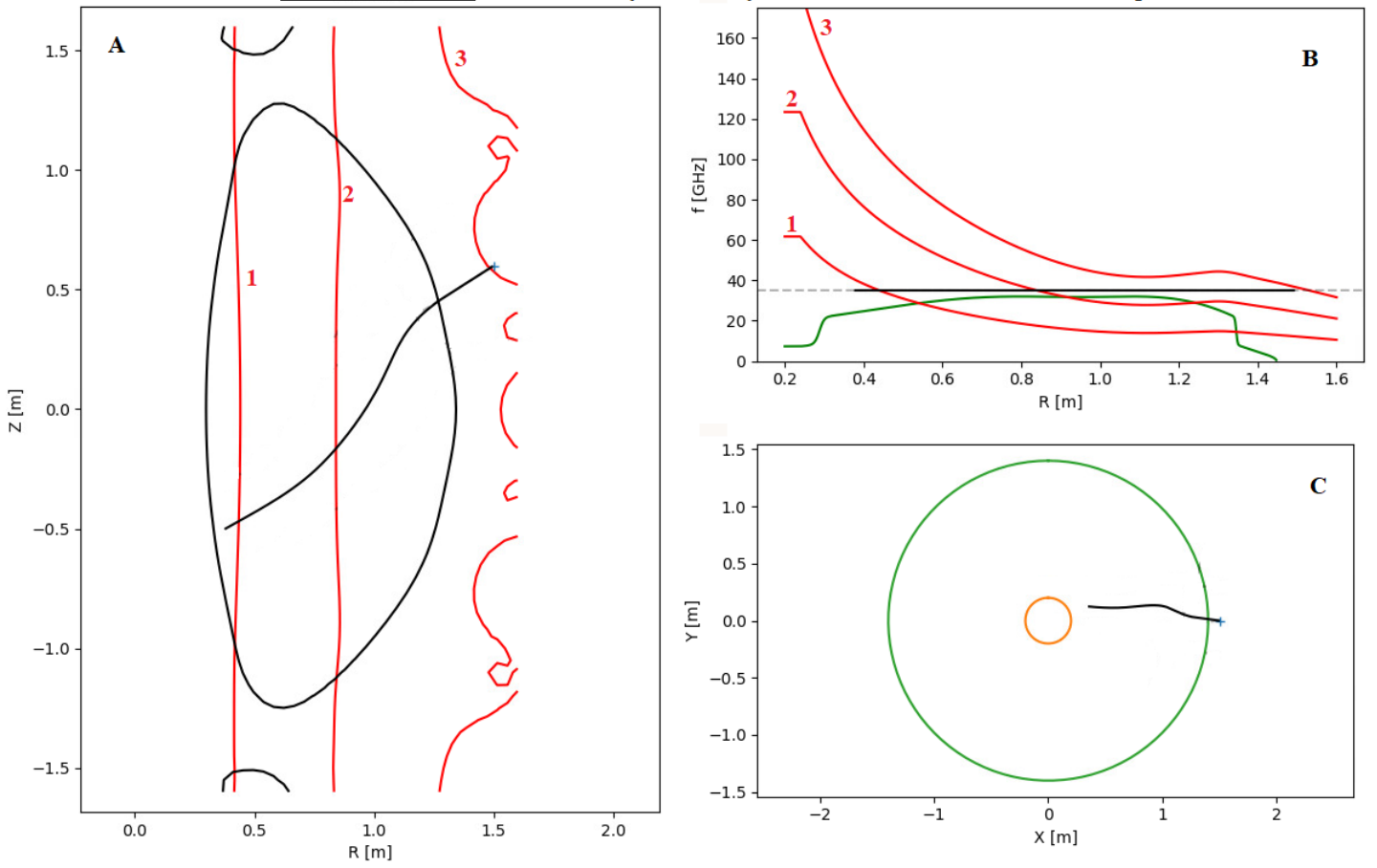


Figure 49: "low beta" scenario due to low n_e : A: Radial and vertical plasma cross section showing the beam path. B: Frequencies of the cyclotron resonances and critical surfaces as a function of radial coordinate. The black horizontal line indicates where the 35GHz O-mode beam will interact with the cyclotron harmonics. C: top-down cross-section of the tokamak and path of the launched beam. This individual simulation corresponds to a toroidal and poloidal launch angle of 6.25° and 32.5° , respectively.

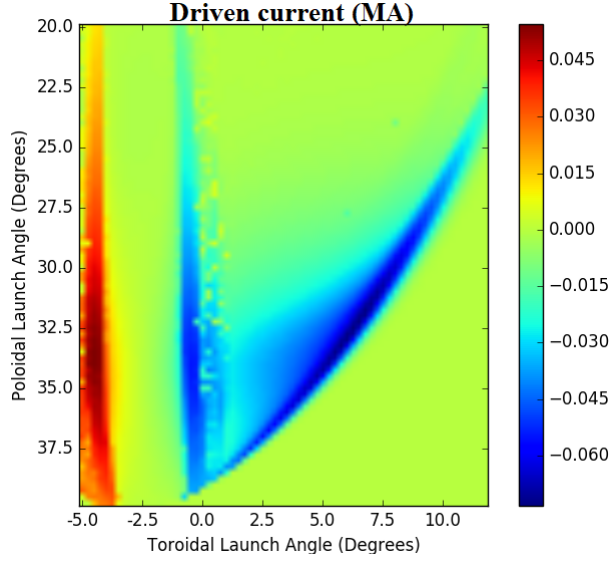


Figure 50: "low beta" scenario due to low n_e : A toroidal and poloidal launch angle parameter sweep detecting the greatest possible driven current efficiency from a 35GHz O-mode beam launched from a particular antenna position and coupling to the first and higher cyclotron harmonics.

Figure 49 shows the launch configuration. Images 49A and 49C show the antenna position and the beam propagation path. Image 49B shows the radial positions where the 35GHz O-mode beam interacts with the cyclotron harmonics as it propagates into the plasma. The red numbers on images 49A and 49B denote the cyclotron harmonics. An angular parameter sweep is again conducted to find the maximum achievable current drive efficiency by optimising the launch angle for this antenna position. Figure 50 shows such a scan. A clear area of strong currents can be seen towards higher toroidal launch angles. The current drive achieved here is good at 0.06 A W^{-1} .

8.1.3 ECCD in a low beta plasmas with strong magnetic fields

Using ECCD to access the lower harmonics in a high density plasma is possible

providing that the cyclotron frequency is sufficiently high. In this section the high beta MAST-U equilibrium shown in figure 45 is artificially modified by increasing the strength of each magnetic field component. MAST-U will be unable to produce magnetic fields of this amplitude. However, this experiment allows for the raising of the cyclotron harmonic frequencies sufficiently so that a 70GHz O-mode beam may couple to the lower cyclotron harmonics near the plasma core.

8.1.3.1 Increasing the magnetic fields by a factor 2.0

In this section the magnetic field components of the high beta MAST-U equilibrium shown in figure 45 are increasing by a factor of 2.0 giving an axial magnetic field strength of approximately 1.12T, resulting in a "low-beta" plasma. Figure 51 shows the modified plasma equilibrium with the increased magnetic field. The O-mode beam was launched with $P = 1.0 \text{ MW}$ and a beam waist of $\omega_0 = 2.0 \text{ cm}$.

Figure 52 shows the launch configuration. Images 52A and 52C show the antenna position and the beam propagation path. Image 52B shows the radial positions where the 70GHz O-mode beam interacts with the cyclotron harmonics as it propagates into the plasma. The red numbers on images 52A and 52B denote the cyclotron harmonics. An angular parameter sweep is conducted to find the maximum achievable current drive efficiency by optimising the launch angle for this antenna position. Figure 53 shows such a scan. The maximum current drive achieved here is $1.25 \times 10^{-4} \text{ A W}^{-1}$.

8.1.3.2 Increasing the magnetic fields by a factor 4.0

In order to attempt to couple the 70GHz O-mode beam more strongly to the fundamental harmonic a third "low beta" plasma is synthesised similar to that in section 8.1.3.1. Here, the MASTU-U high beta equilibrium detailed in section 8.1.1 is modified by increasing the magnetic field components by a factor of 4.0.

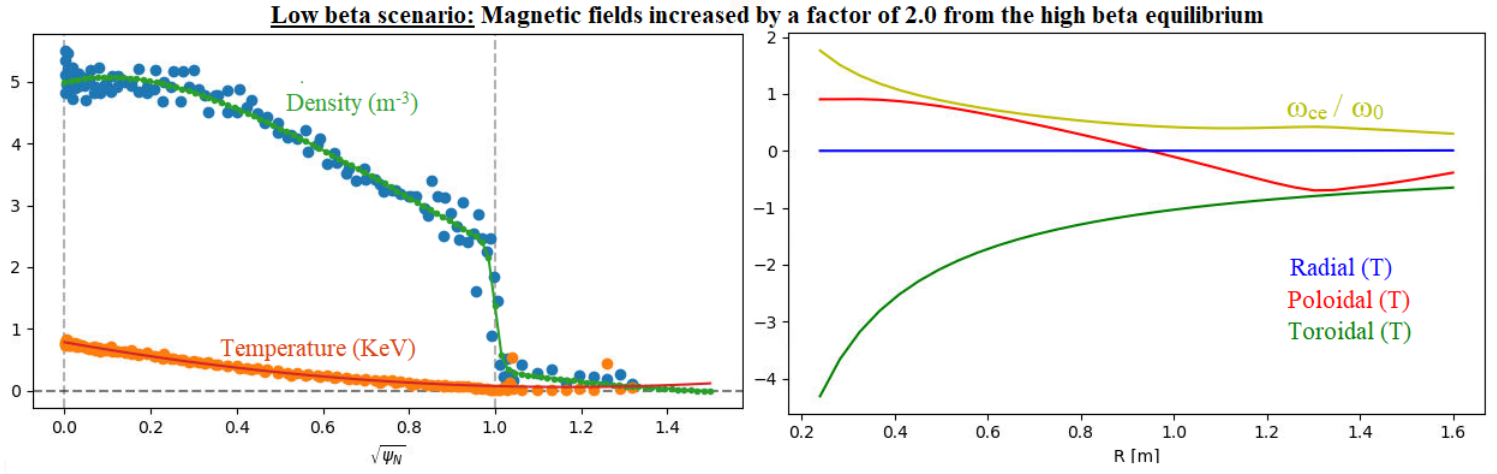


Figure 51: "low beta" scenario due to increasing the magnetic field by a factor of 2.0 from the MAST-U high beta equilibrium. The magnetic field (right panel) has been increased to give an axial magnetic field of $1.12T$. Compared to the original high beta equilibrium shown in figure 45 the temperature and number density (left panel) are unchanged.

Figure 55 shows the launch configuration. Images 55A and 55C show the antenna position and the beam propagation path. Image 55B shows the radial positions where the 70GHz O-mode beam interacts with the cyclotron harmonics as it propagates into the plasma. The red numbers on images 55A and 55B denote the cyclotron harmonics. An angular parameter sweep is once again conducted to find the maximum achievable current drive efficiency by optimising the launch angle for this antenna position. Figure 56 shows such a scan. The maximum current drive achieved here is $2.05 \times 10^{-3} \text{ A W}^{-1}$.

8.1.4 Summary of the ECCD modelling

The present Torbeam calculations detailed in section 8.1.1 have supported the expectation that ECCD in overdense ST plasmas would be an ineffective way of driving

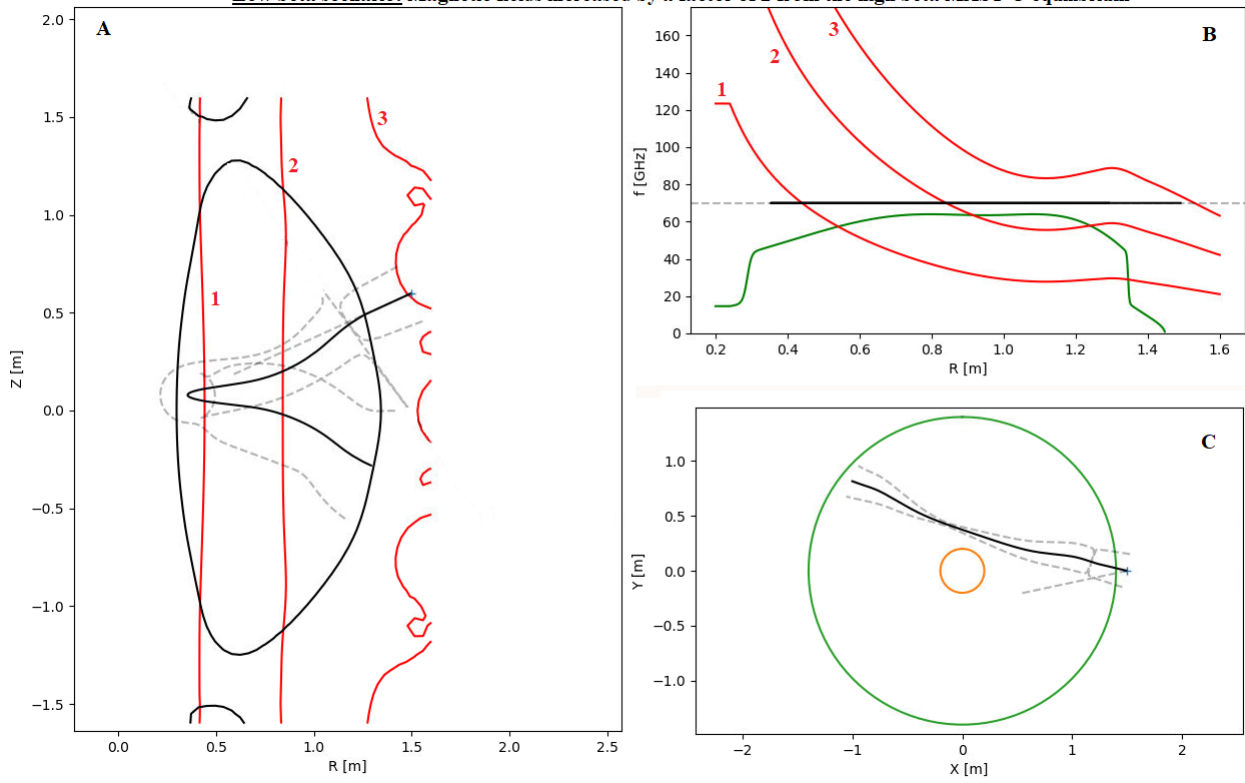


Figure 52: "low beta" scenario due to increasing the magnetic field by a factor of 2.0 from the MAST-U high beta equilibrium. A: Radial and vertical plasma cross section showing the beam path. B: Frequencies of the cyclotron resonances and critical surfaces as a function of radial ordinate. The black horizontal line indicates where the 70GHz O-mode beam will interact with the cyclotron harmonics. C: top-down cross-section of the tokamak and path of the launched beam. This individual simulation corresponds to a toroidal and poloidal launch angle of 12.0° and 24.5° , respectively.

plasma current. The maximum current drive efficiency achieved using the high beta MAST-U plasma equilibrium, with an 70GHz O-mode beam launched from an antenna situated between the P5 and P6 coils, coupling to the second and higher cyclotron harmonics, was a negligible $4.0 \times 10^{-7} \text{ A W}^{-1}$. Conversely, in section 8.1.2 a "low beta" plasma was synthesised. Believed to be a feasible extreme low density limit for MAST-U operation, the number density was reduced from the high beta equilibrium case to a maximum of $1.25 \times 10^{19} \text{ m}^{-3}$. Figure 50 shows that a 35GHz O-mode beam may couple to the first and higher cyclotron harmonics near the core and gave good current drive efficiency at 0.06 A W^{-1} . In section 8.1.3.1 we investigated

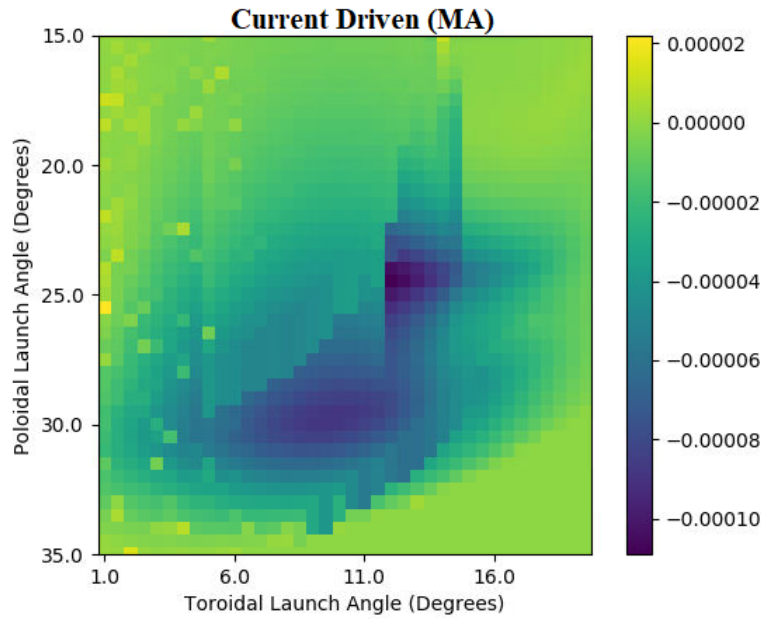


Figure 53: "low beta" scenario due to increasing the magnetic field by a factor of 2.0 from the MAST-U high beta equilibrium. A toroidal and poloidal launch angle parameter sweep detecting the greatest possible driven current efficiency from a 70GHz O-mode beam launched from a particular antenna position coupling to the first and higher cyclotron harmonics.

another "low beta" plasma by artificially increasing the magnetic field strengths of the MAST-U high beta equilibrium by a factor of 2.0 to give 1.12T on the magnetic axis. A 70GHz O-mode beam was coupled to the first and higher cyclotron harmonics, and gave a current drive efficiency of $1.25 \times 10^{-4} \text{ A W}^{-1}$. Finally in section 8.1.3.2 another "low beta" plasma is synthesised by again artificially increasing the magnetic field strength of the MAST-U high beta equilibrium. The field was increased by a factor of 4.0 giving 2.25T on the magnetic axis. A 70GHz O-mode couples more strongly to the fundamental harmonic compared to section 8.1.3.1 and gave a current drive of $2.05 \times 10^{-3} \text{ A W}^{-1}$. Considering the negligible current drive of $4.0 \times 10^{-7} \text{ A W}^{-1}$ achieved in section 8.1.1, it can be said that future steady-state

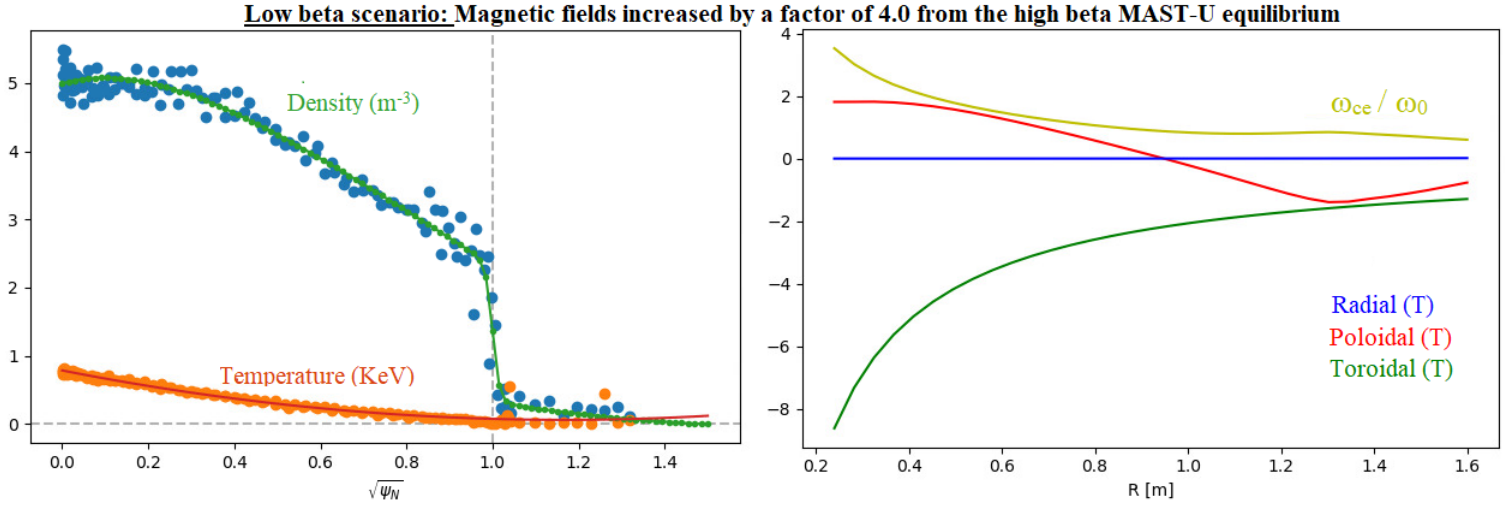


Figure 54: "low beta" scenario due to increasing the magnetic field by a factor of 4.0 from the MAST-U high beta equilibrium. The magnetic field (right panel) has been increased to give an axial magnetic field of $2.25T$. Compared to the original high beta equilibrium shown in figure 45 the temperature and number density (left panel) are unchanged.

fusion reactors using overdense, high beta plasmas may need to investigate sources of current drive outside of ECCD. However, if low density plasmas are a valid option then ECCD may remain a viable technique.

8.2 Electron Bernstein Wave Heating

The bulk of plasma heating is done by neutral beam injection (NBI), and electromagnetic waves in the microwave range. NBI involves accelerating charged particles to high velocities before they are neutralised, allowing for their transition across the strong magnetic fields of a tokamak plasma. This is one of the most prevalent ways of re-fueling a fusion plasma and often makes up a significant part of a fusion machines heating capabilities. On the conventional tokamak ITER the NBI capabilities will

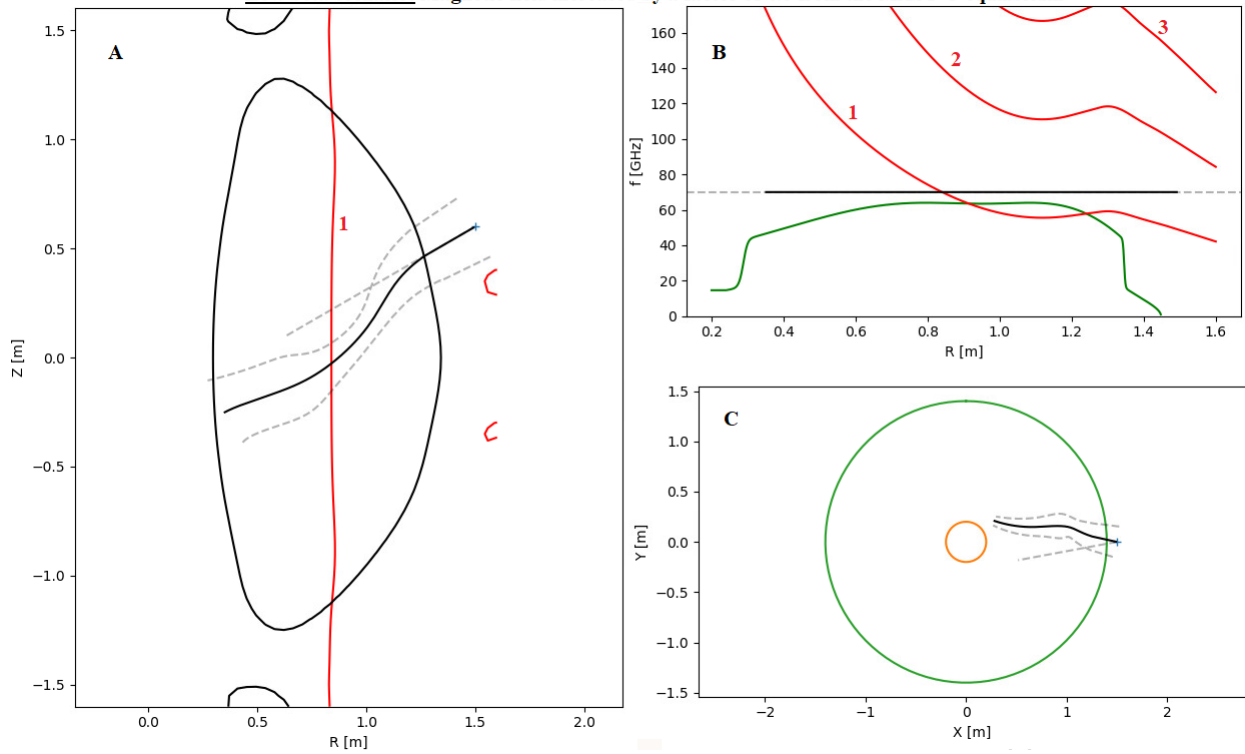


Figure 55: "low beta" scenario due to high magnetic field: A: Radial and vertical plasma cross section showing the beam path. B: Frequencies of the cyclotron resonances and critical surfaces as a function of radial ordinate. The black horizontal line indicates where the 70GHz O-mode beam will interact with the cyclotron harmonics. C: top-down cross-section of the tokamak and path of the launched beam. This individual simulation corresponds to a toroidal and poloidal launch angle of 12.0° and 29.50° , respectively.

be massive, with two systems each capable of operating at 16.7MeV which will make up 82.5% of the total external heating potential [145]. On spherical tokamaks using NBI can be more challenging due to the poloidal magnetic field having comparable strength to the toroidal magnetic field. This causes the gyro-motion of particles to strongly depart from the guiding centre orbit. NBI calculations are generally based upon guiding centre approximations [146] which exclude the classical effect of these gyro-motions. The implication being that calculations become more complex when dealing with spherical tokamaks. Although, NBI still forms a significant fraction of the total heating power on some STs.

Electromagnetic microwave frequency waves are widely used for diagnostics [147]

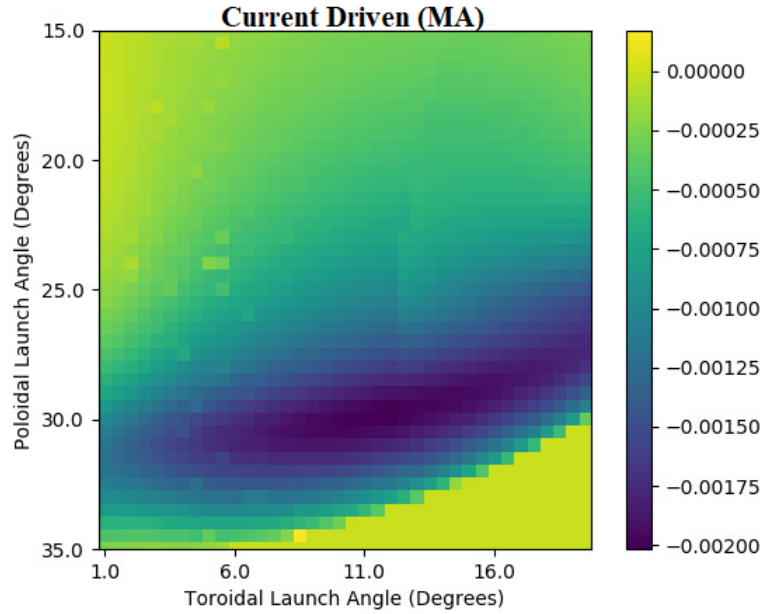


Figure 56: "low beta" scenario due to high magnetic field: A toroidal and poloidal launch angle parameter sweep detecting the greatest possible driven current efficiency from a 70GHz O-mode beam launched from a particular antenna position coupling to the fundamental cyclotron harmonic.

but are also used in conjunction with NBI to form the non-ohmic heating capabilities of tokamaks. Innovation in the development of high-power microwave technologies [148] is enabling microwave heating to form a significant contribution to the overall plasma heating. In conventional tokamaks, microwaves can be launched into the plasma and propagate into stronger magnetic field regions until their angular frequency ($\omega_0 = 2\pi f$) matches some resonance condition. The microwave can couple to the plasma and drive the gyro-motion of the particles, delivering energy. ST plasmas generally have higher values of plasma beta which can complicate this technique. If the microwave should propagate into a high enough number density before it reaches a satisfactory resonance frequency, the wave may interact with its cutoff, as detailed in section 3; it can be be unable to propagate further into the plasma. Such plasmas

are considered to be over-dense and the lower resonant frequencies often cannot be directly reached. One option to circumvent this limitation would be to double the angular frequency of the microwave and couple to the second resonance harmonic, should it reside in underdense plasma. As explored with ray-tracing calculations in section 8.1 this can be a satisfactory technique for driving current in ST plasmas and similarly, this implies it could also be used for heating. However, in highly overdense plasmas the second cyclotron harmonic can also be cut off. One could try to couple to the third or higher harmonics but, again, as demonstrated in section 8.1 the coupling efficiency between the microwave and the plasma becomes progressively weaker.

A second method for using microwave frequency waves to drive current and heat in fusion plasmas may be achieved by using Electron Bernstein Waves (EBWs). EBWs do not have a number density cutoff, they couple well to the cyclotron resonance harmonics [149], and are capable of effective current drive [150]. EBWs are electrostatic waves that are sustained by coherent gyrations of electrons and as such they cannot exist in a vacuum, and must be excited via coupling to externally launched electromagnetic waves. Ordinary-Slow Extraordinary-Bernstein (O-SX-B) mode conversion is one such technique for exciting EBWs. An O-mode wave is launched at an optimal angle to the background magnetic field such that it can mode convert to the SX wave. This conversion is highly localised to the O-mode cutoff, as in this region the O and SX solutions to the cold plasma dispersion relation (sec. 3.2) become degenerate and the two polarizations can pass energy from one state to another. The SX mode wave then turns around before reaching its high-density cut-off and ultimately propagates towards lower density plasma until it approaches the upper hybrid resonance where it becomes increasingly electrostatically polarized and is transformed into an EBW. In this section we investigate the O-SX stage of this conversion process. The O and SX polarisations can be derived from the cold

plasma dispersion (sec. 3.2) relation and are therefore representable in EMIT-3D using the cold plasma approximation. The EBW requires warm plasma effects and cannot be modelled with EMIT-3D. In other words, EMIT-3D (sec. 5) assumes that the plasma species are stationary, and since the EBW is sustained by the coherent gyration (motion) of electrons the representation of this wave is outside of the capabilities of the cold plasma model. The O and SX modes are electromagnetic waves and do not require any particle motion to exist.

Results contained in this section may be used to contribute towards major design decisions for heating schemes on the MAST-U spherical tokamak. In order to improve the reliability of the modelling, several different full-wave codes are used to perform a comparative analysis. These codes are both spatially 3D (EMIT-3D) and 2D (EMIT-2D, FFW, IPF-FDMC). An international collaborative effort by Dr. Bengt Eliasson (FFW [151]), Dr. Alf Köh (IPF-FDMC [152]), Mr. David Woodward (EMIT-3D [96]), and Ms. Lucy Holland (EMIT-2D) has made this possible. The simulation results are primarily from EMIT-3D simulations, with comparisons made with the other codes.

8.2.1 Elliptical Polarisation

In order to properly model the O-SX-B mode conversion process it is necessary to launch an elliptically polarised wave. This is due to the requirement to launch the wave at an angle to the background magnetic field for optimal mode conversion. Should a linearly polarisation be used, the wave would be a mix of O-mode and X-mode. A significant amount of the signal would therefore be rejected at the fast X-mode cutoff, before the wave reached the O-mode cutoff where the O-SX mode conversion can take place. Figure 57 shows the result of an EMIT-3D simulation which represents this effect. The launched beam has a linear polarisation but also propagates at an angle to the background magnetic field, which is parallel to the

toroidal dimension. The launch angle has been chosen for optimum mode conversion efficiency according to equation (95). In order to be a valid solution to Maxwell's equations, this linearly polarised wave must consist of a mixture of O-mode and X-mode polarisations. As such, reflection of the X-mode component of the wave can be seen at the X-mode cutoff.

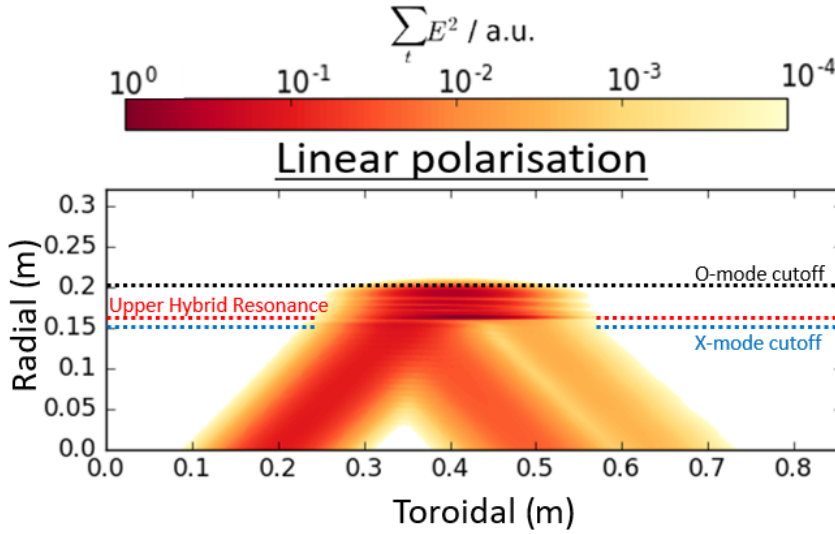


Figure 57: A 2D time-averaged image of an EMIT-3D simulation, taken at the centre of the 3D simulation domain. A linearly polarised O-mode is launched at the optimal angle for mode conversion according to equation (95). Partial reflection of the wave can be seen at the X-mode cutoff, demonstrating the undesirable mix of O-mode and X-mode polarisations.

In order to perform useful simulations the launched beam must represent one that is likely to be used in an experimental device. This would correspond to an elliptically polarised beam, as a pure O-mode polarisation could be theoretically achieved, avoiding the X-mode rejection seen in figure 57. This would increase the achievable mode conversion efficiency. EMIT-3D was updated to include the math-

emational theory developed in [118]; the description of the Gaussian beam remains as described in section 5.4, but the elliptical polarisation is achieved by using equations (161) and (162). An analogous simulation to that shown in figure 57 was ran, using an elliptically polarised beam instead of linearly polarised. The results are shown in figure 58. The total rejected beam now appears to be roughly symmetrical around the null point in the centre. The gap in the rejected beam is formed due to the beam centre matching of the mode conversion condition; the fringes of the beam diverge away from the optimal condition given by equation (95). The fact that each side of the null point are roughly symmetrical indicates that there is now no notable energy being rejected by the X-mode cutoff as was the case when the linearly polarised wave was used; the beam is no longer a significant mixture of O-mode and X-mode polarisations.

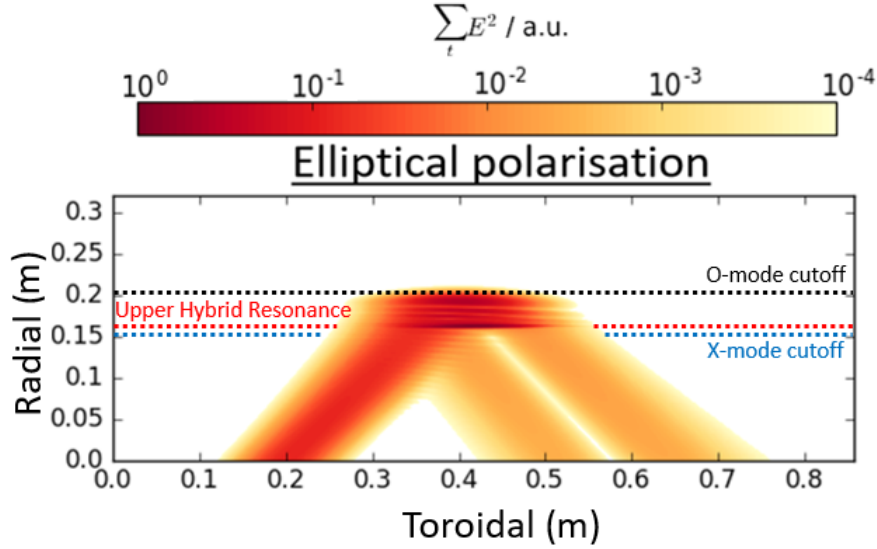


Figure 58: A 2D time-averaged image of an EMIT-3D simulation taken at the centre of the 3D simulation domain. The elliptically polarised O-mode is launched at the optimal angle for mode conversion according to equation 95. There is minimal reflection at the X-mode cutoff, indicating that the launched beam consists majorly of the O-mode polarisation.

8.2.2 Benchmarking of full-wave simulation codes

A benchmarking between the 3D code EMIT-3D and the 2D codes EMIT-2D, IPF-FDMC, and FFW is presented. There are two stages to the benchmarking process. First, in section 8.2.2.1 the beam divergence of that launched with EMIT-3D is compared to that of the 2D codes. The beams in the 3D and 2D codes, respectively, should diverge at different and predictable rates due to the dimensional differences. Second, in section 8.2.2.2 O-SX (O to Slow X) mode conversion is modelled with a simple linearly increasing background number-density gradient. A basic mathematical treatment is presented which seeks to predict the difference in efficiency as the simulations move from 2D to 3D. The numerical results and this analytical

prediction are compared to one another.

8.2.2.1 Beam divergence

In this section a trivial vacuum configuration is used in order to verify basic agreement of mathematically predictable beam divergence differences between the 3D and 2D codes. A 28GHz Gaussian beam is launched, with the focal point situated at the antenna plane. A time-averaged measurement of the simulation can be seen in figure 59.

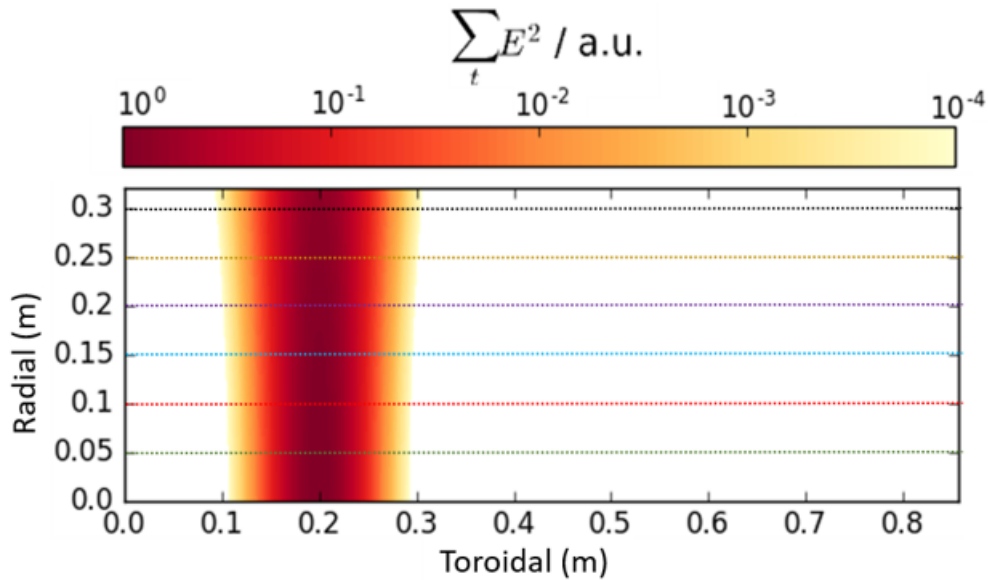


Figure 59: Time-averaged image of an EMIT-3D simulation. The shown 2D plane is taken at the centre of the 3D domain. A 28GHz beam is launched into vacuum, and the beam divergence is measured at each of the coloured lines for the purpose of comparison with the 2D codes EMIT-2D, IPF-FDMC, and FFW.

The antenna plane is located at 0.0m on radial axis. Radial positions of 0.0m, 0.05, 0.10m, 0.15m, 0.20, 0.25m and 0.30m are chosen to analyse the beam and are represented as coloured lines.

In order to launch an electromagnetic beam in a numerical simulation an expression for the time dependent electric field must be obtained. Solutions to the paraxial Helmholtz equation in both 2D and 3D can yield these expressions. These solutions predict a different rate of beam divergence for a 2D and 3D beams. This can be used to benchmark the codes which can form a useful check to see if they perform as expected. The 2D and 3D paraxial Helmholtz equation solutions predict that a Gaussian beam will diverge as $\sqrt{\omega_0/\omega_z}$ and ω_0/ω_z , respectively. Figure 60 shows the results of this comparison.

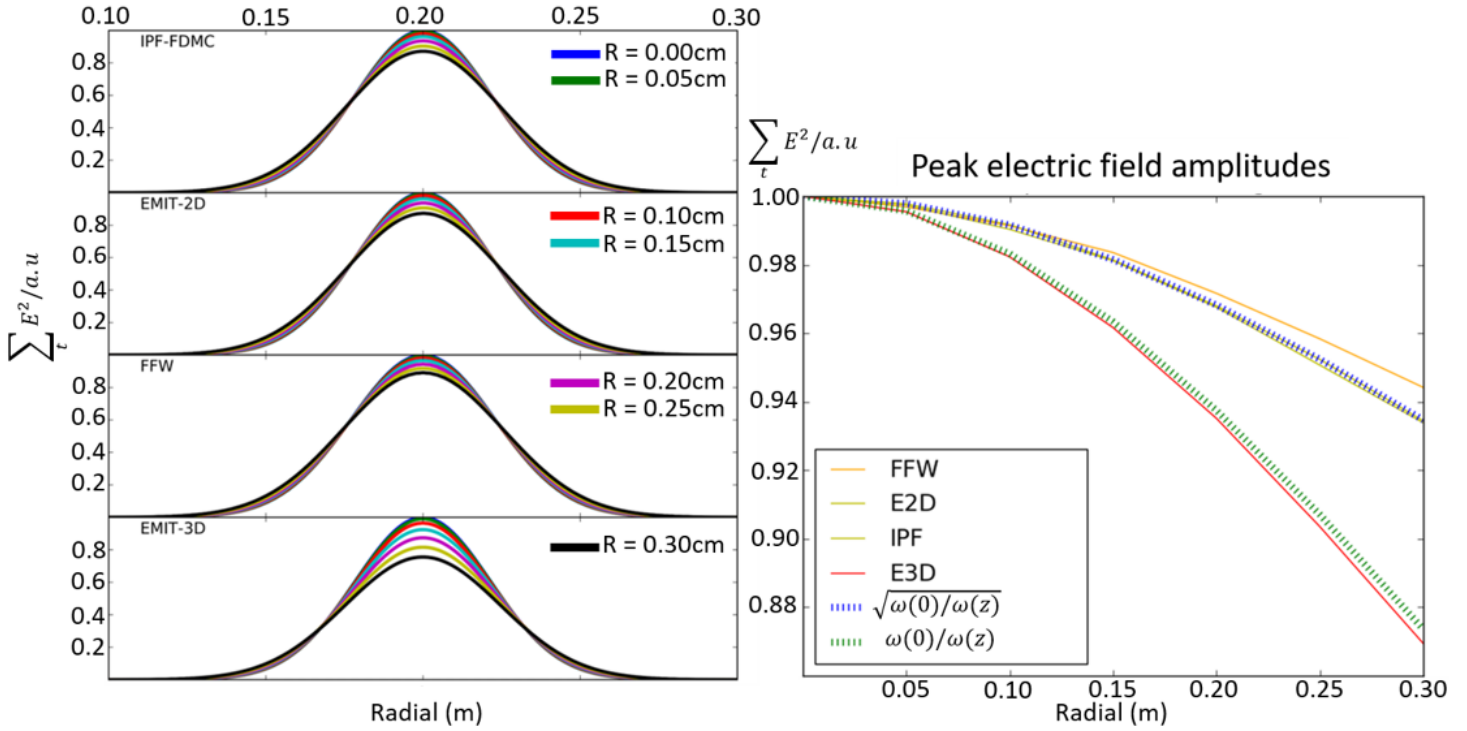


Figure 60: The toroidal beam profiles are measured (left) at distinct radial positions as indicated on figure 59. The peak electric field signals are compared to one another, and against analytical expressions (right).

The signals from each code are shown (left) at the aforementioned positions along the toroidal axis. At the beam centre, the peak of each signal along the radial axis is

also shown (right) and compared to analytical functions. The 2D and 3D codes are broadly found to diverge as expected, with the code FFW (dark yellow) diverting modestly from the expected beam divergence at large radial distances.

8.2.2.2 Mode conversion efficiency in 2D and 3D

With the basic properties of divergence verified in section 8.2.2.1, it is possible to benchmark EMIT-3D against IPF-FDMC, FFW, and EMIT-2D in a more rigorous manner, by modelling O-SX mode conversion. This benchmarking can be done by first analytically estimating (communicating with Dr. Bengt Eliasson) the differences in mode conversion efficiency between the 2D codes and EMIT-3D.

Let the mode conversion window be much wider than the width of the beam. We can also assume that the reflection coefficient (R_{2D}, R_{3D}) has a parabolic dependence such that

$$R_{2D} = Ax^2, \tag{206}$$

$$R_{3D} = A(x^2 + y^2) = Ar^2. \tag{207}$$

This assumption can be justified by observing the analytically calculable [99] fraction of the beam that is successfully mode converted from the O-mode to the X-mode. Figure 61 models this expression for a range of density length-scales (L_n), represented as a unit-less quantity by normalising to the wave-number (k_0).

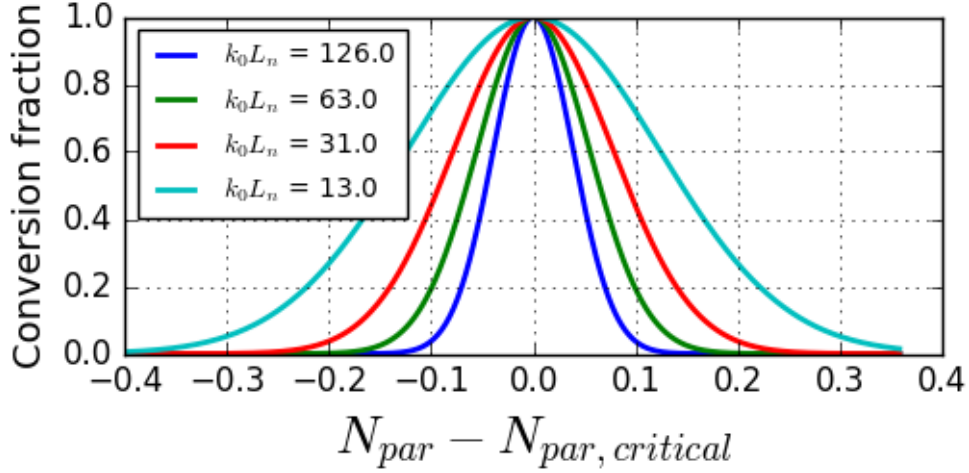


Figure 61: Fraction of incident energy that is successfully O-X mode converted. Various values of $k_0 L_n$ are shown indicating different plasma length-scales. The mode conversion window can be seen to be wider for stronger gradients (lower $k_0 L_n$). N_{par} is the refractive index parallel to the background magnetic field. $N_{par,critical}$ is the parallel refractive index required for optimum mode conversion, calculated by equation (95).

Observing figure 61 the parabolic nature of the transmission coefficient (and therefore the reflection coefficient) can be seen. At very small length-scales ($k_0 L_n < 2.0$) Mjølhus's formula has been seen to diverge from modelled values of the reflection coefficient in 2D full-wave simulations [153]. Despite this, the reflection coefficient remains parabolic. For any experimental beam, the intensity must be a function of position; in 2D $I_{2D} = I(x)$, and in 3D $I_{3D} = I(r)$. From the definition of power

$$P_{2D} = \int_{-\infty}^{\infty} I_{2D}(x) dx, \quad (208)$$

$$P_{3D} = \iint_{-\infty}^{\infty} I_{3D}(r) dx dy = 2\pi \int_0^{\infty} I_{3D}(r) r dr. \quad (209)$$

The reflected power is the product of the power and the reflective coefficient

$$P_{R,2D} = \int_{-\infty}^{\infty} I_{2D}(x) R_{2D} dx = \int_{-\infty}^{\infty} I_{2D}(x) x^2 dx, \quad (210)$$

$$P_{R,3D} = \iint_{-\infty}^{\infty} I_{3D}(r) R_{3D} dx dy = 2\pi \int_0^{\infty} I_{3D}(r) r^2 r dr, \quad (211)$$

and the effective reflective coefficient is the ratio between the reflected power and incident power

$$R_{eff,2D} = \frac{\int_{-\infty}^{\infty} I_{2D}(x) x^2 dx}{\int_{-\infty}^{\infty} I_{2D} dx}, \quad (212)$$

$$R_{eff,3D} = \frac{\int_0^{\infty} I_{3D}(r) r^3 dr}{\int_0^{\infty} I_{3D}(r) r dr}. \quad (213)$$

Applying this model specifically to a Gaussian beam, from equation (160) the electric field profile varies as

$$E(x, z)_{2D} = A_{2D} \exp\left(\frac{-x^2}{\omega(z)^2}\right), \quad (214)$$

$$E(r, z)_{3D} = A_{3D} \exp\left(\frac{-r^2}{\omega(z)^2}\right), \quad (215)$$

where A_{2D} and A_{3D} are some constants. The intensity is proportional to the square of the electric field

$$I(x, z)_{2D} = A_{2D}^2 \left[\exp\left(\frac{-x^2}{\omega(z)^2}\right) \right]^2 \quad (216)$$

$$I(r, z)_{3D} = A_{3D}^2 \left[\exp\left(\frac{-r^2}{\omega(z)^2}\right) \right]^2. \quad (217)$$

Using the expressions for the intensity of the Gaussian beam to calculate the effective reflective coefficients

$$R_{eff,2D} = \frac{\int_{-\infty}^{\infty} \left[\exp\left(\frac{-x^2}{\omega(z)^2}\right) \right]^2 x^2 dx}{\int_{-\infty}^{\infty} \left[\exp\left(\frac{-x^2}{\omega(z)^2}\right) \right]^2 dx} = \frac{\omega(z)^2}{4} \quad (218)$$

$$R_{eff,3D} = \frac{\int_0^{\infty} \left[\exp\left(\frac{-r^2}{\omega(z)^2}\right) \right]^2 r^3 dr}{\int_0^{\infty} \left[\exp\left(\frac{-r^2}{\omega(z)^2}\right) \right]^2 r dr} = \frac{\omega(z)^2}{2}, \quad (219)$$

which indicates that the reflection coefficient of the beam modelled in 2D should be roughly half of that modelled in 3D.

With a theoretical model in place to give predictive framework to the full-wave simulations, a mode conversion simulation is performed and comparisons of the mode conversion efficiency between EMIT-3D, EMIT-2D, IPF-FDMC and FFW are conducted. A 28GHz O-mode beam is launched from vacuum into a magnetised plasma. The beam is focused at the antenna plane, and has a waist radius of $\omega_0 = 4\lambda_0$, where λ_0 is the vacuum wavelength. The magnetised plasma has a homogeneous background magnetic field of $B = 0.85T$ which gives a normalised cyclotron frequency of $Y = \omega_{ce}/\omega_0 \approx 0.85$. The density gradient is modelled as

$$n_e(z) = (z - z_{n,start}) \frac{2\pi}{\lambda_0} \frac{1}{k_0 L_n} = \frac{z - z_{n,start}}{L_n}, \quad (220)$$

where $z_{n,start} = 0.15m$, and the value of the normalised density length-scale is set to $k_0 L_n = 25.0$. The density gradient then only varies along the radial axis. The parallel wave-vector is matched for optimal mode conversion as modelled by equation (95), by launching the O-mode wave at an angle of $\theta = 43.0^\circ$ to the background magnetic field. At the time of these simulations, EMIT-2D was unable to model elliptically polarised waves. In order to perform a comparison between EMIT-3D and EMIT-2D, an analogous simulation was run using a linearly polarised wave. For the comparison between EMIT-3D, IPF-FDMC, and FFW, elliptically polarised waves

were launched which more closely represents the anticipated experiments. These simulations can be seen in figure 62 for both the linear (left) and elliptical (right) cases.

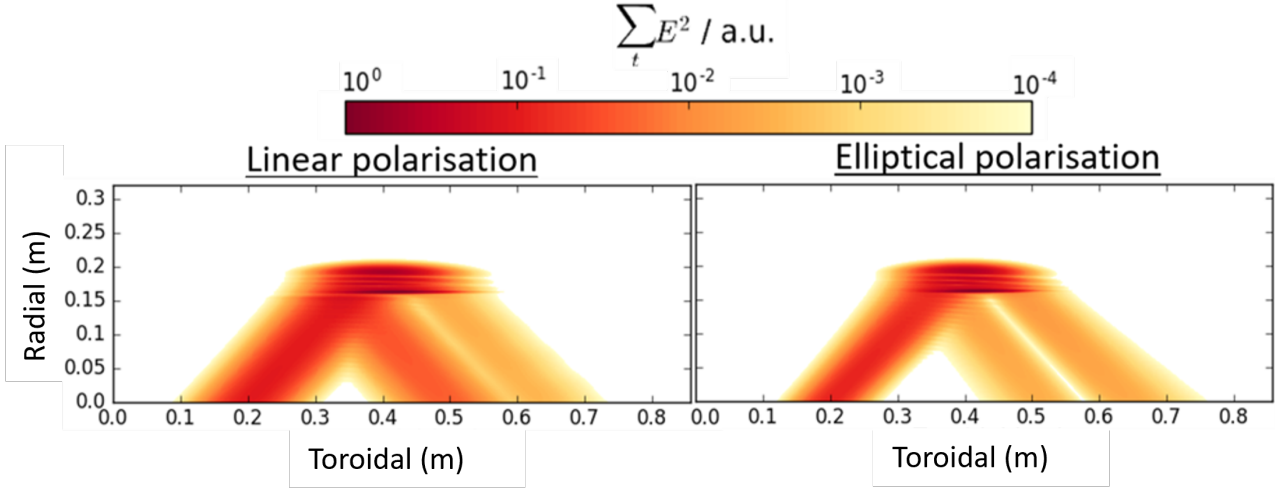


Figure 62: Toroidal-radial plane taken at the centre of the injected beam for an O-SX mode conversion simulation using EMIT-3D. A linearly launched beam (left) and an elliptically polarised beam (right) are compared.

At the radial position $R = 0m$, the plane perpendicular to the path of the beam propagation (toroidal-poloidal) is shown in figure 63 for both the linear (left) and elliptical (right) polarisations. The signal of the launched beam can be seen to be centered at about $x = 0.25m$. In order to calculate the mode conversion efficiency, this is compared to the rejected beam which is centered about $x = 0.55m$. In both the linear and elliptical cases there is a null-point in the centre of the rejected beams, which corresponds to the part of the incident beam which strongly matched the wave-number conditions for mode conversion, expressed by equation (95). In the linear polarisation this null-point is less pronounced; a small, albeit strong beamlet appearing at about $x = 0.46m$ can be seen which corresponds to the rejected X-mode that overlaps the rejected O-mode null-point. This rejected X-mode is an indication

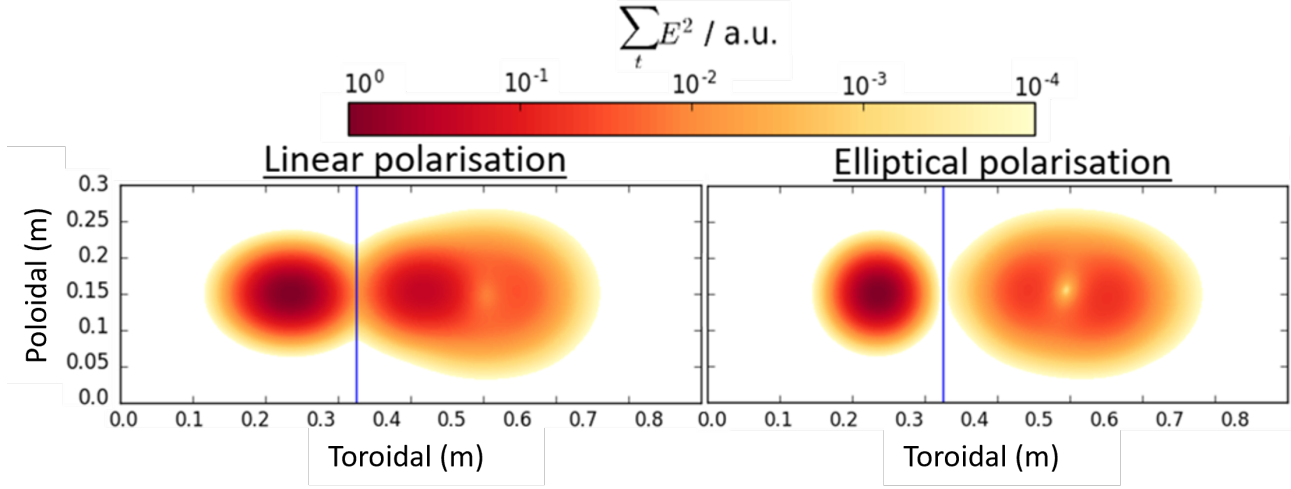


Figure 63: Perpendicular plane for an EMIT-3D O-SX mode conversion simulation used a linearly launched beam (left) and an elliptically polarised beam (right).

that the launched O-mode beam was not pure in its polarisation, and consisted of some O-mode/X-mode hybrid, as is to be expected with launching linear polarised beams at intermediate angles ($0 < \theta < \pi/2$) to the background magnetic field. Observing the elliptical case (right) it is of interest to see that while the launched beam is symmetrical, the rejected signal is not. This implies that there could be some important 3D effects coming into play when modelling O-SX mode conversion. The quantitative results of these simulations are presented in two stages; firstly for the comparison between EMIT-3D and EMIT-2D using the linear polarisation, and secondly using the elliptical polarisation to compare EMIT-3D, IPF-FDMC, and FFW.

Two detection methods are used for a more thorough comparison. The 2D codes EMIT-2D, IPF-FDMC, and FFW do not feature the poloidal axis, and the most simple method ignores this plane. In this 1D case, the incident and reflected beams are integrated over the toroidal dimension, at the radial position of $R = 0.0m$. Since EMIT-3D does include the poloidal axis, the centre of the beam is taken,

which corresponds to the poloidal position of $P = 0.15m$. Doing this, allows for the detection methods used in each code to be identical. This is powerful because any efficiency differences between the 3D and 2D codes may indicate that there are 3D effects which propagate into the radial-toroidal plane that the 2D codes may not be representing due to their reduced dimensionality.

The second detection method is unique to EMIT-3D and utilises the poloidal plane. The mode conversion efficiency is calculated by integrating over the 2D beam surfaces in the poloidal-toroidal plane. This 2D detection method is more rigorous as it respects the multi-dimensional nature of the beam. According to the above mathematical treatment, the mode conversion efficiency is expected to drop due to the conversion window being smaller in 3D. This 2D detection method helps to validate the mathematics, and will help identify if there are any important 3D effects that have been overlooked, which require consideration when modelling O-SX mode conversion in the 2D codes EMIT-2D, IPF-FDMC, and FFW.

Name of Code	Detection Method	Conversion Efficiency
EMIT-3D	2D	54.0%
EMIT-3D	1D	66.5%
EMIT-2D	1D	67.0%

Table 4: Comparative mode conversion efficiencies between the 2D (EMIT-2D) and 3D (EMIT-3D) full-wave codes when modelling O-SX mode conversion efficiency using a beam launched with a linear polarisation as seen in figure 62 (left).

Using the linearly polarised wave, the results of the comparison between EMIT-3D and EMIT-2D are shown in table 4. Using the 1D detection method, the two codes show excellent agreement when comparing the achieved O-X mode conversion efficiency. This is somewhat unsurprising, as the numerical algorithms are very similar. When using the 2D detection method, the mode conversion efficiency drops

in EMIT-3D sharply, as expected.

Name of Code	Detection Method	Conversion Efficiency
EMIT-3D	2D	73.0%
EMIT-3D	1D	88.8%
IPF-FDMC	1D	86.4%
FFW	1D	86.4%

Table 5: Comparative mode conversion efficiencies between the 2D (FFW, IPF-FDMC) and 3D (EMIT-3D) codes when modelling the O-SX mode conversion efficiencies of an O-mode beam launched with an elliptical polarisation, as seen in figure 62 (right).

Using the elliptically polarised wave, the results of the comparison between EMIT-3D, IPF-FDMC, and FFW are shown in table 5. These codes have very good agreement for the case of 1D detection. This is a marked result as each code has been developed individually using different numerical techniques, and provides re-assurance for their future comparison in more complex simulations that may be more challenging to interpret. Comparing the 2D detection method of EMIT-3D to the 1D method of IPF-FDMC and FFW, the conversion efficiency again drops in EMIT-3D as expected. Importantly, the above analytical treatise seems to well predict the differences in efficiency between 2D and 3D codes, and the error is within a few percentage points. This implies that any 3D effects of the mode conversion mechanism are negligible for O-SX modelling under the basic simulation parameters used in this section. This is a good result as it gives reliability towards the numerically cheap 2D codes. However, it cannot be said that 3D effects are negligible in O-SX experiments relevant to MAST-U as the plasma is markedly more complex than represented in these simulations.

8.2.3 MAST-U equilibria

The benchmarking mode conversion simulation detailed in section 8.2.2 used a simple plasma geometry. The background magnetic field was homogeneous and parallel to the toroidal dimension, and the density gradient has been prescribed simply by the analytical expression (220). While these simplistic plasma profiles are useful in order to identify the functionality of numerical tools, form comparisons between them, and validate certain theoretical models, they are not sufficient to satisfactorily represent a spherical tokamak (ST) plasma. In reality the density profile of ST plasmas will feature some curvature due to the toroidal nature of the device, which has not been modelled by equation (220). The magnetic field is probably the most significant difference which needs to be accounted for. In ST plasmas the magnetic fields can have aggressive pitch angles which vary quickly over a short spatial distance. The microwave imaging system SAMI [154] measured the magnetic pitch angles of MAST to be on the order of $\theta = 30^\circ$. The time and fiscal investments required to physically develop an EBW heating system that can function on MAST-U is tremendous. Numerical simulations are comparatively of negligible cost. Every effort must then be made to accurately simulate every aspect of a potential EBW heating system before efforts towards experimental construction can commence. In this section we advance the O-SX mode conversion simulations by introducing a MAST-U, high beta equilibrium profile in order to represent the density and magnetic field profiles of a ST plasma. This is an important step towards reliable and therefore defensible predictions towards the viability of EBW heating on MAST-U.

An important numerical issue with the modelling of the interaction between electromagnetic waves and strong number density gradients must be noted. Whereas the gradient of the benchmarking cases studied in section 8.2.2 was a gentle $k_0 L_n = 25.0$, the MAST-U equilibrium, H-mode plasma edge is much more aggressive. Detailed in section 8.2.3.1, the density gradients are approximately $k_0 L_n = 4.25$. This causes an

interesting numerical effect which is likely unique to cold plasma codes that cannot correctly model the upper hybrid resonance and Electron Bernstein Waves (EBWs). After O-X mode conversion, the energy in the X-mode polarisation interacts with the upper hybrid resonance where in experiment it would couple to the plasma, possibly converting to an electrostatic EBW. Cold plasma waves cannot simulate this, and the X-mode energy builds up near the upper hybrid resonance where the wavelength decreases with time. Subject to the density gradient, after sufficiently large energies have built up, the X-mode begins to ‘leak’ out of the plasma. This is an un-physical effect due to that the numerical grid in space no longer can represent the short wavelength upper hybrid waves when the number of grid points per wavelength becomes less than two (the Nyquist theorem). This leakage initially caused erroneous interpretation of the full-wave results, as the mode-conversion efficiencies seemed to be far lower than was expected. Figure 64 shows a time-trace of three EMIT-3D simulations modelling O-X mode conversion.

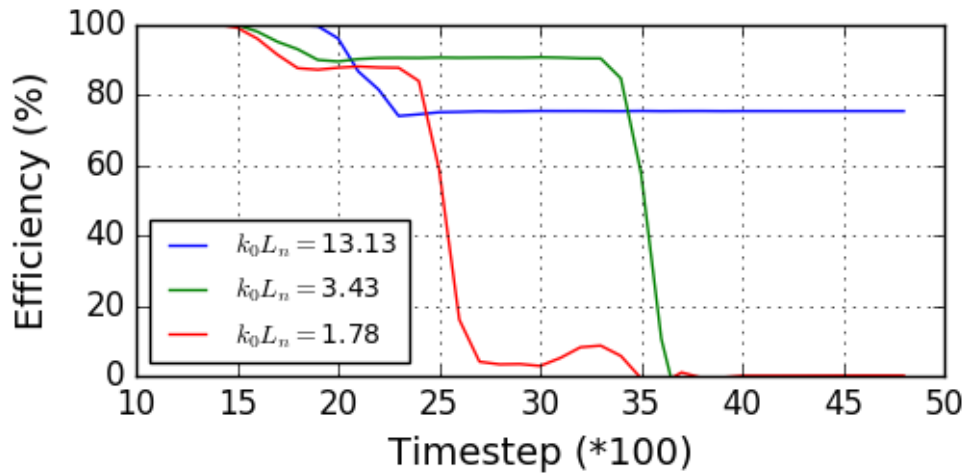


Figure 64: Time-trace of the O-X mode conversion efficiency.

These simulations were conducted under the same parameters as those in the benchmarking cases, of section 8.2.2; a simple plasma geometry, with a linear density gra-

dient and homogeneous magnetic field. The most gentle gradient of $k_0 L_n = 13.13$ (blue) can be seen to plateau at around time-step 2250, where the efficiency remains constant throughout the rest of the simulation. This signal represents the more easily interpreted case, as the mode-conversion efficiency could be measured at any point after saturation has been determined. The intermediate density gradient case $k_0 L_n = 3.43$ (green) closely resembles the gradient of the MAST-U equilibrium. This signal can be seen to plateau earlier, at around time-step 2000. The conversion efficiency remains constant until around time-step 3400, at which point a sharp decline can be seen. This decline represents the point at which the X-mode signal has built up sufficiently at the upper hybrid resonance, and began to ‘leak’ out of the plasma. As such, for the correct interpretation of the results, the measurement of the mode-conversion efficiency must be carefully taken to be after the signal has plateaued, but before leakage occurs.

8.2.3.1 Results

MAST-U has a major radius of $R = 0.85m$, typical minor radius of $a = 0.65m$, maximum plasma current of $2.0MA$, and a maximum background magnetic field strength of $B_0 = 0.75T$ at $R = 0.75m$ [155]. An equilibrium profile was provided by CCFE corresponding to an H-mode, high plasma- β , high elongation scenario. The poloidal cross section of the equilibrium profile is shown in figure 65. Two potentially feasible antenna positions for the O-X-B heating system are identified, as

$$\text{antenna 1} \quad : \quad R = 1.856m, Z = 0.95m \quad (221)$$

$$\text{antenna 2} \quad : \quad R = 1.868m, Z = 0.10m. \quad (222)$$

Referencing the MAST-U schematic in figure 44, these antenna positions have been chosen for similar reasons to that justified in section 8.1. Antenna 1 is situated

in-between the P5 and P6 poloidal magnetic field coils, and Antenna 2 is located close to the equatorial plane.

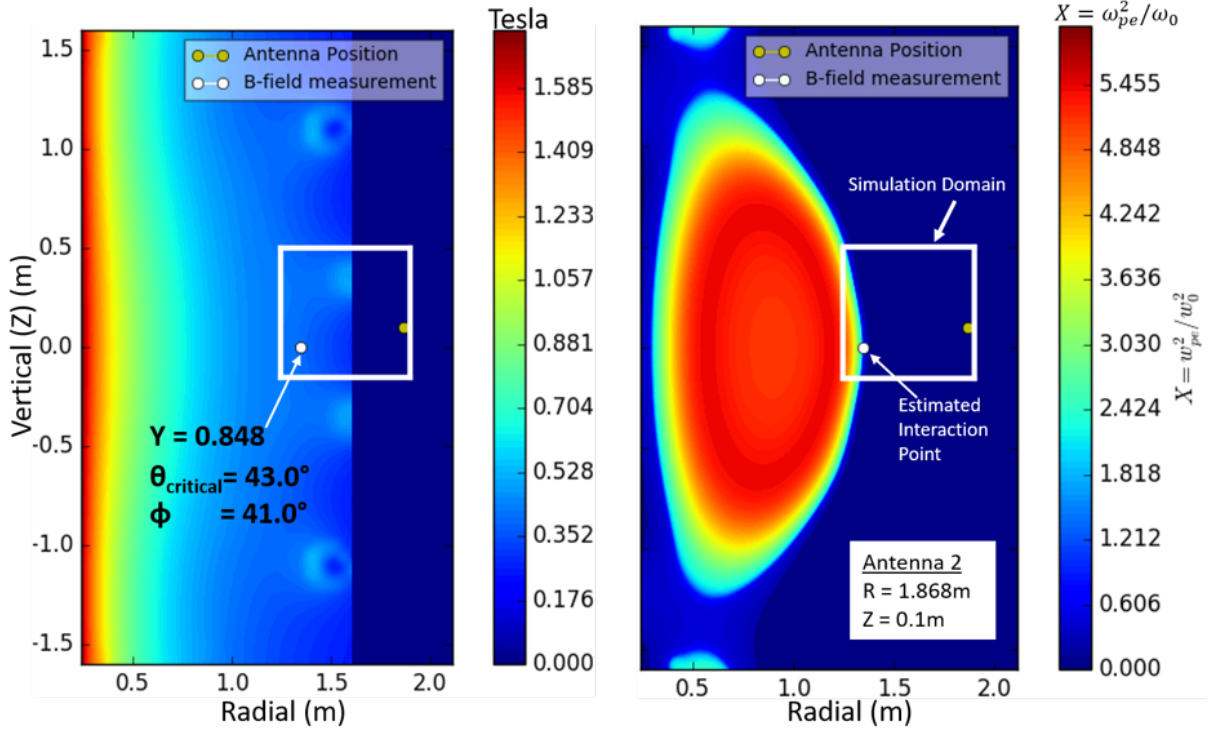


Figure 65: Cross-section of the MAST-U high beta, high elongation equilibrium provided by CCFE. The white square indicates the sub-domain used in the full-wave calculations. The yellow and white dots are the antenna position, and the estimated location of O-SX mode conversion, respectively. The magnetic field properties at the location of the white dot are used for the beam launch configuration.

The equatorial launch position (antenna 2) was chosen due to the likelihood of the reduced complexity of the interpretation of numerical results.

The density length-scales of the equilibrium profile was measured. Two locations were used, one close to the mid-plane and the other much more polar. These are

intended to correlate to the approximate position of interaction of waves launched from antennas 2 and 1, respectively, and the average normalised length-scale was $k_0 L_n = 4.25$. With the simplified plasma geometry used in section 8.2.2.2 (a linear density gradient varying only radially, and a homogeneous background magnetic field), the O-SX mode conversion efficiency was modelled. Figure 66 shows the results. Denoted in yellow and green dashed lines are the the MAST-U equilibrium profile density length-scale relevant to antenna 2 and 1.

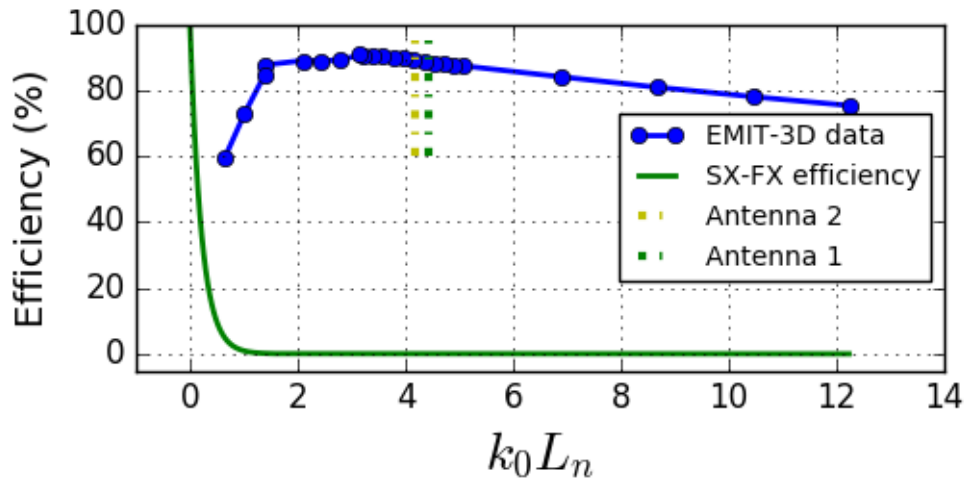


Figure 66: O-SX mode conversion efficiency as a function of the back-ground density length-scale. The vertical yellow and green dashed lines represent the measured length-scale of the MAST-U equilibrium profile pertinent to antenna positions 2 and 1, respectively.

Also plotted in figure 66 and shown by the solid green line, is an analytical expression [156]

$$\eta_{SX-FX} = \exp \left(-\pi k_0 L_n Y^2 \sqrt{\frac{(\omega_{UH}/\omega_{ce}) - 1}{X}} \right), \quad (223)$$

which predicts the efficiency of direct slow X-mode to fast X-mode (SX-FX) coupling. At length-scales greater than approximately $k_0 L_n = 3.6$ the density length-

scale and conversion efficiency feature an inverse, roughly constant relationship. At intermediate length-scales of approximately $1.75 < k_0 L_n < 3.6$ the efficiency drops slightly, and plateaus. The reasoning behind this is unknown. Below $k_0 L_n = 1.75$ the efficiency begins a sharp decline, as would be expected due to the increasing efficiency of direct SX-FX coupling. Since the density length-scales of the MAST-U equilibrium are comfortably in the higher length-scale region ($k_0 L_n > 3.6$), the interpretation of the mode conversion results should not require consideration of the finer physical details associated with lower length-scales.

The MAST-U equilibrium profiles are given on a grid of 200 by 200 points, with a spatial resolution of $\Delta R = 6.8mm$ and $\Delta Z = 16.0mm$. This grid is far too poorly resolved considering that the wavelength of the beam is $\lambda_0 \approx 1.0cm$. The equilibrium profiles must then be interpolated so that they can be used within EMIT-3D. The Piecewise Cubic Hermite Interpolation Polynomial (PCHIP) algorithm [157] imported from the SciPy library [158] was used to do this. After interpolation the number density profile along with each component of the background magnetic field have $\Delta R = \Delta Z = (1/20)\lambda_0$ and are imported into EMIT-3D at run-time. The magnetic field vector at the approximated position of interaction (white dot in fig. 65) is measured. This is used for two considerations. First, to calculate the toroidal launch angle required for optimum mode conversion, calculated with equation (95). Second, to match the O-mode polarisation to the poloidal magnetic field pitch angle. The magnetic field vector was assessed to have a magnitude of $B = 0.85T$ with vector components $\theta_B \approx 0.0^\circ$ and $\phi_B \approx 41.0^\circ$. θ_B is the angle between the toroidal dimension and the magnetic field vector in the radial-toroidal plane. ϕ_B is similarly defined, except in the toroidal-vertical plane. The microwave is launched at an angle of $\theta = 43.0^\circ$ and $\phi = \phi_B$. An elliptical polarisation is used in order to ensure that the wave is close to a pure O-mode, avoiding large signal-rejection at the fast X-mode cutoff. Figure 67 shows the results of the matched mode conversion simulation. The

injected and rejected signals can be seen in the lower left corner, and the centre, respectively.

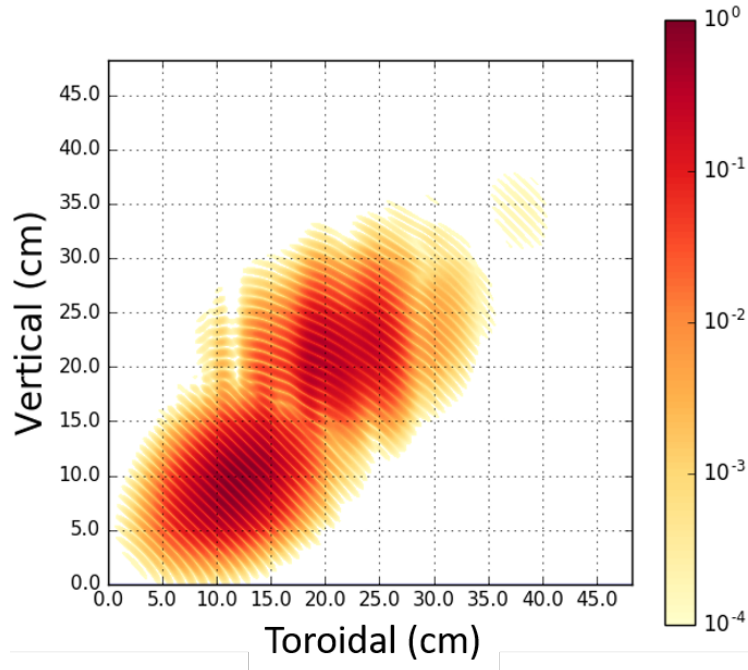


Figure 67: O-SX Mode conversion simulation. An elliptical O-mode beam is launched towards a plasma consisting of stationary MAST-U density and 3D magnetic field equilibrium profiles. The perpendicular toroidal-vertical 2D plane is taken at the antenna plane (radial position $R = 0m$). The beam is launched at angles of $\theta = 43.0^\circ$ and $\phi = 41.0^\circ$.

Within the rejected signal, striations can be seen which are the result of the MAST-U equilibrium profile featuring a perturbed cut-off surface. The characteristic central null is notably absent, as opposed to the simulations conducted in section 8.2.2.2. This may be due to the MAST-U equilibrium featuring a curved, perturbed cutoff surface, or it could indicate that the wave was not properly matched for mode conversion. This simulation, along with another using $\phi = 0.0$ are represented in table 8.2.3.1.

Poloidal angle	Toroidal angle	Conversion efficiency
0.0°	43.0°	$\eta = 0.5\%$
41.0°	43.0°	$\eta = 62.0\%$

Table 6: Full-wave simulation results obtained with EMIT-3D using the H-mode MAST-U equilibrium with the beam launched from the near-equatorial (antenna 2) position.

Using a heavily mismatched poloidal angle of $\phi = 0.0$ gives almost no mode conversion, as would be expected. However, matching the optimal mode conversion conditions only gave an efficiency of 62.0%, which is surprisingly low. Considering figure 66, one would expect to be able to achieve an efficiency of around $\eta = 88.0\%$, noting that the MAST-U equilibrium length-scales are marked with green and yellow lines. The 2D codes FFW and IPF-FDMC achieved efficiencies of $\eta = 95\%$ and $\eta = 93.8\%$, respectively. It is expected that the 2D codes predict higher mode conversion efficiencies than 3D codes due to the mathematical reasoning described in section 8.2.2.2. Both FFW and IPF-FDMC attained higher efficiencies when the MAST-U equilibrium was used as opposed to the simplified plasma used in section 8.2.2.2, which is expected due to the normalised length-scale reducing from $k_0 L_n = 25.0$ to approximately $k_0 L_n = 4.2$. EMIT-3D did not share this success, and predicted a reduced mode conversion efficiency. In an attempt to resolve these discrepancies, the curvature of the density-gradient was investigated. The MAST-U density equilibrium was artificially flattened, as shown in figure 68.

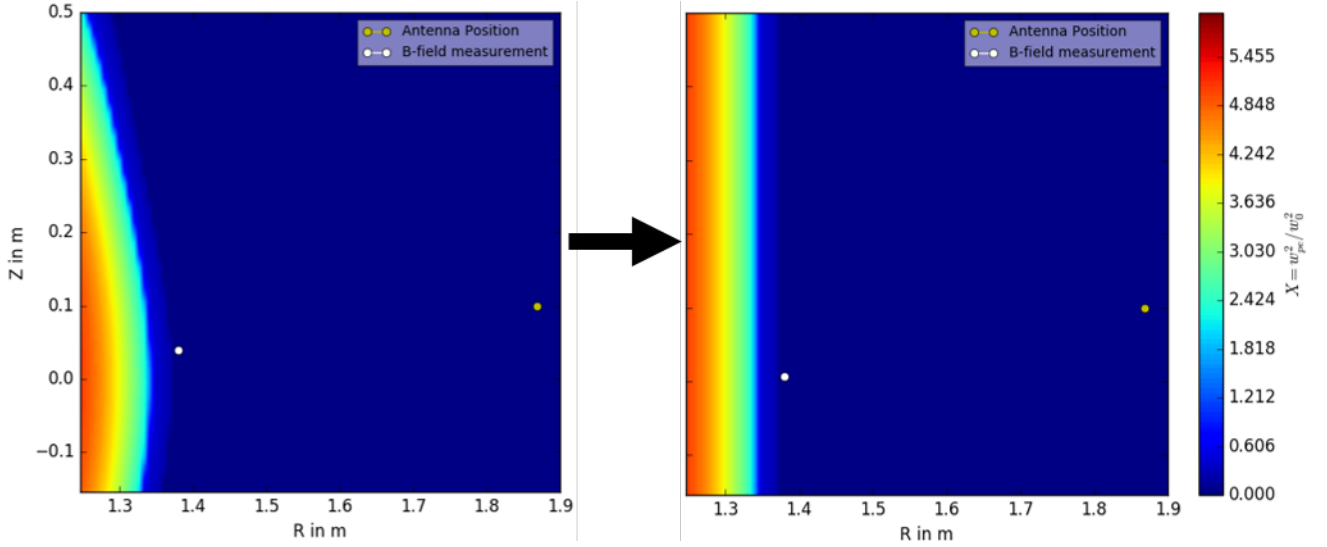


Figure 68: The simulation domain shown in figure 65 is artificially flattened, in order to determine the role of curvature in the mode conversion efficiency. Post-flattening, the density profile more closely resembles that used in section 8.2.2.2. The yellow dot indicates the antenna position, and the white dot is the estimated point of wave-plasma interaction where the magnetic field vector is measured.

This flattening resulted in a rise of mode conversion efficiency to $\eta = 67.0\%$. This corresponds to a rise of approximately 5 percentage points, but does not explain as to the discrepancy between the attained value, and the expected value of approximately $\eta = 88.0\%$. The lacklustre mode conversion efficiency may be somewhat explained by the curvature of the magnetic field having a known detrimental effect on the conversion efficiency [159]. Although, this should be able to be somewhat mitigated by adjusting the focal point of the electromagnetic wave such that, at the point of mode conversion, the curvature of the beam matches the curvature of the magnetic field. It is also possible that the estimation of the interaction point is inaccurate, leading to slight mismatches in the launch conditions. A 2D vertical-toroidal parameter scan would be of great use in further understanding the O-X

mode conversion efficiency in complex plasma environments, although this would be expensive to conduct in 3D.

8.2.4 Summery of the EBW heating modelling

EMIT-3D was further developed to include the ability of launching an elliptically polarised wave for the purpose of modelling O-X mode conversion. This was achieved and is detailed by comparing figures 57 and 57. The full-wave 3D code EMIT-3D, and 2D codes EMIT-2D, IPF-FDMC, and FFW were benchmarked against one another measuring divergence, and performed as expected as shown in figure 60. More rigorously EMIT-3D was benchmarked against the other codes for the modelling of mode conversion in a simple geometry. Addressed in tables 4 and 5 the conversion mechanism performed as expected, with excellent agreement between the 2D codes IPF-FDMC and FFW. EMIT-2D predicted a poor mode conversion efficiency in comparison which is due to the launched beam being of linear polarisation. When compared to a linearly polarised beam launched in EMIT-3D the two codes have excellent agreement. Using elliptical polarisations EMIT-3D performed comparably with IPD-FDMC and FFW when the 1D detection method was used, and saw an expected drop in mode conversion efficiency when the full 3D nature of the code was respected by using a 2D detection system. A critical nuance of cold plasma full-wave calculations was identified and corrected for in figure 64. EMIT-3D was seen to predict strong mode conversion efficiencies of up to 90% at shorter length-scales in figure 66. Finally, an H-mode MAST-U density and magnetic field profile was used to perform experimentally relevant simulations. These resulted in a lack-lustre mode conversion efficiency of 62%. The most likely explanation for this is some mistake in matching the beam's polarisation to the background magnetic field, and further simulations conducting parameter scans in launch angle space would be beneficial to understanding this result.

9 Conclusion

Having seen significant development, the full-wave, 3D, cold plasma code EMIT-3D has been used to study a variety of mechanisms relating to the use of microwave beams in fusion plasma. These studies fall under three categories; Doppler back-scattering and cross-polarisation Doppler back-scattering modelling, ECCD, and EBW heating. In this chapter we provide a conclusion to each of these section while where relevant detailing future work.

9.1 Cross-polarisation Doppler back-scattering

The CP-DBS work verified the functionality of EMIT-3D by confirming the previously known scaling relationship shown in figure 35. The back-scattering efficiencies measured in section 7.3 also have excellent agreement with the underlying theory. An important interaction effect between back-scattered and reflected cross-polar signals was identified which will need to be considered carefully when conducting experimental measurements. Furthermore, the back-scattering efficiency was found to have a strong dependency on the background density length-scale. Significant potential non-WKB effects were identified at $|k_o - k_x|/(2\pi/L_n) \leq 1.0$ at experimentally relevant length-scales ($0.9 < L_n(cm) < 1.8$). Finally, an asymmetry in the cross-polar back-scattered electric fields was noticed, and was explored in both the standard and flat-top background density profiles. These studies were the first of their kind, and as such it may be premature to conclude precisely which measures should be taken to assist in experimental success.

Regarding the relationship between scattering efficiency and density length-scale, simulations conducted at a range of magnetic field parameters are desirable to understand if the normalised cyclotron frequency has any important influence. Furthermore, changing the turbulence fluctuation ratio $(\delta B/B)/(\delta n/n)$ would be critical

as if there exists a strong relationship between this length-scale effect and the electromagnetic nature of the turbulence itself this must be understood. Indeed, if the turbulence fluctuation ratio has a strong role here then absolute measurements of said ratio may be challenging. However, the background density length-scale is a simple metric experimentally. Should the turbulence fluctuation ratio be independent of this length-scale effect or easily predictable then absolute measurements of the turbulence could be feasible.

Interestingly, the effect of non-WKB effects on the back-scattering efficiency seem to become significant at $|k_o - k_x|/(2\pi/L_n) = 1.0$ which corresponded to $L_n = 2.0\text{cm}$ in our study and can be seen from figure 41. This regime is experimentally relevant and corresponds to the steep and early knee of the pedestal. Understanding how these non-WKB effects behave at a wider range of simulation parameters not investigated here (varying the normalised cyclotron frequency and turbulence fluctuation ratio) are critical to understand how the scattering mechanism will behave in a general fusion plasma. As a first step we have identified the modest influence of potential non-WKB effects to be at most tens of percent in the specific set of parameters outlined in section 7. We have also shown that inequality (113) can, at least in the cases investigated in this work, signify the beginning of a non-WKB regime around values of $|k_o - k_x|/(2\pi/L_n) = 1.0$.

The unexplained asymmetry in the structure of the back-scattered cross-polar electric fields remains a further experimental challenge. While this is less significant compared to the length-scale dependence of the back-scattering efficiency it remains a difficulty which the diagnostic design must respect. Further simulations are required to explore this effect.

It is clear from the complex nature of the interaction between electromagnetic waves and a magnetised plasma that much more work is required to achieve a good understanding of the relative mechanisms. The CP-DBS diagnostic seeks to exploit

an interaction which is influenced by a number of fundamental plasma parameters in ways which we simply do not understand. Full-wave, 3D numerical simulations are paramount to improving our understanding.

9.2 Electron cyclotron current drive

The ray-tracing code Torbeam was using in section 8.1.1 to simulate the coupling between electromagnetic waves and the higher cyclotron frequencies which are the lowest directly accessible in modern, high density, high beta spherical tokamak plasma experiments. The ECCD technique was deemed inappropriate for such plasmas. While there was moderate current driven in synthesised "low-beta" plasmas, generated by artificially lowering the number density, these do not generally reflect cutting edge plasma experiments. This is partly because the bootstrap current is widely considered to be essentially for the steady state operation of tokamak devices, and this intrinsically driven current favours higher density machines.

9.3 Electron Bernstein wave heating

Significant development of the EMIT-3D code was conducted, enabling it to model O-X mode conversion in cold plasmas. The code was successfully benchmarked against EMIT-2D, IPF-FDMC, and FFW giving reliability in the simulated physics. Excellent agreement and strong mode conversion efficiencies was seen between the codes when modelling simple plasma profiles. However, EMIT-3D predicted lacklustre mode conversion efficiencies when a complex MAST-U density and magnetic field equilibrium was used. The most likely explanation for this fall in efficiency is that the electromagnetic wave was launched with some angle mismatch between its polarisation and the background magnetic field lines. The code remains in a strong position to conduct further mode conversion studies in the future, and this drop in

efficiency could be investigated by parameter scans though the launched polarisation of the beam. Further use of EMIT-3D in this area would be of great value to the EBW heating technique since the code is 3D in nature and EMIT-3D, IPF-FDMC, and FFW are all 2D. Using exclusively 2D codes to model EBW heating may leave the work vulnerable to unexpected mechanisms which require three dimensions to fully materialise.

10 Appendix

10.1 Plane-wave solution to the homogeneous wave equation

Maxwell's equations include Ampère's and Faraday's laws, respectively,

$$\nabla \times \mathbf{B} = \mu_0 \mathbf{J} + \mu_0 \frac{\partial \mathbf{D}}{\partial t} \quad (224)$$

$$\nabla \times \mathbf{E} = -\frac{\partial \mathbf{B}}{\partial t} \quad (225)$$

This form of equations is more similar to that which Maxwell himself produced. Ampère's law in this form is more complete. We have made no assumptions so the medium at this stage, and Ampère's law includes both bound and free forces. Here we have

$$\mathbf{J} = \mathbf{J}_F + \mathbf{J}_B, \quad (226)$$

$$\mathbf{D} = \epsilon_0 \mathbf{E} + \mathbf{P}, \quad (227)$$

$$\mathbf{B} = \mu_0(\mathbf{H} + \mathbf{M}), \quad (228)$$

where

- \mathbf{J}_F and \mathbf{J}_B are free and bound currents.
- \mathbf{D} and \mathbf{B} are the Displacement Field and Magnetic Field respectively. They represent the overall fields.
- \mathbf{E} and \mathbf{H} are the Electric Field and Magnetic Field Strength, respectively. They represent the external electric and magnetic fields applied across a particular medium which arise as a result of free charges and currents.

- \mathbf{P} and \mathbf{M} which are the Polarisation Field and Magnetisation Field, respectively. These terms represent the internal electric and magnetic fields which arise from bound charges and currents, and occur as a result of applying an external electric/magnetic field across a particular medium.

The Polarisation Field (or Polarisation Density) represents the density of permanent or induced electric dipole moments $\mathbf{P} = \epsilon_0(\epsilon_r - 1)\mathbf{E}$. Analogously to the Polarisation Field the Magnetisation Field (or Magnetisation Density) represents the density of permanent or induced magnetic dipole moments $\mathbf{M} = (\partial m / \partial V)\mathbf{e}$, where ∂m is the elementary magnetic moment and ∂V is the volume element. It would be good to expand on \mathbf{P} and \mathbf{M} to discuss ϵ_r and capacitance, electric dipole moments, and magnetic dipole moments. In a vacuum there are no internal forces, so there are no bound charges or currents and therefore there are no Polarisation Fields and no Magnetisation Fields. Maxwell's equations then become

$$\nabla \times \mathbf{H} = \epsilon_0 \frac{\partial \mathbf{E}}{\partial t}, \quad (229)$$

$$\nabla \times \mathbf{E} = -\mu_0 \frac{\partial \mathbf{H}}{\partial t}. \quad (230)$$

We have used $\mathbf{B} = \mu_0 \mathbf{H}$ in Faraday's law to make it consistent with Ampère's law. This is possible because $\mathbf{M} = 0$ in vacuum. We can then couple these equations together to form a generalised wave equation for vacuum. We are not making any assumptions about the form of the electromagnetic wave at this stage.

$$\nabla \times (\nabla \times \mathbf{E}) = \frac{\partial}{\partial t} (\nabla \times \mathbf{B}) = \mu_0 \epsilon_0 \frac{\partial^2 \mathbf{E}}{\partial t^2}. \quad (231)$$

Using a vector identity $\nabla \times (\nabla \times \mathbf{A}) = \nabla(\nabla \cdot \mathbf{A}) - \nabla^2 \mathbf{A}$ where \mathbf{A} is any vector. As we are in vacuum there is no charge density and $\nabla \cdot \mathbf{E} = 0$ so we get

$$\nabla^2 \mathbf{E} - \mu_0 \epsilon_0 \frac{\partial^2 \mathbf{E}}{\partial t^2} = 0. \quad (232)$$

This is a 3D wave equation that describes electromagnetic waves in vacuum. In order to solve this an expression for the electric field must be found, and simplifying into 1D makes this easier. To do this we will assume that the described electromagnetic wave is propagating along the x-axis. Additionally we assume that the electromagnetic wave's electric field only has one component and is parallel to the y-axis $\mathbf{E} = E_0\hat{e}_y$. We also need to assume that we are modelling a plane wave. This allows us to state that for a given distance along z there is no variation of the electric or magnetic fields along the y-axis or x-axis. The wave equation now becomes

$$\frac{\partial^2 E_y}{\partial z^2} - \mu_0\epsilon_0 \frac{\partial^2 E_y}{\partial t^2} = 0. \quad (233)$$

In order to find a solution to this we need to try and deduce what a possible solution might look like. There is a trivial solution at $E_y = 0$, however since we have two partial differential equations with respect to z and t then the solution must be $f(z, t)$. One of the most simple forms this might make is $E_y = t - z/c$ where we have divided by c because t and z/c must be of the same dimensions in order to appropriately apply the addition operator, and we know that electromagnetic waves have a characteristic speed of c . We also know that electromagnetic waves oscillate. Additionally Fourier showed that any complex oscillation can be represented by a combination of cos functions. With this in mind we should include the cos function in our deduced solution. You can use the sin function as well and the end result is essentially the same. Some intricacies are brought up when converting to complex form/

$$E_y = \cos(z/c - t). \quad (234)$$

Because we are now dealing with a trigonometric function, it would be convenient if we could represent $t - z/c$ in terms of 2π . An example of an increasing time now

might look something like

$$t = 0(2\pi), t = 0.1(2\pi), \dots, t = A(2\pi), \quad (235)$$

where A is some number. We can do something similar for z/c , hence our solution becomes

$$E_y = \cos(2\pi(z/c - t)). \quad (236)$$

We are now describing something that is propagating along x at the speed of x , that has a sinusoidal electric field variation. This is beginning to sound more like an electromagnetic wave, however we also know that electromagnetic waves can differ in how often they exhibit this sinusoidal variation. We need to include the frequency of the wave into the deduced solution. Experimenting with the \cos function shows that we can make a wave oscillate more, or less, but altering the variable f in $\sin(f * 2\pi)$. In addition to this \sin must operate on a unit-less number. Currently our function has units of *time* and multiplying by frequency will solve this problem. In light of this we can include frequency into our deduced solution as

$$E_y = \cos(2\pi f(z/c - t)). \quad (237)$$

Expanding the brackets, and using the fundamental definition of angular frequency $\omega = 2\pi f$ and wave-number $k = \omega/c$ we obtain

$$E_y = \cos(kz - \omega t). \quad (238)$$

We also know that electromagnetic waves have different amplitudes to one another. We can easily include this by multiplying by some peak amplitude, E_0 , which gives

$$E_y = E_0 \cos(kz - \omega t). \quad (239)$$

We can use this expression in it's complex form by applying Euler's identity.

$$e^{i\theta} = \cos(\theta) + i \sin(\theta). \quad (240)$$

If we take the only the real components of Euler's identity we have

$$\Re\{e^{i\theta}\} = \cos(\theta) \quad (241)$$

Now we can apply our solution from equation (239) into the real parts of Euler's identity in equation (241) to give

$$\Re\{E\} = \Re\{E_0 e^{i(kz - \omega t)}\}, \quad (242)$$

where generally the \Re notation is dropped giving

$$E = E_0 e^{i(kz - \omega t)}, \quad (243)$$

You can then expand this solution to the 1D wave equation to allow a plane wave to propagate along any 3D vector. This can be done through the vector \mathbf{r} which is simply an axis along which we evaluate the electromagnetic wave. Then our solution becomes

$$\mathbf{E} = E_0 e^{i(\mathbf{k} \cdot \mathbf{r} - \omega t)}, \quad (244)$$

where for a given vector \mathbf{k} , suppose you choose \mathbf{r} along the direction of \mathbf{k} and denote this the x-axis, then $\mathbf{k} \cdot \mathbf{r} = kx$. We can then use this 3D plane wave solution as an approximate solution to any wave-equation. We can also combine several waves of the form (244) to produce any other wave.

10.2 Non-zero background flow dispersion relation

Observing the Force Balance equation we want to have each component of the equation in terms of \mathbf{E}_1 so that we can eliminate \mathbf{E}_1 through matrices. This

requires us to eliminate \mathbf{v}_1 and \mathbf{B}_1 in favour of \mathbf{E}_1 . An expression for \mathbf{B}_1 can simply be obtained from rearranging Faraday's equation. Looking firstly at Faraday's law, we can rewrite this as

$$\mathbf{B}_1 = \frac{\mathbf{k} \times \mathbf{E}_1}{\omega} \quad (245)$$

An expression for \mathbf{v}_1 is achieved by combining our expression for \mathbf{J}_1 from equation with Gauss' law, Faraday's law and Ampère's law. Rearranging the expression for \mathbf{J}_1 in favour of \mathbf{v}_1 forms

$$\mathbf{v}_1 = \frac{1}{qn_0} [\mathbf{J}_1 - qn_1\mathbf{v}_0]. \quad (246)$$

Substituting in Gauss law for n_1

$$\mathbf{v}_1 = \frac{1}{qn_0} \left[\mathbf{J}_1 - q\mathbf{v}_0 \frac{\epsilon_0 i \mathbf{k} \cdot \mathbf{E}}{q} \right], \quad (247)$$

where \mathbf{J}_1 can then be eliminated in favour of \mathbf{B}_1 and \mathbf{E}_1 by using Ampère's law

$$\mathbf{v}_1 = \frac{1}{qn_0} \left[\frac{i \mathbf{k} \times \mathbf{B}_1}{\mu_0} + \frac{i\omega \mathbf{E}_1}{\mu_0 c^2} - \mathbf{v}_0 \epsilon_0 i \mathbf{k} \cdot \mathbf{E}_1 \right]. \quad (248)$$

Finally, Faraday's law is used to substitute for \mathbf{B}_1 as

$$\mathbf{v}_1 = \frac{1}{qn_0} \left[\frac{i \mathbf{k} \times \mathbf{k} \times \mathbf{E}_1}{\mu_0 \omega} + \frac{i\omega \mathbf{E}_1}{\mu_0 c^2} - \mathbf{v}_0 \epsilon_0 i \mathbf{k} \cdot \mathbf{E}_1 \right] = \frac{i \mathbf{k} \times \mathbf{k} \times \mathbf{E}_1}{\mu_0 \omega q n_0} + \frac{i\omega \mathbf{E}_1}{\mu_0 c^2 q n_0} - \frac{\mathbf{v}_0 \epsilon_0 i \mathbf{k} \cdot \mathbf{E}_1}{q n_0}. \quad (249)$$

This expression for \mathbf{v}_1 can now be used in conjunction with the expression for \mathbf{B}_1 in the Force Balance equation

$$\omega' \left(\frac{i\mathbf{k} \times (\mathbf{k} \times \mathbf{E}_1)}{\mu_0 \omega q n_0} + \frac{i\omega \mathbf{E}_1}{\mu_0 c^2 q n_0} - \frac{\mathbf{v}_0 \epsilon_0 i\mathbf{k} \cdot \mathbf{E}_1}{q n_0} \right) = q \left[\mathbf{E}_1 + \left(\frac{i\mathbf{k} \times (\mathbf{k} \times \mathbf{E}_1)}{\mu_0 \omega q n_0} + \frac{i\omega \mathbf{E}_1}{\mu_0 c^2 q n_0} - \frac{\mathbf{v}_0 \epsilon_0 i\mathbf{k} \cdot \mathbf{E}_1}{q n_0} \right) \times \mathbf{B}_0 + \left(\mathbf{v}_0 \times \frac{\mathbf{k} \times \mathbf{E}_1}{\omega} \right) \right] \quad (250)$$

or

$$\frac{i\mathbf{k} \times (\mathbf{k} \times \mathbf{E}_1)}{\mu_0 \omega q n_0} + \frac{i\omega \mathbf{E}_1}{\mu_0 c^2 q n_0} - \frac{\mathbf{v}_0 \epsilon_0 i\mathbf{k} \cdot \mathbf{E}_1}{q n_0} - \frac{q}{\omega'} \left[\mathbf{E}_1 + \left(\frac{i\mathbf{k} \times (\mathbf{k} \times \mathbf{E}_1)}{\mu_0 \omega q n_0} + \frac{i\omega \mathbf{E}_1}{\mu_0 c^2 q n_0} - \frac{\mathbf{v}_0 \epsilon_0 i\mathbf{k} \cdot \mathbf{E}_1}{q n_0} \right) \times \mathbf{B}_0 + \left(\mathbf{v}_0 \times \frac{\mathbf{k} \times \mathbf{E}_1}{\omega} \right) \right] = 0 \quad (251)$$

Equation (251) will form the basis for eliminating \mathbf{E}_1 by setting up an $\bar{\mathbf{M}} \cdot \mathbf{E}_1 = 0$ matrix. In order to do this we need to decompose equation (251) into its directional components ($\hat{e}_x, \hat{e}_y, \hat{e}_z$).

Decomposition of equation (251) along with combining matrix expressions and then assuming that \mathbf{k} is in the xz plane, so that $\mathbf{k}_y = 0$, allows the following to be formed

$$\begin{bmatrix} M_{xx} & M_{xy} & M_{xz} \\ M_{yx} & M_{yy} & M_{yz} \\ M_{zx} & M_{zy} & M_{zz} \end{bmatrix} \cdot \begin{bmatrix} \mathbf{E}_{1x} \\ \mathbf{E}_{1y} \\ \mathbf{E}_{1z} \end{bmatrix} = 0 \quad (252)$$

$$M_{xx} = \frac{i(-k_z^2)}{\mu_0 \omega q n_0} + \frac{i\omega}{\mu_0 c^2 q n_0} + \frac{-i\epsilon_0 \mathbf{v}_{0x} \mathbf{k}_x}{q n_0} - \frac{q}{\omega'} + \frac{i\epsilon_0 \mathbf{B}_{0z} \mathbf{v}_{0y} \mathbf{k}_x}{\omega' n_0} - \frac{q}{\omega'} (-\mathbf{v}_{0z} \mathbf{k}_z) \quad (253)$$

$$M_{xy} = \frac{-i\mathbf{B}_{0z} (-k_x^2 - k_z^2)}{\omega' \mu_0 \omega n_0} - \frac{i\omega \mathbf{B}_{0z}}{\omega' \mu_0 c^2 n_0} - \frac{q}{\omega' \omega} \mathbf{v}_{0y} \mathbf{k}_x \quad (254)$$

$$M_{xz} = \frac{i(\mathbf{k}_z \mathbf{k}_x)}{\mu_0 \omega q n_0} + \frac{i\epsilon_0 \mathbf{B}_{0z} \mathbf{v}_{0y} \mathbf{k}_z}{\omega' n_0} - \frac{q}{\omega' \omega} \mathbf{v}_{0z} \mathbf{k}_x - \frac{i\epsilon_0}{q n_0} \mathbf{v}_{0x} \mathbf{k}_z \quad (255)$$

$$M_{yx} = \frac{-i\mathbf{B}_{0z}(\mathbf{k}_z^2)}{\omega' \mu_0 \omega n_0} + \frac{i\omega \mathbf{B}_{0z}}{\omega' \mu_0 c^2 n_0} + \frac{i\epsilon_0 \mathbf{B}_{0z}(-\mathbf{v}_{0x} \mathbf{k}_x)}{\omega' n_0} - \frac{i\epsilon_0}{q n_0} \mathbf{v}_{0y} \mathbf{k}_x \quad (256)$$

$$M_{yy} = \frac{i(-k_x^2 - k_z^2)}{\mu_0 \omega q n_0} + \frac{i\omega}{\mu_0 c^2 q n_0} - \frac{q}{\omega'} - \frac{q}{\omega' \omega} (-\mathbf{v}_{0x} \mathbf{k}_x - \mathbf{v}_{0z} \mathbf{k}_z) \quad (257)$$

$$M_{yz} = \frac{-i\mathbf{B}_{0z}(-\mathbf{k}_z \mathbf{k}_x)}{\omega' \mu_0 \omega n_0} + \frac{i\epsilon_0 \mathbf{B}_{0z}(-\mathbf{v}_{0x} \mathbf{k}_z)}{\omega' n_0} - \frac{i\epsilon_0}{q n_0} \mathbf{v}_{0y} \mathbf{k}_z \quad (258)$$

$$M_{zx} = \frac{i(\mathbf{k}_x \mathbf{k}_z)}{\mu_0 \omega q n_0} - \frac{q}{\omega' \omega} (\mathbf{v}_{0x} \mathbf{k}_z) - \frac{i\epsilon_0}{q n_0} \mathbf{v}_{0z} \mathbf{k}_x \quad (259)$$

$$M_{zy} = \frac{-q}{\omega' \omega} \mathbf{v}_{0y} \mathbf{k}_z \quad (260)$$

$$M_{zz} = \frac{i(-k_x^2)}{\mu_0 \omega q n_0} + \frac{i\omega}{\mu_0 c^2 q n_0} - \frac{i\epsilon_0 \mathbf{v}_{0z} \mathbf{k}_z}{q n_0} - \frac{q}{\omega'} - \frac{q}{\omega' \omega} (-\mathbf{v}_{0x} \mathbf{k}_x) \quad (261)$$

Where ω' is now

$$\omega' = im[\mathbf{v}_{0x} \mathbf{k}_x + \mathbf{v}_{0z} \mathbf{k}_z - \omega] \quad (262)$$

Since we're in the xz plane we can write $\mathbf{k}_x = \mathbf{k}_\perp = k \sin \theta$ and $\mathbf{k}_z = \mathbf{k}_\parallel = k \cos \theta$ where θ is the angle between $\mathbf{B}_\parallel = \mathbf{B}_{0z}$ and wave propagation direction since we're considering plane waves. This is an important step before normalising as we use the relation for refractive index $N = \frac{\omega k}{c}$ and let $\mathbf{U} = \frac{\mathbf{v}_0}{c}$ where $\mathbf{U}_x = \frac{v_x}{c}$, $\mathbf{U}_y = \frac{v_y}{c}$, $\mathbf{U}_z = \frac{v_z}{c}$. By this

$$\omega' = im[\mathbf{v}_{0x} k \sin \theta + \mathbf{v}_{0z} k \cos \theta - \omega] \quad (263)$$

$$\omega' = im[\mathbf{U}_x \omega N \sin \theta + \mathbf{U}_y \omega N \cos \theta - \omega] \quad (264)$$

$$\omega' = im\omega[N(\mathbf{U}_x \sin \theta + \mathbf{U}_y \cos \theta - \frac{1}{N})] \quad (265)$$

It's also key to note that each element in matrix (252) has equal dimensions, and since we have $\bar{\mathbf{M}} \cdot \mathbf{E} = 0$ we can multiply through by a scalar with no consequence to the R.H.S of the equation. This allows us to look at any single element to obtain a normalisation factor which we can apply on $\bar{\mathbf{M}}$.

Observing M_{zy} as it is the most simple element, we have

$$M_{zy} = \frac{-q}{\omega'\omega} \mathbf{v}_{0y} k \cos \theta \quad (266)$$

$$M_{zy} = \frac{-q}{im\omega[N(\mathbf{U}_x \sin \theta + \mathbf{U}_y \cos \theta - \frac{1}{N})]} \mathbf{U}_y N \cos \theta \quad (267)$$

$$M_{zy} = \frac{iq}{m\omega} \frac{\mathbf{U}_y \cos \theta}{[(\mathbf{U}_x \sin \theta + \mathbf{U}_y \cos \theta - \frac{1}{N})]} \quad (268)$$

In order to make M_{zy} dimensionless we would have to multiply through by $\frac{m\omega}{iq}$. This is our normalisation factor.

With this in mind, we can now normalise each element of matrix (252). Let $\mathbf{U}_\theta = (\mathbf{U}_x \sin \theta + \mathbf{U}_y \cos \theta - \frac{1}{N})$

$$M_{xx} = -\frac{N^2 \cos^2 \theta}{X} + \frac{1}{X} - \frac{\mathbf{U}_x N \sin \theta}{X} + \frac{1}{NU_\theta} - \frac{iY \mathbf{U}_y \sin \theta}{X U_\theta} - \frac{\mathbf{U}_z \cos \theta}{U_\theta} \quad (269)$$

$$M_{xy} = -\frac{iY N}{X U_\theta} + \frac{iY}{X NU_\theta} + \frac{\mathbf{U}_y \sin \theta}{U_\theta} \quad (270)$$

$$M_{xz} = \frac{N^2}{X} \sin \theta \cos \theta - \frac{iY \mathbf{U}_y \cos \theta}{X U_\theta} + \frac{\mathbf{U}_z \sin \theta}{U_\theta} - \frac{\mathbf{U}_x N \cos \theta}{X} \quad (271)$$

$$M_{yx} = \frac{iY N \cos^2 \theta}{X U_\theta} - \frac{iY}{X NU_\theta} + \frac{iY \mathbf{U}_x \sin \theta}{X U_\theta} - \frac{\mathbf{U}_y N \sin \theta}{X} \quad (272)$$

$$M_{yy} = -\frac{N^2}{X} + \frac{1}{X} + \frac{1}{NU_\theta} - \left(\frac{\mathbf{U}_x \sin \theta + \mathbf{U}_z \cos \theta}{U_\theta} \right) \quad (273)$$

$$M_{yz} = -\frac{iY N \sin \theta \cos \theta}{X U_\theta} + \frac{iY \mathbf{U}_x \cos \theta}{X U_\theta} - \frac{\mathbf{U}_y N \cos \theta}{X} \quad (274)$$

$$M_{zx} = \frac{N^2}{X} \sin \theta \cos \theta + \frac{\mathbf{U}_x \cos \theta}{U_\theta} - \frac{\mathbf{U}_z N \sin \theta}{X} \quad (275)$$

$$M_{zy} = \frac{\mathbf{U}_y \cos \theta}{U_\theta} \quad (276)$$

$$M_{zz} = -\frac{N^2 \sin^2 \theta}{X} + \frac{1}{X} - \frac{\mathbf{U}_z N \cos \theta}{X} + \frac{1}{NU_\theta} - \frac{\mathbf{U}_x \sin \theta}{U_\theta} \quad (277)$$

It's necessary to investigate the reliability of these results before using them to conduct further research. Taking the matrix comprised of elements (269) \rightarrow (277) and setting $\mathbf{v}_0 = 0$ we would expect to find a scalar which we could multiply said matrix through by to give the previous textbook result shown in matrix. This is not what we see, while this is not reassuring it does not mean that these results are wrong. It is possible to obtain the same solution from two different equations, although further analysis is required. It is possible to return to matrix(X) by multiplying through by a 3x3 matrix. This 3x3 matrix is very complicated and requires computationally simultaneously solving equations to obtain but it does exist. This is reassuring but it is not a conclusive result.

Setting $\mathbf{v}_0 = 0$ and using elements (269) \rightarrow (277) to plot the dispersion relation analogous the method using in section, we would expect an identical result to that obtained in figure. Figure shows such an analysis.

References

- [1] I. Arto *et al.*, *Energy Sustain. Dev.*, 2016, **33** 1-13.
- [2] J. Klugman *et al.*, *J. Econ. Inequal.*, 2011, **9** 249–288.
- [3] Department for Economic and Social affairs, “World populations prospects 2019”, 2019, [United Nations](#).

- [4] Department for Business & Energy & Industrial Strategy, “Uk energy statistics, 2019 & q4 2019”, 2019, [London: The Stationery Office](#).
- [5] Department for Business & Energy and Industrial Strategy, “Fuel used in electricity generation and electricity supplied (et 5.1 - quarterly)”, 2020, [London: The Stationery Office](#).
- [6] D. MacKay, “Sustainable energy - without the hot air”, 2008, [UIT Cambridge](#).
- [7] Department for Business & Energy & Industrial Strategy, “Electricity generation costs”, 2016, [London: The Stationery Office](#).
- [8] Committee on Climate Change, “Biomass in a low-carbon economy”, 2018, [UK Gov: Committee on Climate Change](#).
- [9] Department for Business & Energy & Industrial Strategy, “Energy trends”, 2020, [London: The Stationery Office](#).
- [10] BP, “Bp statistical review of world energy”, 2020, [BP](#).
- [11] N. E. Agency and the International Atomic Energy Agency, “Uranium 2016: Resources, production and demand”, 2016, [OECD](#).
- [12] W. N. Association, “Nuclear power in france”, 2019, [WNA](#).
- [13] World Bank, “Databank: World development indicators”, 2010, [WB](#).
- [14] J. Trancik, *Nature*, 2014, [507 302](#).
- [15] N. Taylor *et al.*, *Fusion Eng. Des.*, 2017, [124 1177-1180](#).
- [16] A. Harmes *et al.*, *Principles of Fusion Energy*. *World Scientific*, 2000.
- [17] E. Blackman, *University of Rochester*, 2021, [ast104](#).
- [18] J. Friedberg, *Plasma Physics and Fusion Energy*. *Cambridge University Press*, 2007.

- [19] C. Braams and P. Stott, *Nuclear Fusion. Half a Century of Magnetic Confinement Research*. IOP Publishing Ltd, 2002.
- [20] J. Parisi J. Ball, *The Future of Fusion Energy*. World Scientific, 2018.
- [21] D. Reiter *et al.*, *Plasma Phys. Control. Fusion*, 1991, **33** 1579.
- [22] M. Kovari *et al.*, *Nucl. Fusion*, 2018, **58** 026010.
- [23] I. Cook *et al.*, *Fusion Eng. Des.*, 2002, **63-64** 25-33.
- [24] United States General Accounting Office., “Nuclear weapons. challenges remain for successful implementation of doe’s tritium supply decision”, 2000, [GAO](#).
- [25] P. Pereslavytsev *et al.*, *Fusion Eng. Des.*, 2016, **109-111** 1207-1211.
- [26] S. Segantini *et al.*, *Fusion Eng. Des.*, 2020, **154** 111531.
- [27] M. Mahdavi and E. Asadi, *Open J. Microphys.*, 2013, **3** 8–11.
- [28] G. Martin *et al.*, *Open J. Microphys.*, 2017, **6** 171-179.
- [29] D. Clery, *Science*, 2015, **348** 854-856.
- [30] B. Lloyd, *Plasma Phys. Control. Fusion*, 1998, **40** A119.
- [31] P. Heinrich, *Plasma Phys. Control. Fusion*, 2007, **49** R1.
- [32] Y.-K. Peng and D. Strickler, *Nucl. Fusion*, 1986, **26** 769.
- [33] G. Bateman, *MHD instabilities*. MIT Press, 1979.
- [34] D. Robertson, *Plasma Phys. Control. Fusion*, 1999, **41** A143.
- [35] F. Troyon *et al.*, *Plasma Phys. Control. Fusion*, 1984, **26** 209.
- [36] E. Strait *et al.*, *Phys. Rev. Lett.*, 1995, **74** 2483.
- [37] J. Reusch *et al.*, *Phys. Plasmas*, 2018, **25** 056101.
- [38] L. Spitzer, *Phys. Fluids*, 1958, **1** 253.

- [39] R. Hemsworth, *Nucl. Fusion*, 2006, [46 E01](#).
- [40] T. Jones *et al.*, *Fusion Eng. Des.*, 1999, [47 205-231](#).
- [41] T. Oikawa *et al.*, *Nucl. Fusion*, 2001, [41 1575](#).
- [42] F. D. Halpern *et al.*, *Phys. Plasmas*, 2008, [15 062505](#).
- [43] M. Kikuchi, *Nucl. Fusion*, 2008, [30 265](#).
- [44] H. Wilson *et al.*, *Nucl. Fusion*, 2004, [44 917](#).
- [45] M. Roberto and R. Galvao, *Nucl. Fusion*, 1992, [32 1666](#).
- [46] M. Gryaznevich *et al.*, *Fusion Eng. Des.*, 2017, [123 177 - 180](#).
- [47] P. Carle *et al.*, *Rev. Sci. Instrum*, 2016, [87 11E104](#).
- [48] T. J. McGuire, *US Patent Specification*, 2018, [US2014/0301518](#).
- [49] M. Mazzucato, *The Entrepreneurial State*. Penguin, 2018.
- [50] M. Gryaznevich *et al.*, *Phys. Rev. Lett.*, 1998, [80 3972](#).
- [51] J. Harrison *et al.*, *Nucl. Fusion*, 2019, [59 11](#).
- [52] J. Berkery *et al.*, *Nucl. Fusion*, 2020, [62 8](#).
- [53] G. Garstka *et al.*, *Nucl. Fusion*, 2006, [46 8](#).
- [54] A. Palmer *et al.*, *61st Annual Meeting of the APS Division of Plasma Physics*, 2019, [64 11](#).
- [55] M. Ono *et al.*, *Nucl. Fusion*, 2000, [40 3Y](#).
- [56] J. Menard *et al.*, *Nucl. Fusion*, 2017, [57 10](#).
- [57] V. Gusev *et al.*, *Tech. Phys.*, 1999, [44 1054–1057](#).
- [58] V. Minaev *et al.*, *J. Phys.: Conf. Ser*, 2018, [0194 012001](#).
- [59] G. Ludwig *et al.*, *Braz. J. Phys.*, 2003, [33 4](#).
- [60] Y. Ono *et al.*, *Nucl. Fusion*, 2003, [43 8](#).

- [61] N. Holtkamp, *Fusion Eng. Des.*, 2007, **82** 427-434.
- [62] D. Start, *Phys. Rev. Lett.*, 1998, **80** 4681.
- [63] G. Wagner *et al.*, *Phys. Rev. Lett.*, 1982, **49** 1408.
- [64] K. Miyamoto, *Plasma physics for controlled fusion*. Springer, 2016.
- [65] P. Abdoul *et al.*, *arXiv:1408.0742*, 2014, **1408** 0742.
- [66] A. Murari *et al.*, *Nucl. Fusion*, 2012, **52** 063016.
- [67] E. Fredrickson *et al.*, *Nucl. Fusion*, 1986, **26** 849.
- [68] J. Callen, *Phys. Rev. Lett.*, 1977, **39** 1540.
- [69] W. Solomon *et al.*, *Phys. Rev. Lett.*, 2014, **113** 135001.
- [70] J. Zielinski *et al.*, *Phys. Plasmas*, 2017, **24** 024501.
- [71] C. Horton *et al.*, *ITER Physics*. World Scientific Publishing, 2015.
- [72] A. Hirose, *Phys. Rev. Lett.*, 2003, **92** 025001.
- [73] J. Hillesheim *et al.*, *Plasma Phys. Control. Fusion*, 2015, **58** 014020.
- [74] M. Barnes *et al.*, *GS2 team*, 2020, [Zendo](#).
- [75] J. Drake *et al.*, *Phys. Plasmas*, 1976, **20** 1341.
- [76] G. Chen *et al.*, *Plasma Phys. Control. Fusion*, 2020, **62** 085009.
- [77] D. J. Applegate *et al.*, *Plasma Phys. Control. Fusion*, 2007, **49** 1113.
- [78] N. T. Gladd *et al.*, *Phys. Fluids*, 1980, **23** 1183.
- [79] D. Dickenson *et al.*, *Plasma Phys. Control. Fusion*, 2013, **55** 074006.
- [80] D. Told *et al.*, *Phys. Plasmas*, 2008, **15** 102306.
- [81] H. Doerk *et al.*, *Phys. Rev. Lett.*, 2011, **106** 155003.
- [82] P. Catto, *Phys. Fluids*, 1981, **24** 243.

- [83] J. Connor, *Plasma Phys. Control. Fusion*, 1990, **32** 10.
- [84] C. Roach *et al.*, *Plasma Phys. Control. Fusion*, 2005, **47** B323.
- [85] A. B. Rechester and M. N. Rosenbluth, *Phys. Rev. Lett.*, 1977, **40** 38.
- [86] A. B. Rechester and T. H. Stix, *Phys. Rev. Lett.*, 1975, **36** 587.
- [87] K. Wong *et al.*, *Phys. Rev. Lett.*, 2007, **99** 135003.
- [88] W. Guttenfelder *et al.*, *Phys. Rev. Lett.*, 2011, **106** 155004.
- [89] A. Rechester *et al.*, *Phys. Rev. Lett.*, 1978, **40** 38.
- [90] J. Drake *et al.*, *Phys. Rev. Lett.*, 1980, **44** 994.
- [91] A. Gondhalakar *et al.*, *Masachusetts Institute of Technology Report*, 1978, [PFC/RR-78-15](#).
- [92] W. Guttenfelder *et al.*, *Phys. Plasmas*, 2012, **19** 022506.
- [93] D. R. Smith *et al.*, *Plasma Phys. Control. Fusion*, 2011, **53** 3.
- [94] M. Hirsch *et al.*, “Doppler reflectometry for the investigation of propagating density perturbations”, *Plasma Phys. Control. Fusion*, 2001, **43** 1641.
- [95] H. M. *et al.*, in *Proceedings of 4th International Reflectometry Workshop, Cadarache, France, 1999, report*, [EUR-CEA-FC-1674](#).
- [96] D. Thomas *et al.*, *Nucl. Fusion*, 2016, **56** 026013.
- [97] E. Gusakov and A. Surkov, *Plasma Phys. Control. Fusion*, 2004, **46** 1143.
- [98] X. Zou *et al.*, *Phys. Rev. Lett.*, 1995, **75** 1090.
- [99] E. mj/olhus, *Radio Science*, 1990, **26** 1321-1339.
- [100] M. Boyd and J. Sanderson, *The physics of plasmas. Cambridge University Press*, 2003.
- [101] K. Budden, *Proc. R. Soc. Lond. A*, 1952, **1215** 215–233.

- [102] T. J. Team, *Plasma Phys. Control. Fusion*, 1991, **33** 1453.
- [103] M. Mockler *et al.*, *9th European Conference on Antennas and Propagation (EuCAP)*, 2015, 1-5.
- [104] A. Taflove and S. Hagness, *Phys. Plasmas*, 1996, **3** 4046.
- [105] J. Schneider, *Understanding the finite-difference time-domain method*, 2010, [WSU](#).
- [106] U. Inan and R. Marshall, *Phys. Plasmas*, 1996, **3** 4046.
- [107] K. Yee, *IEEE Trans. Antennas Propag.*, 1966, **14** 302.
- [108] T. Williams, *University of York*, 2014, [uk.bl.ethos.647055](#).
- [109] T Williams, *Full-Wave Simulation of High-Frequency Electromagnetic Propagation Through Inhomogeneous Plasma*, 2014, [Whiterose](#).
- [110] M. Thomas, *3D full-wave modelling of microwave interactions with plasma density fluctuations*, 2018, [Whiterose](#).
- [111] T. Williams *et al.*, *Plasma Phys. Control. Fusion*, 2014, **56** 075010.
- [112] K. A *et al.*, *Plasma Phys. Control. Fusion*, 2008, **50** 085018.
- [113] M. Thomas *et al.*, *arXiv*, 2017, [arXiv:1710.03028v1](#).
- [114] A. Köhn *et al.*, *Plasma Phys. Control. Fusion*, 2008, **50** 085018.
- [115] A. Ram and S. Schultz, *Physics of Plasmas*, 2000, **7** 4084.
- [116] R. Courant *et al.*, *IBM Journal of Research and Development*, 1967, **11** 215-234.
- [117] O. Svelto, *Principles of Lasers*. Springer, 2010.
- [118] F. Hansen *et al.*, *Plasma Phys. Control. Fusion*, 1985, **27** 1077.
- [119] R. Groebner and C. T.N., *Plasma Phys. Control. Fusion*, 1998, **40** 673.

- [120] B. Dudson and J. Leddy, *Plasma Phys. Control. Fusion*, 2017, **59** 054010.
- [121] F. L. Hinton and H. R. D., *Rev. Mod. Phys*, 1976, **48** 239.
- [122] J. Hugill, *Nucl. Fusion*, 1983, **23** 331.
- [123] B. Scott, *Plasma Phys. Control. Fusion*, 2006, **48** B277.
- [124] L. Spitzer, *Physics of Fully Ionized Gases*. Dover Publications, inc., 1962.
- [125] J. Leddy *et al.*, *Plasma Phys. Control. Fusion*, 2015, **57** 125016.
- [126] D. R. Nicholson, *Introduction to Plasma Theory*. John Wiley and Sons, 1983.
- [127] Y. Klimontovich, *Ann. Phys*, 1982, **39** 417.
- [128] S. Braginskii, *Reviews of Plasma Physics*, 1965, **1** 205-311.
- [129] B. Scott, *Plasma Phys. Control. Fusion*, 2006, **48** B277.
- [130] B. Scott, *Phys. Plasmas*, 2005, **12** 102307.
- [131] W Dorland and G. Hammett, *Phys. Fluids B*, 1993, **5** 812.
- [132] M. Beer and G. Hammett, *Phys. Plasmas*, 1996, **3** 4046.
- [133] A. Mikhailovskii and T. V., *Plasma Physics*, 1971, **13** 9.
- [134] P. Manz *et al.*, *Plasma Phys. Control. Fusion*, 2018, **60** 085002.
- [135] V. Zheleznyakov *et al.*, *Sov. Phys. Usp*, 1983, **26** 877.
- [136] T Lehner *et al.*, *Europhys. Lett.*, 1989, **8** 759.
- [137] L Vahala *et al.*, *Phys. Fluids B*, 1992, **4** 619.
- [138] H. Sun *et al.*, *Plasma Phys. Control. Fusion*, 2015, **57** 125011.
- [139] J. Pinzón *et al.*, *Plasma Phys. Control. Fusion*, 2017, **59** 035005.
- [140] S. Coda *et al.*, *Plasma Phys. Control. Fusion*, 2000, **42** B311.
- [141] C. Petty *et al.*, *Nucl. Fusion*, 2017, **57** 116057.

- [142] E. Poli *et al.*, *Comput. Phys. Commun.*, 2001, **136** 90.
- [143] G. Fishpool *et al.*, *J. Nucl. Mater.*, 2013, **438** S356-S359.
- [144] E. Havlíčková *et al.*, *Plasma Phys. Control. Fusion*, 2015, **57** 115001.
- [145] B Schunke *et al.*, *Rev. Sci. Instrum.*, 2016, **87** 02C101.
- [146] R. Solano, *Phys. Plasmas*, 1996, **3** 1187.
- [147] G. Hartfuss HJ. Thomas, *Fusion Plasma Diagnostics with mm Waves*. Wiley Online Library, 2013.
- [148] M. Thumm, *Nucl. Fusion*, 2019, **59** 07300.
- [149] H. Laqua, *Plasma Phys. Control. Fusion*, 2007, **49** R1.
- [150] J Urban, *Nucl. Fusion*, 2011, **51** 8.
- [151] B. Eliasson *et al.*, 2020, STEP Report, WP 4.2(a): Fourier Full-Wave (FFW) simulations of O-X-B mode conversion. Technical report.
- [152] A. Köhn *et al.*, *Plasma Phys. Control. Fusion*, 2018, **60** 075006.
- [153] A Köhn *et al.*, *Phys. Plasmas*, 2011, **18** 082501.
- [154] D. A. Thomas *et al.*, *Nucl. Fusion*, 2016, **56** 026013.
- [155] CCFE, 2019, MAST Upgrade Research Plan, November 2019. Technical report.
- [156] V Francesco, *Electron Bernstein emission diagnostic of electron temperature profile at W7-AS Stellarator*, 2003, [IPP](#).
- [157] F. Fritsch and R. Carlson, *SIAM Journal on Numerical Analysis.*, 1980, **13** 238-246.
- [158] P. Virtanen and R. Gommers, *Nature Methods.*, 2020, **12** 261–272.
- [159] E. Gospodchikov *et al.*, *Plasma Phys. Control. Fusion.*, 2012, **54** 045009.